Low Energy Electrodynamics of High T_c Superconductors

Printed by: PrintPartners Ipskamp B.V., Enschede, The Netherlands

ISBN 90-9010803-3

Rijksuniversiteit Groningen

Low Energy Electrodynamics of High T_c Superconductors

Proefschrift

ter verkrijging van het doctoraat in de
Wiskunde en Natuurwetenschappen
aan de Rijksuniversiteit Groningen
op gezag van de
Rector Magnificus, Dr. F. van der Woude
in het openbaar te verdedigen op
vrijdag 17 oktober 1997
des namiddags te 4.15 uur

door

Bokke Johannes Feenstra

geboren op 12 februari 1969
te Rijs

Promotor: Prof. Dr. D. van der Marel

Contents

Chapter 1

Introduction

For both fundamental and applied purposes high T_c superconductivity has been a much studied subject for researchers in many different disciplines, ever since its discovery by Bednorz and Müller in 1986 [1]. Considerable effort has been put into comprehending the mechanism of the pairing, giving rise to critical temperatures much higher than expected from conventional ideas. Up to 1986 the highest T_c achieved was 23 K for Nb_3Ge, which has been increased to the contemporary record of 134 K for $Hg_2Ba_2Ca_2Cu_3O_{10-\delta}$ at ambient pressure. The critical temperature of this compound can be raised up to 164 K by applying high pressure.

For the characterization of the cuprates, optical measurement techniques such as Fourier Transform Spectroscopy are playing a major role, yielding information about the dielectric function of the sample over a wide frequency range [2]. A problem with conventional reflectometry is that one obtains information about just one independent parameter, requiring the use of Kramers-Kronig relations to acquire the complete dielectric response. In this case the experimentally covered frequency range needs to be extended to zero and infinite frequency, requiring the employment of low- and high frequency extrapolations, thereby enhancing the uncertainty in the resulting dielectric function. This problem can be circumvented by using special techniques such as ellipsometry [3], or by measuring both transmission *and* reflection on the same sample.

A similar problem exists in experiments performed in the mm-wave region, where one usually aims to measure both the surface resistance (R_s) and the surface reactance (X_s). A large amount of data has been obtained using resonant cavity techniques, either in a perturbative or in an endplate mode [4–6]. From the shift in resonance frequency and the change in resonance width, caused by the introduction of the sample, one can obtain both the real and imaginary parts of the dielectric function. Another method to obtain the complex dielectric function at mm-wave frequencies is to measure both the phase and the amplitude using a Mach-Zehner interferometer in a quasi-optical configuration [7]. If only the amplitude is measured over a *broad* frequency range the complex optical response function can also be determined, as will be shown in chapter 6 of this thesis. In this case we can infer the amplitude and phase information from the height and the position of the interference peaks.

1.1 Pairing Symmetry

One of the most important questions which has been addressed in the last ten years, is the *mechanism* leading to the pairing in the high T_c oxides. Several theoretical models have been proposed, ranging from the interlayer coupling model of Anderson and Chakravarty [8], the spin fluctuation theory advocated by for instance Pines and Scalapino [9, 10] to models using plasmon mediated superconductivity [11] or bipolarons [12]. A possible way to settle this question experimentally is to establish the *symmetry* of the pairing, and therefore the superconducting energy gap. Although it might be difficult to decide unquestionably what the mechanism is, on the basis of the symmetry one will be able to rule out certain propositions. For conventional superconductors the Cooper pairs have a simple isotropic s-wave symmetry predicted by BCS-theory [13]. This means that the gap will have the same nonzero value of 2Δ everywhere in k-space (fig. 1.1a). In the novel ceramic superconductors the situation appears to be different. More and more experimental evidence is being collected, showing that there are certain points or lines of points in momentum space where the energy gap is zero, i.e. nodes [14–18]. This would be the case if the wave function of the Cooper pairs were for instance to have a d-wave symmetry. Than the gap would be zero if $k_x = \pm k_y$, which implies furthermore that it would have a different sign in certain parts of k-space (fig. 1.1b). Both properties will have very important implications from

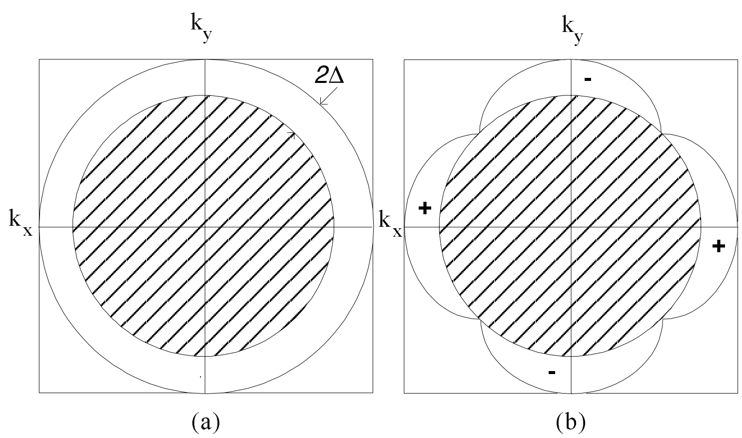

Figure 1.1: *The energy gap for two possible pairing symmetries: s-wave (a) and d-wave (b). The s-wave symmetry has an isotropic gap value of 2Δ, while for a d-wave symmetry the gap vanishes and changes sign at $k_x = \pm k_y$.*

both a fundamental and an applied point of view.

The d-wave scenario is especially attractive in the high T_c's since the on-site Coulomb repulsion is very large, making them so-called Mott-Hubbard insulators in the undoped case. In case of a d-wave pairing symmetry the two electrons composing the Cooper pair avoid being on the same site, thereby lowering their energy.

1.2 mm-Wave Properties

In the process of establishing the symmetry of the order parameter of the high temperature superconductors, electrodynamical properties such as the penetration depth (λ) and the dynamical conductivity (σ_1) yield important information. For instance, the temperature dependence of λ can shed light on the presence of nodes in the energy gap. For a conventional BCS-superconductor, the intrinsic behavior shows an *exponential* temperature dependence, caused by the opening of a finite energy gap in the excitation spectrum in the superconducting state. In the ordinary BCS-description using electron-phonon coupling as the attractive force forming Cooper pairs this gap is isotropic in momentum space. However, it was shown by Annet and co-workers in 1991 [19], that for a superconductor having lines of nodes within the gap, for instance in case of a d-wave symmetry, this dependence is linear. At temperatures lower than 40 K Hardy *et al.* [4] observed the linear temperature dependence in a $YBa_2Cu_3O_{6.95}$ single crystal using a split-ring resonator at 1 GHz.

The linear behavior, believed to be intrinsic was however initially never observed in thin films. Several groups found other dependencies ranging from T^2 to exponential [6, 20–22], presumably originating from extrinsic sources such as resonant impurity scattering or weak links [19, 23, 24]. De Vaulchier *et al.* [25] were the first to confirm the linear dependence in a $YBa_2Cu_3O_{7-\delta}$ thin film using mm-wave transmission. They also noticed the coexistence of the T^2 dependence and a large λ_L, using the *absolute* information obtained by this technique. The coexistence was taken to be evidence for the extrinsic nature of the nonlinear dependence, i.e. weak links [24].

Other unconventional behavior at mm-wave frequencies can be observed in the dynamical conductivity, σ_1 [26–28]. Unlike the reduced σ_1 expected for a BCS-superconductor, the conductivity is largely *enhanced* in going into the superconducting state, showing a broad peak at temperatures ranging from 40 to 70 K. The amplitude and position of the peak are highly frequency dependent, showing some similarities with a BCS-coherence peak [29, 30]. However, the maximum in σ_1 for the cuprates originates from an anomalously reduced scattering rate (,) below T_c, having a larger influence on the conductivity than the decreasing quasiparticle density. Using Zn-doping in $YBa_2Cu_3O_{6.95}$ single crystals Bonn *et al.* [31] were able to show that the maximum in conductivity is reduced if the disorder in the material is enhanced, as one would expect if this is caused by , . The strong reduction of , indicates that ordinary electron phonon scattering cannot be the *main* scattering mechanism. This is further supported by the linear temperature dependence of the dc-resistivity in the normal state, indicating that the "normal" state doesn't follow ordinary Fermi liquid predictions.

1.3 Fundamental and Applied Aspects of the use of Thin Films

The main focus of this dissertation will be on the characterization of superconducting *thin films* using optical spectroscopy in several different frequency ranges. Apart from the fundamental interest in the high T_c cuprates, superconducting thin films are also of considerable significance in the development of devices using superconducting technology. Although high temperature superconductors have already proven to be useful for applications, the major breakthrough expected in 1986 has not yet been established. A large effort has thus been put into characterizing thin films [5,6,22] and understanding the (fundamental) reasons for the existence of phenomena hampering their use, such as their relatively large residual surface resistance. The surface resistance of HTSC thin films and single crystals has been measured using a variety of different techniques. Some of the important ones are cavity perturbation techniques [32–34] and coherent THz spectroscopy [27,28].

Already from the start of high temperature superconductivity [1], it was clear that making high quality films needed for applications is extremely difficult. For instance, attaining and sustaining the right stoichiometry has proven to be a major problem. This became especially clear in the search for the intrinsic temperature dependence of the penetration depth [4,5,32]. Two years after its prediction by Annet and co-workers, the linear behavior was confirmed in single crystals [4], however confirmation in thin films wasn't realized until 1996 [25].

Another problem in making thin films is the occurrence of twinning and grain boundaries [24]. Zhang and co-workers showed that for an untwinned $YBa_2Cu_3O_{6.95}$ single crystal the surface resistance is lower [32]. This implies that one reduces the loss in thin films by minimizing the twinning.

However, the problem to make thin films with a low (residual) surface resistance is not restricted to the actual deposition and processing. The fundamental, intrinsic properties of the high T_c materials also impose a challenge to the material scientists. It was shown by Nuss *et al.* [27], using coherent THz spectroscopy, that upon entering the superconducting state the optical conductivity is enhanced, reaching a maximum in the temperature range of 40 to 70 K. The maximum in conductivity also appears in the surface resistance since under the conditions generally encountered in HTSC's these are directly proportional. The maximum can be explained by assuming an anomalously large reduction of the quasiparticle scattering rate just below T_c, and is therefore an *intrinsic* source of absorption that one has to deal with. The conductivity and therefore the absorption remain rather high, even at low temperatures. The exact position of the maximum is highly dependent on frequency, and is difficult to be interpreted as a coherence peak, predicted by BCS-theory. Another indication that the coherence factors giving rise to a peak in σ_1 don't play a major role of importance in high T_c's is the absence of the Hebel-Slichter peak in NMR-data. An interesting consequence of the reduced scattering is that one is able to *reduce* the peak in R_s and its overall magnitude artificially by *increasing* the impurity content. This effect was demonstrated by Bonn *et al.*, by replacing a fraction of the Cu-atoms by Zn impurities [31].

The discussion about the exact symmetry of the pairing is, in addition to its fundamental importance, also relevant to the application of the cuprates. If, as many people nowadays believe, the symmetry is d-wave [35], this will have important consequences. In this situation, there are points or lines in k-space where the energy gap is zero, implying the presence of quasiparticles already at infinitesimally small energies and temperatures. This means that in a d-wave superconductor even at extremely low temperatures, a finite residual conductivity will remain. This was shown theoretically by P. A. Lee [36] who found that a d-wave superconductor will have a universal conductivity at $T = 0$ irrespective of the impurity content, at least for low concentrations. Zhang *et al.* [32] showed that in $YBa_2Cu_3O_{6.95}$ single crystals in both the a- and b-axis direction the residual conductivity is indeed approaching the predicted value.

In view of all of the aforementioned information, it is clear that further studies have to be performed in order to realize a situation where HTSC thin films will surpass the existing conventional superconducting technology.

A very interesting fundamental consequence specific to thin films, is related to their dimensionality. There is vast experimental evidence that the cuprates are highly anisotropic in directions parallel and perpendicular to the copper-oxygen planes [37]. For very thin films, one approaches the situation in which we are dealing with an isolated two-dimensional superconductor. This may lead to a Kosterlitz-Thouless-Berezinskii transition [38, 39], which was claimed to have been observed experimentally in $Bi_2Sr_2CaCu_2O_8$ single crystals [40] and in both $Tl_2Ba_2CaCu_2O_8$ and $YBa_2Cu_3O_{7-\delta}$ thin films [41, 42].

Measuring thin films using the aforementioned resonant cavity technique is usually rather complicated, since the only option one has is to utilize the film as the endplate of the cavity. This inevitably leads to leakage, thereby complicating the analysis. We will show in the course of this dissertation that measuring the mm-wave transmission through a thin film can be a good and relatively simple alternative to measure its electromagnetic properties and quality.

1.4 The Quest for the Energy Gap in High T$_c$ Superconductors

The symmetry of the energy gap can uncover the interior of a superconductor, revealing information about the pairing mechanism. While conventional superconductors *do* obey predictions of the BCS-theory having an isotropic s-wave symmetry, the situation in the cuprate superconductors is still unclear. People have speculated about more possibilities than can be mentioned here, ranging from Josephson coupled layers resulting in anisotropic s-wave symmetry [8], spin fluctuation mediated superconductivity leading to d-wave symmetry [9] to gapless superconductivity [43].

The energy gap, its presence, magnitude and symmetry has therefore been studied extensively by numerous techniques, such as ARPES, tunneling and optical spectroscopy [16, 44, 45]. In conjunction with information obtained from other experiments, d-wave symmetry seems to be the most likely candidate to explain the observed results. However, it is often impossible to distinguish a d-wave from a highly anisotropic s-wave gap, as for example with ARPES results due to the insufficient resolution. Therefore one needs additional information about the phase of the energy gap to decide if there are indeed points in k-space where the gap crosses zero and consequently changes sign. This information can be obtained in experiments such as a corner squid, or π-junctions deposited on a tricrystal substrate [14, 15]. *These* experiments also point at a symmetry having nodes in the gap for most high T_c materials.

FIR or mm-wave spectroscopy has proven to be valuable in the late fifties when it was used to verify experimentally the existence of the energy gap in several elemental superconductors [46, 47]. Similar studies have been performed on the cuprates in order to measure their energy gap [45, 48, 49]. Up to now this has not produced the results necessary to resolve the controversy about the symmetry of the pairing. For an s-wave superconductor one expects to see a reflectivity of 100 % for frequencies below the gap, since there are no available states. However, since the superconductors are also very good metals, the deviation from this perfect reflectivity for frequencies exceeding 2Δ will be fairly small and therefore close to the experimental uncertainty. Also, one should consider intrinsic causes for the apparent absence of a clearly defined energy gap in FIR spectra. One of the most plausible reasons is a d-wave symmetry for the pairing wave function, where the zero's will lead to a finite absorption at all temperatures and frequencies. This means a finite conductivity or a reflectivity that won't reach the perfect 100 % at any frequency, since in FIR reflectometry one averages over the entire Fermi surface. One way to enhance the features related to the gap in reflectivity, in order to lift them beyond the usual uncertainty, is to use a grazing angle of incidence Θ [50]. This amplifies the absorption in the superconductor by a factor close to $1/\cos(\Theta)$. This technique was used in our group to show that in $La_{2-x}Sr_xCuO_4$ the gap shows a behavior resembling a d-wave type symmetry rather than the conventional s-wave [51].

Another way to improve the sensitivity to energy gap features is to measure the transmission through a *thin* film. In this case one can focus on measuring a deviation from zero transmission which is easier than measuring a change in 100 % reflectivity. An example of this, clearly showing the presence of a gap, will be highlighted in chapter 5.

1.5 Scope of this Dissertation

In this dissertation we will treat several aspects of the optical characterization of superconducting thin films. In chapter 2 we will treat some of the background material needed for the rest of the dissertation. The possible symmetries for the high T_c superconductors will be discussed in conjunction with their experimental implications. Special attention will be paid to the temperature dependence of both the penetration depth, λ, and the real part of the conductivity, σ_1. The case of a pure superconductor as well as the changes induced by a deliberate introduction of impurities will be treated. Also included in this chapter is an overview of experiments measuring phenomena related to non-equilibrium superconductivity, in particular those making use of optical excitation.

In chapter 3 the formalism for calculating the transmission and reflection coefficients of stratified (in particular two-layer) systems will be treated. Special attention will be paid to experimental situations where the incident angle is nonzero. In such cases the response of the two possible polarizations of the electric field reveals significant information on all crystal directions. Furthermore we will show how one can obtain both the real and imaginary part of the dielectric function in the case where transmission *and* reflection of a thin film are measured.

The experimental setup developed in the initial part of my graduate research will be described in detail in chapter 4. This setup was used for both the mm-wave transmission experiments and the Photo Induced Activation of Mm-wave Absorption (PIAMA) experiments performed at the free electron laser user facility in Nieuwegein (FELIX).

In chapter 5 experimental results obtained using Fourier Transform Spectroscopy in the FIR region are presented. Results on a NbN thin film, a conventional superconductor, will be given. Furthermore a new technique developed in our group, Grazing Angle of Incidence Reflectometry will be introduced, illustrated by showing results on NbN and $Tl_2Ba_2Ca_2Cu_3O_{10}$. This technique can be used to measure the c-axis response of the high T_c cuprates when the incident beam is reflected by the ab-plane, by making use of different polarizations. For the use of this technique in related experiments, for example on $La_{2-x}Sr_xCuO_4$, and its employment to measure the energy gap one should refer to [51].

In chapter 6, we will treat mm-wave transmission experiments performed on superconducting thin films. First, results obtained on two conventional superconductors, MoGe and NbN, will be shown. Both superconductors are simple BCS-systems, as is demonstrated by our results. The same experiments have been performed on several high T_c superconductors. Results on a series of $DyBa_2Cu_3O_{7-\delta}$ films with different thicknesses will be presented.

A new technique called Photo Induced Activation of Mm-wave Absorption (PIAMA) is introduced in chapter 7. This technique can be used to study the quasiparticle dynamics in superconductors. Results on both conventional (NbN) and high T_c superconductors ($DyBa_2Cu_3O_{7-\delta}$) will be shown, demonstrating the existence of a surprisingly long-lived non-equilibrium state in the latter.

References

[1] J. G. Bednorz and K. A. Müller, Z. Phys. B **64**, 189 (1986).

[2] for a review see: D. B. Tanner and T. Timusk, Chapter 5 of *Physical Properties of High Temperature Superconductors*, vol. III, D. M. Ginsburg ed. (World Scientific, London, 1992), p. 363.

[3] Arnulf Röseler, *Infrared Spectrometric Ellipsometry*, (Akademie-Verlag, Berlin, 1990).

[4] W. N. Hardy, D. A. Bonn, D. C. Morgan, Ruixing Liang and Kuan Zhang, Phys. Rev. Lett. **70**, 3999 (1993).

[5] Dong Ho Wu, Jian Mao, S. N. Mao, J. L. Peng, X. X. Xi, T. Venkatesan, R. L. Greene and Steven M. Anlage, Phys. Rev. Lett. **70**, 85 (1993).

[6] N. Klein, N. Tellmann, S. A. Wolfe and V. Z. Kresin, J. Supercond. **5**, 195 (1992).

[7] U. Dähne, Y. Goncharov, N. Klein, N. Tellmann, G. Kozlov and K. Urban, J. Supercond. **8**, 129 (1995).

[8] S. Chakravarty, A. Sudbo, P. W. Anderson and S. Strong, Science **261**, 337 (1993).

[9] P. Monthoux and D. Pines, Phys. Rev. Lett. **69**, 961 (1992).

[10] N. Bulut, D. J. Scalapino and S. R. White, Phys. Rev. B. **47**, 2742 (1993).

[11] V. L. Ginzburg, Sov. Phys.-Usp. **13**, 335 (1970).

[12] A. Alexandrov, J. Ranninger and S. Robaszkiewicz, Phys. Rev. B **33**, 4526 (1986).

[13] J. Bardeen, L. N. Cooper and J. R. Schrieffer, Phys. Rev. **108** (5), 1175 (1957).

[14] D. A. Wollman, D. J. van Harlingen, W. C. Lee, D. M. Ginsberg and A. J. Leggett, Phys. Rev. Lett. **71**, 2134 (1993).

[15] J. R. Kirtley, C. C. Tsuei, J. Z. Sun, C. C. Chi, L. S. Yu-Jahnes, A. Gupta, M. Rupp and M. B. Ketchen, Nature **373**, 225 (1995).

[16] Z.-X. Shen, D. S. Dessau, B. O. Wells, D. M. King, W. E. Spicer, A. J. Arko, D. Marshall, L. W. Lombardo and A. Kapitulnik, Phys. Rev. Lett. **70**, 1553 (1993).

[17] T. E. Mason, G. Aeppli, S. M. Hayden, A. P. Ramirez and H. A. Mook, Phys. Rev. Lett. **71**, 919 (1993).

[18] T. P. Devereaux, D. Einzel, B. Stadtlober, R. Hackl, D. H. Leach and J. J. Neumeier, Phys. Rev. Lett. **72**, 396 (1994).

[19] James Annet, Nigel Goldenfeld and S. R. Renn, Phys. Rev. B **43**, 2778 (1991).

[20] A. T. Fiory, A. F. Hebard, P. M. Mankiewich and R. E. Howard, Phys. Rev. Lett. **61**, 1419 (1988).

[21] M. R. Beasley, Physica C **209**, 43 (1993).

[22] Zhengxiang Ma, R. C. Taber, L. W. Lombardo, A. Kapitulnik, M. R. Beasly, P. Merchant, C. B. Eom, S. Y. Hou and Julia M. Phillips, Phys. Rev. Lett. **71**, 781 (1993).

[23] P. J. Hirschfeld and N. Goldenfeld, Phys. Rev. B **48**, 4219 (1993).

[24] J. Halbritter, Phys. Rev. B **48**, 9735 (1993).

[25] L. A. de Vaulchier, J. P. Vieren, Y. Guldner, N. Bontemps, R. Combescot, Y. Lemaitre and J. C. Mage, Europhys. Lett. **33** (2), 153 (1996).

[26] D. A. Bonn, P. Dosanjh, R. Liang and W. N. Hardy, Phys. Rev. Lett. **68**, 2390 (1992).

[27] Martin C. Nuss, P. M. Mankiewich, M. L. O'Malley, E. H. Westerwick and Peter B. Littlewood, Phys. Rev. Lett. **66**, 3305 (1991).

[28] F. Gao, J. W. Kruse, C. E. Platt, M. Feng and M. V. Klein, Appl. Phys. Lett. **63** (16), 2274 (1993).

[29] M. Tinkham, *Introduction to Superconductivity*, (McGraw-Hill, New York, 1975 and Krieger, New York, 1980).

[30] O. Klein, E. J. Nicol, K. Holczer and G. Grüner, Phys. Rev. B **50**, 6307 (1995).

[31] D. A. Bonn, S. Kamal, Kuan Zhang, Ruixing Liang, D. J. Baar, E. Klein and W. N. Hardy, Phys. Rev. B **50**, 4051 (1994).

[32] Kuan Zhang, D. A. Bonn, S. Kamal, Ruixing Liang, D. J. Baar, W. N. Hardy, D. Basov and T. Timusk, Phys. Rev. Lett. **73**, 2484 (1994).

[33] Steven M. Anlage, Dong-Ho Wu, J. Mao, S. N. Mao, X. X. Xi, T. Venkatesan, J. L. Peng and R. L. Greene, Phys. Rev. B **50**, 523 (1994).

[34] T. Jacobs, S. Shridhar, C. T. Rieck, K. Scharnberg, T. Wolf and J. Halbritter, J. Phys. Chem. Solids **56** (12), 1945 (1995).

[35] For an excellent review see: D. J. Scalapino, "The case for $d_{x^2-y^2}$ pairing in the cuprate superconductors", Phys. Rep. **250**, 329 (1995).

[36] Patrick A. Lee, Phys. Rev. Lett. **71**, 1887 (1993).

[37] For a review, see: K. Levin *et al.*, Physica C **175**, 449-522 (1991).

[38] J. M. Kosterlitz and D. J. Thouless, J. Phys. C **6**, 1181 (1973).

[39] V. L. Berezinskii, Zh. Exsp. Teor. Fiz. **59**, 907 (1970) [*ibid.* Sov. Phys. JETP **32** , 493 (1971)].

[40] S. Martin, A. T. Fiory, R. M. Fleming, G. P. Espinosa and A. S. Cooper, Phys. Rev. Lett. **62**, 677 (1989).

[41] D. H. Kim, A. M. Goldman, J. H. Kang and R. T. Kampwirth, Phys. Rev. B **40**, 8834 (1989).

[42] Y. Matsuda, S. Komiyama, T. Terashima, K. Shimura and Y. Bando, Phys. Rev. Lett. **69**, 3228 (1992).

[43] Vladimir Z. Kresin and Stuart A. Wolfe, Phys. Rev. B **51** (2), 1229 (1995).

[44] Christophe Renner, *Low Temperature Scanning Tunneling Microscopy and Spectroscopy of layered superconductors*, Ph.D. Thesis, University of Geneva (1993).

[45] Z. Schlesinger, R. T. Collins, F. Holtzberg, C. Feild, G. Koren and A. Gupta, Phys. Rev. Lett. **65**, 801 (1990).

[46] R. E. Glover III and M. Tinkham, Phys. Rev. **104**, 844 (1956).

[47] D. M. Ginsberg and M. Tinkham, Phys. Rev. **118**, 990 (1960).

[48] K. Kamarás, S. L. Herr, C. D. Porter, N. Tache, D. B. Tanner, S. Etemad, T. Venkatesan, E. Chase, A. Inam, X. D. Wu, M. S. Hedge and B. Dutta, Phys. Rev. Lett. **64**, 84 (1990).

[49] D. van der Marel, M. Bauer, E. H. Brandt, H.-U. Habermeier, D. Heitmann, W. König and A. Wittlin, Phys. Rev. B **43** (10), 8606 (1991).

[50] H. S. Somal, B. J. Feenstra, J. Schützmann, Jae Hoon Kim, Z. H. Barber, V. H. M. Duijn, N. T. Hien, A. A. Menovsky, Mario Polumbo and D. van der Marel, Phys. Rev. Lett. **76** (9), 1525 (1996).

[51] H. S. Somal, Ph.D. Thesis, University of Groningen, in preparation.

Chapter 2

Theoretical and Historical Background

In this chapter some of the aspects of the optical properties of superconductors at mm-wave frequencies will be treated in detail. Furthermore attention will be paid to the ongoing controversy surrounding the most important question in the field of high T_c superconductivity: "What is causing the superconductivity at such high temperatures?" We will concentrate mainly on the implications of the superconducting state and its symmetry, leaving the task to answer the abovestated question to the theoreticians.

In the first section while briefly introducing some of the contemporary theories, we will present some of the most likely candidates for the symmetry of the superconducting wave function. Furthermore the implications of particular symmetries for several experimentally observable properties will be discussed. In section 2.2 we will discuss the essential optical properties, leading to a proper understanding of the concepts used in the experimental part of this thesis. The penetration depth, λ and the optical conductivity, σ_1 will be treated in relation to some of the experimental results, that are believed to exhibit the intrinsic behavior of the HTSC's. The chapter will be concluded with an overview of the work done on non-equilibrium superconductivity, including recent photoconductivity experiments, and earlier attempts to study the dynamics of the excited states using pump-probe like experiments.

2.1 Symmetries and their Implications

2.1.1 Miscellaneous Theories

Since Bednorz and Müller discovered superconductivity in $La_{2-x}Ba_xCuO_4$ at 32 K [1], many possible pairing states have been put forward as *the* solution to a very complicated problem [2, 3]. Here we would like to mention but a few, restricting ourselves to the most prominent ones, even though we realize that prominent can also be a temporary state. Strictly speaking, one can divide the current theories into two major streams. This division originates from the rather uncommon *normal* state properties exhibited by the cuprate superconductors. In table 2.1 several of the normal state properties have been indicated along with the expected behavior for the case of an ordinary Landau Fermi liquid [4]. We see that many of the normal state properties do not follow the expected

property	symbol	FL-behavior	HTSC's
susceptibility	χ	constant	constant
electronic specific heat	C_v(el)	$\sim T + T^3 \ln T$	$\sim T$
dc- resistivity	ρ	$\sim T^2$	$\sim T$
Hall coefficient	R_H	constant	large and T-dep.
NMR relaxation rate (Y and O)	$1/T_1T$	constant	constant
NMR relaxation rate (Cu)	$1/T_1T$	constant	Non-Korringa-like

Table 2.1: *Temperature dependencies of several normal state properties, compared to the behavior expected for a Fermi liquid. The experimentally observed dependencies given in the last column are measured for optimally doped samples.*

behavior. Reasons for the observed discrepancies can be:

1 The low dimensionality of these materials

2 The close proximity of the superconducting state to the antiferromagnetic insulator, leading to a strong influence of magnetic correlations

3 The low carrier concentration

4 The normal state temperatures might be too high, and therefore the actual Fermi liquid state is obscured by the onset of superconductivity

5 The dominant wave vectors and frequencies might be too high

BCS-theory relies heavily on the assumption that the normal state can be described by a Fermi liquid (FL). The observed discrepancies in the normal state therefore gave rise to an ambivalence in the approaches that were used to explain the occurrence of superconductivity. The first three points mentioned above urge theoreticians to adopt a new, non-Fermi liquid-like, description of the observed normal state, of which some examples will be shown later in this section. The last two points lead to a more conventional breakdown of the Fermi liquid description, hence additional assumptions are used to widen the scope of the FL-theory.

Non-Fermi Liquid Theories

An example of the first class of theories, using a non-Fermi liquid like description, is the interlayer coupling model of Anderson and co-workers [5]. This is a variation to the idea proposed by Anderson already in 1987 of having a resonating valence bond (RVB) state as the alternative to the FL [6]. In the interlayer coupling model the highly anisotropic superconductors is treated as a stack of conducting layers. The carriers are considered to be *spinons* and *holons*, an idea originating from the Luttinger liquid theory. However, the Luttinger liquid theory is considered to be strictly 1-dimensional and in order to apply this idea to the cuprates, Anderson and co-workers had to postulate its existence in two dimensions. The separation of spin and charge degrees of freedom within a CuO layer causes the transport in the c-axis direction to be incoherent. However, if the holons would be able to form pairs, tunneling becomes *coherent*, thereby lowering the energy of the groundstate and giving rise to the formation of a superconducting state. The symmetry of the groundstate is predicted to be highly anisotropic s-wave, where the gap in reciprocal space has the following functional form:

$$\Delta(\mathbf{k}) \;=\; \Delta_0[\cos(k_x\,a) \;-\; \cos(k_y\,a)]^4 \;+\; \Delta_1 \tag{2.1}$$

where Δ_0 and Δ_1 are the maximum and the minimum amplitude of the gap respectively and a is the in-plane lattice constant. A pictorial representation of this and other gap symmetries treated in this section can be seen in fig. 2.1 given in the following section, where the properties of the symmetries and their implications on the physical properties will be treated in more detail. The suppression of the gap occurs along the (110) direction. A very large suppression might even lead to nodes within the gap, and thereby sign changes, which are believed to be seen in many experimental results [7–9]. The resulting symmetry is called *extended* s-wave (s^*), since it maintains the symmetry of the underlying lattice. A possible functional form of this state, which has eight nodes in k-space is

$$\Delta(\mathbf{k}) \;=\; \Delta_0[\cos(k_x\,a) \;+\; \cos(k_y\,a)] \tag{2.2}$$

The interlayer coupling model has been successful for instance in explaining the c-axis transport properties [10], and the presence of a re-entrant c-axis plasmon in the superconducting state [11,12]. However, the correlation between the c-axis plasmon frequency and T_c, predicted by the theory as well, was disproved experimentally [13].

A second theory can be considered to be somewhat more conventional since, although abandoning the FL picture, the electron-phonon interaction is considered to be the dominant coupling mechanism. This leads to the formation of polarons or even *bipolarons* forming the bosons undergoing a Bose-Einstein condensation at T_c [14, 15] For instance Mott, Alexandrov and other authors proposed bipolarons as being a key element in understanding high T_c superconductivity [16–18]. Many of the observed properties of the cuprates are explained by this theory, such as the formation of the pseudo, c.q. spin gap given the fact that the bipolaron form either spin singlet or triplet pairs separated by an energy gap. Also the normal state linear resistivity and the Hall effect are explained, while in the superconducting state for instance the isotope effect and the thermoelectric power can be described using bipolarons. However, this theory leans heavily on the assumption of preformed pairs, existing above T_c upto the temperature at which the pseudo-gap closes. Experimentally there has been little evidence of the conduction carriers having a charge of 2e, existing in the pseudo-gap region.

A final non-FL approach is the "marginal" Fermi liquid suggested by Varma and co-workers [19]. In the marginal FL theory, it is postulated that the energy scale determining the excitation spectrum is given by the temperature of measurement rather than *any* intrinsic scale in the Hamiltonian. Using this phenomenological ansatz, several normal and superconducting properties can be explained. Among these are the observation of a Fermi surface similar to the band structure calculations, angular resolved photo emission results and neutron scattering data.

Fermi Liquid Theories

Turning our attention to the FL approaches, we can once again subdivide this class into various avenues to tackle the problem. Here we would like to introduce the "nearly antiferromagnetic" [20–22] and the "nearly localized" [23–25] Fermi liquids. The main difference between these approaches is the dominant physics considered to be driving the problem, which is the proximity to either a magnetic phase, or a localization instability respectively.

The nearly antiferromagnetic Fermi liquid theory has been proposed by Scalapino and co-workers, and also Pines and co-workers have done much work in this direction [26, 27]. Based on the observed correlation of resistivity and optical conductivity data with NMR and neutron scattering experiments, scattering by spin fluctuations are believed to be the dominant quasiparticle scattering mechanism. This knowledge obtained from the normal state then leads to the natural assumption that instead of the usual phonon-coupling used in BCS-theory [28], the exchange of anti-ferromagnetic spin fluctuations leads to the formation of a superconducting state. The co-existence of the antiferromagnetic and the superconducting groundstate in the phase diagram is an additional indication of the importance of magnetism in these materials. Moreover, also experimentally the existence of an antiferromagnetic background in the superconducting state has been confirmed [29]. In contrast to BCS-theory, this mechanism has been shown theoretically to give rise to critical temperatures comparable to the ones observed. The spin fluctuation mediated superconductivity leads naturally to a $d_{x^2-y^2}$ wave function of which the gap function can be described by

$$\Delta(\mathbf{k}) \;=\; \Delta_0[\cos(k_x\, a) \;-\; \cos(k_y\, a)] \tag{2.3}$$

where the four nodes are sited in the (110) direction. It is important note that in this case the symmetry of the energy gap function is *lower* than the symmetry of the underlying lattice. Some of the successes of this theory are the explanation of the linear temperature dependence of the dc-resistivity, the non-Drude like conductivity and the non-Korringa like behavior of the NMR-data.

More complex states involving a linear combination of some of the single component order parameter mentioned above have been proposed. An example of such a state is $s{+}id$ [30], a state which seems to be supported by recent tunneling results [31]. The gap function for this state can be expressed in the following fashion

$$\Delta(\mathbf{k}) \;=\; \Delta_0[\zeta + i(1-\zeta)(\cos(k_x\, a) \;-\; \cos(k_y\, a))] \tag{2.4}$$

where ζ is the fraction of s-component admixed in the $d_{x^2-y^2}$ state. However, in such a case one would expect a second phase transition [32] for which there exists no experimental evidence.

The "nearly localized" Fermi liquid theory is build upon the strong analogies between the d-electrons of the cuprates and the f-electrons of the heavy fermions, yielding many similarities in the observed experimental behavior. These similarities can be seen for instance in the resistivity and the Hall coefficient. This approach is motivated by the proximity of the superconducting state to a metal-insulator transition, where the insulating state is characterized by Mott localization. The transition to the insulating state in this case is driven by the diverging effective mass of the carriers, rather than a vanishing number of carriers. The starting point for the theoretical description is hence, as in the heavy fermion problem, the extended Hubbard Hamiltonian. The main focus of this formulation is indeed to describe the normal state, while it is assumed that the corresponding picture of the superconducting state will emerge from there. Since it is argued that the superconducting state is obscuring the onset of a more "coherent" state in which the ordinary FL description would be valid, it is tempting to speculate that the coherence and the superconducting transition are intimately related.

Finally we need to mention a few other suggestions that have been put forward as being important if not crucial in the formation of a superconducting state at surprisingly high temperatures. First the existence of Fermi surface nesting, and therefore a enhanced scattering amplitude for certain momenta can have an important effect on the quasiparticle dynamics. Secondly, it has been proposed that the high critical temperature could be explained by the inclusion of a van Hove singularity close to the Fermi energy.

From the summary given above it is clear that despite the enormous effort on both the theoretical and experimental side, leading to the improvement of existing techniques and the development of new ideas, a clear consensus on the underlying mechanism has not yet been reached.

2.1.2 Symmetries

The most important pairing symmetries have already been mentioned in the previous section, where their functional form in momentum space was given. In fig. 2.1 these symmetries have been plotted along with their gap amplitude, $|\Delta|$, and their phase, ϕ. $|\Delta|$ and ϕ have been plotted as a function of the angle in k-space, Θ. One of the most prominent properties of the gap *amplitude* is the presence of nodes or lines of nodes. In the upper two cases, the isotropic and anisotropic s-wave symmetries these are absent, yielding a finite energy gap over the entire k-space. The nodes, present for the extended s-wave and the $d_{x^2-y^2}$-wave symmetry, will have a strong impact on the thermo- and electrodynamical properties in the superconducting state. In the following discussion we will focus our attention on the isotropic s-wave and the $d_{x^2-y^2}$ wave states, being representative for pairing states without and with nodes respectively. The essential differences between states within these classes will be indicated when needed.

In table 2.2 we have given some of the important properties in the superconducting

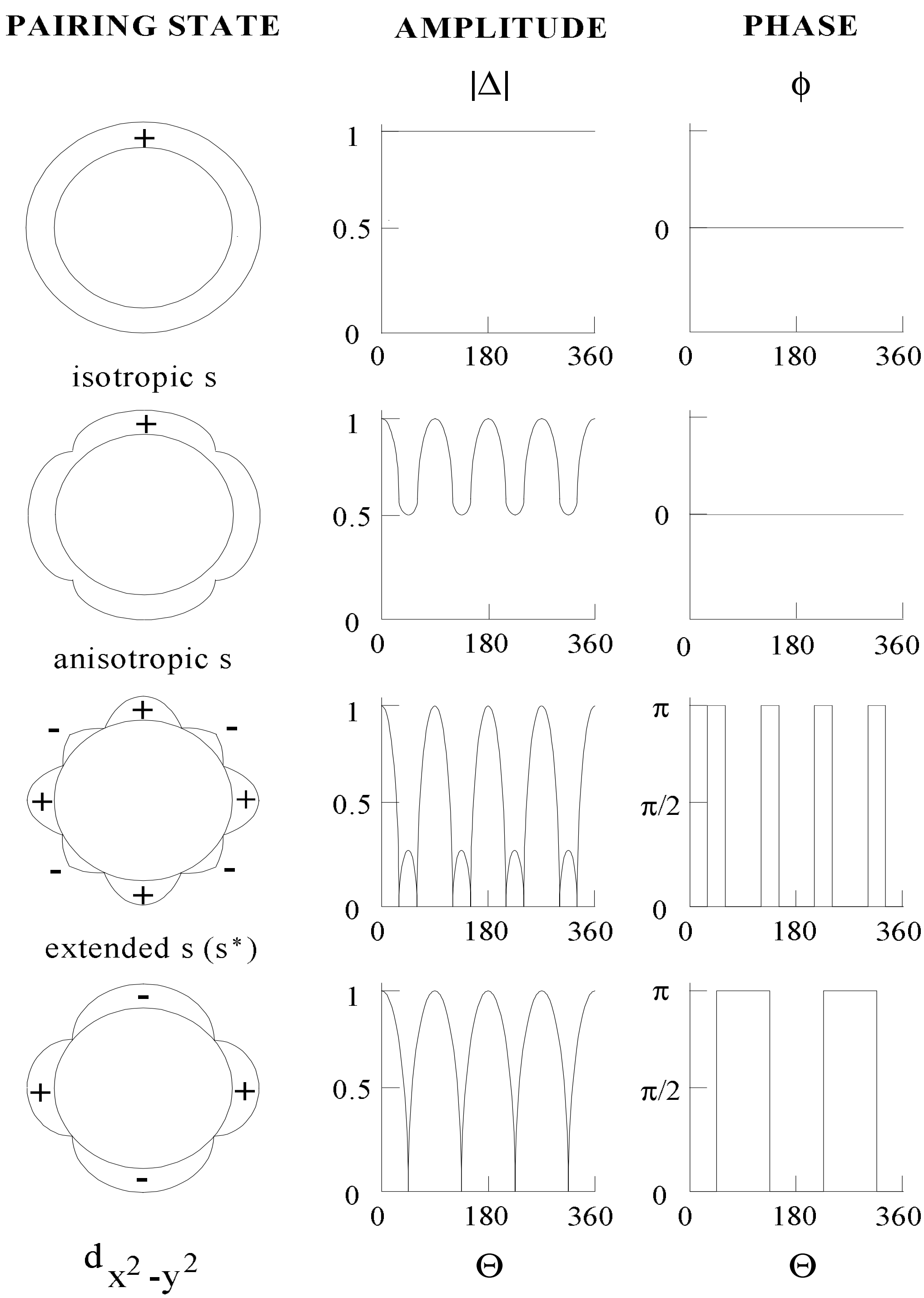

Figure 2.1: *Pairing symmetries in momentum-space, shown together with their amplitude and phase.*

state along with the expected behaviors for both s- and $d_{x^2-y^2}$-wave symmetry. In the last column the generally observed behavior has been stated, although consensus has not yet been reached on all accounts. As before we have restricted the list to the behavior seen for

property	symbol	s-wave	d-wave	HTSC's
penetration depth	λ	$\sim e^{2\Delta/kT}$	$\sim$ T	$\sim$ T
electronic specific heat	C_v	$\sim e^{2\Delta/kT}$	$\sim$ T	$\sim$ T
conductivity	σ_1	$\sim e^{2\Delta/kT}$	$\sim T^2$	$\sim$ T
coherence peak		+	+/-	-
Hebel-Schlichter peak		+	+/-	-
phase shift over 90°		0	π	π

Table 2.2: *List of properties in the superconducting state. Also indicated are the predicted behaviors for both the s-wave and the $d_{x^2-y^2}$-wave case. In the last column the experimental observations are listed.*

optimally doped materials. The aim of the list is merely to give an indication of the current status of the problem, not to be a complete overview of all possible properties. The plus and minus signs listed at certain properties indicate its presence or absence respectively.

The first three properties, λ, C_v and σ_1 mainly reflect the presence of the nodes. In the case of having an s-wave symmetry, there is a threshold energy value 2Δ necessary to create quasiparticles. Therefore these quantities, due to their close correlation with the quasiparticles density, exhibit *exponential*, i.e. activated behavior. For a superconductor having nodes in the gap however, it is possible to create excitations already at an infinitesimally low energy. Hence already at very low temperatures thermally excited quasiparticles will be present giving rise to a *power-law* temperature dependence rather than the exponential temperature dependence expected for a nodeless gap. For any superconductor having lines of nodes in the gap and an orthorhombic or tetragonal structure, such as for instance the $d_{x^2-y^2}$-state, the intrinsic power-law dependence was proven to be linear [33]. We have restricted ourselves to the intrinsic temperature dependence, whereas the influence of extrinsic scattering sources such as impurities will be treated in the next section, where we will focus on the penetration depth and the real part of the conductivity at microwave frequencies. From the observed temperature dependencies we can conclude that there are indeed lines of nodes present in the gap-symmetry, however a definite statement about the exact symmetry cannot be made. Since one averages over the complete Fermi surface, it is impossible to distinguish the d-wave symmetry from for instance extended s-wave by their intrinsic behavior. Both the isotropic and the anisotropic s-wave cases will lead to an exponential behavior, inhibiting a distinction also in this case. A final note of caution is the temperature dependence of the real part of the conductivity σ_1. In a self-consistent study of the temperature dependencies of both the real and imaginary part of the conductivity, Bonn *et al.* [34] showed that σ_1 has a strong *linear* dependence in contrast to the quadratic behavior expected for a $d_{x^2-y^2}$-wave symmetry [35].

An important quantity predicted by BCS-theory is the coherence peak in σ_1, or equivalently the Hebel-Schlichter peak in the NMR relaxation rate $1/T_1$. This effect, originating from the opening of the energy gap and the development of the singular density of states at the gap edge, has been observed before in elemental, s-wave superconductors. The +/- sign listed for a d-wave superconductor for both peaks indicate that the peaks should in principle be observed in these materials as well. However, some (intrinsic) properties strongly suppress their amplitudes, namely [36]

- The singularity at the gap edge in a d-wave single particle density of states is *logarithmic*, in contrast to the *square-root* singularity for an s-wave gap.
- The coherence factor for the magnetic susceptibility vanishes at q $\sim (\pi, \pi)$ in the case of a $d_{x^2-y^2}$ symmetry.
- The inelastic scattering tends to suppress the peak, just like for an s-wave gap.

Both peaks have not been observed experimentally for the high T_c cuprates [37, 38], although in the early days another, much broader peak in σ_1 was erroneously interpreted as being a coherence peak [39]. This provides no undisputable evidence for a $d_{x^2-y^2}$-wave symmetry, but strongly suggests that the simple s-wave picture cannot be used.

All the quantities mentioned above are only sensitive to the amplitude of the gap. As already mentioned in the argument above, in this case it is only possible to distinguish states with and without nodes, while for instance a distinction between the extended s-wave and $d_{x^2-y^2}$-wave symmetry cannot be made. In order to distinguish such states, obtaining information about the *phase* of the gap function, or equivalently the phase of the wave function is crucial. As we can see in fig. 2.1, the phase of the gap function changes by a factor of π at each node. This means that the phase measured at two particular places in k-space separated by a 90° angle will be the same for the extended s-wave case, while it is different by a factor of π for a d-wave superconductor. This implies experimentally that if one is able to measure the tunneling from the a-axis into the b-axis direction, a d-wave superconductor will show a markedly different behavior than every possible s-wave symmetry.

This observation led to a large experimental effort, attempting to establish the phase difference. Several experiments, such as a SQUID fabricated on the a- and b-faces of a $YBa_2Cu_3O_{7-\delta}$ single crystal [40] and superconducting rings containing an even or odd number of π-junctions demonstrate the behavior expected for a d-wave superconductor [9]. A note of caution should be added here, since in a recent series of tunneling experiments by Dynes *et al.* it was argued that an appreciable s-wave component was found, leading to a finite Josephson current [31, 41]. In fact, for a more exotic order parameter, such as the *s+id* state, the phase would vary continuously with the angle Θ. On the other hand, such states would also imply the breaking of time reversal symmetry, which is contradicted by results seen in SQUID experiments [42]. Moreover, measurements of the penetration depth close to T_c have indicated that the critical behavior in cuprates is consistent with the 3D XY model, implying that we are dealing with an order parameter having a single complex component, i.e. *one* phase and *one* amplitude [43, 44].

Other techniques, sensitive to the symmetry of the superconducting gap need to be mentioned here, such as Angular Resolved Photo Electron Spectroscopy and Raman spectroscopy. Also results obtained using these techniques point towards a $d_{x^2-y^2}$-symmetry [45, 46].

2.2 mm-Wave Properties of Superconductors

In this section some of the properties of a superconductor in the mm-wave region will be reviewed. The concepts needed to understand the experimental results treated in chapter 6 will be introduced. Furthermore, we will try to give an overview of the current status of understanding. Special attention will be paid to the influence of the impurities on both the real and the imaginary part of the dielectric function.

2.2.1 General Electromagnetic Response

Main focus of the research in the microwave and mm-wave range, is to measure the complex response function of the system to perturbing electromagnetic fields, via for instance resonant cavity techniques or by non-resonant quasioptical methods. The experimentally accessible quantity in this case is the surface impedance, defined as the ratio of the electric field E and the total induced current J

$$Z_s = R_s - iX_s = \frac{E}{\int_0^\infty Jdz} = \sqrt{\frac{4\pi i\omega}{c^2\left(\sigma_1 - i\sigma_2\right)}} \tag{2.5}$$

where R_s and X_s are the surface resistance and surface impedance respectively, which can be written in terms of the real and imaginary part of the conductivity:

$$\begin{aligned} R_s &= \frac{2\pi\omega}{c^2}\left(\frac{(\sigma_1^2+\sigma_2^2)^{1/2}+\sigma_2}{\sigma_1^2+\sigma_2^2}\right)^{1/2} \\ X_s &= \frac{2\pi\omega}{c^2}\left(\frac{(\sigma_1^2+\sigma_2^2)^{1/2}-\sigma_2}{\sigma_1^2+\sigma_2^2}\right)^{1/2} \end{aligned} \tag{2.6}$$

Hence, from the surface impedance the desired optical response functions can be calculated analytically, provided that both R_s and X_s are known.

In order to make the expressions in eq. (2.6) somewhat more transparent we consider a few limiting cases. In the normal state, i.e. in case of a metal, $\sigma_1 \gg \sigma_2$ and R_s and X_s become identical, the so-called Hagen-Rubens limit.

$$R_s = X_s = \sqrt{\frac{2\pi\omega}{c^2}\frac{1}{\sigma_1(T)}} \tag{2.7}$$

In the superconducting state, at temperatures sufficiently low compared to T_c, the opposite limit is valid, $\sigma_2 \gg \sigma_1$. In addition, the imaginary part of the conductivity can be written in terms of the superfluid contribution, $\sigma_2 = c^2/4\pi\omega\lambda^2$, and R_s and X_s become:

$$\begin{aligned} R_s &= \frac{8\pi^2}{c^4}\omega^2\lambda^3(T)\sigma_1(T) \\ X_s &= \frac{4\pi}{c^2}\omega\lambda(T) \end{aligned} \tag{2.8}$$

From these expressions it is evident that the penetration depth, λ(T) can be determined directly by measuring the surface reactance, X_s. In order to acquire information about the absorptive response, σ_1(T) as well, the surface resistance has to be determined, and hence the penetration depth needs to be known. The best way to achieve this is obviously to measure λ(T) on the same sample, but it is also possible to postulate a temperature dependence, or to use experimental results obtained on similar samples.

In the remainder of this section we will separate the discussion into two parts: the first part focuses on the inductive response (σ_2 or ϵ'), directly connected the penetration depth λ and therefore to the superfluid density. We will treat some of the important results that have contributed considerably to the contemporary understanding of the superconducting state, such as the temperature dependence of λ at low temperatures, both for high purity samples and in the case that impurity scattering is included.

The second part will be devoted to the absorptive part of the optical properties, i.e. σ_1 or ϵ''. This contribution is directly related to the quasiparticles density and therefore yields important information on for instance their scattering rate, γ. The scattering rate will be treated in detail, also in connection with the introduction of impurities. The temperature dependence of σ_1 in the low temperature limit will be treated. An important issue concerning the temperature dependence of both λ and σ_1 which is omitted here, is its behavior at temperatures close to T_c. A large body of work has been done to determine the critical exponents for the temperature dependence of the fluctuation contributions to both λ and σ_1. These exponents can be used to establish the universality class to which the high T_c superconductors belong [43, 44].

2.2.2 Penetration depth, λ

Already very early it was realized that by measuring the temperature dependence of the penetration depth, being a measure of the superfluid density, essential information about the pairing symmetry can be obtained. Much of the early work, both experimentally and theoretically was done in connection with the heavy fermion superconductors, e.g. UPt_3 and UBe_{13}, showing an unconventional behavior [47]. The gap function in these materials is believed to have a p-wave symmetry, therefore in most of the theoretical studies the attention was focused on this particular symmetry. However, many of the obtained conclusions are equally valid for a d-wave symmetry having lines of nodes in the gap.

In this treatment we will restrict ourselves to case of a single order parameter having either an s-wave or a d-wave symmetry, by virtue of the following experimental information:

- The superfluid consist of singlet pairs, as shown in measurements of the Knight shift [48].

- The order parameter consists of a single, complex component, as can be concluded from for instance the temperature dependence of the penetration depth close to T_c [43] and phase sensitive measurements testing the existence of time reversal symmetry [42].

The second point is still under scrutiny, but for now we will assume this is indeed the case. These observations limit the options to four possible symmetries mentioned already before in the previous section: (an)isotropic s (s^+), extended s (s^*), $d_{x^2-y^2}$ or d_{xy}, where we assume that the main coupling occurs within the CuO-plane and therefore we can omit the d_{xz} and d_{yz} symmetries.

Temperature Dependence

The fact that the penetration depth λ(T) provides information about the symmetry of the pairing via its temperature dependence can be easily seen, starting from its definition

$$\frac{1}{\lambda^2(T)} = \frac{4\pi e^2}{c^2 m^*} n_s(T) \tag{2.9}$$

where n_s(T) is the effective density of superconducting particles at temperature T. Therefore, in case of a symmetry having a finite energy gap at all points in k-space (not necessarily isotropic) at sufficiently low temperatures the number of thermally excited quasiparticles will be exceedingly small. This leads to an exponential temperature dependence for λ

$$\frac{\lambda^2(0)}{\lambda^2(T)} \approx 1 - \sqrt{\frac{2\pi\Delta_0}{k_B T}} e^{-\Delta_0/k_B T} \tag{2.10}$$

where Δ_0 is the (minimum) size of the energy gap. The wavefunction can be shown to be proportional to the energy gap and hence exhibits the same symmetry.

In order to determine the temperature dependence of λ it is thus sufficient to calculate the number of Bogoliubov quasiparticles n_n(T) at all temperatures, since $n_s(T) = n_{tot} - n_n(T)/2$. This is defined, in absence of Fermi liquid corrections by [33]

$$n^n_{ij} = \frac{m}{\hbar} \int \frac{d^2k}{(2\pi)^3 |v|} v_i v_j \int d\xi_k \frac{\beta}{2} \mathrm{sech}^2 \left(\frac{\beta E_k}{2} \right) \tag{2.11}$$

where the integral is over the Fermi surface, v is the Fermi velocity, $\beta = 1/k_B T$, ξ_k is the normal state band energy measured with respect to the chemical potential and E_k is the quasiparticle energy, given by

$$E_k^2 = \xi_k^2 + |\Delta_k|^2 \tag{2.12}$$

The quasiparticle density given in eq. (2.11) is a tensor, which is of particular importance in $YBa_2Cu_3O_{7-\delta}$ due to the presence of the chains, giving rise to a considerable anisotropy in the penetration depths in the a- and b-axis directions [49]. For clarity we should mention here that λ_a, λ_b and λ_c are defined as the penetration depth for which the screening currents are flowing in the a, b and c-direction respectively.

From this it is evident that if the energy gap Δ_k vanishes at certain places in k-space that some of the components of eq. (2.11) will approach zero as a power-law in T at low temperatures. This leads to a penetration depth at low temperatures exhibiting a behavior of the form

$$\frac{\lambda^2(0)}{\lambda^2(T)} \approx 1 - \left(\frac{k_B T}{\Delta_{max}}\right)^{\nu} \tag{2.13}$$

where ν is a coefficient depending on the type of node (lines or points) and the orientation of the node relative to the applied magnetic field. Under both restrictions mentioned before, only two values of ν are relevant, namely $\nu = 1$ for *all* possible singlet pairing states having lines of nodes and, as we will see later, $\nu = 2$ when impurity scattering is taken into account.

In fig. 2.2 the strikingly different behavior for the isotropic s-wave and a $d_{x^2-y^2}$-symmetry is illustrated. Shown is the normalized penetration depth $[\lambda(0)/\lambda(T)]^2$, i.e. the

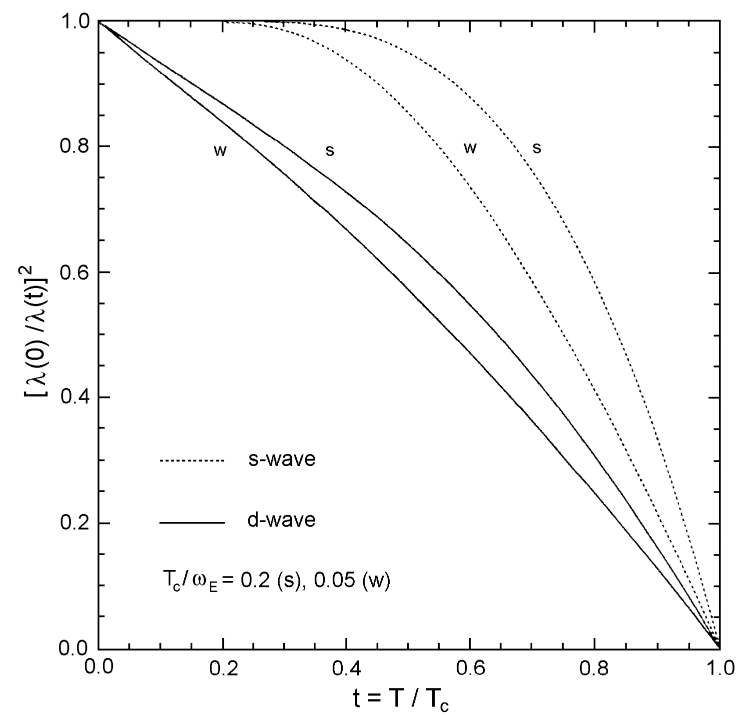

Figure 2.2: *Normalized penetration depth vs. reduced temperature $t = T/T_c$. Presented are the strong (s) and weak (w) coupling results for the s as well as the d-wave case. From reference [50].*

superfluid density, as a function of the reduced temperature. The letters s and w denote the strong- and weak coupling case, respectively, characterized by the ratio T_c/ω_E. Here ω_E is the characteristic excitation energy of the frequency dependent part of $\lambda_{k,k'}(n-m)$, the coupling function between the quasiparticles and spin fluctuations [50]. The d-wave calculations were done assuming a model in which the exchange of anisotropic antiferromagnetic spin fluctuations stabilizes the superconducting state, leading naturally to an order parameter with a $d_{x^2-y^2}$-symmetry. The linear dependence for the d-wave penetration depth is evident, clearly distinguishable from the exponential behavior of the s-wave superconductor. Furthermore it can be seen that strong coupling effects do not affect the actual temperature dependence, although the absolute magnitude is slightly altered.

Influence of Impurities on the Temperature Dependence of λ

Having established the intrinsic behavior, it is interesting to investigate what will happen when a certain number of impurities is introduced in the superconductor. It is a well-known fact that the inclusion of non-magnetic scatterers can affect a d-wave superconductor rather drastically, hence suppressing T_c considerably. In fact, from experiments we know that a fair number of for instance Zn or Ni impurities alters the behavior of the electrodynamical properties, while T_c remains nearly constant. One way to circumvent this problem theoretically is to assume that the scattering is in the *unitary* limit, i.e. resonant scattering. In this way, only a small number of scatterers is needed to alter the transport properties considerably, while T_c is suppressed only slightly. Many groups have calculated the influence of impurities on the penetration depth, both in the unitary and the Born (weak scattering) limit [35, 50–52] and in this section we will discuss their findings focusing on the latter limit by virtue of the reason mentioned above.

Rather than explaining all the theoretical details, we would like to show the general formalism used in these calculations, and thereafter focus on the results. For the results at low temperatures, it is assumed that the main contribution to the scattering of quasiparticles is elastic, originating from impurity scattering. At higher temperatures also the inelastic contribution, for instance due to spin fluctuations will be important and needs to be included. Furthermore, the scattering is assumed to be isotropic, i.e. s-wave like.

To determine the penetration depth or the superfluid density for a superconductor it is necessary to calculate the electromagnetic response tensor K, defined as

$$\vec{j} \; = \; K\,\vec{A} \tag{2.14}$$

where $\vec{j}$ is the induced current density and $\vec{A}$ is the applied vector potential. Namely, if the kernel K is diagonal, the penetration depth can be calculated using $(4\pi/c)K_{ii} = \lambda_i^{-2}$. This shows moreover that it is possible to determine the anisotropy of the penetration depth, simply by calculating λ for all possible directions of the current flow, i. In the simplest BCS-like model for an anisotropic superconductor in the presence of elastic scattering the kernel is described by [51]

$$K_{ij} \; = \; \frac{e^2}{c}\langle v_i(k)v_j(k)\int_0^\infty d\omega\,\tanh\frac{\omega}{2T}Re(\frac{\Delta_k^2}{(\tilde{\omega}^2\,-\,\Delta_k^2)^{3/2}})\rangle \tag{2.15}$$

where the real part of this expression is related to the penetration depth and the imaginary part is used to calculate the optical conductivity via $\sigma_1(\omega, q = 0) = -(c/\omega)\mathrm{Im}(K(\omega, q = 0))$. The optical conductivity will be treated in the next part of this section.

The expression for K looks reasonably straightforward, which is however somewhat deceiving due to a number of definitions present. First of all $\langle .. \rangle$ denotes the angular average over an arbitrary Fermi surface. Then the frequency is normalized by the introduced interaction as $\tilde{\omega} = \omega - \Sigma_0$, where the impurity self energy is given by

$$\Sigma_0 = \frac{,\, G_0}{c^2 - G_0^2} \tag{2.16}$$

G_0 is the integrated diagonal Green's function averaged over disorder, $G_0 = -i\langle \tilde{\omega}/(\tilde{\omega}^2 - \Delta_k^2)^{1/2} \rangle$. In contrast to the frequency, the renormalization of the gap vanishes for symmetry reasons in the case of a $d_{x^2-y^2}$ gap.

We want to emphasize the purpose of the parameters c and , . The first, c is defined as the cotangent of the scattering phase shift, indicating the *strength* of the scattering. In terms of the before mentioned limiting cases, $c = 0$ corresponds to the unitary limit, while $c \gg 1$ corresponds to the Born limit. The second, , is the scattering rate parameter

$$, = \frac{n_i n}{\pi N_0} \tag{2.17}$$

which depends on the number of scatterers n_i, the electron density n, and the density of states at the Fermi level N_0. By means of adjusting , the impurity concentration used in the calculations will be altered In fig. 2.3 the general behavior of the normalized superfluid density n_s/n, upon raising the impurity concentration can be observed. Here n_s/n was calculated in the unitary limit, i.e. resonant scattering. In this way the changes in the superfluid density are already apparent at rather low doping concentrations (small ,) while T_c remains unaltered. It is evident that upon the introduction of impurities, the temperature dependence turns from linear in the pure case to quadratic at higher concentrations. Moreover, since for all curves the same normalization constant was used, also the superfluid density at zero temperature becomes smaller, or equivalently the London penetration depth becomes longer.

In fact, from the curve calculated for , $= 0.01$ we see that for intermediate impurity concentrations, both a quadratic and a linear dependence occurs. This is, as was pointed out by for instance Ueda and Rice [53], a behavior reminiscent of having a "gapless" state at low temperatures, crossing over to the pure response at higher temperatures. Indeed, due to the introduction of impurities a nonzero density of states N(0) appears at the Fermi level, where N(0) is obviously strongly dependent on the impurity concentration. At somewhat higher temperatures, at energies large compared to the energy related with the newly introduced states, the system will actually recover it intrinsic dependence, as if it were a pure material. Therefore it is easy to see that at a certain temperature T^*, closely related to N(0), or equivalently , a crossover from a T^2 to a linear dependence will be observed.

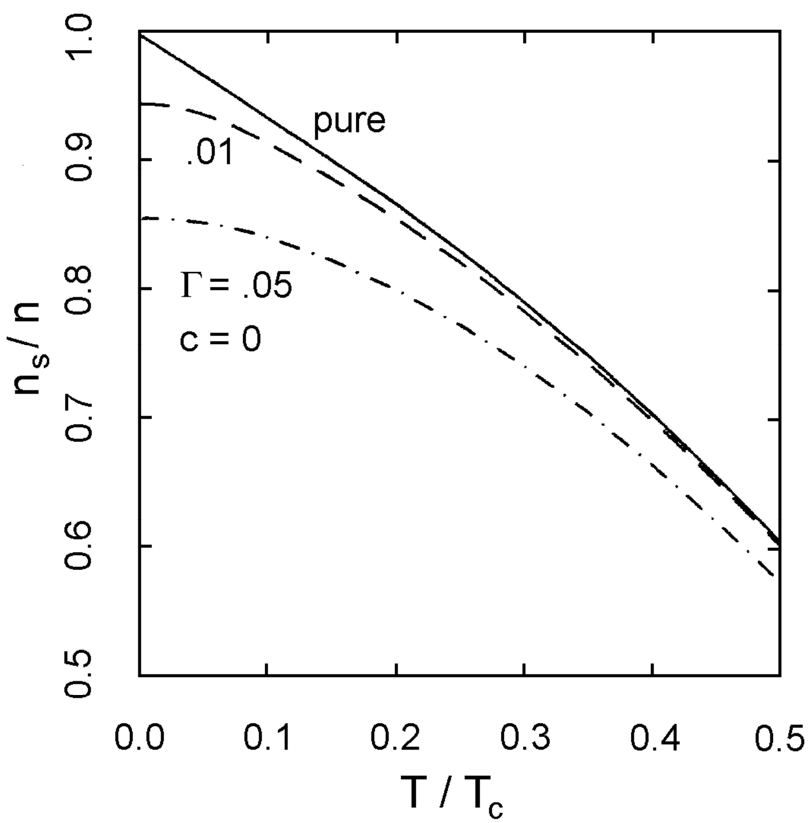

Figure 2.3: *Normalized superfluid density n_s/n vs. reduced temperature, for several impurity concentrations indicated by the value of , . The results were obtained in the unitary scattering limit, c = 0. From reference [51].*

To make this statement somewhat more quantitative, one can write the temperature dependence of the penetration depth approximately as

$$\lambda = \frac{\delta\lambda_0 + bT^2}{T^* + T} \tag{2.18}$$

where $\delta\lambda_0$ accounts for the change in the London penetration depth, induced by the impurities. Eq. (2.18) reduces to a linear behavior for $T \gg T^*$, while for $T \ll T^*$ it becomes quadratic. Fitting this expression at low and high temperatures, yields $\mathrm{T}^* \approx c_1/c_2$ where c_1 and c_2 are the proportionality constants for the linear and quadratic case, respectively. The linear coefficient $c_1 = \ln 2\, \lambda_0/\Delta_0$, while for a d-wave superconductor, in the resonant scattering limit $\mathrm{c}_2 \approx \pi\lambda_0/(6\gamma\Delta_0)$. In this expression γ expresses the direct relation to the normalized residual density of states at the Fermi level. γ was numerically determined to be approximately $0.63(, \Delta_0)^{1/2}$ for the case of low temperatures and small impurity concentrations $\gamma \ll \Delta_0$. Finally, using the expressions for c_1 and c_2 the crossover temperature can be estimated by

$$T^* \;=\; \frac{6\,\ln 2\,\gamma}{\pi} \;\approx\; 0.83\sqrt{,\,\Delta_0} \tag{2.19}$$

Using an estimate for the energy gap, $\Delta_0/T_c = 3$ and taking , $/T_c = 0.035$, the crossover temperature becomes $T^* \approx 0.27\,T_c$. This results is in fair agreement with the results obtained in reference [54], where the crossover behavior in $YBa_2Cu_3O_{7-\delta}$ thin films was studied extensively.

In fig. 2.4 a direct comparison is made between the calculated results and results measured upon Zn-substitution by Bonn *et al.* [34]. The agreement is rather well, although

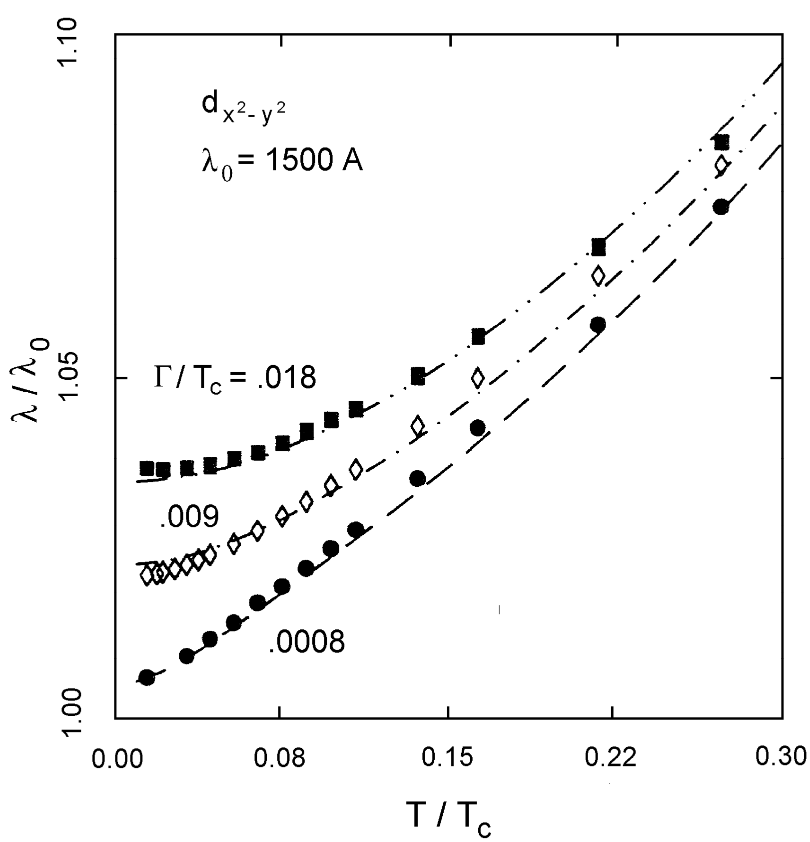

Figure 2.4: *Comparison of the calculated temperature dependence of the penetration depth with data acquired on a $YBa_2Cu_3O_{7-\delta}$ single crystal [34]. The Zn doping in the experimental data was: pure (circles), 0.15 % Zn (diamonds) and 0.31 % Zn (squares). From reference [35].*

it should be added that there exists a rather broad range, within about a factor 2, of values for , $/T_c$ yielding similar fits. The ratio of the values for the two doped curves

(0.018/0.009) was chosen such that it corresponds to the ratio of the doping concentrations (0.31%/0.15%). The zero temperature penetration depth, for the pure system, was taken to be 1500 $\AA$, while the maximum gap size was $\Delta_0/T_c = 3$.

Other Approaches leading to a Linear Temperature Dependence for λ

It should be mentioned that in addition to the d-wave hypothesis, also other approaches can lead to a linear temperature dependence of the penetration depth.

One approach is to take into account the phase fluctuations of the order parameter, which are believed to be important due to the low carrier concentration and the low dimensionality of the high T_c superconductors [55–57]. The basic approach to obtain the superfluid density and thereby the penetration depth is the following. In the same way as above, the relation between the current density along a certain direction and the applied vector potential yields a kernel K_1 which can be directly related to λ. The difference is that in this case one assumes that the *main* temperature dependence for the order parameter at low temperatures is induced by phase fluctuations rather than fluctuations in its amplitude, which is assumed to be approximately constant. Under these assumptions K_c and K_{ab} are both linear, implying the same linear dependence for λ_c and λ_{ab} as well. Using a mass anisotropy of 25, $T_c = 90.9\,K$, a coherence length $\xi_0 = 10\,\AA$ and $\lambda(0) = 2600\,\AA$, Roddick and Stroud obtained a slope $d\lambda/dT = 3.5\,\AA/K$ [56]. This value is in fair agreement with the experimentally observed value of 4.2 $\AA/K$ [7]. However, there is a substantial dependence of the slope on the value taken for $\lambda(0)$ yielding slopes which are considerably smaller than $1\,\AA/K$ for more realistic estimates of $\lambda(0)$ ($\pm 1500\,\AA$). In fact, also Coffey concludes that the fluctuation contribution results in a linear temperature dependence having a slope of approximately $10^{-4}\lambda_0$, yielding about 0.15 $\AA/K$, similar to the results obtained in [56] assuming a shorter zero temperature penetration depth. Also Emery and Kivelson claim to observe, using a similar approach, a quantitative agreement with the experimental data, although no values are presented in reference [55].

One of the key predictions, which could be used to determine the merit of the different descriptions of the linear *planar* response, is the appertaining response in the *c-axis* direction. In the case of the fluctuation induced T-dependence, this linear term should be observed in the c-axis direction as well, taking off even steeper at low temperatures [56]. Klemm and Liu showed, starting from a rather different ansatz, that the response in the direction perpendicular to the CuO layers might be used to disentangle certain states [58]. They show that if one assumes that the CuO *chains* in $YBa_2Cu_3O_{7-\delta}$ are normal, coupled to the superconducting planes via the proximity effect, a linear $\lambda(T)$ can be obtained for *both* s- and d-wave symmetry. Assuming two CuO layers per unit cell, the fits to the experimental data are obtained by adjusting the coupling between neighboring bilayers and within a single bilayer. However, if the c-axis penetration depth is calculated using the same set of parameters, a clear distinction between the s- and d-wave pairing appears. In this case, λ_c for the s-wave symmetry clearly shows the expected activated behavior, while the d-wave curve shows a behavior very similar to the planar response.

Unfortunately, upto now only a few reports have been published on the temperature dependence of λ_c [59,60]. Complicating the picture even further, these reports show a strikingly different behavior, where one [60] exhibits a steep T-dependence close to being linear. The other results show a T-dependence which is much flatter than for λ_{ab}, resembling the activated behavior expected for a finite gap.

Another model making use of the coupling between the superconducting and the intersecting normal, metallic chains was proposed by Combescot and Leyronas [61]. As for the model proposed by Klemm and Liu, the use of chains restricts the analysis to $YBa_2Cu_3O_{7-\delta}$, whereas experimentally similar behavior has been observed for other high T_c's. By taking an attractive pairing interaction within the planes and the chains as opposed to a repulsive interaction *between* the planes and the chains, several experiments can explained. In order to account for the experiments that favor a d-wave like explanation, the sign of the order parameter within the planes and chains was taken to be opposite.

One of the main problems of the abovementioned models is the crossover behavior from a linear to a quadratic temperature dependence upon the introduction of impurities. In most models starting from an s-wave assumption, the inclusion of additional disorder tends to smear out the anisotropy, causing the response to retain a behavior reminiscent of an isotropic gap. As shown above, the $d_{x^2-y^2}$-symmetry provides a natural explanation for the experimental behavior.

2.2.3 Optical Conductivity, σ_1

Although the penetration has caught most of the attention, also the real part of the conductivity σ_1 provides information on the existence of low-lying excitations in the same way as λ.

Temperature Dependence

Let us first consider the temperature dependence at low temperatures. In order to investigate the consistency of the inclusion of resonant scatterers we will follow the same approach as in the case for the penetration depth, treated before. The kernel K is calculated for the case of resonant impurity scattering, assuming that at low temperatures inelastic processes can be neglected. The optical conductivity can then be determined using the imaginary part of K.

As for λ, one can distinguish several limiting regimes, where we will first focus on the situation that $\omega \ll$, Δ_0/T. In this regime a second distinction, completely analogous to the case of λ can be made, namely $T \ll T^*$ and $T \gg T^*$. The optical conductivity can be shown to be [62]:

$$\begin{aligned}
\sigma_1 &\approx \sigma_0 \left[1 + \frac{\pi^2}{12}\left(\frac{T}{\gamma}\right)^2\right], \qquad && T \ll T^* \\
\sigma_1 &\approx \frac{2}{3}\sigma_0 \left(\frac{T}{\Delta_0}\right)^2 \ln^2\frac{4\Delta_0}{T}, \qquad && T \gg T^*
\end{aligned} \tag{2.20}$$

demonstrating that σ_1 shows a quadratic temperature dependence in the low-frequency regime for both cases. γ is defined as given above, while

$$\sigma_0 \;=\; \frac{ne^2}{m\pi\Delta_0(0)} \tag{2.21}$$

is the residual conductivity for a d-wave superconductor. This is a rather remarkable result, to which we will come back later.

Intuitively, one would perhaps expect a linear behavior as in the case of λ due to the dependence of σ_1 on the quasiparticle density. However, for a d-wave superconductor, a non-trivial dependence of the scattering rate on energy should be taken into account, resulting in quadratic dependence. Please note, that both T and T^2 should be compared to the exponential dependence for the case of a conventional superconductor. The T^2-dependence is clearly demonstrated in fig. 2.6, where σ_1 has been calculated for several impurity concentrations. If the low temperature behavior is calculated in the high frequency regime,

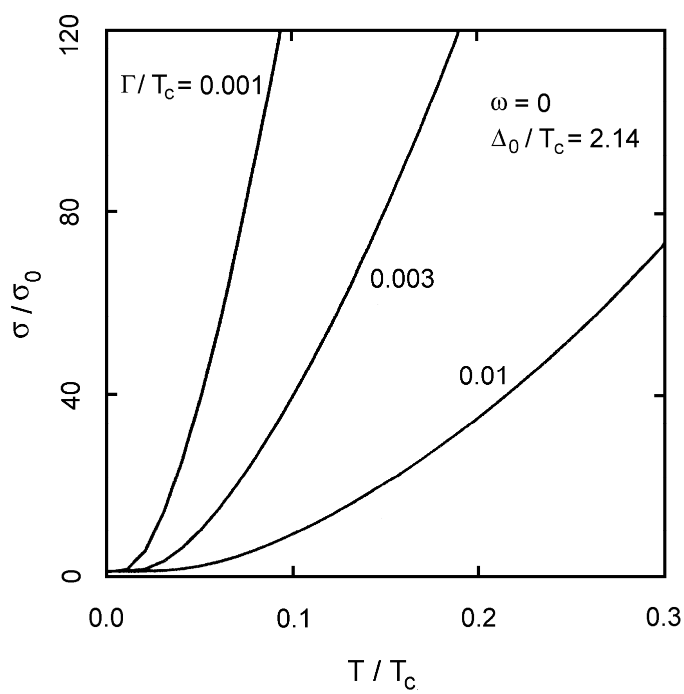

Figure 2.5: *Normalized conductivity vs. reduced temperature for several impurity concentrations. From reference [62].*

for $T \gg T^*$, one obtains:

$$\sigma_1 \;\approx\; \left(\frac{ne^2}{m}\right)\frac{\pi^2,}{2\omega^2}\ln^{-2}\frac{4\Delta_0}{T} \tag{2.22}$$

while for $T \ll T^*$ the behavior is equivalent to the quadratic dependence shown above. Therefore at intermediate frequencies in between both regimes given in (2.20) and (2.22) σ_1 will show a quasilinear crossover dependence.

"Coherence" Peak and Drop in Scattering Rate

Before comparing the results obtained above to the experimental data, the temperature region closer to T_c needs to be included as well. In this case, it is no longer valid to simply take the elastic impurity scattering as the sole source of quasiparticle scattering. Also inelastic processes will become important at such temperatures, and need to be taken into account. The additional term needs to be included in the self energy Σ_0. In the approach followed in for example reference [62], spin fluctuations are taken to be the main inelastic contribution. Obviously this choice is driven by the assumption that the spin fluctuation mediated superconductivity leads naturally to a $d_{x^2-y^2}$-symmetry, but it should be noted that the results given below do not rely entirely on this assumption. Any electronic scattering channel which is depleted below T_c will yields qualitatively similar results. The spin fluctuation scattering time τ_{sp} in the superconducting state has been calculated in reference [63] using parameters similar that those used to calculate the NMR relaxation rate. It was shown that τ_{sp} varies as $(T/T_c)^3$.

In fig. 2.6 the results of the calculations are shown along with the experimental data presented in reference [34]. The conductivity was measured on the same crystal as the one used for the penetration depth measurements shown in fig. 2.4, thereby allowing a consistent study of the influence of impurity doping on both quantities. It is evident that when the same parameters are used for σ_1 as those given before for the penetration depth, the fit to the optical conductivity is much less satisfactory. Although the position and the height of the peak, resulting from the rapid (T^3) decreasing contribution of the spin fluctuation scattering, reproduces the experimental behavior reasonably well, the correspondence at low temperature is much worse.

First of all, the experimental conductivity at the lowest possible temperatures is much higher than the calculated results. This might possibly be attributed to extrinsic effects, such as twinning, since measurements on untwinned samples show a much lower residual conductivity [49]. Secondly, the experimental temperature dependence shows a strong linear term, whereas the calculated conductivity always approaches the lowest temperatures as T^2. As mentioned above, a quasi-linear dependence can be obtained in the intermediated frequency regime, where $\omega\tau \approx 1$. However, since a rather large range of scattering times is covered in the three panels of fig. 2.6, this explanation would certainly not apply to all cases.

Universal Conductivity at 0 K

We now return to the residual conductivity σ_0 given above, also in the context of the discrepancy shown in the preceding part of this section. It was shown by Lee [64] that for a d-wave superconductor, the residual conductivity at $T = 0$ induced by impurity scatterers in the unitary limit, will have universal value, given by eq. (2.21). This implies that, at least for reasonably low impurity concentrations the zero temperature conductivity will be *in*dependent of the number of impurities. This result, which is at first sight rather surprising, can be understood if we recall that the introduction of impurities not only

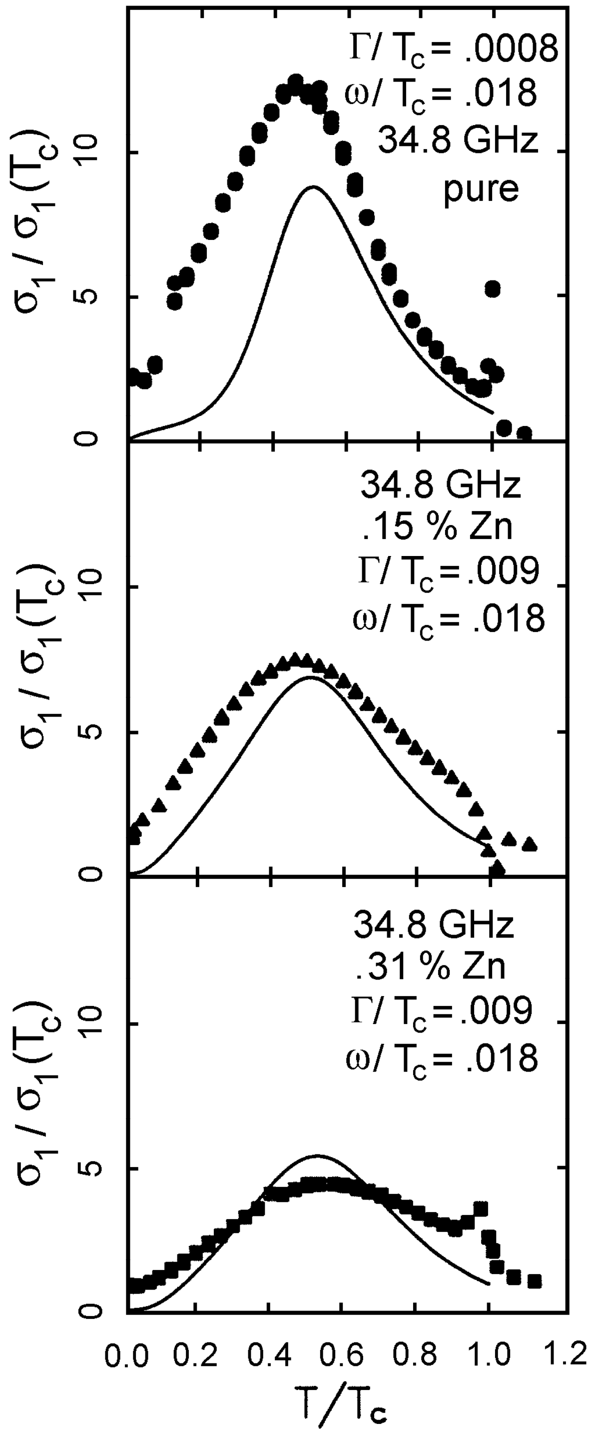

Figure 2.6: *Normalized conductivity vs. reduced temperature compared to experimental results presented in [34], for several impurity concentrations. From reference [35].*

changes the scattering rate, but also introduces new states at the Fermi level. At relatively low concentrations these effects cancel, yielding a conductivity which is independent of the number of scatterers. Using $1/\tau \approx 2k_BT_c$ and $\Delta_0/k_BT_c \approx 2$ we estimate that $\sigma_0 \approx 0.3\,\sigma_{dc}(T_c)$. Zhang *et al.* reported in an untwinned $YBa_2Cu_3O_{7-\delta}$ single crystal a residual conductivity close to this value [49], however in most measurements performed upto now, the experimental resolution was insufficient to establish the existence of this universal value beyond a reasonable doubt.

2.2.4 Observations in Thin Films

In the preceding sections we have focused on the experimental results obtained on single crystals, both pure and contaminated. Much of the contemporary data have been acquired on thin superconducting films. Obviously one of the main motivations to measure the behavior of thin films is their potential use in superconducting circuitry. However, the fabrication of high quality thin films has been proven to be rather complicated, due to for instance oxygen diffusion. At the present stage, also thin films results are converging toward the intrinsic behavior seen before in single crystals.

A large difference for measuring thin films, as compared to single crystals, is the variety of experimental techniques available in the micro- and mm-wave range. Whereas for single crystals in most cases resonant cavity techniques have been employed, for thin films also non-resonant, quasioptical methods have been used. One of the pioneering groups using quasioptical methods to study a large variety of materials in the mm-wave range were Kozlov and co-workers [65, 66]. Using multiple backward wave oscillators, they cover the frequency range from 5 to 40 cm^{-1}, obtaining both phase and amplitude information.

Using a similar technique, de Vaulchier *et al.* were able to measure the linear penetration depth expected for a d-wave superconductor in high quality $YBa_2Cu_3O_{7-\delta}$ thin films [67]. In this case, they concentrated on the amplitude measurement, by wedging the substrate and thereby destroying the phase information. A major advantage of this technique with respect to the cavity techniques, is the fact that an absolute value for the microscopic properties is obtained. By scaling the data of Hardy *et al.*, using their knowledge of the absolute London penetration depth, de Vaulchier *et al.* showed that the slope of the linear dependence measured in their films is the same as for single crystals (4.2 $\mathring{A}/K$).

Furthermore, de Vaulchier *et al.* showed that the crossover from a linear to a quadratic temperature dependence is connected with a corresponding increase in the zero temperature penetration depth, reminiscent of presence of additional scatterers. In fact, in most earlier studies in thin films this quadratic temperature dependence was found [68, 69], although it was often erroneously interpreted as the exponential dependence expected for a conventional superconductor.

A complication of performing experiments at higher frequencies, combined with the improved quality of the films, is that $\omega\tau$ become comparable or even larger than 1. Hence the assumption that both λ and σ_1 are frequency independent breaks down, as was shown by Dähne *et al.* [70].

Also the first indications of the unconventional behavior of σ_1 below T_c were acquired on thin films, by THz time domain spectroscopy [39]. This technique consists of measuring the system response to a fast pulse (fs) of submm-radiation, emitted by a bridging element. Due to the short pulse duration, the pulse contains a broad spectrum of frequencies, ranging from 0.1 to 1.4 THz. In this way both amplitude and phase (using a reference beam having an adjustable path length) can be measured over a broad range of frequencies. Nuss *et al.* showed that σ_1 is enhanced considerably upon entering the superconducting state, having a peak at lower temperatures. Also in this thesis, similar results on $DyBa_2Cu_3O_{7-\delta}$ thin films will be presented (chapter 6).

The peak is, as shown above, described well by a rapid decrease of scattering below T_c and causes the surface resistance R_s to remain rather high. In fact, this behavior leads to the counterintuitive dependence of R_s on the impurity concentration, namely that a lower quality film has a lower surface resistance. This occurs, since a higher impurity density limits the rise in σ_1 and therefore reduces R_s.

In conclusion we can say that although the results for the high T_c thin films are converging toward reflecting the intrinsic properties for both the real and the imaginary part of the dielectric function, these same intrinsic properties such as the presence of nodes seriously inhibit the use of the cuprates in applications on a large scale so far.

2.3 Nonequilibrium Superconductivity

In this section we will review some of the earlier experiments probing non-equilibrium superconductivity in both conventional and unconventional superconductors. We will attempt to give an overview of the current understanding, both experimentally and theoretically, thereby introducing the concepts that will be important in the course of chapter 7, where we will demonstrate experimental results on both NbN and $DyBa_2Cu_3O_{7-\delta}$ using Photo Induced Activation of Mm-wave Absorption (PIAMA).

2.3.1 Low T_c Superconductors

We will focus on the optical experiments and omit similar non-equilibrium studies in which tunnel junctions were used [71]. In case of low injection currents results obtained using this technique show many similarities with the results obtained using an optical configuration. At high injection currents an additional complication appears, caused by the presence of a so-called branch imbalance. This means that the occupation numbers for the quasiparticle branches having k and $-k$ will be different. In optical techniques this problem is inherently circumvented, since the excess quasiparticles are created by breaking up Cooper pairs, thus automatically producing two quasiparticles having a momentum equal to k and $-k$. The first observation of non-equilibrium effects in a superconductor, using an optical configuration, was made by L. R. Testardi in 1971 [72]. He measured the change in resistivity of a Pb-film during and after illuminating the superconductor with a 40 μs pulse at 514 nm. Upon lowering the temperature to values far below T_c part of the observed signal persisted, while the transient followed the pulse instantly. Using the observed magnitudes of the changes in the normal state, Testardi concluded that heating could not account for the effects at low temperatures. The observed recombination time was approximately 1 μs, which suggested the presence of a bottleneck in the decay process. Also in other materials such as Al and Zn similar recombination times were observed [73].

As was pointed out earlier by Rothwarf and Taylor [74] however, one needs to be careful in interpreting experimentally obtained relaxation times. They modeled the non-equilibrium superconductor using two straightforward rate equations describing the rate at which the densities of both quasiparticles and phonons change.

$$\begin{aligned} \frac{dN}{dt} &= I_0 + \beta N_\omega - RN^2 \\ \frac{dN_\omega}{dt} &= \frac{RN^2}{2} - \frac{\beta N_\omega}{2} - \frac{N_\omega - N_{\omega T}}{\tau_\gamma} \end{aligned} \tag{2.23}$$

where N is the total number of quasiparticles, I_0 is the number of quasiparticles injected, β is the probability of breaking a Cooper pair by a phonon, N_ω is the number of phonons, $N_{\omega T}$ is the number of phonons in thermal equilibrium, R is the recombination coefficient and τ_γ^{-1} is the probability of a phonon to disappear by other means than pair-breaking. In equation (2.23) only phonons with $\hbar\omega > 2\Delta$ are included, since these are the only ones having sufficient energy to break up Cooper pairs. It is important to realize that quasiparticles with a large excess energy, will lose part of their energy by creating phonons. When these phonons have an energy larger than the superconducting energy gap, they can once again break up a pair, thereby maintaining the non-equilibrium state. An important property of the sample is therefore the *phonon-escape time*, τ_{pes}, i.e. the rate at which high energy phonons leak into the substrate. A long τ_{pes} will affect the measured relaxation time strongly. Obviously, when τ_{pes} is comparable to the recombination time, the presence of high energy phonons will enhance the experimentally observed quasiparticle lifetime by the so-called phonon trapping factor, equal to $(1+\tau_\gamma/\tau_B)$ [74]. Here τ_B is the phonon lifetime against pair-breaking and τ_γ is the lifetime of high energy phonons lost by other mechanisms. The phonon-escape time can be estimated by calculating the acoustic matching of the film and the substrate. For instance in the case of a film of thickness d, which is larger or comparable to the phonon mean free path against pair-breaking (Λ) one can show that

$$\frac{\tau_{eff}}{\tau_r} = \frac{4d}{\eta\Lambda} \tag{2.24}$$

In this case τ_{eff} is the measured effective recombination time, while τ_r is the actual recombination time. Furthermore, η is the phonon transmission coefficient at the film-substrate interface, which depends highly on the used materials. Therefore a prudent choise of substrate material, having a sound velocity and a density comparable to the superconductor under investigation needs to be made [75]. In earlier studies, phonon trapping factors ranging from 9 for Al on glass [76] upto 29 for Sn on Z-cut quartz [77], yield experimentally obtained recombination times close to microseconds.

Models

Other, more elaborate theoretical models were developed by Parker (the T*-model) [78] and Owen and Scalapino (the μ^*-model) [79]. In the first model both the quasiparticle density and the phonon density at energies larger than 2Δ are assumed to attain a distribution corresponding to a higher temperature T*, while the low energy phonons ($E < 2\Delta$) remain at ambient temperature. Using the Rothwarf-Taylor equations they calculated the relative significance of relaxation and recombination processes as a function of temperature and excess energy. Using the modified heating model Parker was able to explain the experimental data of Testardi, as well as data from Sai-Halasz *et al.* [77]. The latter results were obtained by measuring the reflectivity at 70 GHz during and after a 60-90 ns pulse.

The reason for the much closer agreement of this model compared to a simple heating model, is the fact that the optical energy is concentrated among the high energy phonons, resulting in a larger number of such phonons and therefore a higher effective temperature. The characteristic time of the system in this model will be the recombination time, and therefore much faster than the usual characteristic thermal time constants. Contrary to the fair agreement between the measured and calculated changes in reflectivity, Sai-Halasz *et al.* observed a time delay between the pump pulse and the change in reflectivity which cannot be accounted for within the T*-model.

An improvement of this model was suggested by Chang and co-workers [80]. They assumed the quasiparticle distribution to be described by a Fermi function at temperature T*, which allowed them to solve the kinetic equations for the phonons exactly. This leads to a distribution function consisting of a linear combination of two Bose functions, one at ambient temperature and one at T*, whereas the linear combination is different for energies below and above the energy gap. The kinetic equation approach was first put forward by Bardeen *et al.* [81] to calculate the thermal conductivity, and will also be employed in chapter 7 to calculate the recombination lifetime of quasiparticles in high T_c's.

The second alternative mentioned above, the μ^*-model [79], assumes that the mixture of Cooper pairs and quasiparticles has a different ratio than the one determined by the ambient temperature. Stating furthermore that the quasiparticles thermalize much faster than they recombine, Owen and Scalapino postulated a model in which there is thermal equilibrium, but no chemical equilibrium. Calculating the energy gap as a function of the excess quasiparticle density, utilizing the modified quasiparticle chemical potential, they were able to explain Testardi's data. Moreover, they predicted superconductivity to be enhanced at low excess concentrations, which has been confirmed experimentally [82]. In addition to the enhanced superconductivity at low concentrations, they predicted a first order phase transition to the normal state at high laser powers. The existence of the latter was not confirmed by Sai-Halasz *et al.*.

A model combining both ideas mentioned above (T* and μ^*), was put forward by Elesin [83]. He solved the kinetic equations for both quasiparticles and phonons numerically in the case of a source having a specific energy in between 9 and 10 times the energy gap. The physical picture emerging from these calculations is that normal state droplets are growing into the superconductor, where the size and velocity of the droplets depends on the incident laser power. In this way they were able to explain the threshold-like behavior of the nonequilibrium state both as function of temperature and film thickness, leading to the time delay observed by Sai-Halasz *et al.*. However, such a picture would imply a rather long time scale of both growth and decay of the nonequilibrium state whereas this is believed to be much faster on the basis of experimental observations.

2.3.2 High T_c Superconductors

The discovery of the high T_c superconductors also renewed the interest in nonequilibrium superconductivity. The main motivation of these studies has been the possible application the cuprates as a bolometric or a photodetector. However, also from the fundamental point of view a study of the dynamics of quasiparticles is of large interest, especially in connection to the unconventional pairing symmetry. The experimental efforts can be subdivided into two different configurations. The first class are the so-called photoconductivity measurements, in which the influence of a high energy laser (typically higher than 1 eV) on the dc-resistivity is studied. In a second class of experiments (using a so-called pump-probe configuration) the pulse of a high energy laser is split, and the second pulse monitors the changes induced by the first, as a function of time delay. In both classes most of the data showed a combination of a slow and a fast response, usually explained by an equilibrium (bolometric) and a nonequilibrium (nonbolometric) effect, respectively. A summary of the experimentally observed relaxation time constants has been given in table 2.3.

material	$\tau_{fast}(ps)$	$\tau_{slow}(ns)$	Reference
Y123	10^3	several	[84]
Y123	$< 2 \times 10^3$	1000	[85]
Y123	2.2	$> 10^5$	[86]
Y123	1.5	-	[87]
Y123	4	2.5	[88]
Y123	5	> 3	[89]
Y123	0.6	2.7	[90]
Tl2223	0.5	-	[91]
Bi2212	0.5	$> 10^5$	[86]
Bi2223	2	-	[87]

Table 2.3: *Experimentally observed relaxation times for high T_c superconductors.*

Nonequilibrium Responses

Concentrating first on the nonequilibrium effects there have been several suggestions to explain these phenomena.

<u>hot electron effect</u> [92, 93] - An explanation, similar to the T*-model discussed before, where the authors assign different effective temperatures to the quasiparticle and phonon non-equilibrium distributions. The electrons relax via electron-electron and electron-phonon scattering, thereby creating several other low energy electrons and phonons. After recombination the superconductor retains its equilibrium state.

<u>Josephson effect</u> [94] - For granular films a network of Josephson junctions has been used to explain the observed response. Optical absorption causes phase slips to occur, implying a maximum signal just below the transition region where the intergrain coupling weakens. The response followed the square root dependence on the incident power, expected for a network of Josephson junctions.

<u>Photon-assisted vortex motion</u> [95, 96] - The incident radiation induces additional vortex creep and flux flow, thereby causing an enhanced absorption and an increased resistivity. The moving vortices hence generate a voltage detectable as a photoresponse signal.

<u>Photofluxonic effect</u> [97] - The photon temporarily creates a vortex-antivortex pair. Using a current bias, the vortex and antivortex will be separated and a metastable state arises, having a larger resistance.

<u>Kinetic inductance</u> [90, 98] - In this model the Cooper pair density, inversely proportional to the kinetic inductance of the superconductor L_{kin}, is rapidly depressed during the optical pulse. This gives rise to a voltage transient proportional to $I_{bias}(\partial L_{kin}/\partial T)$. This implies also that the kinetic inductance voltage might be negative during the process of quasiparticle recombination. The fast response times summarized in table 2.3 show a rather large spread. It is very plausible that for separate experiments, different explanations apply.

Just as in the case of the conventional superconductors, one will have to take into account a possible bottleneck, due to the presence of high energy phonons, if the phonon escape time is relatively large compared to the recombination lifetime. Since for high T_c thin film mainly substrates are used which are rather similar to the superconducting, in most cases the acoustic matching will be fairly good. For instance for the case of a 50 nm YBCO film on a $LaAlO_3$ substrate Bluzer calculated a phonon escape time of about 80 ps.

In chapter 7 of this thesis, we will present a non-equilibrium study for $DyBa_2Cu_3O_{7-\delta}$ on $LaAlO_3$, rather similar to the sample mentioned before. As the measured timeconstants in our case are 4 to 5 orders of magnitude longer than 80 ps, we conclude that in our case phonon trapping effects can be neglected. In the same chapter we will pay further attention to the difference of non-equilibrium effects for high T_c superconductors compared to the situation for conventional superconductors. In particular, the influence of an unconventional pairing symmetry on the recombination process will be highlighted.

Slow Responses

As can be seen from table 2.3, in most experiments both a fast and a slow response were observed. In most cases the fast response was explained by a nonequilibrium process, while the slow response was attributed to a bolometric effect or, equivalently, an ordinary heating of the sample by the incident radiation. In order to establish the bolometric nature, several different experimental tests were performed. Examples are its existence above T_c [90], its temperature dependence, showing an optimal signal at T_c where dR/dT has a maximum [84] or its dependence on the film thickness and the incident power [98]. However, in some cases the slow response failed to pass these tests [86], and an alternative, nonbolometeric origin was suggested. Some of the above mentioned mechanisms, such as the photon-assisted vortex motion and the photofluxonic effect, could also lead to a long-lived component in the photo-response. Another possible explanation was put forward by Stevens *et al.* [86], who suggested the existence of long-lived localized states formed as a result of photo-excitation.

References

[1] J. G. Bednorz and K. A. Müller, Z. Phys. B **64**, 189 (1986)

[2] For an excellent review about gap symmetries and phase sensitive detection see: D. J. van Harlingen, Rev. Mod. Phys. **67**, 515, (1995).

[3] For a review of the strongly correlated models see: E. Dagotto, Rev. Mod. Phys. **66**, 763, (1994).

[4] For an overview of the normal state properties of the high T_c superconductors see: K. Levin, Ju. H. Kim, J. P. Lu and Qimiao Si, Physica C, **175**, 499 (1991).

[5] S. Chakravarty, A. Sudbo, P. W. Anderson and S. Strong, Science **261**, 337 (1993).

[6] P. W. Anderson, Science **235**, 1196 (1987).

[7] W. N. Hardy, D. A. Bonn, D. C. Morgan, Ruixing Liang and Kuan Zhang, Phys. Rev. Lett. **70**, 3999 (1993).

[8] K. A. Moler, D. J. Baar, J. S. Urbach, Ruixing Liang, W. N. Hardy and A. Kapitulnik, Phys. Rev. Lett. **73**, 2744 (1994).

[9] J. R. Kirtley, C. C. Tsuei, J. Z. Sun, C. C. Chi, L. S. Yu-Jahnes, A. Gupta, M. Rupp and M. B. Ketchen, Nature **373**, 225 (1995).

[10] D. G. Clarke, S. P. Strong and P. W. Anderson, Phys. Rev. Lett. **72**, 3218 (1994).

[11] K. Tamasaku, Y. Nakamura and S. Uchida, Phys. Rev. Lett. **69**, 1455 (1992).

[12] Jae H. Kim, H. S. Somal, M. Czyzyk, D. van der Marel, A. Wittlin, A. M. Gerrits, V. H. M. Duijn, N. T. Hien and A. A. Menovsky, Physica C **247**, 297 (1995).

[13] J. Schützmann, H. S. Somal, A. A. Tsvetkov, D. van der Marel, G. E. J. Koops, N. Koleshnikov, Z. F. Ren, J. H. Wang, E. Brück and A. A. Menovsky, Phys. Rev. B **55**, 11118 (1997).

[14] A. S. Alexandrov and J. Ranninger, Phys. Rev. B **23**, 1796 (1981).

[15] S. Robaszkiewicz, R. Micnas and K. A. Chao, Phys. Rev. B. **23**, 1447 (1981).

[16] N. F. Mott, Nature **327**, 185 (1987).

[17] S. A. Alexandrov, JETP Lett. Suppl. **46**, 107 (1987).

[18] P. Prelovsek, T. M. Rice and F. C. Zhang, J. Phys. C **20**, 229 (1987).

[19] C. M. Varma, P. B. Littlewood, S. Schmitt-Rink, E. Abrahams and A. E. Rückenstein, Phys. Rev. Lett. **63**, 1996 (1989).

[20] N. Bulut, D. Hone, D. J. Scalapino and N. E. Bickers, Phys. Rev. Lett. **64**, 2723 (1990).

[21] A. J. Millis, H. Monien and D. Pines, Phys. Rev. B **42**, 167 (1990).

[22] J. R. Schrieffer, X. G. Wen and S. C. Zhang, Phys. Rev. Lett **60**, 944 (1988).

[23] J. H. Kim, K. Levin and A. Auerbach, Phys. Rev. B **39**, 11633 (1989).

[24] G. Kotliar, P. A. Lee and N. Read, Physica C **153-155**, 538 (1988).

[25] D. M. Newns, M. Rasolt and P. Pattnaik, Phys. Rev. B **38**, 7033 (1988).

[26] N. E. Bickers, D. J. Scalapino and S. R. White, Phys. Rev. Lett. **62**, 961 (1989).

[27] P. Monthoux and D. Pines, Phys. Rev. Lett. **69**, 961 (1992).

[28] J. Bardeen, L. N. Cooper and J. R. Schrieffer, Phys. Rev. **108** (5), 1175 (1957).

[29] J. Tranquada, B. J. Sternlieb, J. D. Axe, Y. Nakamura and S.Uchida, Nature **375**, 561 (1995).

[30] G. Kotliar, Phys. Rev. B **37**, 3664 (1988).

[31] R. Kleiner, A. S. Katz, A. G. Sun, R. Summer, D. A. Gajewski, S. H. Han, S. I. Woods, E. Dantsker, B. Shen, K. Char, M. B. Maple, R. C. Dynes and John Clarke, Phys. Rev. Lett. **76**, 2161 (1996).

[32] D. van der Marel, Phys. Rev. B **51**, 1147 (1995).

[33] James Annet, Nigel Goldenfeld and S. R. Renn, Phys. Rev. B **43**, 2778 (1991).

[34] D. A. Bonn, S. Kamal, Kuan Zhang, Ruixing Liang, D. J. Baar, E. Klein and W. N. Hardy, Phys. Rev. B **50**, 4051 (1994).

[35] P. J. Hirschfeld, W. O. Puttika and D. J. Scalapino, Phys. Rev. B **50**, 10250 (1994).

[36] N. Bulut and D. J. Scalapino, Phys. Rev. Lett. **68**, 706 (1992).

[37] for a review see: D. A. Bonn and W. N. Hardy, Chapter 2 of *Physical Properties of High Temperature Superconductors*, vol. V, D. M. Ginsburg ed. (World Scientific, London, 1996), p. 7.

[38] P. C. Hammel, M. Takigawa, R. H. Heffner, Z. Fisk and K. C. Ott, Phys. Rev. Lett. **63**, 1992 (1989).

[39] Martin C. Nuss, P. M. Mankiewich, M. L. O'Malley, E. H. Westerwick and Peter B. Littlewood, Phys. Rev. Lett. **66**, 3305 (1991).

[40] D. A. Wollman, D. J. van Harlingen, W. C. Lee, D. M. Ginsberg and A. J. Leggett, Phys. Rev. Lett. **71**, 2134 (1993).

[41] A. G. Sun, D. A. Gajewski, M. B. Maple and R. C. Dynes, Phys. Rev. Lett. **72**, 2267 (1994).

[42] A. Mathai, Y. Gim, R. C. Black, A. Amar and F. C. Wellstood, Phys. Rev. Lett. **74**, 4523 (1995).

[43] S. Kamal, D. A. Bonn, Nigel Goldenfeld, P. J. Hirschfeld, Ruixing Liang and W. N. Hardy, Phys. Rev. Lett. **73**, 1845 (1994).

[44] Steven M. Anlage, J. Mao, J. C. Booth, Dong Ho Wu and J. L. Peng, Phys. Rev. B **53**, 2792 (1996).

[45] Z.-X. Shen, D. S. Dessau, B. O. Wells, D. M. King, W. E. Spicer, A. J. Arko, D. Marshall, L. W. Lombardo and A. Kapitulnik, Phys. Rev. Lett. **70**, 1553 (1993).

[46] T. P. Devereaux, D. Einzel, B. Stadtlober, R. Hackl, D. H. Leach and J. J. Neumeier, Phys. Rev. Lett. **72**, 396 (1994).

[47] F. Gross, B. S. Chandrasekhar, D. Einzel, K. Andres, P. J. Hirschfeld, H. R. Ott, J. Beuers, Z. Fisk and J. L. Smith, Z. Phys. B **64**, 175 (1986).

[48] M. Takigawa, P. C. Hammel, R. H. Heffner and Z. Fisk, Phys. Rev. B **39**, 7371 (1989).

[49] Kuan Zhang, D. A. Bonn, S. Kamal, Ruixing Liang, D. J. Baar, D. Basov and T. Timusk, Phys. Rev. Lett. **73**, 2484 (1994).

[50] M. Prohammer and J. P. Carbotte, Phys. Rev. B **43**, 5370 (1991).

[51] Peter J. Hirschfeld and Nigel Goldenfeld, Phys. Rev. B **48**, 4219 (1993).

[52] P. Arberg and J. P. Carbotte, Phys. Rev. B **50**, 3250 (1994).

[53] K. Ueda and T. M. Rice, in *Theory of Heavy Fermions and Valence Fluctuations*, T. Kasuya and T. Saso ed. (Springer, Berlin, 1985), p. 267.

[54] Ju Young Lee, Kathleen M. Paget, Thomas R. Lemberger, Steve R. Foltyn and Xindi Wu, Phys. Rev. B **50**, 3337 (1994).

[55] V. J. Emery and S. A. Kivelson, Nature **374**, 434 (1995).

[56] E. Roddick and D. Stroud, Physica C **235-240**, 1799 (1994).

[57] Mark W. Coffey, Phys. Lett. A **200**, 195 (1995).

[58] Richard A. Klemm and Samuel H. Liu, Phys. Rev. Let. **74**, 2343 (1995).

[59] W. N. Hardy, D. A. Bonn, R. Liang, S. Kamal and K. Zhang, Proc. 7th Int. Symp. on Superconductivity, Kitakyushu, Japan (1994).

[60] Jian Mao, D. H. Wu, J. L. Peng, R. L. Greene and Steven M. Anlage, Phys. Rev. B **51**, 3316 (1995).

[61] R. Combescot and X. Leyronas, Phys. Rev. Lett. **75**, 3732 (1995).

[62] P. J. Hirschfeld, W. O. Puttika and D. J. Scalapino, Phys. Rev. Lett. **71**, 3705 (1993).

[63] S. Quinlan, D. J. Scalapino and N. Bulut, Phys. Rev. B **49**, 1470 (1994).

[64] Patrick A. Lee, Phys. Rev. Lett. **71**, 1887 (1993).

[65] G. Kozlov and A. Volkov, "Coherent Source Submillimeter Wave Spectroscopy" in *Millimeter Wave Spectroscopy on Solids*, G. Grüner ed. (Springer Verlag, 1995).

[66] B. P. Gorshunov, A. V. Pronin, A. A. Volkov, H. S. Somal, D. van der Marel, B. J. Feenstra, Y. Jaccard and J.-P. Locquet Proc. Int. Conf. on Low Energy Electrodynamics in Solids, Ascona Switzerland (1997).

[67] L. A. de Vaulchier, J. P. Vieren, Y. Guldner, N. Bontemps, R. Combescot, Y. Lemaitre and J. C. Mage, Europhys. Lett. **33** (2), 153 (1996).

[68] Zhengxiang Ma, R. C. Taber, L. W. Lombardo, A. Kapitulnik, M. R. Beasly, P. Merchant, C. B. Eom, S. Y. Hou and Julia M. Phillips, Phys. Rev. Lett. **71**, 781 (1993).

[69] N. Klein, U. Dähne, U. Poppe, N. Tellmann, K. Urban, S. Orbach, S. Hensen, G. Müller and H. Piel, J. Supercond. **5**, 195 (1992).

[70] U. Dähne, Y. Goncharov, N. Klein, N. Tellmann, G. Kozlov and K. Urban, J. Supercond. **8**, 129 (1995).

[71] for a review on the complete subject of nonequilibrium superconductivity see: *Nonequilibrium Superconductivity, Phonons and Kapitza Boundaries*, Kenneth E. Gray ed. (Plenum Press, New York, 1981).

[72] L. R. Testardi, Phys. Rev. B **4**, 2189 (1971).

[73] S. B. Kaplan, C. C. Chi, D. N. Langenberg, J. J. Chang, S Jafarey and D. J. Scalapino, Phys. Rev. B **14**, 4854 (1976).

[74] Allen Rothwarf and B. N. Taylor, Phys. Rev. Lett. **19**, 27 (1967).

[75] Steven B. Kaplan, J. Low Temp. Phys. **37**, 343 (1979).

[76] L. N. Smith and J. M. Mochel, Phys. Rev. Lett. **35**, 597 (1976).

[77] G. A. Sai-Halasz, C. C. Chi, A. Denenstein and D. M. Langenberg, Phys. Rev. Lett. **33**, 215 (1974).

[78] W. H. Parker, Phys. Rev. B **12**, 3667 (1975).

[79] C. S. Owen and D. J. Scalapino, Phys. Rev. Lett. **28**, 1559 (1972).

[80] J. J. Chang, W. Y. Lai and D. J. Scalapino, Phys. Rev. B **20**, 2739 (1979).

[81] J. Bardeen, G. Rickazen and L. Tewordt, Phys. Rev. **113**, 982 (1959).

[82] K. E. Gray, Sol. State Comm. **26**, 633 (1978).

[83] V. F. Elesin, Sov. Phys. JETP **44**, 780 (1976).

[84] A. Frenkel, M. A. Saifi, T. Venkatesan, P. England, X. D. Wu and A. Inam, J. Appl. Phys. **67**, 3054 (1990).

[85] W. R. Donaldson, A. M. Kadin, P. H. Ballentine and R. Sobolewski, Appl. Phys. Lett. **54**, 2470 (1989).

[86] C. J. Stevens, T. N. Thomas, S. Choudhury, J. F. Ryan, D. Mihailovic, L. Forro, G. A. Wagner and J. E. Evetts, Proc. Spectroscopic Studies of Superconductors, Ivan Bozovic and Dirk van der Marel ed., (SPIE **2696**, 1996), p. 313.

[87] J. M. Chwalek, C. Uher, J. F. Whitaker, G. A. Mourou, J. Agostinelli and M. Lelental, Appl. Phys. Lett. **57**, 1696 (1990).

[88] A. D. Semenov, G. N. Gol'tsman, I. G. Gogidze, A. V. Sergeev, E. M. Gershenzon, P. T. Lang and K. F. Renk, Appl. Phys. Lett. **60**, 903 (1992).

[89] S. G. Han, Z. V. Vardeny, K. S. Wong, O. G. Symko and G. Koren, Phys. Rev. Lett. **65**, 2708 (1990).

[90] N. Bluzer, Phys. Rev. B **44**, 10222 (1991).

[91] G. L. Eesley, J. Heremans, M. S. Meyer, G. L. Doll and S. H. Liou, Phys. Rev. Lett. **65**, 3445 (1990).

[92] M. Danerud, D. Winkler, M. Lindgren, M. Zorin, V. Trifonov, B. S. Karasik, G. N. Gol'tsman and E. Gershenzon, J. Appl. Phys. **76**, 1902 (1994).

[93] A. D. Semenov, R. S. Nebosis, Yu. P. Gousev, M. A. Heusinger and K. F. Renk, Phys. Rev. B **52**, 581 (1995).

[94] M. Leung, P. R. Broussard, J. H. Claassen, M. Osofsky, S. A. Wolf and U. Strom, Appl. Phys. Lett. **51**, 2046 (1987).

[95] E. Zeldov, N. M. Amer, G. Koren, A. Gupta, R. J. Gambino and M. W. McElfresh, Phys. Rev. Lett. **62**, 3093 (1989).

[96] A. Frenkel, Physica C **180**, 251 (1991).

[97] A. M. Kadin, M. Leung and A. D. Smith, Phys. Rev. Lett. **65**, 3193 (1990).

[98] F. A. Hegmann, D. Jacobs-Perkins, C.-C. Wang, S. H. Moffat, R. A. Hughes, J. S. Preston, M. Currie, P. M. Fauchet and T. Y. Hsiang, Appl. Phys. Lett. **67**, 285 (1995).

Chapter 3

Theory of Spectrometry on Layered Systems

In this chapter the theoretical background behind spectroscopy on stratified systems will be treated. Due to the vast variety of possible cases the treatment will be mainly restricted to those cases used later in the dissertation. Other treatments can be found in references [1–4].

In the first part of section 3.1 we will go through the mathematics to calculate the transmission and reflection coefficient for a two-layer system, taking into account the interference in both the film and the substrate. Furthermore some illustrative examples of special cases will be given. The second part studies the influence of film thickness on the temperature dependence of the transmissivity. We will demonstrate how the sensitivity to the real and imaginary part of the dielectric function changes for different thicknesses. The significance of this analysis will be demonstrated later in chapter 6 of this dissertation, where an experimental study of these concepts is presented.

In section 3.2 we will introduce the subject of reflection using a finite angle of incidence, and its experimental implications. Moreover, including the transmission coefficient we can calculate the absorptivity in a thin film, relevant to the experiments presented in chapter 7. Finally, in section 3.3 we will briefly discuss the possibility to obtain the complex dielectric function ($\epsilon = \epsilon' + i\epsilon''$) analytically, by measuring both reflection *and* transmission on the same sample.

3.1 Transmission

3.1.1 Transmission Through a Two-Layer System

In optical spectroscopy one is able to measure three macroscopic material properties directly, namely the transmissivity T, the reflectivity R and the absorptivity A. Obviously, by virtue of the conservation of energy, it is always true that $T + R + A = 1$. Therefore it is sufficient to measure two properties in order to determine all three. However, since each property has its own requirements leading to quite distinct experimental considerations, it is often difficult to determine even two properties on the same sample. Furthermore, the measured quantities are often *amplitudes*, whereas the phase (as for instance in $\tilde{R} = Re^{i\Phi}$) is undetermined. This inhibits the determination of the microscopic properties of the sample using merely T, A or R. A common way to circumvent this problem is to make use of so-called Kramers-Kronig relations.

$$\Phi(\omega) \;=\; -\frac{2\omega}{\pi}\int_0^\infty \frac{ln\sqrt{R(\omega')}}{(\omega')^2-\omega^2}\,d\omega' \tag{3.1}$$

Since T, R and A, under ordinary circumstances are causal functions, and therefore have their poles in the lower half of the complex plane, one can directly determine Φ using these relations. However, for the use of Kramers-Kronig relations the experimentally determined reflectivity coefficient has to be extrapolated to zero and infinite frequency. The final results are usually rather sensitive to the nature of the used extrapolations.

Knowing both the amplitude and the phase, the real and imaginary part of the dielectric function ϵ or any other optical property, such as the conductivity σ, can be determined. These quantities contain the desired information about the interior of the material such as phonon frequencies, energy gaps, the free electron response etc. The use of Kramers-Kronig transformations is however not the only method to obtain both the real and imaginary part of the response functions. Other approaches, such as ellipsometry, focus on determining two independent quantities experimentally, thus allowing to determine the real and imaginary part analytically. Also, as we will show later in this chapter, using a thin film it is possible to measure both R and T on the same sample and obtain all the required information.

In this section we will focus on an alternative approach, using the interference pattern observed in optical spectra, when the wavelength of the applied radiation is comparable to the sample thickness. Starting point for this analysis are the Fresnel equations, which describe the reflection and transmission coefficients on an interface between two media, having a different refractive index.

$$\begin{aligned}
r_p &= \frac{n_1\cos\phi_1 - n_2\cos\phi_2}{n_1\cos\phi_1 + n_2\cos\phi_2}\\
t_p &= \frac{2n_1\cos\phi_1}{n_1\cos\phi_1 + n_2\cos\phi_2}\\
r_s &= \frac{n_2\cos\phi_1 - n_1\cos\phi_2}{n_2\cos\phi_1 + n_1\cos\phi_2}\\
t_s &= \frac{2n_1\cos\phi_1}{n_2\cos\phi_1 + n_1\cos\phi_2}
\end{aligned} \tag{3.2}$$

Here $n_i = \sqrt{\epsilon_i}$ are the refractive indices of both media, ϕ_i are the angles of propagation in the respective media and the suffixes p and s indicate the state of polarization of the incident light. The *p*-polarized light has its electric field vector parallel to the plane of incidence, while this is perpendicular for the *s*-polarized radiation. From this we can calculate the reflection and transmission coefficients at each interface of a stratified medium. At this point we will concentrate on the transmission through a two-layer system although other examples will be given later. For clarity the two-layer system is drawn in fig. 3.1, together with the directions of the beam and the indices indicating the respective media. The angles

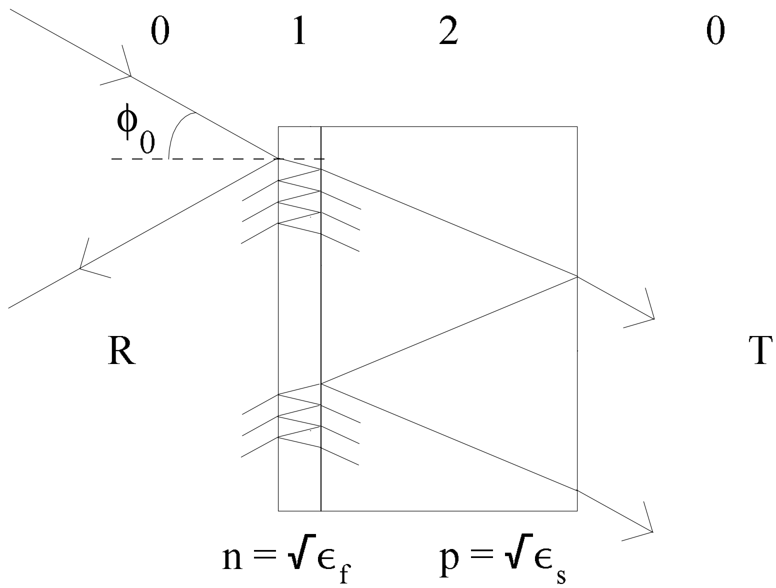

Figure 3.1: *Transmission and reflection on a two layer system, indicating the multiple reflections.*

between the directions of propagation of the waves in the respective media are interrelated via Snell's law

$$\sin\phi_0 \;=\; n\,\sin\phi_1 \;=\; p\,\sin\phi_2 \tag{3.3}$$

From this it immediately follows that in the case of an absorbing medium, where the index of refraction is complex, the angle ϕ_i will be complex as well. The physical reason for this can be easily understood if we consider the planes of equal phase and the planes of equal amplitude for the incident waves. For an isotropic, absorbing medium, the planes of equal phase will be perpendicular to the direction of propagation. However, since the reduction in amplitude of the wave in the medium depends on the distance travelled in the medium, the planes of equal amplitude will be parallel to the surface of separation, which is in most cases a plane boundary. Therefore, only in the case of normal incidence the planes of equal phase and equal amplitude will be parallel to one another. Also the distinction between the s- and p-polarized light vanishes at normal incidence.

Assuming for now that the light is incident normal to the surface, we obtain the following Fresnel coefficients for the first interface

$$\begin{aligned} r_{01} &= -r_{10} = \frac{1-n}{1+n} \\ t_{01} &= \frac{t_{10}}{n} = \frac{2}{1+n} \end{aligned} \tag{3.4}$$

Following the incident beam we see that it first crosses the interface between medium 0 and medium 1, where a fraction t_{01} is transmitted. At the next interface, between medium 1 and 2, the radiation has acquired a phase shift equal to $e^{i\phi}$ and a fraction t_{12} is transmitted. The phase angle ϕ is equal to kd_1n where k is the wavevector of the incident light ($k = 2\pi\nu/c$) and d_1 is the thickness of the first layer. However, part of the beam reflected on the interface between medium 1 and 2 ends up in the second layer after being reflected from the interface $1 \rightarrow 0$, in total having picked up a factor of $r_{12}r_{10}t_{12}e^{2i\phi}$. Summing over all contributions, the final transmission coefficient through the first layer will be:

$$\tau_{02} = \frac{t_{01}t_{12}e^{i\phi}}{1 - r_{12}r_{10}e^{2i\phi}} \tag{3.5}$$

where we have used the well-known expression for a geometrical series to include all the contributions. A similar contribution will arise from the multiple reflections within the second layer so that the transmission through the entire system, t_{lr} is described by

$$t_{lr} = \frac{\tau_{02}t_{20}e^{i\psi}}{1 - r_{20}\rho_{20}e^{2i\psi}}, \qquad \psi = kd_2p \tag{3.6}$$

where the phase factor ψ indicates the phase shift acquired by the beam traversing the substrate once. Please note that also the part of the beam being reflected at the last interface will give rise to interferences within the film, which are included in ρ_{20}.

$$\rho_{20} = r_{21} + \frac{t_{21}r_{10}t_{12}e^{2i\phi}}{1 - r_{10}r_{12}e^{2i\phi}} \tag{3.7}$$

Obviously, in order to calculate the experimentally obtained transmission coefficient, we have to take the absolute value of eq. (3.6), since we are dealing with intensities instead of field amplitudes, i.e. $T_{lr} = |t_{lr}^2|$.

Using identical arguments as given above, the reflectivity coefficient, r_l can be calculated, including all interference factors.

$$r_l = \rho_{02} + \frac{\tau_{02}r_{20}\tau_{20}e^{2i\psi}}{1 - r_{20}\rho_{20}e^{2i\psi}} \tag{3.8}$$

where the summed contribution of the film is embodied in the phase factors $\tau_{02}, \tau_{20}, \rho_{02}$ and ρ_{20}.

$$\begin{aligned} \rho_{02} &= r_{01} + \frac{t_{01}r_{12}t_{10}e^{2i\phi}}{1 - r_{10}r_{12}e^{2i\phi}} \\ \tau_{20} &= \frac{t_{21}t_{10}e^{i\phi}}{1 - r_{10}r_{12}e^{2i\phi}} \end{aligned} \tag{3.9}$$

The definitions for τ_{02} and ρ_{20} were already given in the course of the derivation of the transmission coefficient, as were the phase angles ϕ and ψ.

Evident from the transmission and reflection coefficients formulated above, is that the thicknesses of the layers play an essential role in the determination of the interference pattern of the complete system. The phase of the pattern is thus mainly determined by the *product* knd. An example of the implications of this observation can be seen in chapter 6.

Relevant Examples

In the remainder of this section we will focus on the transmission coefficient, t_{lr}. During our experiments the first layer (1) will be a (superconducting) film, deposited on a substrate (2). Since the thickness of the film is much smaller than the wavelength, we are only sensitive to the period of the interference effects arising within of the substrate. Therefore usually also the transmission through an uncovered substrate is measured and modeled using eq. (3.6), simply by setting $\mathrm{d}_1 = 0$. We thus *experimentally* obtain the values for both the real and the imaginary part of the refractive index of the substrate. These values are subsequently used in the analysis of the transmission through the two-layer system.

Before we proceed to discuss the two-layer system and the influence of the film and substrate properties in more detail, some illustrative examples will be given, making use of eq. (3.6), applying some reasonable assumptions and approximations.

Comparison $\mathbf{T}_{left\rightarrow right}$ and $\mathbf{T}_{right\rightarrow left}$

In a way completely analogous to the argument above we can formulate the transmission through the same sample for a beam incident on the interface on the right hand side. This yields:

$$t_{rl} \;=\; \frac{t_{02}\tau_{20}e^{i\psi}}{1 \;-\; \rho_{20}r_{20}e^{2i\psi}}\,, \qquad \psi \;=\; kd_2p \tag{3.10}$$

From the expressions for τ_{02} and τ_{20} given in eqs. (3.5) and (3.9) we obtain

$$\tau_{20} \;=\; p\tau_{02} \tag{3.11}$$

while furthermore $t_{02} \;=\; t_{20}/p$. This implies that, as expected, the transmission for light traversing from right to left is equal to the transmission for light traversing from left to right. Most importantly, they will have an identical phase.

Bare Substrate

In the case that we are dealing with a simple, uncovered dielectric, we can state that $d_1 = 0$. Furthermore we are dealing with a *frequency independent* dielectric constant $p = \eta + i\kappa$ where both η and κ are real numbers. Then eq. (3.6) reduces to:

$$t_{sub} \;=\; \frac{4p}{2p^2\cos\psi \;-\; 2i\sin\psi} \tag{3.12}$$

In fig. 3.2 we show several calculated transmission spectra for different dielectric constants to illustrate the general behavior as a function of both η and κ. We see that increasing

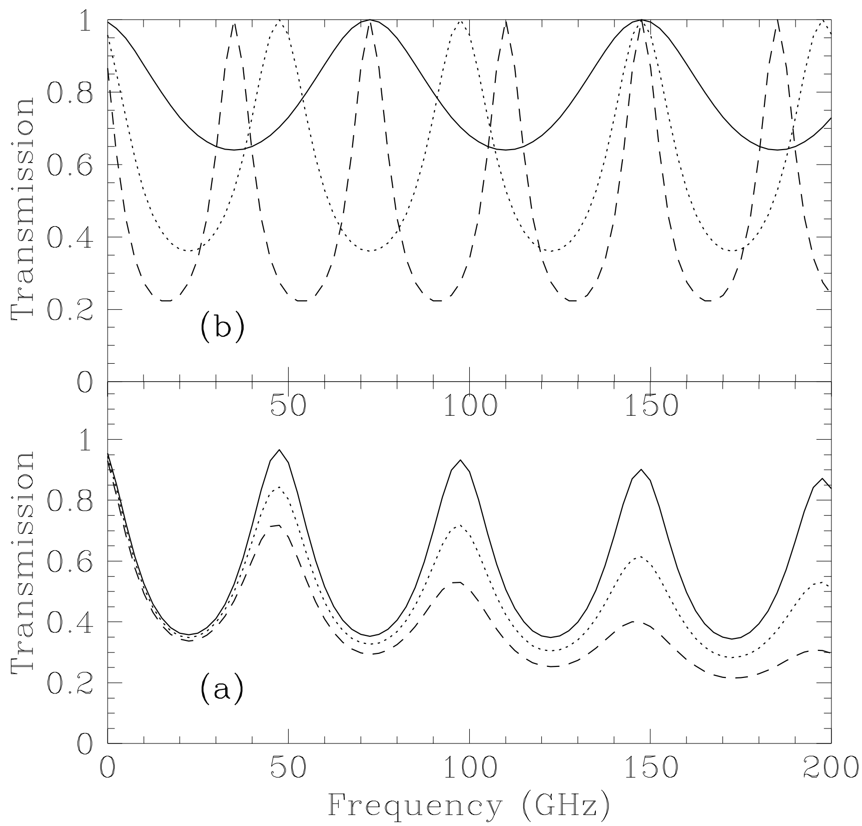

Figure 3.2: *Dependence of transmission of a bare dielectric on a: η at fixed $\kappa = 0$ (η=2: solid line, η=3: dotted line, η=4: dashed line) and b: κ at fixed $\eta = 3$ (κ=0.01: solid line, κ=0.05: dotted line, κ=0.10: dashed line).*

the real part of the refractive index, η, reduces the distance between the peaks, as well as the absolute transmission in the minima. If the absorption coefficient, κ, is enhanced we see that the magnitude of the maxima is reduced and the overall transmission becomes "tilted".

Wedged Substrate

Another approximation one can make, starting from the two-layer system, is to neglect the interference effect within the substrate. This has large experimental relevance since a commonly used trick in transmission spectroscopy is to wedge the substrate, thereby destroying the phase coherence and thus the interference. In this way one measures directly the transmission through the thin film, except for a constant factor, and is therefore able to obtain for instance its temperature dependence [5]. Equation 3.6 then reduces to:

$$t_{wed} \;=\; (\frac{2p}{1+p})\,\frac{2n}{n(1+p)\cos\phi - i(p+n^2)\sin\phi} \tag{3.13}$$

where n is the *complex* dielectric function of the film and p is the dielectric constant of the substrate.

Free Standing Film

We can go one step further, and omit the substrate completely. We then end up having a free standing film, which is an idealized case, but rather instructive as we will see later on. Starting from eq. (3.13) we can take $p = 1$ resulting in

$$t_{free} \;=\; \frac{2n}{2n\cos\phi \;-\; i(1+n^2)\sin\phi} \tag{3.14}$$

In transmission experiments usually the studied films are optically thin, meaning that we are allowed to apply the so-called *thin film limit.* This means that we take $\phi \ll 1$, or equivalently $kd_1n \ll 1$. Taking $\cos\phi \approx 1$ and $\sin\phi \approx \phi$ yields

$$t_{free} \;=\; \frac{1}{1 \;-\; \frac{ikd_1}{2}(1+\epsilon)} \tag{3.15}$$

where we replaced n^2 by ϵ. Since we are interested in the relative significance of the real and the imaginary part of the dielectric function we use $\epsilon = \epsilon' + i\epsilon''$. The transmission is then given by

$$T_{free} \;=\; |t^2_{free}| \;=\; \left[1 + \left(\frac{\pi\nu d_1\epsilon''}{c}\right)^2 + \left(\frac{2\pi\nu d_1\epsilon''}{c}\right) + \left(\frac{\pi\nu d_1(\epsilon'+1)}{c}\right)^2\right]^{-1} \tag{3.16}$$

Assuming furthermore that $|\epsilon'| \gg 1$ and $(\pi\nu d_1\epsilon'')/c \ll 1$ this reduces further to:

$$T_{free} \;=\; |t^2_{free}| \;=\; \left[1 + \left(\frac{2\pi\nu d_1\epsilon''}{c}\right) + \left(\frac{\pi\nu d_1\epsilon'}{c}\right)^2\right]^{-1} \tag{3.17}$$

From this expression it is evident that the thickness plays an important role in determining the relative significance of the real and imaginary parts. For thin films the absorptive term ($\sim \epsilon''$) on the right hand side of equation (3.17) will dominate, while for thicker films, the reactive term ($\sim \epsilon'$) will be most significant. From eq. (3.17) one can estimate a *critical* thickness (d_c), at which the real and imaginary part are equally important:

$$d_c = \frac{2c\epsilon''}{\pi\nu(\epsilon')^2} \tag{3.18}$$

We will return to the critical thickness in section 3.1.2 and in chapter 6.

Maxima and Minima in the Interference Pattern

It is interesting to focus on the maxima in the Fabry-Perot interference pattern of the film-substrate system for several reasons. At these frequencies, it is relatively straightforward to determine the film properties analytically from the complete expression given in eq. (3.6). Moreover, at these frequencies the effect of the film on the transmission coefficient is most severe, allowing a very precise determination of the absolute magnitude of the conductivity of the film. To demonstrate this we return to equations (3.4) to (3.7). Substituting all Fresnel coefficients at the respective interfaces by their values in terms of the dielectric properties of the film and the substrate yields

$$\begin{aligned} \tau_{02} &= \frac{2n}{(p+1)n\cos\phi \,-\, i(\epsilon+p)\sin\phi} \\ \rho_{20} &= (\frac{p-n}{p+n})\left(1+\frac{p(n-1)e^{i\phi}}{p-n}\tau_{02}\right) \end{aligned} \tag{3.19}$$

By substitution of τ_{02} the latter can be further reduced to

$$\rho_{20} = \frac{(p-1)n\cos\phi \,+\, i(\epsilon-p)\sin\phi}{(p+1)n\cos\phi \,-\, i(\epsilon+p)\sin\phi} \tag{3.20}$$

We are interested in the experimental transmission coefficient, involving transmitted intensities, therefore eq. (3.6) becomes

$$T = |t_{lr}^2| = 4p^2\left|\frac{\tau_{02}}{(1+p)e^{-i\psi}+(1-p)\rho_{20}e^{i\psi}}\right|^2 \tag{3.21}$$

Substituting eqs. (3.19) and (3.20) into (3.21) and assuming that the thin film limit is valid, we finally obtain

$$T_{lr} = \frac{1}{\cos\psi\,\cos\phi}\left[\frac{1}{1\,-\,(\frac{n^2+p^2}{2np})\tan\psi\,\tan\phi\,-\,i(\frac{1+p^2}{2p})\tan\psi\,-\,i(\frac{1+n^2}{2n})\tan\phi}\right] \tag{3.22}$$

In case of a maximum in transmission through the bare substrate, we can state $\sin\phi = 0$ and $\cos\phi = 1$.

$$T^{max} = \frac{1}{1\,+\,kd_1\epsilon''\,+\,\left(\frac{kd_1\epsilon''}{2}\right)^2\,+\,\frac{k^2d_1^2}{4}(1+\epsilon')^2} \tag{3.23}$$

which is, as expected, completely equivalent to the result for the free standing film, given before in eq. (3.16). In case of a minimum the opposite is valid, $\sin\phi = 1$ and $\cos\phi = 0$, resulting in

$$T^{min} = \frac{4p^2}{(1+p^2)^2\,+\,(1+p^2)(kd_1\epsilon'')^2\,+\,2kd_1(1+p^2)\epsilon''\,+\,(kd_1|p^2+\epsilon'|)^2} \tag{3.24}$$

Also in this case, taking $p = 1$ yields the free standing film results given in eq. (3.15), since we neglected the interference effects within the film, by assuming that the thin film limit is valid. Please note, that one has to be very careful in defining maxima and minima. In fact, for a superconducting film on a substrate, the maxima and minima in the transmission of the entire system will be interchanged in the superconducting state, as compared to the normal state. Therefore I will use the terms maximum and minimum strictly in relation to the transmission through a bare substrate.

3.1.2 Influence of the Thickness on the Temperature Dependence of the Transmission Coefficient

In order to get a feeling for the influence of specific material properties on the transmission coefficient we need to adopt a model to work with. There have been strong objections to the use of the Drude model, and especially at higher frequencies it is well established that the class of high T_c superconductors does not follow the ordinary metallic description very well, as can be seen for instance in the linear frequency dependence of the scattering rate γ. However, at low frequencies this description still works sufficiently well, and therefore we will make use of this fairly straightforward model. We can henceforth describe the dielectric function of the film using the well-known two-fluid description [6, 7].

$$\epsilon \;=\; 1 + \frac{2i\sigma}{\nu} \;=\; \epsilon_\infty - \frac{\nu_{pn}^2(T)}{\nu(\nu + i\gamma(T))} - \frac{\nu_{ps}^2(T)}{\nu^2} \tag{3.25}$$

Here $\nu_{pn}(T)$ is the normal state plasma frequency, $\gamma(T)$ is the scattering rate, $\nu_{ps}(T)$ is the superfluid plasma frequency and ν is the measurement frequency. We recall that $\epsilon'' = 2\sigma_1/\nu$ above T_c, and $\sigma_1 \to 1/\rho_{dc}$ for low frequencies. Furthermore, $\epsilon' = -c^2/(2\pi\nu\lambda)^2$ at low temperatures and is therefore directly related to the penetration depth of the material. This enables us to obtain, in addition to its temperature dependence, an absolute value for λ using $\nu_{ps}\ [\mathrm{cm}^{-1}] \;=\; 1/2\pi\lambda$.

For the measurements presented in this dissertation, the scattering rate γ remains larger than the measurement frequency ν, so that λ and σ_1 have only a weak frequency dependence. Mm-wave experiments performed under conditions where $\nu > \gamma$ have been reported by Dähne *et al.* [8]. Even though in our case λ and σ_1 show no frequency dependence, we would like to emphasize the importance of the fact that the available frequency range is as broad as possible. Therefore we calculated the frequency dependence of the dielectric properties in and around our frequency range (4 - 6 cm^{-1}) and plotted these in fig. 3.3. The values we used for these calculations are given in table 3.1. Next, we used the properties from fig. 3.3 to determine the transmission through a film deposited on a wedged substrate (eq. (3.13)), in order to concentrate on the phenomena directly correlated to the thin film. The result is shown in fig. 3.4, where again the part in between the two vertical dash-dotted lines is our available frequency. In fig. 3.3a we see that ϵ' is enhanced by about a factor of 10^4 (note the logarithmic scale) upon entering the superconducting state. This is due to the presence of the superfluid density, i.e. the δ-function at zero-frequency,

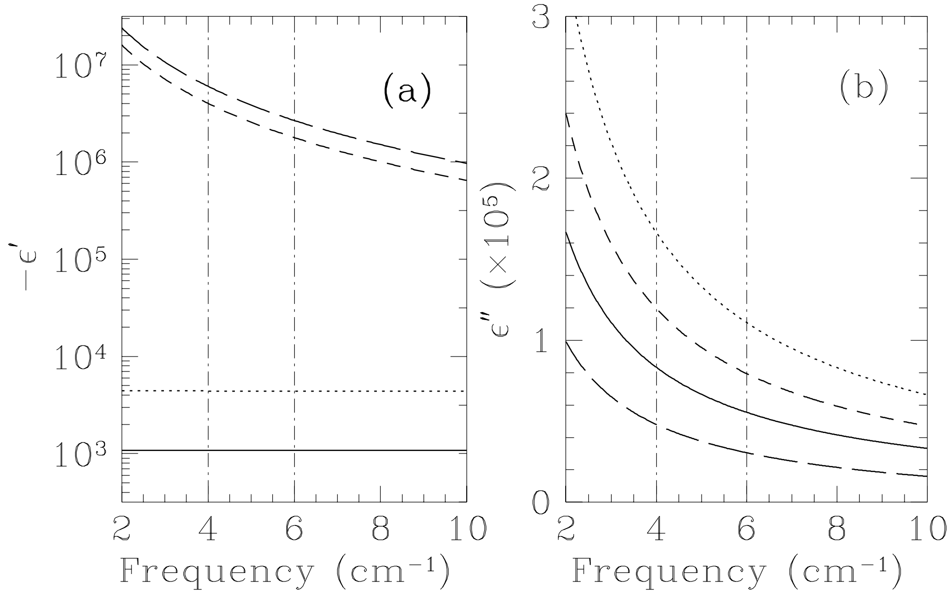

Figure 3.3: *Frequency dependence of the real (a) and imaginary (b) part of ϵ, plotted for several different temperatures (270 K: solid line, 90 K: dotted line, 60 K: short dashed line, 4 K: long dashed line). The area in between the two vertical dash-dotted lines is our available frequency range.*

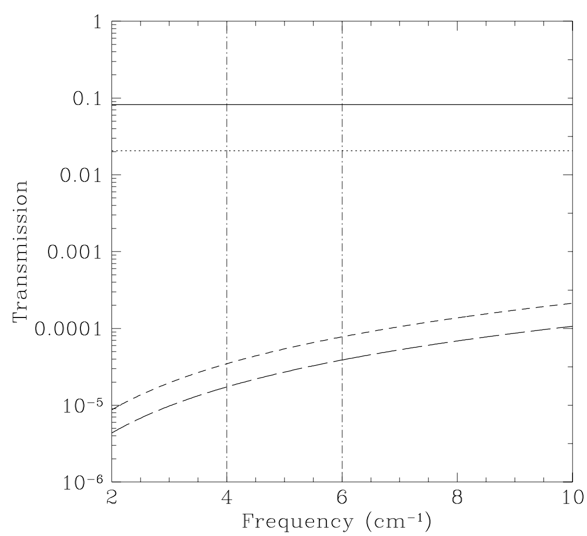

Figure 3.4: *Frequency dependence of the transmission through a thin film on a wedged substrate, plotted for several different temperatures (270 K: solid line, 90 K: dotted line, 60 K: short dashed line, 4 K: long dashed line). The area in between the two vertical dash-dotted lines is our available frequency range.*

Temp. (K)	ν_{pn} (cm^{-1})	γ (cm^{-1})	ν_{ps} (cm^{-1})	σ_1 (Ω^{-1}cm^{-1})	λ(Å)
270	10^4	300	0	5500	-
90	10^4	150	0	11000	-
60	6000	75	8000	8000	2000
4	2000	20	9800	3000	1620

Table 3.1: *Parameters used for the calculation of the frequency dependence of ϵ', ϵ'', and T_{wed}, presented in figs. 3.3 and 3.4.*

showing its typical $1/\nu^2$ frequency dependence. In fig. 3.3b we see that the magnitude of ϵ'' is in between the values of ϵ', being much larger in the normal state and much smaller in the superconducting state. ϵ'' has a $1/\nu$ dependence as expected for a frequency independent σ_1, since $\epsilon = 1 + 2i\sigma/\nu$. The transmission we obtain using these parameters shows a frequency independent behavior in the normal state, but attains a strong frequency dependence below T$_c$, which can be recognized if the available frequency range is sufficiently broad.

An additional advantage of having a broad frequency range can be inferred from fig. 3.2. We see that for typical values of η = 3 to 4, the available frequency range from 4 to 6 cm^{-1} covers approximately a single oscillatory period. The addition of a source at higher frequencies would allow the use of 2 or 3 periods for the analysis, facilitating this considerably. It is hence evident that the use of substrates having a high value for η and/or a large thickness is advantageous.

Now that we adopted a model for the dielectric function of the film, we can return to eq. (3.18) and calculate the critical thickness as a function of the microscopic optical properties of the film. Since the magnitudes of both contributions ϵ' and ϵ'' is very different for a normal metal or a superconductor (due to the presence of the superfluid), d$_c$ can be calculated for two distinct cases. Assuming that $\nu^2 \ll \gamma^2$ we find that

$$d_c \approx \frac{2c\gamma^3}{\pi\nu^2\nu_{pn}^2} \qquad \text{(metal)} \qquad (3.26)$$

$$d_c \approx \frac{32\pi^3\nu_{pn}^2\nu^2\lambda^4}{c^3\gamma} \qquad \text{(superconductor)} \qquad (3.27)$$

Taking common values for 123-superconductors (γ = 100 cm^{-1}, ν = 5 cm^{-1}, ν_{pn} = 10^4 cm^{-1} and λ = 2000 Å), we obtain that $d_c \sim 2.5\,\mu$m in the normal state, while $d_c \sim 0.4$ Å for T$\ll$ T$_c$. Consequently, for most thin films the transmission in the normal state will be determined by σ_1, while in the superconducting state it will be determined by λ.

However, an indication that this assumption may not be valid in all cases can be seen in fig. 3.5. In this figure the temperature dependence of the transmission coefficient is

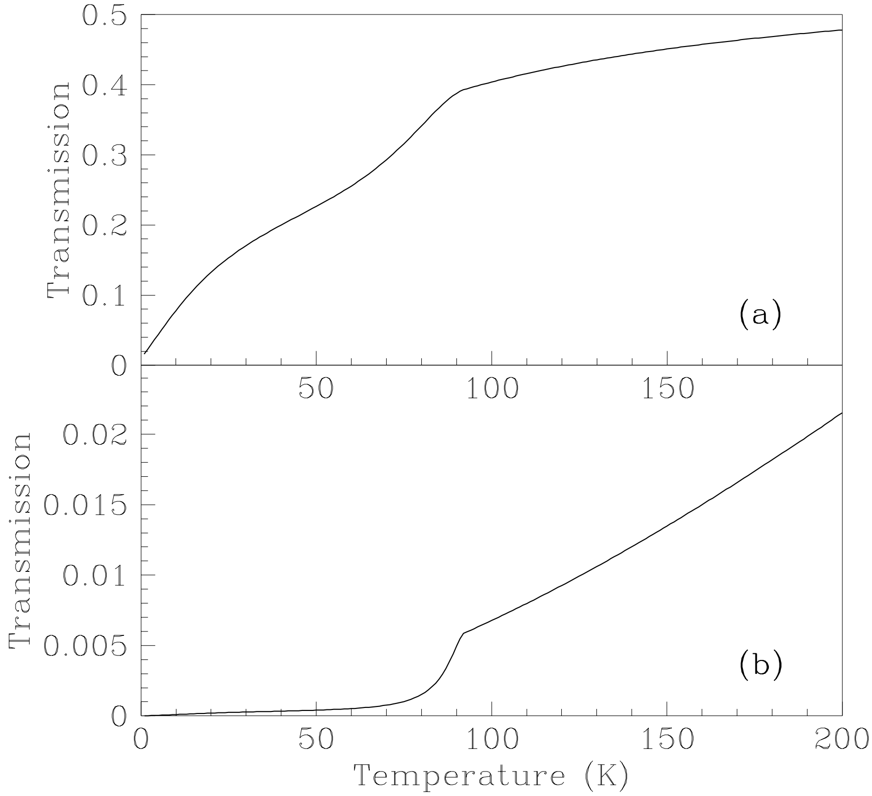

Figure 3.5: *Temperature dependence of the transmission through a superconducting thin film, shown for two different thicknesses a: 24 Å and b: 1000 Å*

shown for two different film thicknesses, 24 and 1000 Å. We used a BCS-like temperature dependence for the penetration depth, represented by the empirical Gorter-Casimir expression [9]

$$\frac{\lambda(T)}{\lambda(0)} = \left[1 - \left(\frac{T}{T_c}\right)^4\right]^{-1/2} \tag{3.28}$$

and an idealized, linear temperature dependence for the resistivity ($\sim 1/\sigma_1$) down to 0 K. The parameters used for this calculation are summarized in table 3.2. It is evident from the shape of the curve around T_c that σ_1, being continuous at T_c, plays a far more prominent role in the case of the thin film (a), whereas the distinct kink at T_c for the thicker film is caused by the presence of the superfluid appearing in ϵ' ($\sim 1/\lambda^2$).

Equivalently to having a critical thickness for fixed dielectric properties, by fixing the thickness and accounting for the temperature dependence of the dielectric properties one can estimate the temperature range at which the real and imaginary contributions will be equally important. In fig. 3.6 the critical thickness, d_c, is presented as a function of temperature. For this calculation we used the penetration depth results obtained on a

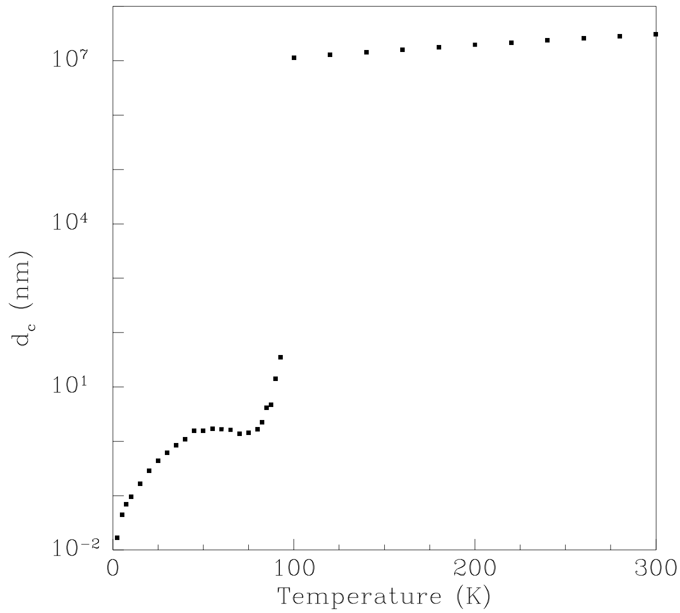

Figure 3.6: *Temperature dependence of the critical thickness d_c.*

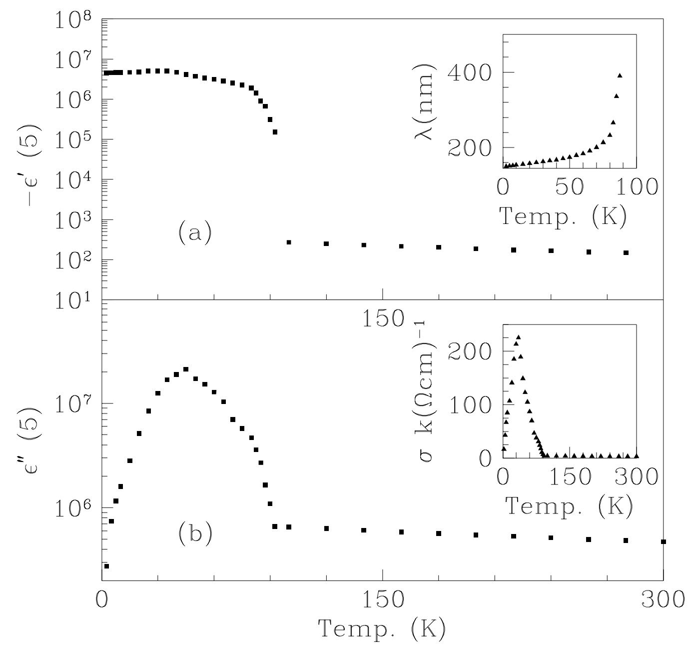

Figure 3.7: *a: Temperature dependence of ϵ' and ϵ'', used for the calculation of d_c shown in fig. 3.6. In the insets the temperature dependence of λ and σ_1 are shown in the upper and lower panel respectively.*

property		
d	(Å)	24-2000
$\sigma(300)$	$(\Omega^{-1}\mathrm{cm}^{-1})$	4000
$\lambda(0)$	(Å)	4000
γ	(cm^{-1})	300
η		4
ν	(GHz)	150
T_c	(K)	92

Table 3.2: *Parameters used for the calculation of the temperature dependence of the transmissivity for different film thicknesses, shown in fig. 3.5.*

$YBa_2Cu_3O_{7-\delta}$ single crystal, reported in reference [10] while for σ_1 we used results on a similar single crystal, presented in reference [11]. The temperature dependences of λ and σ_1 are shown in insets of fig. 3.7. The real and imaginary part of ϵ, calculated at our center frequency ($\nu = 5\,\mathrm{cm}^{-1}$), are plotted in the upper and lower panel of fig. 3.7 respectively. The additional curvature at low temperatures is a results of the scattering rate γ becoming comparable or even smaller than ν. The critical thickness changes rapidly around T_c, indicating that for most thin films, the transmission is dominated by ϵ'' in the normal state, while it is governed by ϵ' in the superconducting state. For the single crystals used in this calculation, the crossover region around T_c is rather small. A more specific experimental analysis using the measured values for $DyBa_2Cu_3O_{7-\delta}$ will be given in the chapter 6.

3.2 Reflection using an Oblique Angle of Incidence

Semi-infinite Medium

We return to eq. (3.2) where the Fresnel coefficients are given for an arbitrary interface and angle of incidence. During the entire analysis presented above we assumed to be working under normal incidence conditions, whereby the distinction between the p-polarized and s-polarized light disappears. However, the use of a non-zero angle of incidence in a polarized reflection measurement on an anisotropic medium, yields valuable information in *all* three directions of the crystal axes. Intuitively this can be easily understood by realizing that one polarization (p) will contain the planar response, having the axial response admixed, while the s-polarization is only sensitive to the planar response. This means that we can use the information known from the s-polarization to extract the information about the c-axis stored in the p-polarized reflectivity.

In this section we will briefly discuss some of the mathematics involved and also hint at the physical implications. In chapter 5 we will return to this topic and demonstrate its strength by polarized reflectivity measurements performed on a $Tl_2Ba_2Ca_2Cu_3O_{10}$ thin film at an incidence angle equal to 45°. A more detailed description and many experimental results obtained with the so-called Polarized Angle Resolved Infrared Spectrometry technique (PARIS), are described in reference [12].

The measurement configuration is depicted in fig. 3.8, where we have indicated the directions of the polarizations and the crystal axes. We assume that the crystal structure

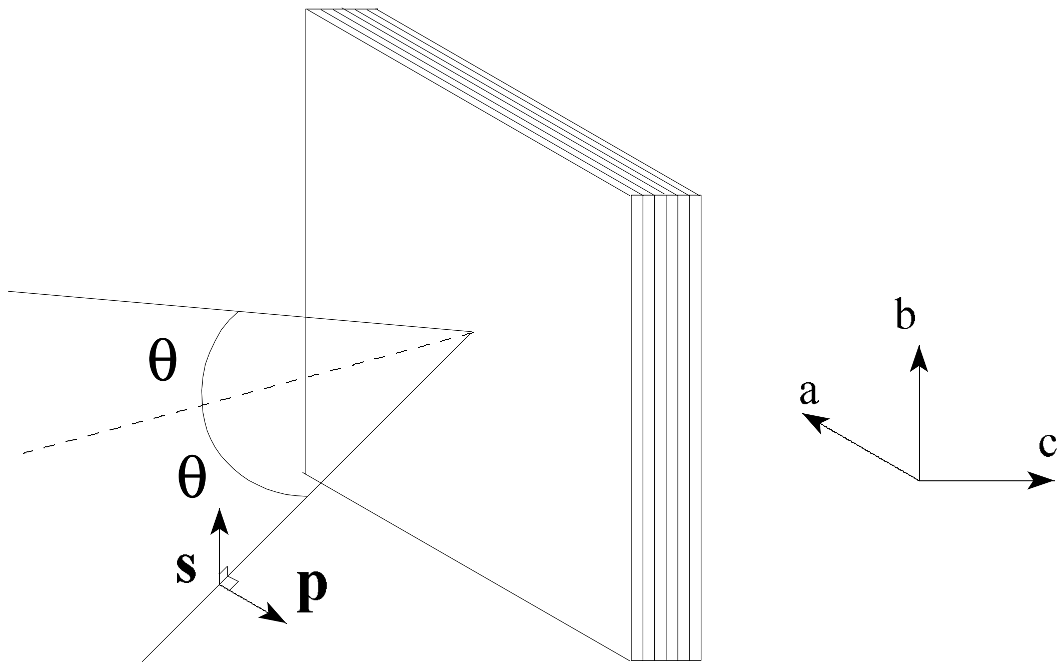

Figure 3.8: *Configuration for reflectivity measurements at an oblique angle of incidence, θ.*

of the high T_c superconductor under investigation is tetragonal, and hence there will be no anisotropy in the in-plane dielectric function. In order to describe the *total* response of the reflecting ab-plane *and* the c-axis direction perpendicular to this plane, we have to start with the complex Fresnel reflection coefficients for a uniaxial crystal. The optical axis is oriented perpendicular to the reflecting surface, hence we can write the reflection coefficients as [3]

$$\begin{aligned} r_s &= \frac{\cos\theta - \sqrt{n_o^2 - \sin^2\theta}}{\cos\theta + \sqrt{n_o^2 - \sin^2\theta}} \\ r_p &= \frac{n_o n_e \cos\theta - \sqrt{n_e^2 - \sin^2\theta}}{n_o n_e \cos\theta + \sqrt{n_e^2 - \sin^2\theta}} \end{aligned} \tag{3.29}$$

Here θ is the incident angle and n_o and n_e are the ordinary and extraordinary refractive indices respectively. Since we are measuring reflected *intensities*, the phase Φ, given by $\tilde{R} = Re^{i\Phi}$, has to be determined using Kramers-Kronig relations. In doing this for a non-zero angle of incidence one needs to be careful, since experimental uncertainties might lead to having negative values for Φ. This would then lead to spurious negative values for the optical conductivity calculated using R and Φ. When both quantities R and Φ are known and non-negative, we can proceed and determine ϵ_o and ϵ_e by solving eq. (3.29) in terms of r_s and r_p

$$\begin{aligned} \epsilon_o &= \sin^2\theta + \left(\frac{1-r_s}{1+r_s}\right)^2 \cos^2\theta \\ \epsilon_e &= \sin^2\theta \left[1 - \epsilon_o \left(\frac{1-r_p}{1+r_p}\right)^2 \cos^2\theta\right]^{-1} \end{aligned} \tag{3.30}$$

Given ϵ_o and ϵ_e we can calculate other interesting response functions such as the optical conductivity and the loss function.

The expressions stated above, can be applied directly to the reflectivity measurements on the high T_c superconductors. The ordinary dielectric function ϵ_o then corresponds to the sample response within the ab-plane, while ϵ_e corresponds to the response in the c-axis direction, perpendicular to the plane.

Using the large anisotropy present in these materials, we can derive an approximate expression for the reflectivity, and thereby the absorptivity, of the *p*-polarized light, knowing that the sample surface corresponds to the ab-plane.

$$A_p \approx 1 - R_p = 4\frac{\mathrm{Re}(x \cdot l^*)}{|1 + x \cdot l^*|^2} \tag{3.31}$$

Here we have introduced

$$\begin{aligned} x &= \frac{1}{n_{ab}} \\ l &\equiv \frac{1}{\cos\theta}\sqrt{1 - \frac{1}{\epsilon_c}\sin^2\theta} \end{aligned} \tag{3.32}$$

To get a physical feeling of the implications of eq.3.31, we use that in the limit of metallic conductivity, $Im(n_{ab}) \gg 1$. This means that $1/Im(n_{ab})$ can be used as the expansion parameter of a Taylor series. Furthermore we assume that $|\sin^2\theta/\epsilon_c| \ll 1$, so that the leading term of the series expansion becomes

$$1 - R_p = \frac{2\sin^2\theta}{\mathrm{Im}(n_{ab})\cos\theta} Im\left(-\frac{1}{\epsilon_c}\right) \tag{3.33}$$

Note that $Im(-\epsilon_c^{-1})$ is precisely the definition of the loss function in the c-axis direction, having peaks at the resonance frequencies, such as transverse optical phonons and plasmons. Since n_{ab} is featureless in the low frequency region in case of metallic planar behavior, this implies that the absorptivity of the p-polarized light measured in the *ab-plane* will have peaks at the resonant frequencies characteristic for the *c-axis* direction. This phenomenon is closely related to the physical mechanism leading to the well-known Berreman effect for dielectric overlayers on metallic substrates [13]. Due to for instance surface roughness, this effect can even be present in reflectivity measurements at smaller incidence angles, where the distinction between s- and p-polarization becomes smaller [14]. The correspondence between the structure in the ab-plane reflectivity and the c-axis resonances might easily lead be misinterpreted as a correlation between the c-axis phonon modes and the ab-plane electronic degrees of freedom [15,16].

Thin Film

In the previous part of this section we have estimated the absorption for the case of a semi-infinite anisotropic superconducting film in order to get a physical feeling for the influence of the angle of incidence on the observed spectra. For the semi-infinite layer we could neglect transmission and calculate the absorption coefficient directly from the reflectivity. Using the same formalism we will now calculate the absorption coefficient within a thin film on a semi-infinite substrate. In this case both transmissivity and reflectivity need to be taken into account.

The physical interest is the comparison of the frequency dependence of the absorptivity of the film and the frequency dependence of the experimental data obtained by Photo Induced Activation of Mm-wave Absorption (PIAMA) presented in chapter 7. In this particular case therefore, we are merely interested in the absorption within the *film*, not the absorptivity of the entire sample. Hence we assume that the substrate is semi-infinite, thereby neglecting the interference within the substrate. This is reasonable since the transmission coefficient at the dielectric-air interface $(2 \rightarrow 0)$ will be rather high, while the reflectivity coefficient for the beam at the dielectric-film interface $(2 \rightarrow 1)$ will be large. Henceforth the secondary contribution to the absorption within the film will be very small and interference effects only give rise to a minor correction.

The complex transmission and reflection coefficients given in the beginning of this chapter (eqs. (3.6) and (3.8)) can also be used in this case, provided that the appropriate Fresnel coefficients are used. We can rewrite the coefficients for the sake of clarity as

$$\begin{aligned} t_{lr}^x &= \frac{t_{01}^x t_{12}^x e^{i\phi^x}}{1 - r_{01}^x r_{12}^x e^{2i\phi^x}} \\ r_l^x &= \frac{r_{01}^x + r_{12}^x e^{2i\phi^x}}{1 - r_{01}^x r_{12}^x e^{2i\phi^x}} \end{aligned} \tag{3.34}$$

where we used that $r_{01} = -r_{10}$ and $t_{01}t_{10} = 1 - r_{01}^2$, while x is the suffix indicating either p-polarized or s-polarized light. The Fresnel coefficients for both polarizations on the subsequent interfaces for the case of an anisotropic film on an isotropic substrate are given by [3]

$$
\begin{aligned}
r_{01}^{p} &= \frac{n_{ab}n_c\cos\theta_0 \;-\; \sqrt{n_c^2-\sin^2\theta_0}}{n_{ab}n_c\cos\theta_0 \;+\; \sqrt{n_c^2-\sin^2\theta_0}} \\
r_{12}^{p} &= \frac{-n_{ab}n_c\cos\theta_2 \;+\; p\sqrt{n_c^2-p^2\sin^2\theta_2}}{n_{ab}n_c\cos\theta_2 \;+\; p\sqrt{n_c^2-p^2\sin^2\theta_2}} \\
r_{01}^{s} &= \frac{\cos\theta_0 \;-\; \sqrt{n_{ab}^2-\sin^2\theta_0}}{\cos\theta_0 \;+\; \sqrt{n_{ab}^2-\sin^2\theta_0}} \\
r_{12}^{s} &= \frac{-p\cos\theta_2 \;+\; \sqrt{n_{ab}^2-p^2\sin^2\theta_2}}{p\cos\theta_0 \;+\; \sqrt{n_{ab}^2-p^2\sin^2\theta_2}}
\end{aligned}
\tag{3.35}
$$

for the case that the optical axis of the uniaxial film is perpendicular to its boundaries. The transmission coefficients can be determined using

$$
\begin{aligned}
t_{ij}^{p} &= 1+r_{ij}^{p} \\
t_{ij}^{s} &= 1+r_{ij}^{s}
\end{aligned}
\tag{3.36}
$$

where i and j are the indices denoting the respective media. We have adopted the notation applicable to the high T_c superconductors, i.e. n_{ab} denotes the planar complex index of refraction and n_c denotes the c-axis response. Furthermore, p is the substrate refractive index and θ_0 and θ_2 are the incident angle and the angle of propagation within the substrate respectively. These angles are related via Snell's law

$$
\frac{\sin\theta_0}{\sin\theta_2} \;=\; p \tag{3.37}
$$

The phase factors, ϕ^x, appearing in eq. (3.34) are given by

$$
\begin{aligned}
\phi^{p} &= kd_1\left(\frac{n_{ab}}{n_c}\right)\sqrt{n_c^2-\sin^2\theta_0} \\
\phi^{s} &= kd_1\sqrt{n_{ab}^2-\sin^2\theta_0}
\end{aligned}
\tag{3.38}
$$

where k is the wavevector and d_1 is the thickness of the film. The only phase factor appearing in the expressions above stems from the film, due to the approach to neglect the interference effects in the substrate for our purpose, i.e. to calculate the absorptivity within the film. The absorptivity can finally be calculated by

$$
A_{film}^{x} \;=\; 1 \;-\; |t_{lr}^{x}|^2 \;-\; |r_{l}^{x}|^2 \tag{3.39}
$$

where x indicates as before the two possible polarizations.

In chapter 7 it will be shown that the dielectric properties of the substrate, such as Reststrahlenbands in between the transverse and longitudinal phonon frequencies will severely modify the absorptivity within the film due to the altered matching at the film-substrate interface. Physically speaking, a higher reflectivity at the interface enhances the effective average path length the rays traverse within the film, causing an enhanced absorption at these frequencies. This phenomenon is commonly referred to as the Berreman-effect [13].

3.3 Calculation of the Complex Dielectric Function From T and R

As explained earlier in this chapter, one of the main problems in infrared spectrometry is to acquire both the real and the imaginary part of the dielectric function from the available experimental information. Frequently Kramers-Kronig relations are used to obtain the phase information in addition to the measured reflection coefficient. The combination of phase and amplitude can then be used to determine the complex ϵ. In this section we will discuss the possibility of measuring both the transmissivity, T, and the reflectivity, R, of the same thin film. Since these are two independent parameters, the full complex dielectric function ϵ can be obtained analytically. In Chapter 5 an experimental example using a NbN-film will be presented.

Common practice in FTIR-spectroscopy is to measure the transmission through the film+substrate system and a bare substrate. By division of these spectra the contribution of the substrate is eliminated and the transmission coefficient of the film throughout the measured frequency range is obtained. Please note that in order to do so, the thickness of the substrate used in the reference measurement has to be identical to the one on which the film is deposited, otherwise absorption contributions present in the substrate do not cancel completely.

The obtained transmission and reflection coefficients can hence be modeled using the expression for a single layer. Since also the thickness of the film is of the order of several tens of nm, i.e. much smaller than the wavelength, we can in addition neglect the interference effects within the film. At the first interface (air→film) the reflected intensity is defined as:

$$R \;=\; \left(\frac{1-n}{1+n}\right)^2 \;=\; \frac{(\eta-1)^2\,+\,\kappa^2}{(\eta+1)^2\,+\,\kappa^2} \tag{3.40}$$

Although the sinusoidal contribution due to interference can be neglected in the film, the multiple reflections still have to be taken into account for the absorption in order to obtain the right formulation for the reflectivity and transmission coefficients. We can define the absorbed intensity for a single pass inside the film as:

$$\phi \;=\; e^{-4\pi k d/\lambda} \tag{3.41}$$

Applying as before the expression for the geometrical series one obtains

$$
\begin{aligned}
T &= \frac{(1-R)^2\phi}{1-(R\phi)^2} \\
R_{tot} &= R + \frac{R(1-R)^2\phi^2}{1-(R\phi)^2} = R(1+T\phi)
\end{aligned}
\tag{3.42}
$$

equivalent to eqns. (3.6) and (3.8). Using the first part of eq. (3.42) we obtain

$$
R = \frac{1}{1+T\phi}\left(1 \pm \sqrt{T^2 - T\phi + \frac{T}{\phi}}\right) \tag{3.43}
$$

which yields, when substituted into the second part of eq. (3.42)

$$
R_{tot} = 1 \pm \sqrt{T^2 - T\phi + \frac{T}{\phi}} \tag{3.44}
$$

Solving in terms of the extinction coefficient κ finally yields

$$
k = \frac{\lambda}{4\pi d}\ln(\frac{1}{\phi}) \tag{3.45}
$$

where now ϕ has been written in terms of the experimentally obtained reflection and transmission coefficients, R_{tot} and T.

$$
\phi = -\frac{(1-R_{tot})^2 - T^2}{2T} \pm \sqrt{\left(\frac{(1-R_{tot})^2 - T^2}{2T}\right)^2 + 1} \tag{3.46}
$$

Only the solution using the summation is physically relevant. The real part of the optical constant can be extracted from eq. (3.40)

$$
\eta = \frac{1+R}{1-R} \pm \sqrt{\left(\frac{1+R}{1-R}\right)^2 - \kappa^2 - 1} \tag{3.47}
$$

where the reflection coefficient R can be written in terms of the experimentally observed variables by using eq. (3.42)

$$
R = \frac{R_{tot}}{1+T\phi} \tag{3.48}
$$

From the obtained complex refractive index, all desired optical constants can be determined analytically.

In case that interference effects are non-negligible, the derivation given above becomes rather cumbersome, and one needs to use numerical methods to obtain both the real and complex part of n.

References

[1] Max Born and Emil Wolf, *Principles of Optics*, (Pergamon Press Ltd., Oxford, 1959).

[2] Arnulf Röseler, *Infrared Spectrosopic Ellipsometry*, (Akademie-Verlag, Berlin, 1990).

[3] R. M. A. Azzam and N. M. Bashara, *Ellipsometry and Polarized Light*, (North-Holland, Amsterdam, 1987).

[4] O. S. Heavens, *Optical Properties of Thin Solid Films*, (Butterworths Scientific Publications Ltd., London, 1955).

[5] L. A. de Vaulchier, J. P. Vieren, Y. Guldner, N. Bontemps, R. Combescot, Y. Lemaître and J. C. Mage, Europhys. Lett. **33** (2), 153 (1996).

[6] C. J. Gorter and H. B. G. Casimir, Z. Phys. **35**, 963 (1934).

[7] D. van der Marel, M. Bauer, E. H. Brandt, H.-U. Habermeier, D. Heitmann, W. König and A. Wittlin, Phys. Rev. B **43**, 8606 (1991).

[8] U. Dähne, Y. Goncharov, N. Klein, N. Tellmann, G. Kozlov and K. Urban, J. Supercond. **8**, 129 (1995).

[9] M. Tinkham, *Introduction to Superconductivity*, (McGraw-Hill, New York, 1975 and Krieger, New York, 1980).

[10] W. N. Hardy, D. A. Bonn, D. C. Morgan, Ruixing Liang and Kuan Zhang, Phys. Rev. Lett. **70**, 3999 (1993).

[11] D. A. Bonn, Ruizing Liang, T. M. Riseman, D. J. Baar, D. C. Morgan, Kuan Zhang, P. Dosanjh, T. L. Duty, A. MacFarlane, G. D. Morris, J. H. Brewer, W. N. Hardy, C. Kallin and A. J. Berlinsky, Phys. Rev. B **47**, 11314 (1993).

[12] H. S. Somal, Ph D Thesis, University of Groningen, in preparation.

[13] D. W. Berreman, Phys. Rev. **130**, 2193 (1963).

[14] T. Leskova, J. Keller and K. F. Renk, Physica C **225**, 190 (1994).

[15] M. Reedyk and T. Timusk, Phys. Rev. Lett. **69**, 2705 (1992).

[16] D. van der Marel, J. H. Kim, B. J. Feenstra and O. Wittlin, Phys. Rev. Lett. **71**, 2676 (1993).

Chapter 4

Experimental Setup

4.1 Introduction

For the purpose of doing mm-wave spectroscopy on high T_c superconductors, during my graduate research a multi purpose setup has been developed. With this setup experiments such as reflection and transmission can be performed in the frequency range of 4 to 6 cm^{-1}. In this chapter the setup will be explained in detail. Besides the above mentioned experiments a slightly modified version of the same setup has been used to perform Photo Induced Activation of Mm-Wave Absorption (PIAMA) experiments. These experiments were done at the FOM-Institute for Plasma Physics in Nieuwegein, where we were given the opportunity to make use of the Free Electron Laser (FELIX). Details of these experiments will be given along with a short explanation of the principles of a free electron laser.

4.2 mm-Wave Transmission Experiments

Doing experiments in the micro- and mm-wave range one has to face a "build-in" duality. On the one hand, coming from the lower frequencies where ordinary electronics can be used, the wavelength of the radiation is becoming smaller. This makes that waveguides, which are usually employed in the range from 1 to 100 GHz (N.B.: 300 Ghz = 10 cm^{-1} = 1 mm) become extremely small and hard to handle. On the other hand, coming from the high frequency side, the wavelength is becoming longer. This results in difficulties such as diffraction, since the wavelength becomes comparable to the size of the optical components such as mirrors and lenses. One solution to this problem is to use so-called *quasi-optics*, which means that one uses large mirrors and large lenses.

Another problem in this frequency range is to achieve a reasonable bandwidth. In many experiments resonant cavities are used, thereby exchanging the bandwidth for a higher sensitivity. However, in order to obtain amplitude *and* phase information in a direct transmission measurement, one needs to use a broadband source. Conventional sources such as Gunn oscillators and impatt diodes have an intrinsic bandwidth of only a few percent. Furthermore, at lower frequencies, where the wavelength becomes very long, the

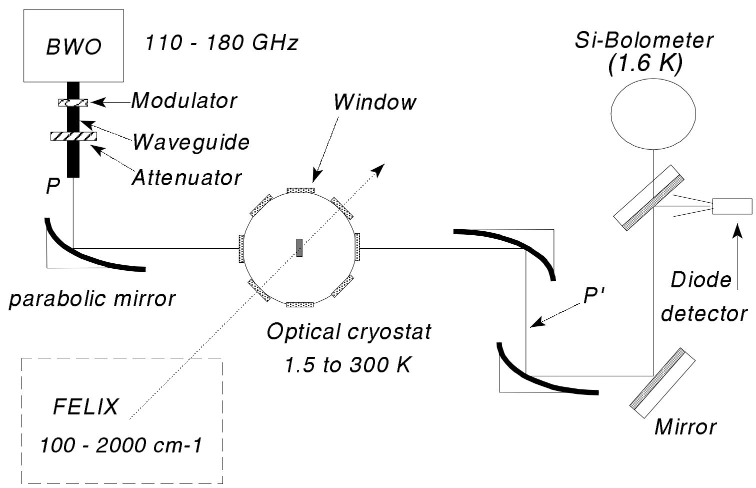

Figure 4.1: *Experimental Setup used for the mm-wave transmission measurements. The free electron laser in the dashed box is optional and only used during the Photo Induced Activation of Mm-Wave Absorption (PIAMA) experiments.*

use of waveguides is limiting the operational bandwidth. Therefore we have chosen to operate at a frequency where we can use quasi-optical methods to manipulate the beam, starting with a source that has a relatively broadband output spectrum. The complete experimental setup is shown in fig. 4.1. The part in the dashed box is not used for the ordinary transmission measurements and will be explained in detail in the following section.

As a source we use a Backward Wave Oscillator (BWO) with an output power several tens of milliwatts [1]. A schematic diagram of a BWO is given in fig 4.2. Its useful range of radiation is from 110 to 180 GHz. The frequency of the radiation is continuously tunable by changing the high voltage from 0.5 to 1.5 kV. Changing the high voltage alters the velocity of the electron beam (3) traveling along a fine grid (6). The electron beam is focused using a magnetic field coming from two permanent magnets (5) packetized with the actual tube, making the total source fairly compact and robust. The interaction of the electrons with the grid results in the production of Bremsstrahlung (7) that is traveling in the opposite direction. The radiation is coupled out via a waveguide (8). The power supply for the BWO is home-build, and has a high voltage stability of about 10^{-5}, which is necessary in order to obtain monochromatic radiation. The range of frequencies enables us to measure complete Fabry-Perot resonant spectra of our samples, thereby yielding complete phase information via the amplitude and position of the peaks.

The BWO-output first traverses a modulator, thereby creating the ac-response necessary for the detector (usually 100 - 200 Hz for the Si-bolometer). Then an attenuator is used to avoid a nonlinear response of the detector. Next the radiation is coupled out of the waveguide using a Gaussian horn, yielding a fairly well directed beam and is treated quasi-

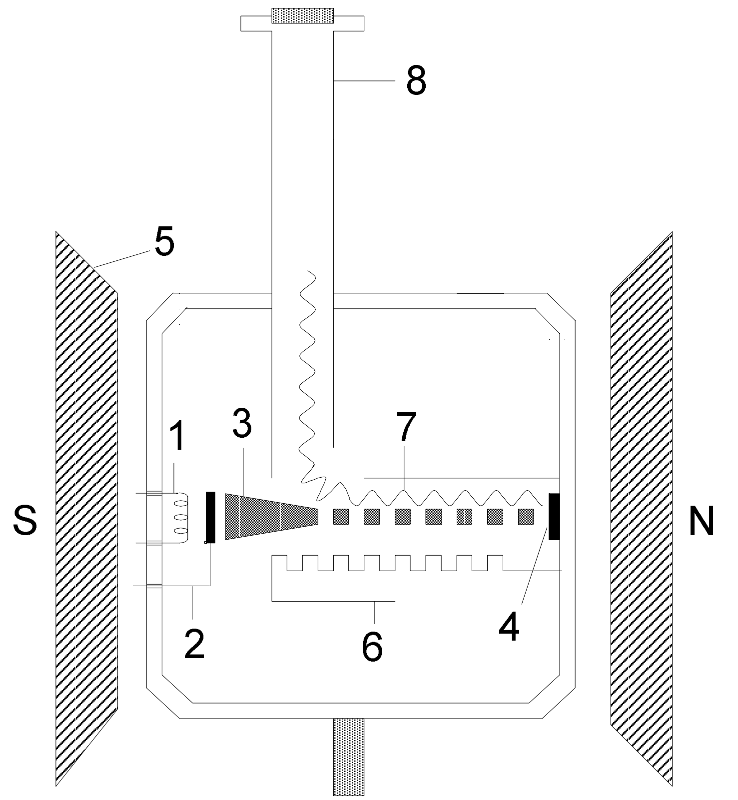

Figure 4.2: *Schematic diagram of a Backward Wave Oscillator. 1-heating wire, 2-cathode, 3-electron beam, 4-anode, 5-permanent magnets, 6-fine metallic grid, 7-mm-wave radiation, 8-output waveguide.*

optically thereafter. The beam is focused into the cryostat through a quartz window, onto the (superconducting) thin film using an off-axis parabolic mirror, placed slightly away from the focal point. This creates a 3 :1 image of the waveguide output (P) in the center of the cryostat. The use of mirrors facilitates the alignment and is therefore favored over the available polyethylene lenses. A good alternative would be the use of lenses made of TPX, since these are transparent for visible light and have a low refractive index in the mm-wave range.

The cryostat is a special Variox type with an enlarged sample space, made by Oxford Instruments, and can be regulated in temperature from 1.6 to 300 K. The temperature is measured using a RhFe sensor situated on the cold plate, and a Pt1000 resistor placed very close to the sample, ensuring a stable temperature. Apart from the quartz in- and output windows there are 6 additional optical accesses, two with polyethylene and two with KRS-5 windows, while the other two are blanked. All optical accesses consist of three different windows, one at room temperature, one at 77 K and one at 4 K. This reduces the intensity of the radiation, but allows the use of exchange gas. During most of the experiments presented later in this thesis, the windows at 77 K have been removed, in order to increase the transmitted power. The sample is loaded from the top and can be taken out while the cryostat remains cold. Using a sample-change compartment on top of the cryostat samples can be changed within 5 minutes, without breaking the vacuum within the cold chamber.

After the cryostat the transmitted radiation is subsequently picked up using a second off-axis parabolic mirror. This creates a second image P′ (1:1) which can be used for room temperature measurements. A third parabolic mirror is used to produce a parallel beam, that can propagate over a reasonable distance before being focused onto either one of two detectors, a highly sensitive but slow Si-bolometer operating at 1.6 K, or a fast, but less sensitive waveguide diode detector. Both detectors are used in combination with a lock-in amplifier. The modulation frequencies are 100-200 Hz and about 6 kHz for the Si-bolometer and the diode detector respectively. The complete setup is being controlled by computer making use of either Viewdac or Labview as the operating system.

A recent addition is the implementation of a fully automated sample positioning system using a stepper motor. The construction, shown in fig 4.3, uses a tube for the downward motion and a wire for the upward motion, thereby minimizing the heat load on the sample-holder. Before measuring, the strain on the sampleholder is released. During measurements three sequential scans as a function of frequency are taken at a fixed temperature, namely sample (film + substrate), bare substrate and a reference aperture. All three are part of one sampleholder, which can be reproducibly moved into three different positions. The reference aperture is used to yield *absolute* transmission coefficients for both sample and substrate, which are then used in the rest of the analysis. The frequency dependence of other components in the setup (attenuator, BWO) is thereby taken into account. It is important to realize that we are dealing with interference effects, and therefore we divide both the sample and the bare substrate single beam spectra by a reference hole. This is different than the common practice for FIR-transmission measurements where the sample spectrum is divided by the bare substrate, in order to obtain the film-response. In that case one has to realize that it is essential to have exactly the same thickness for the substrate used in both measurements. Even though a low resolution will solve the problem of the interference effects, a strong absorption will cause a problem. Since we model the substrate properties separately and enter the experimentally obtained dielectric function into the film+substrate analysis we are not restricted to using the same thickness.

Another common problem in doing mm-wave spectroscopy, both in a quasioptical setup and with the use of waveguides, is the existence of *standing waves.* Since the wavelength is comparable to the distances in the setup, standing waves will appear, making it more difficult to compare spectra taken on different samples directly since the standing wave pattern will be modified. A solution to this problem in waveguides is the use of *isolators*, damping out the amplitude of the reflected beam. In quasioptics this is more complicated, and therefore we utilize a small ($\sim$ 10 V) ac-voltage superposed on the high voltage. This slightly modifies the outgoing frequency, thereby also changing the standing wave pattern, thus effectively averaging over several different standing wave patterns.

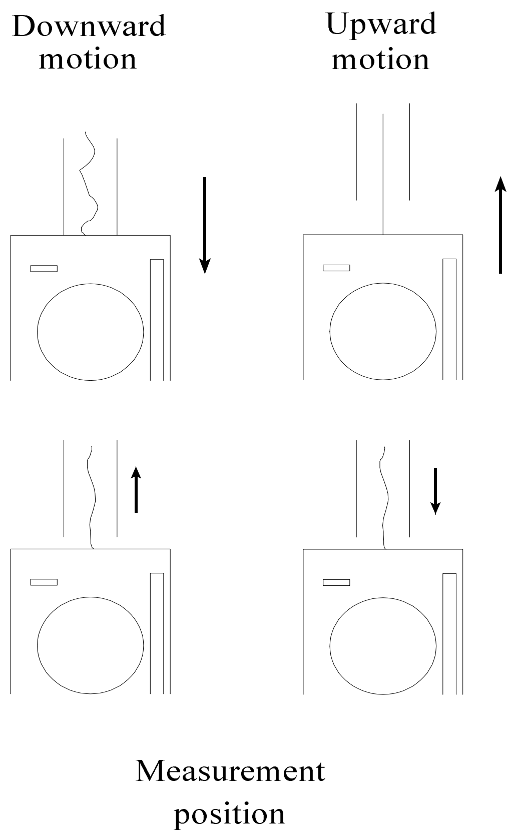

Figure 4.3: *Schematic diagram of the automated sample positioning system, minimizing the heat load on the sampleholder.*

Apart from the above described frequency dependent measurements, we can also fix the frequency and measure the transmission as a function of temperature. In this case the absolute value of the transmission is harder to achieve since a separate reference run has to be made. This means that one is more sensitive to long term instabilities of for instance the source or the slight motion of the sampleholder as a function of pump rate. Therefore the information obtained in the frequency dependent measurements is used to set the absolute scale.

4.3 Photo Induced Activation of Mm-Wave Absorption (PIAMA)

The same setup as described above, has been used in another series of experiments performed at the FOM-institute for Plasma Physics in Nieuwegein, where we made use of the free electron laser (FELIX). FELIX was used as the pump source in a pump-probe like experiment, Photo Induced Activation of Mm-Wave Absorption (PIAMA). Before proceeding with the physical details of this technique we will first explain the operation principle of a free electron laser [2]. In section 4.3.2 the principle of measurement will be explained, demonstrating the influence of the FIR-radiation on the response at mm-wave frequencies. Finally in section 4.3.3 some of the experimental specifics of this measurement will be discussed. Results using PIAMA on both a conventional (NbN) and a high T_c superconductor ($DyBa_2Cu_3O_{7-\delta}$) will be portrayed in chapter 7.

4.3.1 Operation Principle of FELIX

The heart of a free electron laser is depicted in fig 4.4. The electron beam is created by

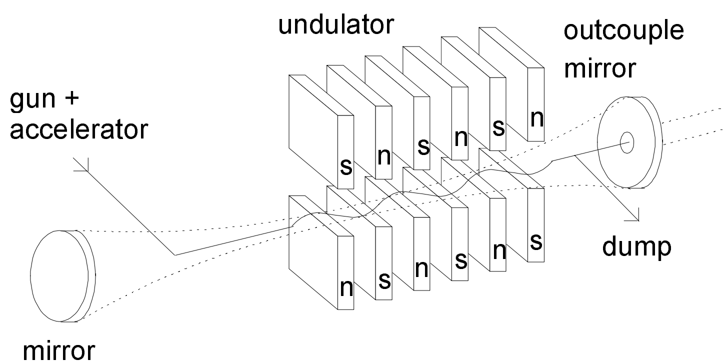

Figure 4.4: *Schematic setup of the free electron laser (FELIX). The accelerated electron beam is injected in the undulator where the infrared radiation is produced by a wiggling motion of the electrons in a periodic magnetic field.*

an rf-gun, and is propagating in bunches. These electrons are then accelerated to achieve a relativistic electron beam, entering the actual laser section, where they are decelerated by the undulator. This is a series of magnets with alternating poles, creating a spatially periodic magnetic field. The electrons perform a wiggling motion causing them to radiate, having a wavelength (λ_0) equal to [3]:

$$\lambda_0 = \frac{\lambda_u}{2\gamma^2}(1 + K^2) \tag{4.1}$$

Here λ_u is the period of the undulator field and K is a dimensionless parameter that depends on the magnetic field amplitude. Furthermore γ is determined by the energy of the incoming electron, given by γmc^2. The optical radiation is confined within the cavity resonator, and is amplified on successive trips by the newly injected electrons. The remaining power of the electron beam after traversing the undulator is dumped.

One of the major advantages of a free electron laser is evident from eq. (4.1) This is the fact that a free electron laser is continuously tunable over a broad frequency range, by changing either the energy of the incoming electrons, or the undulator field strength, changing K. By using two accelerators FELIX can span the frequency range from 100 to 2000 cm^{-1}. The first accelerator produces an electron beam having a maximum energy of 25 MeV, while the second one ranges upto 45 MeV. The latter is used to produce the higher frequencies. The generic time structure of the FELIX output is shown in fig 4.5. The output consists of 5 to 10 μs long macropulses separated by 200 ms. Within the so-

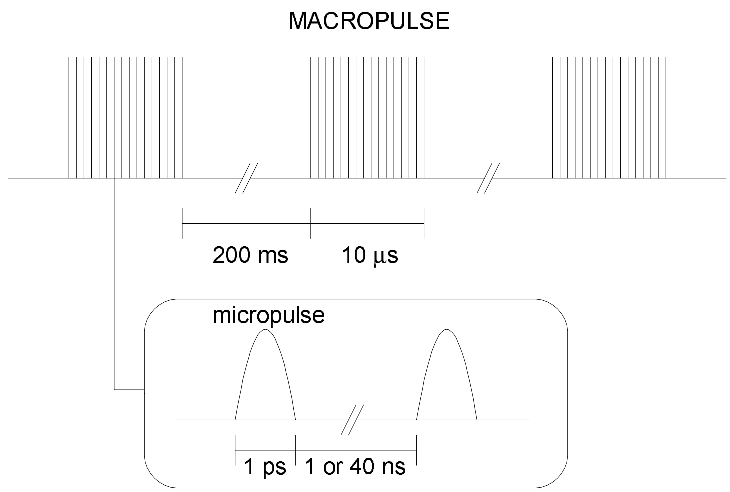

Figure 4.5: *Time structure of FELIX, showing the specifications of both the micropulse and the micropulse.*

called *macro*pulse there are a large number of *micro*pulses with a duration of 1 to several picoseconds and a repetition rate of nominally 1 GHz, i.e. the frequency of the rf-gun. All the parameters mentioned above can be altered upto a certain extent, making the free electron laser suitable for temporally resolved experiments on multiple timescales.

4.3.2 Principle of Measurement

The principle of measurement largely resembles the idea of a pump-probe experiment. However, in most pump-probe experiments, two pulses from the same source are delayed with respect to each other, where the second pulse probes the effects induced by the first. In our case the setup consists of two separate parts utilizing two *different* frequency sources. The main part of the setup, depicted in fig. 4.1 is used to measure the transmission of mm-wave radiation through a superconducting thin film. The backward wave oscillator, described in the previous section, produces a *continuous* beam of mm-waves, since we are only interested in *changes* in the mm-wave intensity. To induce changes in the mm-wave intensity an additional source, the free electron laser (FELIX, indicated in the dashed box in fig. 4.1) is utilized. A pulsed FIR-beam coming from FELIX, temporarily changes the state of the superconducting thin film. This changes the dielectric function and therefore results in a temporary change in the transmissivity at frequencies much lower than the pump frequency of FELIX.

We assume that the superconducting state can be described using a two fluid picture [4], where both the superconducting and the normal fluid coexist. The total conductivity of the superconductor can then be described by

$$\sigma = \sigma_n(f_n) + \sigma_s(1 - f_n) \tag{4.2}$$

where f_n is the normal fluid fraction and hence $1-f_n$ is the superfluid fraction, f_s. Putting this into the expression for the transmission through a superconducting film on a substrate (eq. (3.6), page 48) yields:

$$T = \frac{t_s^2}{(1 - f_n)^2 + (2\pi\nu_{mm}\tau f_n + t_s)^2} \tag{4.3}$$

where we have assumed the thin film limit $(2\pi\nu_{mm}nd/c \gg 1)$, ν_{mm} is the mm-wave frequency and τ is the quasiparticle scattering rate. The first term in the denominator $(\sim (1 - f_n)^{-2})$ represents the dispersive part of the conductivity, whereas the second term $(\sim f_n^{-2})$ is related to the dissipative part. Furthermore:

$$t_s = \frac{4\pi\nu_{mm}\lambda^2(0)}{dc} \tag{4.4}$$

where $\lambda(0)$ is the zero temperature penetration depth and d is the film thickness.

Most importantly, the FIR radiation will perturb temporarily the delicate balance between the superfluid and the normal fluid density, by creation of quasiparticles. This can be done both optically, provided the energy of the incident photons is large enough, or thermally by simply heating the sample, for instance due to phonon absorption. We see that changing f_n will also alter the dynamic impedance at low frequencies, and therefore the transmission at mm-wave frequencies will be affected. Since we are probing the system response at such low frequencies, in principle we are only *in*directly sensitive to changes related to phonons, while the modified electronic properties are directly observed.

From eq. (4.3) we learn furthermore that also the sign of the photo-induced signal can provide important information about the quasiparticle dynamics. In fact, if $\omega\tau \gg 1$ the first term in the denominator will be dominant, and we see that $T \sim (1 - f_n)^{-2}$, yielding an *in*crease of transmission when the quasiparticle density increases. However, if $\omega\tau$ is of the order or larger than 1, the second, dissipative term will become more prominent in the induced changes, causing the transmission to be *reduced* when f_n increases, since $T \sim (f_n)^{-2}$. The interplay between the quasiparticle dynamics, in particular the scattering time τ, and the significance of the inductive and dissipative parts of the electromagnetic response function of the superconductor provides an interesting playground. This playground will be explored in more detail in connection with the observed responses in chapter 7.

4.3.3 Practicalities

As can be seen in fig. 4.1 the infrared beam coming from FELIX is entering the cryostat under an angle of 45°, through a KRS-5 window. In fig 4.6 we show the transmission through the window for the relevant frequencies. The transmission is featureless and fairly

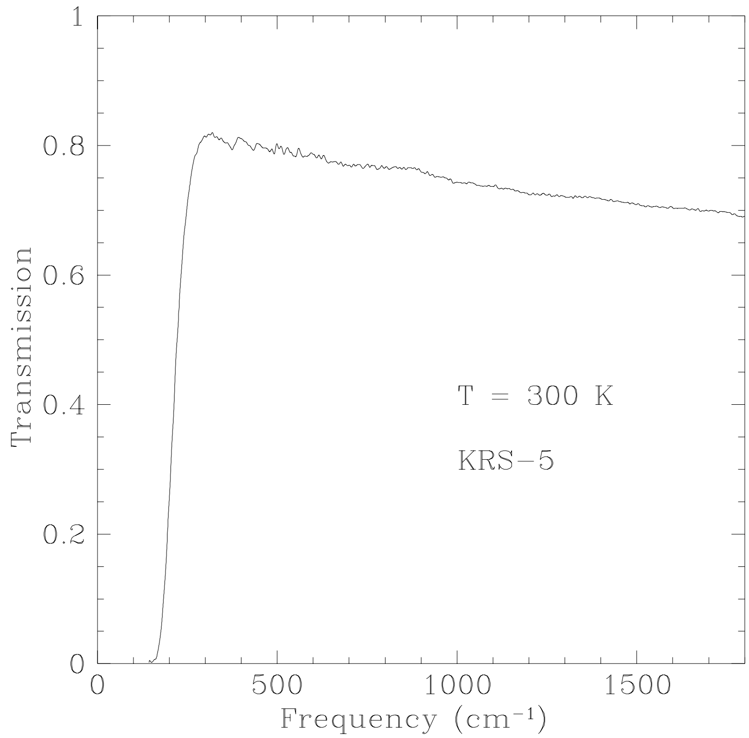

Figure 4.6: *Transmission through the KRS-5 window, used during the PIAMA experiments.*

frequency independent for frequencies downto 250 cm^{-1}. At this frequency the transmission goes to zero due to a strong phonon Reststrahlenband.

The beam is incident on the thin film having an unfocused diameter of about 10 mm. The diameter of the inner KRS-5 window is 10 mm, meaning that the beam covers the whole sample (10x10mm) making the excitation as homogeneous as possible. The infrared beam induces a change in the dynamic impedance of the sample and therefore changes the transmission at mm-wave frequencies. The temporal evolution of the Photo Induced Activation of Mm-Wave Absorption is monitored using a fast waveguide diode detector, and an (even faster) oscilloscope. The total detection system has a integrating time constant of approximately 1 μs, limiting our time resolution to the macropulse. Moreover, the time constant of the differentiating circuit connected to the diode, was measured independently to be 45 μs. All the data presented in chapter 7 have been corrected for this by convoluting the transients with an exponential response function.

The optimization of the position of the beam is initially done by measuring the direct transmission through a reference hole replacing the sample. Thereafter the induced change in mm-wave transmission is used to improve the position further. The power and the stability of FELIX are checked by using a power meter directly in front of the first window, while at some frequencies the transmitted power directly behind the cryostat is measured. This yields the attenuation of the beam due to the windows and can then be used to obtain the absolute power incident on the sample. In case of the studies as a function of power we used two options to attenuate the beam, yielding very distinct information. First it is possible to shorten the pulse length, thereby lowering the average power, but leaving the pulse height of the individual micropulses unaltered. Second we used attenuating materials such as dielectric films to reduce the instanteneous power.

Using eq. (4.3) we can make a rough estimate of what the magnitude of the induced signals will be. For a superconductor at the lowest possible temperature, assuming that all electrons are paired eq. (4.3) reduces to

$$T = \frac{t_s^2}{1 + t_s^2} \tag{4.5}$$

Assuming $\lambda(0) = 1500\ \mathring{A}$, $d = 1000\ \mathring{A}$ and $\nu_{mm} = 5\ cm^{-1}$ the transmission is approximately 10^{-5}. Assuming furthermore that the induced changes due to the presence of the FIR pulses of FELIX are of the order of a few percent, we know that the changes to be detected will be approximately 10^{-7} times the starting output power. This means that the dynamic range of the setup needs to be at least one order of magnitude better than that. Furthermore this implies that this technique is limited to thin films, since for the thicker films the unperturbed transmitted signal will be insufficient.

References

[1] for an detailed description of the BWO and its use in (sub)mm spectroscopy on solids see: G. Kozlov and A. Volkov, "Coherent Source Submillimeter Wave Spectroscopy" in *Millimeter Wave Spectroscopy on Solids*, G. Grüner ed. (Springer Verlag, 1995).

[2] for a more detailed description of the specifications of FELIX see: *The International Free Electron Laser User Facility FELIX*, internal report of the FOM Institute for Plasma Physics, Nieuwegein, The Netherlands.

[3] Guido Knippels, *The Short-Pulse Free-Electron Laser: Manipulation of the Gain Medium*, Graduate Dissertation, (1996).

[4] C. J. Gorter and H. B. G. Casimir, Z. Phys. **35**, 963 (1934).

Chapter 5

FIR Spectroscopy on Conventional and High T_c Superconductors

Optical spectroscopy has always played an important role in the characterization of superconductors. FIR spectroscopy offers several advantages, such as a bulk sensitivity and information covering a wide range of frequencies in a single measurement. The first great success of FIR and mm-wave spectroscopy was the observation of the energy gap in the excitation spectrum of conventional superconductors such as Al [1] and Pb [2].

Also in the high T_c era, far-infrared spectroscopy has been used extensively in order to study both superconducting and normal properties, such as the energy gap [3], a non-Drude like frequency dependence [4], the Holstein shift [5] and the pseudo-gap [6]. Unlike in the case of the conventional, elemental superconductors, no clear gap in the quasiparticle excitation spectrum is observed. Several explanations have been proposed ranging from clean limit behavior [7] to the occurrence of a d-wave symmetry [8]. The use of FIR-spectroscopy is complicated further due to the size of the energy gap, which coincides with the characteristic phonon frequencies. Moreover, the uncertainty in the measured reflection coefficient is about 1% due to experimental difficulties. This hampers the distinction of a large reflectivity for a well conducting material in the normal state, and the perfect reflectivity expected in the superconducting state.

In this chapter we will present several improvements to the usual FIR spectroscopy, illustrated via results on NbN and $Tl_2Ba_2Ca_2Cu_3O_{10}$.

5.1 Experimental Setup

The data presented in this chapter are obtained using Fourier Transform Infrared Spectroscopy. Using a Michelson interferometer, the reflected intensity is recorded as a function of path difference of the two beams traversing the interferometer. The obtained spectrum, a so-called interferogram can be directly converted using a Fourier transformation into a reflected intensity as a function of frequency. The frequency limits are mainly determined by the optical equipment, such as beamsplitters and sources. Therefore, by using multiple configurations the reflectivity can be obtained throughout the entire infrared region.

The measurements were carried out in a rapid scan Bruker 113v Spectrometer. In most of the cases an Oxford continuous-flow cryostat was used to cool the samples. One of the sets of data (oblique incidence reflectometry on $Tl_2Ba_2Ca_2Cu_3O_{10}$) was obtained at the High Field Magnet Laboratory in Nijmegen, using a similar setup with a CryoVac variable-temperature exchange-gas cryostat. All spectra have been obtained using a liquid-He cooled Si-bolometer as a detector. In case of the reflectivity data the absolute scale has been determined using a Au mirror as a reference, while the absolute transmission was determined using a bare substrate as a reference. Via these procedures the contraction of the cold finger is taken into account as well.

5.2 FIR-Spectroscopy on NbN for Normal Incidence Conditions.

NbN is generally considered to be a conventional superconductor, which follows the BCS-description. It is a member of the so-called A-15 compounds, a name that originates from the common crystal structure these bi-elemental superconductors share. The elements come from the IV- and V group of the periodic system and form mechanically and chemically very stable superconductors with a fairly high critical temperature. Some other examples are NbC ($T_c = 11$ K), Nb_3Sn ($T_c = 18$ K) and Nb_3Ge having the highest recorded T_c for this family of 23 K. The properties mentioned above are the reason that these materials are now widely used many applications such as for instance superconducting magnets. Also, the merit of a relatively large energy gap allows the use of NbN in SIS junctions used for the detection of submillimeter radiation.

5.2.1 Sample Preparation

The NbN-film of 55 nm thickness was deposited on an MgO substrate using DC reactive magnetron sputtering. This was done in a gas composition of 3.0% CH_4 / 30.0 % N_2 / Ar, at a temperature of approximately 840 °C [9]. T_c was enhanced to 17 K, by the inclusion of carbon, as was checked by dc-resistivity measurements.

5.2.2 FIR Reflection and Transmission

Both reflection and transmission measurements were performed on the same 55 nm thick NbN film. The results can be seen in figs. 5.1 and 5.2. The changes occurring due to the onset of superconductivity gap can be observed even easier, if we plot R, normalized to its value just above T_c, as was done in the inset of fig. 5.1.

The resolution used for both spectra was 2 cm^{-1}. As a reference for the reflectivity, R, we used a gold mirror, while the absolute value of the transmission data, T, was obtained by division of the sample spectra by the transmission measured through an MgO-substrate at the same temperatures. Using the information of the transmission data, we scaled the

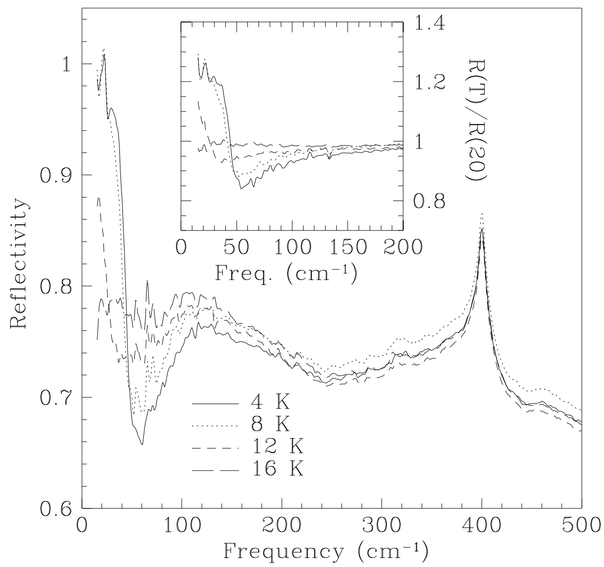

Figure 5.1: *FIR-reflectivity of a 55 nm thick NbN film, deposited on an MgO substrate, for several temperatures (4 K: solid, 8 K: dotted, 12 K: short dashed and 16 K: long dashed line). Inset: normalized reflectivity, indicating the changes related to the onset of superconductivity.*

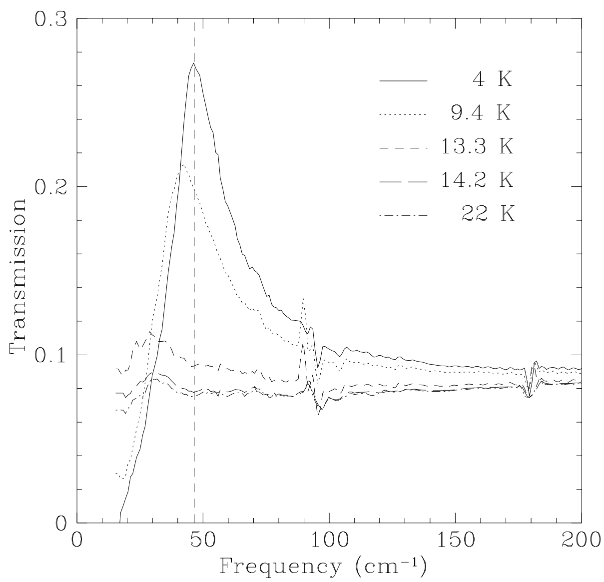

Figure 5.2: *FIR-transmissivity of a 55 nm thick NbN film, deposited on an MgO substrate, for several temperatures (4 K: solid, 9.4 K: dotted, 13.3 K: short dashed, 14.2 K: long dashed and 22 K: dashed-dotted line).*

reflectivity, assuming that at very low frequencies ($\ll 2\Delta$) the absorption within the sample is negligible.

Obviously, due to the finite thickness of the film, in both reflectivity and transmission, part of the substrate response is still visible in the spectra shown in figs. 5.1 and 5.2. MgO has two transverse optical phonons at 403 and 650 cm^{-1}, while the absorptivity is non-zero at frequencies higher than approximately 250 cm^{-1} [10]. Therefore, below 250 cm^{-1} the reflectivity and transmission spectra are mainly determined by the response of the NbN film.

The recorded temperatures are approximately 2 to 3 degrees lower than the actual sample temperature. For instance excess radiation coming from the FIR-source and a non-ideal thermal contact between the sample and the sampleholder, cause the real sample temperature to be slightly higher than the temperature of the cold finger on the He-flow cryostat. The determination of the real temperature is aided for instance by the dc-resistivity and the mm-wave transmission measurements presented in the next chapter. In the latter case the use of an exchange gas provides an accurate measurement of the sample temperature.

Both R and T show a clear opening of the superconducting gap. This demonstrates the advantage of the use of thin films in observing the energy gap in far infrared spectroscopy. The reflectivity for a highly conducting metallic film is close to 1, as can be seen easily from

$$R = \left(\frac{1-\tilde{n}}{1+\tilde{n}}\right)^2 = \frac{(\eta-1)^2 + \kappa^2}{(\eta+1)^2 + \kappa^2} \tag{5.1}$$

For a highly metallic film $\eta \approx \kappa$, while in addition both quantities are very large, yielding a reflectivity close to 1. The frequency dependence of the reflectivity for a thick metallic film, having $\nu_{pn} = 10,000\,\mathrm{cm}^{-1}$ and $\gamma = 110\,\mathrm{cm}^{-1}$ (thus yielding $\sigma_{dc} = 15,000\,(\Omega\mathrm{cm})^{-1}$) has been shown in fig. 5.3 as the solid line. Also indicated as the dashed line is the perfect reflectivity expected for a superconductor having an energy gap of 43 cm^{-1} (dashed line). This frequency would be the gap value for a superconductor having T$_c$ = 17 K and a BCS-gap ratio of 3.52. The difference in reflectivity is within 1%, showing that it will be difficult to distinguish the perfect reflectivity expected at frequencies below 2Δ for a superconductor, from the high reflectivity in the normal state, inhibiting a direct identification of the gap frequency.

Also plotted in fig. 5.3 is the reflectivity curve calculated for p-polarized light at an incident angle of 80° (dotted line). This shows that one way to circumvent the problem of high reflectivity in the normal state is the use of a grazing angle of incidence (Θ) and p-polarized light. This configuration enhances the absorptivity by approximately a factor of $\cos^{-1}\Theta$, as was demonstrated in reference [8]. An example of this approach will be treated later in this chapter.

Especially in the reflectivity data, it appears that the gap has not entirely opened yet at the lowest measured temperature, presumably due to the thermal problems stated above. From the transmission data we estimate that the maximum size of the gap (2Δ) is around 46 cm^{-1}. This value yields a BCS-ratio equal to $2\Delta/k_B T_c = 3.8$, in fair agreement

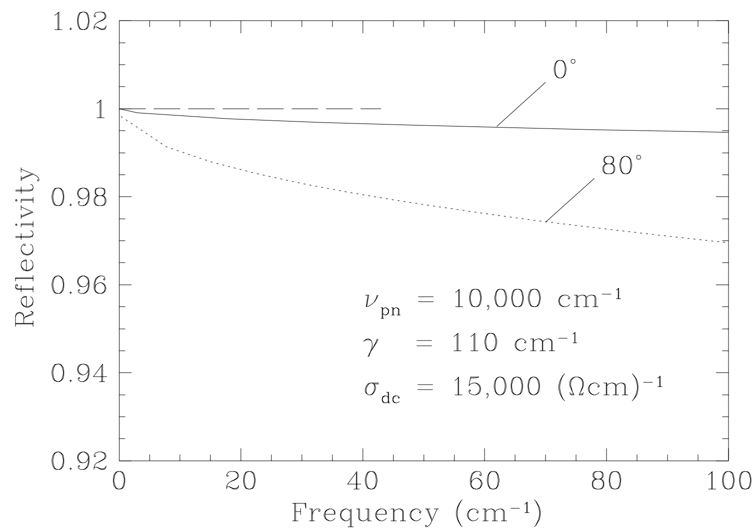

Figure 5.3: *Calculated reflectivity at two incident angles (0°: solid line, 80°: dotted line). for a highly conducting metallic film, having* $\nu_{pn} = 10,000\,\mathrm{cm}^{-1}$ *and* $\gamma = 110\,\mathrm{cm}^{-1}$*, yielding* $\sigma_{dc} = 15,000\,(\Omega\mathrm{cm})^{-1}$*. Also shown is the perfect reflectivity upto the gap value (dashed line). The gap value is assumed to be* $2\Delta = 43\,\mathrm{cm}^{-1}$ *according to the BCS-ratio, having a* T_c of 17 *K.*

with other reported values ranging from 3.9 [11] to 4.4 [12], supporting the conclusion that NbN is a strong coupling superconductor. The small remaining discrepancy between these values and our measured value can be attributed to the fact that the gap is not completely developed.

5.3 Reflectometry using an Oblique Angle of Incidence

In the previous section we have shown that for a superconductor having a high conductivity in the normal state, it is troublesome to obtain information about the superconducting energy gap via the ordinary spectroscopic techniques. We demonstrated that a possible method to circumvent this problem is the use of thin films. In this section we will introduce an second alternative approach: the employment of a large angle of incidence. The large angle of incidence enhances the absorption in the film, thereby enhancing the visibility of absorption related features, facilitating for instance the identification of a gap edge. This will demonstrated in the first part of this section, on the basis of results on a thick NbN film.

Combined with use of the two different light polarizations, s and p, this technique provides furthermore the opportunity to probe the c-axis response while using the ab-surface of a film or single crystal platelets as the reflecting surface. In this way the response perpendicular to the CuO planes can be investigated even in the absence of sufficiently large single crystals. As an example we studied a c-axis oriented epitaxial film of $Tl_2Ba_2Ca_2Cu_3O_{10}$.

5.3.1 Energy Gap Study in NbN using a Grazing Angle of Incidence

The first illustration of the use of grazing of incidence spectroscopy will be the determination of the energy gap in a conventional superconductor. For this purpose a 400 nm thick NbN film was grown in the same way as mentioned in the previous section. Focusing on the inset of fig. 5.4 first, we see the reflectivity at normal incidence, plotted for several temperatures (4, 10 and 16 K). The reflectivity was normalized to its value in the normal

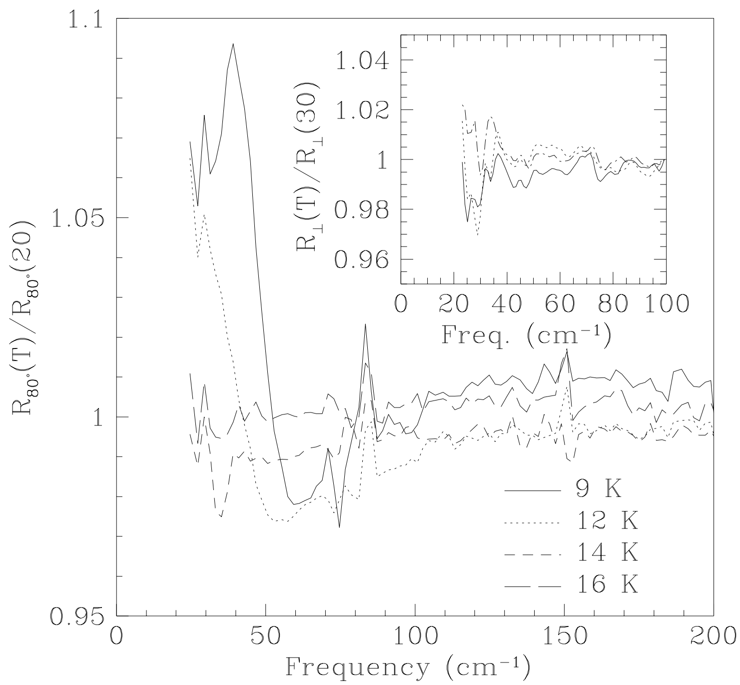

Figure 5.4: *Normalized reflectivity of a 400 nm thick NbN film, using an 80° incident angle, clearly demonstrating the appearance of the superconducting gap. Inset: normalized reflectivity for 4 K (solid line), 10 K (dotted line) and 16 K (dashed line).*

state (at 30 K). No features related to the onset of superconductivity and the opening of an energy gap can be observed. Especially at the frequency range of interest (below 50 cm^{-1}), the uncertainty becomes too large ($\pm$ 1%) to recognize a gap feature.

However, if the reflectivity of the same film is measured using an 80° incident angle, as shown in the larger panel of fig. 5.3, the enhanced reflectivity due to the onset of superconductivity can be easily seen.

It can be shown [13], that using the formulation given in section 3.2 on page 60 the absorptivity for a uniaxial metallic crystal using a non-zero angle of incidence Θ can be written as

$$A_p \approx \frac{1}{\cos\Theta}\sqrt{\frac{4\nu}{\sigma}} \tag{5.2}$$

In the superconducting state the situation changes, since now the dielectric function is dominated by its real part, related to the penetration depth. The absorptivity becomes

$$A_p \approx \frac{64\pi^3}{\cos\Theta}\frac{\nu^2\lambda^3\sigma}{c^3} \tag{5.3}$$

Both equations show that in the limits discussed above, the absorptivity can be enhanced by approximately a factor of $1/\cos\Theta$, which for our case, where $\Theta = 80°$, is close to a factor of 6.

Optical Conductivity

Having a reflectivity spectrum in the normal state, at grazing incidence, the absolute reflectivity coefficient R can be determined. Using R and performing a Kramers-Kronig transformation we obtained the optical conductivity, of which the real part has been plotted in the upper panel of fig. 5.5. The suppression of conductivity, due to the formation of the energy at low frequencies is evident. The absolute magnitude of σ_1 at all temperatures can be excellently described by assuming a conventional isotropic s-wave behavior and $2\Delta = 48cm^{-1}$, as indicated by the solid lines.

In the normal state the conductivity was described by a Drude response, having $\sigma_{dc} = 15,000\,(\Omega\mathrm{cm})^{-1}$ and $\gamma = 110\,\mathrm{cm}^{-1}$. The upturn at lower frequencies for the curves below T_c is reminiscent of the presence of thermally excited quasiparticles.

The validity of the outcome of the grazing angle experiment can be verified as well, by subsequently utilizing the parameters obtained in a model calculation to describe the normalized transmission data, presented in the previous section. Also in this case the agreement is outstanding, both for the magnitude and for the temperature dependence.

5.3.2 C-axis Properties of $Tl_2Ba_2Ca_2Cu_3O_{10}$ measured by Oblique Angle Reflectometry

One of the most remarkable properties of the high T_c compounds is the anisotropy of many of its properties, such as dc-resistivity, optical conductivity and the penetration depth. In many theories attempting to describe the cuprates, the low dimensionality plays an important role, and a thorough study of the anisotropy will present insight on the true merit of these models. However, the fairly large single crystals expedient for optical studies are not always available, and therefore it is useful to have an alternative experimental technique to determine the c-axis properties. PARIS spectroscopy provides

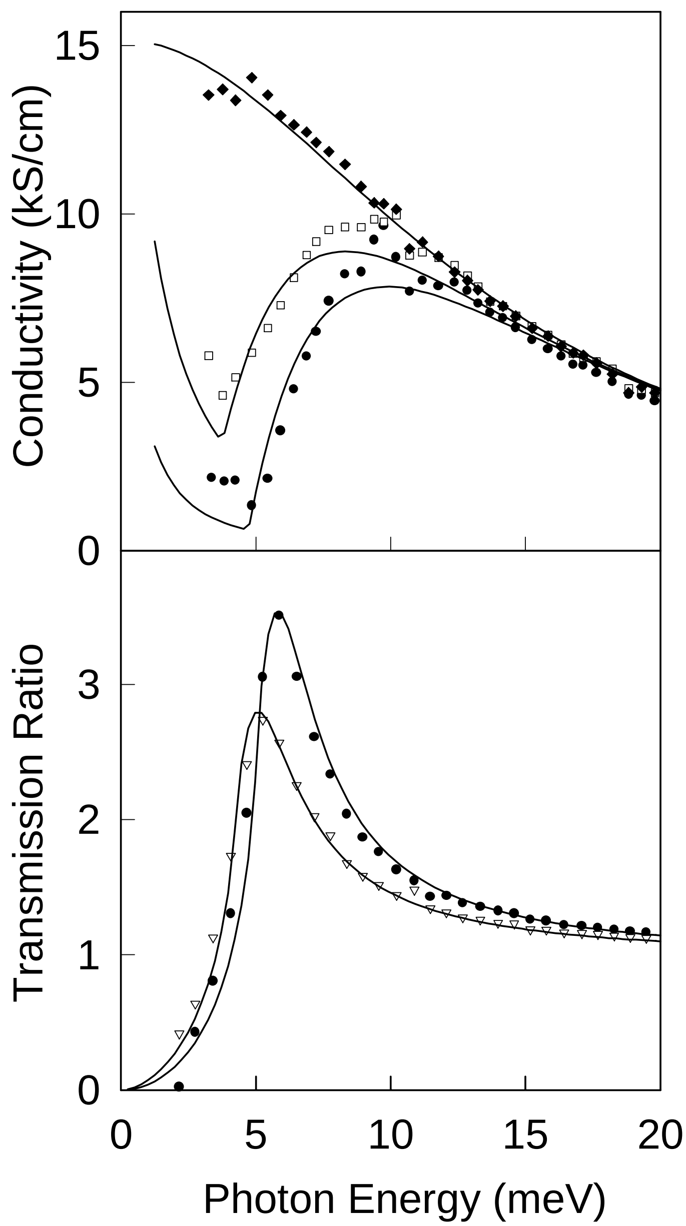

Figure 5.5: *Upper panel: Optical conductivity of a 400 nm thick NbN film, calculated from 80° angle of incidence reflection spectra for 9 K (closed circles, 13 K (open squares) and 18 K (closed diamonds). Solid curves: Theoretical calculations assuming isotropic s-wave pairing. Lower panel: Measured transmissivity ratios of the 55 nm thick NbN on Mgo (T(9.4 K)/T(22 K), closed circles; T(13.3 K)/T(22 K), open triangles). The solid curves are calculated using the same parameters as for the calculated conductivity of the top panel.*

such an alternative, for which c-axis oriented films and single crystal platelets can be used to acquire the desired response perpendicular to the CuO planes. The formalism of having a uniaxial medium, and a nonzero angle of incidence, conditions for which the reflection coefficients for p- and s-polarized light are distinct, has been explained in chapter 3 on page 58.

Sample Preparation

The $Tl_2Ba_2Ca_2Cu_3O_{10}$ films were grown on (100) $LaAlO_3$ substrates, by sputter deposition at ambient temperature in a symmetrical rf-diode sputtering system from two identical 1/2 in. targets. The targets were prepared by annealing an oxide powder mixture having initially a Tl:Ca:Ba:Cu ratio of 2:2:2:3 in a sealed quartz tube at 800-900 °C for several hours. The obtained films were post-annealed at approximately 890 °C for a few hours, while wrapping the films in a gold foil along with a Tl-containing pellet, in order to minimize the loss of Tl. The films were typically 5000 $\AA$ thick and had critical temperatures ranging from 120 to 123 K [14].

Reflectivity at a 45° Incident Angle

In fig. 5.6 we see the absolute reflectivity of $Tl_2Ba_2Ca_2Cu_3O_{10}$ in the far-infrared range for both s- and p-polarization, measured at 108, 163 and 300 K. As expected, the reflectivity for the p-polarized light is higher throughout the frequency and temperature range of our measurement. The s-polarization shows a response which is quite representative for the planar response of the high T_c materials. It is more or less featureless and has the linear non-Drude frequency dependence also seen in other cuprates.

A marked difference between the reflection spectra of both polarizations is the existence of strong absorption lines at 400 and 620 cm^{-1}. These are caused by the excitation of c-axis longitudinal optical phonons, which is strongly supported by their absence in the R_s spectra. The small glitches at the same frequencies in the R_s spectra are caused by the imperfect polarizer, leading to leakage of p-polarization into the s-polarized light. By comparing the resonant frequencies with reflectivity measurements on polycrystalline $Tl_2Ba_2Ca_2Cu_3O_{10}$ samples, we can easily identify the two phonon peaks [15]. Also lattice dynamics calculations for $Tl_2Ba_2Ca_2Cu_3O_{10}$ by Kulkarni *et al.* [16] predict c-axis longitudinal phonons at frequencies in the vicinity of the measured ones. According to these calculations, there are two A_{2u} longitudinal optical modes situated at 421 and 616 cm^{-1}. The former corresponds to a vibration along the c-axis of the oxygen atoms in the CuO_2 and BaO planes against the Ca atoms. The latter corresponds to the vibration along the c-axis of the oxygen atoms in the BaO planes and the Ca atoms against the oxygen atoms in the central CuO_2 planes.

Planar and c-Axis Conductivity

In fig 5.7 the c-axis conductivity is displayed for various temperatures. Below T_c there is a tendency of depression in the c-axis conductivity below 600 cm^{-1}. We can compare

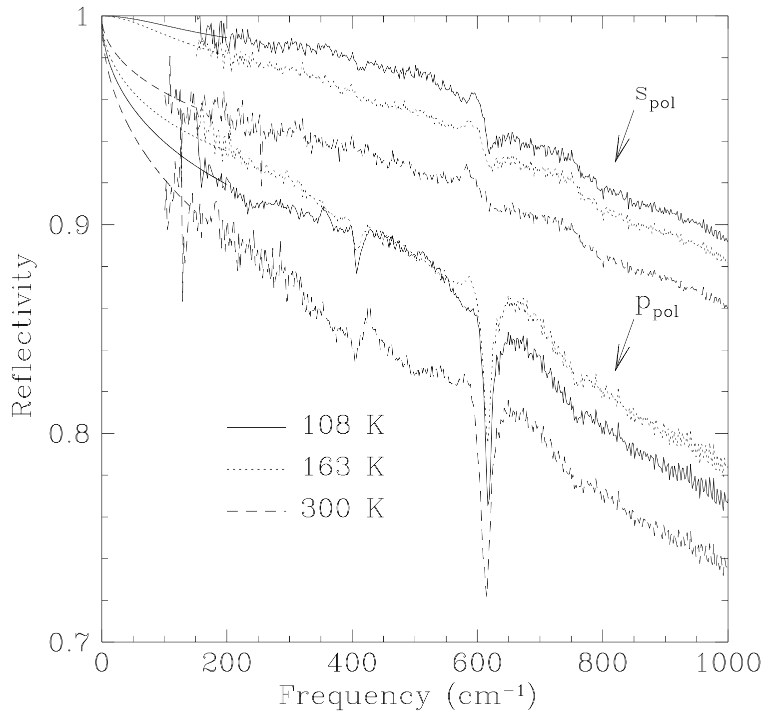

Figure 5.6: *Reflectivity of $Tl_2Ba_2Ca_2Cu_3O_{10}$ for s-polarized light (upper three curves) and p-polarized light (lower three curves), measured at a 45° incidence angle, along with the used extrapolation. The temperatures are 108 (solid line), 163 (dashed line) and 300 K (dotted line).*

our results with the c-axis conductivity of $YBa_2Cu_3O_{7-\delta}$ above and below T_c determined from reflection measurements on the *ac*-face of single crystals by Bauer [17] and Homes *et al.* [18]. According to these authors, there is a gap-like depression of conductivity at low temperatures below 600 cm^{-1}, but there is no clear evidence of a true BCS-like gap. In fact, the presence of a residual conductivity at low frequencies could indicate the existence of an unconventional gap symmetry, having nodes in certain directions in k-space. Hence the situation for $YBa_2Cu_3O_{7-\delta}$ is quite similar to what we have found in our own investigation of $Tl_2Ba_2Ca_2Cu_3O_{10}$.

c-Axis Loss Function and c-Axis Plasmon

In fig. 5.8 the c-axis loss-function, $\mathrm{Im}(-\epsilon_c)^{-1}$ is shown at various temperatures. The c-axis loss function is less susceptible to errors introduced by the Kramers-Kronig transformation than the c-axis conductivity, as can be seen by eq. (3.33) on page 60. Again, the peaks at the two longitudinal optical phonon frequencies are clearly recognizable. Both modes show a slight temperatures dependence, shifting up by about 5 cm^{-1} upon lowering the

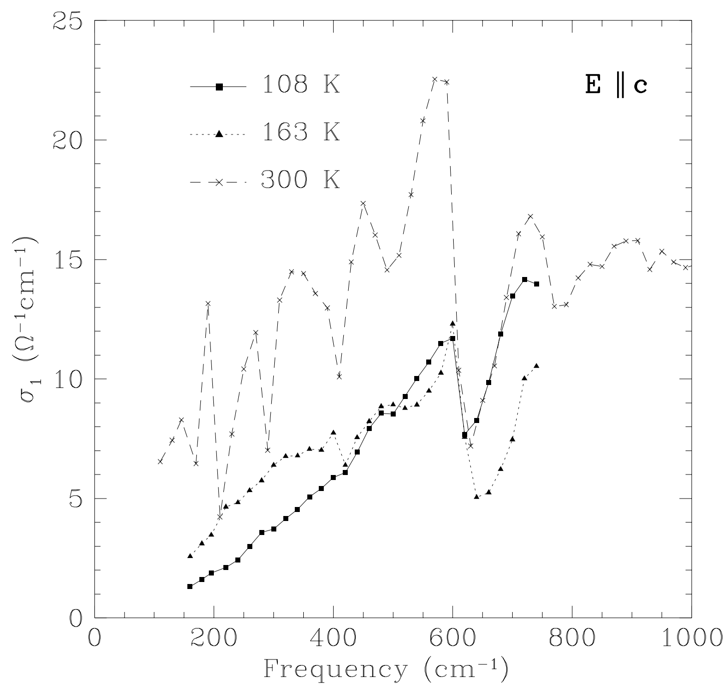

Figure 5.7: *The c-axis conductivity of $Tl_2Ba_2Ca_2Cu_3O_{10}$ for 108 (squares), 163 (triangles) and 300 K (crosses).*

temperature from 300 to 108 K. This is due to the phonon *hardening* commonly present if one lowers the temperature.

The electronic background in the c-axis loss function is more or less flat both at room temperature and at 163 K. However, in the 108 K loss function (i.e. in the superconducting state) there is a large rise in the electronic background contribution, mainly at low frequencies. This might be interpreted as the high-frequency tail of the loss-function peak due to the formation of the c-axis optical plasmon of the superconducting electrons. Based on this observation, we could place an upper limit of 200 cm^{-1} on the c-axis plasmon frequency.

Due to the large anisotropy in these materials the plasma frequency in the direction perpendicular to the layers is pushed to rather low energies, possibly into the mm-wave region. This observation calls for a more extensive and consistent study of the high T_c superconductors at energies below the range usually covered with Fourier Transform Spectroscopy. Promising possibilities are for instance quasioptical mm-wave spectroscopy and precise calorimetric measurements. Using this last technique Tsui *et al.* were able to determine the plasma frequency in $Bi_2Sr_2CaCu_2O_8$ indirectly by extrapolating its magnetic field dependence down to zero field, leading to an estimated value of about 5.3 cm^{-1} [19].

The situation for the c-axis plasmon is remarkably different from the in-plane plasmon. For most high T_c superconductors, such as $La_{2-x}Sr_xCuO_4$, $YBa_2Cu_3O_{7-\delta}$ and $Bi_2Sr_2CaCu_2O_8$, the in-plane plasmon energy is around 1eV (8000 cm^{-1}) [20], while the

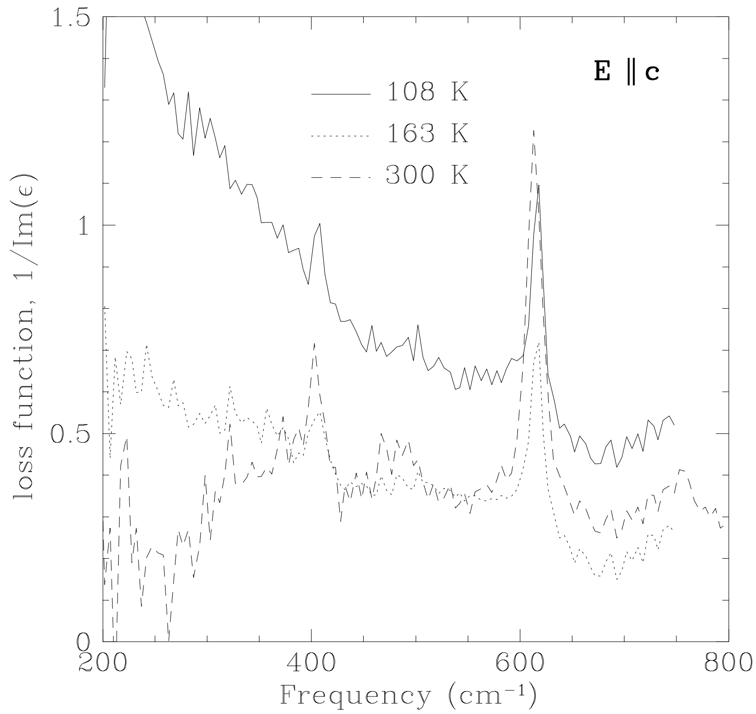

Figure 5.8: *Reflectivity of $Tl_2Ba_2Ca_2Cu_3O_{10}$ for s-polarized light (upper three curves) and p-polarized light (lower three curves), measured at 45° incidence angle together with the used extrapolation. The temperatures are 108 (solid line), 163 (dashed line) and 300 K (dotted line).*

c-axis plasmon energy seems to vary appreciably for the different systems. In the case of $YBa_2Cu_3O_{7-\delta}$ there is a zero-crossing of ϵ_c at approximately 100 cm^{-1}, i.e. below the lowest transverse optical phonon mode, and corresponds to a longitudinal mode of mixed vibrational and electronic character [17]. At temperatures closer to T_c, the crossing shifts to lower frequencies and eventually disappears, due to an enhanced damping of the mode. A similar behavior has been observed in $La_{2-x}Sr_xCuO_4$, where the lowest longitudinal out-of-plane plasma mode is found around 50 cm^{-1} [21, 22].

Band structure calculations based on the local density approximation (LDA) can be used to determine intra- and interband plasmon frequencies. Uspenskii and Rashkeev have done calculations for $Bi_2Sr_2CaCu_2O_8$ [23] for which they obtained bare plasma frequencies of about 3.3 eV and 0.9 eV, for the in-plane and out-of-plane mode respectively. Incorporating also screening the in-plane plasmon frequency is reduced to about 1.5 eV. Calculations for $YBa_2Cu_3O_{7-\delta}$ give unscreened intraband plasma frequencies (determined from a properly weighted Fermi velocity) of 3.5, 4.2 and 1.05 eV for the a, b and c-axis directions respectively [24]. Knowing that $\omega_p^{scr} = \omega_p/\sqrt{\epsilon}$, we can deduce that the screened plasmon energies have to be approximately twice as small as the unscreened ones. For

$La_{2-x}Sr_xCuO_4$ the LDA results for the screened in-plane and out-of-plane plasmons are 1.9 and 0.4 eV, respectively [25, 26]. We see that the experimental values for the in-plane plasma frequencies for the optimally doped samples are about half the theoretical values obtained from LDA-calculations. For the c-axis plasmon this discrepancy is even more dramatic, and the overestimation of LDA amounts to one or more orders of magnitude. The larger discrepancy can be attributed to the fact that, in contrast to the planar response, the c-axis conductivity is in the dirty limit [22, 27]. Hence the anisotropy for the plasmon frequencies is not only determined by the mass anisotropy, but also by the scattering rate anisotropy.

The c-axis plasmon in the high T_c materials and its energy is a subject of ongoing research and is especially interesting in the single-layer materials, such as $La_{2-x}Sr_xCuO_4$, $Tl_2Ba_2CuO_6$ and $Nd_{2-x}Ce_xCu_2O_{4+\delta}$. In particular, in these materials a direct correlation between the plasmon energy and T_c was predicted for the interlayer tunneling model proposed by Anderson and co-workers [28]. This hypothesis exploits the fact that within this model, a large fraction of the superconducting condensation energy E_{cond} is assumed to originate from the coupling between adjacent layers. This implies that T_c can be written in terms of the Josephson coupling energy, but for a few known material constants such as the interlayer distance d and the in-plane lattice constant a. Furthermore, one can express the Josephson plasma frequency ω_J in terms of the same Josephson coupling energy, thereby allowing a direct correlation between T_c and ω_J [29].

$$\hbar^2\omega_J^2 \;=\; \eta E_{cond}\frac{16\pi d e^2}{a^2} \tag{5.4}$$

where η is the fraction of condensation energy contributed by the interlayer coupling mechanism.

The controversy surrounding the prediction for single layer materials mentioned above has not been settled yet. Upto this point the only definite observation has been for $La_{2-x}Sr_xCuO_4$ [21, 22], at a frequency reasonably close to the predicted value (within approximately a factor of 2). At the present stage ω_J has not been found for other single layer materials, whereas for $Tl_2Ba_2CuO_6$ the upper limit has been determined at 50 cm^{-1} [30].

5.4 Conclusions

We demonstrated the use of two different approaches, aimed to tackle the problem of distinguishing highly conducting samples from *super*conducting ones. By employing a large angle of incidence (80°) the absorption related features in the reflectivity spectra are enhanced by approximately a factor of $1/\cos\Theta$. The feasibility of this technique was illustrated on the basis of results for NbN, in which case a clear gap, in conformity with the value expected from BCS-relations, was identified.

Furthermore we demonstrated the feasibility of the same technique to obtain the dielectric function in the directions parallel and perpendicular to the optical axis of a uniaxial sample. We applied this technique to a thin film of $Tl_2Ba_2Ca_2Cu_3O_{10}$ in order to study the c-axis infrared response. For this material no single crystals were available which are sufficiently large along the c-axis to allow a direct scattering experiment on the *ac*-face. Although the longitudinal optical phonons in the c-axis direction are clearly in our spectra, we did not find a plasma-related zero crossing of ϵ_c above 200 cm^{-1}, which indicates that 200 cm^{-1} is an upper limit for the out-of-plane plasmon.

References

[1] M. A. Biondi, M. P. Garfunkel and A. O. McCoubrey, Phys. Rev. **102**, 1427 (1956).

[2] R. E. Glover III and M. Tinkham, Phys. Rev. **104**, 844 (1956).

[3] Z. Schlesinger, R. T. Collins, F. Holtzberg, C. Feild, G. Koren and A. Gupta, Phys. Rev. Lett. **65**, 801 (1990).

[4] for a review on this and related topics please refer to: D. B. Tanner and T. Timusk, Chapter 5 of *Physical Properties of High Temperature Superconductors*, vol. III, D. M. Ginsburg ed. (World Scientific, London, 1992), p. 363.

[5] O. V. Dolgov, A. E. Karakozov, A. A. Mikhailovsky, B. J. Feenstra and D. van der Marel, Physica C **229**, 396 (1994).

[6] D. N. Basov, T. Timusk, B. Dabrowski and J. D. Jorgensen, Phys. Rev. B **50**, 3511 (1994).

[7] K. Kamarás, S. L. Herr, C. D. Porter, N. Tache, D. B. Tanner, S. Etemad, T. Venkatesan, E. Chase, A. Inam, X. D. Wu, M. S. Hedge and D. Dutta, Phys. Rev. Lett. **64**, 84 (1990).

[8] H. S. Somal, B. J. Feenstra, J. Schützmann, Jae Hoon Kim, Z. H. Barber, V. H. M. Duijn, N. T. Hien, A. A. Menovsky, Mario Polumbo and D. van der Marel, Phys. Rev. Lett **76**, 1525 (1996).

[9] Z. H. Barber, M. G. Blamire, R. E. Somekh and J. E. Evetts, IEEE Trans. Supercond. **3**, 2054 (1993).

[10] J. R. Jasperse, A. Kahan, J. N. Plendl and S. S. Mitra, Phys. Rev. **146**, 526 (1966).

[11] K. E. Kornelson, M. Dressel, J. E. Eldridge, M. J. Brett and K. L. Westra, Phys. Rev. B. **44**, 11882 (1991).

[12] D. Karecki, R. E. Peña and S. Perkowitz, Phys. Rev. B. **25**, 1565 (1982).

[13] H. S. Somal, Ph D thesis, University of Groningen, in preparation.

[14] W. Y. Lee, J. Vasquez, T. C. Huang and R. Savoy, J. Appl. Phys. **70**, 3952 (1991).

[15] T. Zetterer, M. Franz, J. Schützmann, W. Ose, H. H. Otto and K. F. Renk, Phys. Rev. B **41**, 9499 (1990).

[16] A. Kulkarni, F. W. de Wette, J. Prade, U. Schröder and W. Kress, Phys. Rev. B **41**, 6409 (1990).

[17] M. Bauer, Ph D Thesis, University of Tübingen, 1990.

[18] C. C. Homes, T. Timusk, R. Liang, D. A. Bonn, and W. N. Hardy, Phys. Rev. Lett. **71**, 1645 (1993).

[19] Ophelia K. C. Tsui, N. P. Ong and J. B. Peterson, Phys. Rev. Lett. **76**, 819 (1996).

[20] J. H. Kim, I. Bozovic, J. S. Harris Jr., W. Y. Lee, C. B. Eom and T. H. Geballe, in *Proc. of the University Miami Workshop on Electronic Structure and Mechanism for High Termperature Superconductivity*, J. Ashkenazi ed. (Plenum Press, New York, 1991), p. 251.

[21] K. Tamasaku, Y. Nakamura and S. Uchida, Phys. Rev. Lett. **69**, 1455 (1992).

[22] Jae H. Kim, H. S. Somal, M. Czyzyk, D. van der Marel, A. Wittlin, A. M. Gerrits, V. H. M. Duijn, N. T. Hien and A. A. Menovsky, Physica C **247**, 297 (1995).

[23] Yu. A. Uspenskii and S. N. Rashkeev, Phys. Lett. A **153**, 373 (1991).

[24] E. G. Maksimov, S. N. Rashkeev, S. Yu. Savrasov and Yu. A. Uspenskii, Phys. Rev. Lett. **63**, 1880 (1989).

[25] E. G. Maksimov, I. I. Mazin, S. N. Rashkeev, S. Yu. Savrasov and Yu. A. Unspenskii, Int. J. Mod. Phys. B **2**, 883 (1988).

[26] M. Czyzyk and D. van der Marel, private communication.

[27] D. van der Marel and Jae H. Kim J. Phys. Chem. Sol. **12**, 1825 (1995).

[28] S. Chakravarty, A. Sudbo, P. W. Anderson and S. Strong, Science **261**, 337 (1993).

[29] D. van der Marel, J. van der Eb, J. Schützmann and H. S. Somal, in *Proc. 10th Anniversary HTS Workshop on Physics, Materials & Applications*, B. Batlogg, C. W. Chu, W. K. Chu, D. U. Gubser and K. A. Miller ed., (World Scientific Publishers, New York, 1996), p. 357.

[30] J. Schützmann, H. S. Somal, A. A. Tsvetkov, D. van der Marel, G. Koops, N. Koleshnikov, Z. F. Ren, J. H. Wang, E. Brück and A. A. Menovsky, Phys. Rev. B **55**, 11118 (1997).

Chapter 6

mm-Wave Transmission through Superconducting Thin Films

6.1 Introduction

Many of the contemporary results on the electrodynamical properties of high T_c superconductors in the microwave region have been obtained by exploiting resonant techniques such as cavity perturbation [1–3]. Although these techniques yield results having a very high accuracy, obtaining absolute quantities is rather difficult due to intrinsic experimental complications [4]. By measuring mm-wave transmission through a superconducting thin film one is able to obtain *absolute* information about both the real and the imaginary part of its dielectric function [5]. Already around the formulation of the BCS-theory [6], mm-wave and far infrared transmission through superconducting thin films was used as a sensitive technique to probe the energy gap, present in the excitation spectrum of conventional superconductors such as Pb and Al [7, 8].

We first demonstrate the principle of the transmission measurement by showing some examples in which the optical constants of some dielectric (substrate) materials are determined. In the sections thereafter we present the results of mm-wave transmission measurements performed on both conventional (MoGe, NbN) and a high temperature superconductor ($DyBa_2Cu_3O_{7-\delta}$). The conventional superconductors, the optical response of which is well-established, were mainly investigated in order to demonstrate that we are able to determine the intrinsic properties of the film. We will show the absolute magnitude of properties such as the penetration depth λ, the optical conductivity σ_1 and the permittivity ϵ', resulting from the analysis. In particular, in section 6.4 where we describe the results obtained on a series of $DyBa_2Cu_3O_{7-\delta}$ films with thicknesses ranging from 20 to 80 nm, special attention will be paid to the significance of the film thickness in mm-wave transmission measurements.

6.2 Dielectric Materials

In chapter 3 we have seen that due to the multiple reflections on each interface both the transmitted and the reflected signal from a layered material exhibits an interference pattern. An easy way to observe these interference effects is to measure the transmission of mm-waves through a plan-parallel dielectric material, which has a low absorption coefficient in this frequency range. By measuring the magnitude of the interference peaks and the distance between two adjacent peaks one can experimentally determine the complex dielectric function p of the dielectric, where $p = \eta + i\kappa$. The amplitude of the maxima is directly related to the degree of absorption within the material, κ, and has an optimal value of 1 for an absorptionless dielectric. The distance between two adjacent peaks is determined by the product kpd, where k is the wave vector, $2\pi\nu/c$ and d is the sample thickness. In our experiment k runs from 4 to 6 cm^{-1}. Since both k and d are known very precisely, one can determine the value for η.

Two examples of such interference patterns measured on fused quartz and KRS-5 can be seen in fig. 6.1. The solid lines are transmission coefficients calculated using the formulation

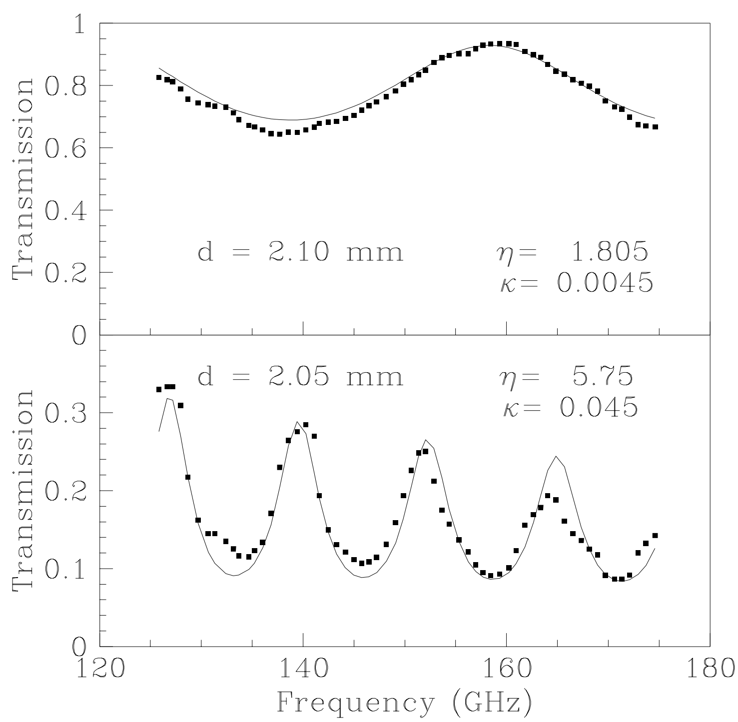

Figure 6.1: *Fabry-Perot resonance spectra for two commonly used window materials, fused quartz (top) and KRS-5 (bottom).*

presented in chapter 3 (see eq. 3.12). These two commonly used window materials show a very distinct response at these frequencies. Fused quartz is often employed as a window for mm-wave as well as MIR radiation, and shows a very high transmission over the entire range, indicative of both a low absorption ($\kappa = 0.0045$) and a low index of refraction, $\eta = 1.805$. This small value is apparent from the distance between the maxima, which is rather large even though the thickness of the quartz sample is 2.10 mm. Moreover, also the high transmission in the minima indicates a small η.

The KRS-5 sample shows several peaks, while the thickness of the sample is the same, indicating that the index of refraction is much larger, $\eta = 5.75$. Also the absolute magnitude of the transmission over the entire range is much lower and the spectrum exhibits the "typical" tilted spectrum for a highly absorbing sample, having $\kappa = 0.045$.

In fig. 6.2 we show another example, the frequency response of two dielectrics commonly used as substrates for high T_c thin films, $LaAlO_3$ and $NdGaO_3$. Also in this case the Fabry-

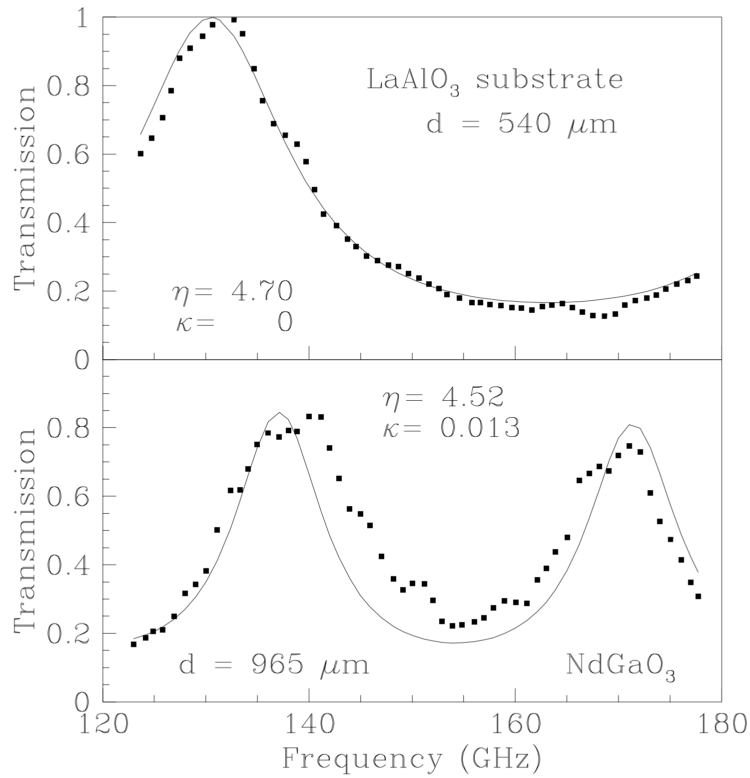

Figure 6.2: *Fabry-Perot resonance spectra for two perovskite substrate materials,* $LaAlO_3$ *(top) and* $NdGaO_3$ *(bottom).*

Perot resonances are well described by the calculated transmission. The response of the $NdGaO_3$ substrate was measured in the early stages of the setup, and therefore showssome remaining discrepancies due to diffraction and spurious leakage, while the $LaAlO_3$ substrate was measured more recently, clearly showing the improved performance. For $LaAlO_3$ the maximum transmission is equal to 1, manifesting that at these frequencies the absorption in this material can be neglected. From the period we obtain that $\eta = 4.70$. In the case of $NdGaO_3$, the maximum amplitude is slightly reduced, suggestive of the presence of a small absorption. The fringes are closer together compared to the case of $LaAlO_3$ due to the larger thickness, since the important parameter determining the period is the product kpd. The obtained optical constants are $\eta = 4.52$ and $\kappa = 0.013$.

In the remainder of this chapter, the optical constants of the used substrate are always determined experimentally by the method described above. Also the temperature dependence of the optical constants is measured since the transmission of the bare substrate and film+substrate are measured subsequentially at a fixed temperature (see chapter 4).

6.3 Conventional Superconductors

In order to check the reliability of the technique, and the performance of our newly build setup, we began by measuring some conventional superconductors, exhibiting BCS-behavior. In doing so, we made sure that we are able to resolve the intrinsic properties of the superconducting thin film. In this section the results on two of these materials, MoGe and NbN, are presented.

6.3.1 MoGe

Introduction

The first example of mm-wave transmission experiments performed on a conventional superconductor were done using an 800 $\AA$ thick MoGe film, provided to us by Prof. S. M. Anlage. The film was deposited on the $<100>$ surface of a 520 μm thick Si substrate, by co-magnetron sputtering from single element sources at ambient temperature. The deposition was done in an Argon atmosphere, at a pressure of 5 mTorr. Rapid substrate rotation (3000 rpm) was used during deposition to improve the sample homogeneity and coverage.

MoGe, being an amporphous superconductor, combines microscopic disorder with a homogeneity on the length scale important for superconductivity (i.e. the coherence length ξ). It therefore attracted some attention in the early eighties, as a testcase to investigate the validity of theories developed at that time, concerning the influence of Anderson localization on superconductivity [9].

Moreover, due to the relatively large penetration depth ($\lambda(0) \sim 7000 - 7700\AA$ [10,11]) one can consider thin films having a thicknes upto several hundred $\AA$ as if they were essentially two-dimensional. This led for instance to the observation of a Kosterlitz-Thouless transition in thin (500-5000 $\AA$) a-MoGe films [10].

Due to the long penetration depth, along with the short coherence length ($\xi(0) = 55\AA$ [11]) MoGe can be classified as an extreme type II superconductor, similar as the high T_c's. Henceforth a renewed interest in thin MoGe layers, and multilayer structures using Ge as the intermediate layer, was initiated after the discovery of the high T_c compounds. Using artificial multilayer structures one is able to perform a range of experiments which are very difficult or even impossible to acchieve within a genuine high T_c superconductor. For instance, by changing the interlayer thickness, one can modify the Josephson coupling between the superconducting layers and thus study the influence of the coupling on superconductivity. Also, due to the low dimensionality of the thin film, one can investigate the behavior of an individual layer independently. Furthermore, through the use of materials such as MoGe, in which the critical field, H_{c2} is considerably lower, one attain access to the entire H,T-phase diagram.

Main focus of the research on artificial layered structures has therefore been on studying the vortex dynamics. Important questions that are addressed are the number of different phases, their character and which of these phases exhibit zero resistivity. Using MoGe/Ge multilayers White *et al.* [11] and Steel *et al.* [12] were able to show the crossover from a region in which the vortices in one particular layer are coupled to the vortices in the adjacent layer, to a situation at higher temperatures and/or fields where the vortices are completely decoupled, i.e. 2-dimensional. A similar system was used to demonstrate that the existence of Josephson vortices in between the superconducting layers does not produce the (in)famous sign reversal in the vortex Hall effect [13].

In our case the main goal in studying MoGe was to establish whether we are able to probe the intrinsic BCS-properties of the thin film, using mm-wave transmission experiments.

Results

The critical temperature of the MoGe film was checked by dc-resistivity measurements, presented in fig. 6.3. The low temperature region has been expanded and can be seen in the inset. The dc-resistivity shows a nearly temperature independent behavior in the

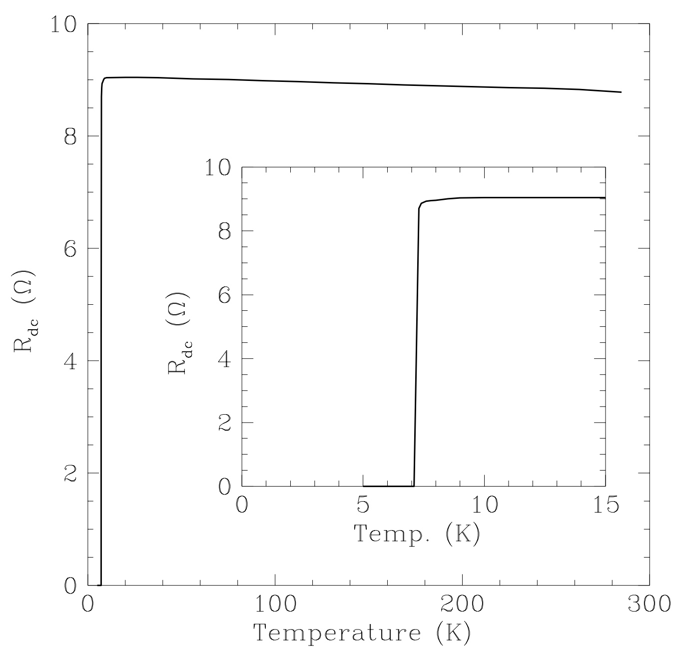

Figure 6.3: *dc-Resistivity measurements for an 800 Å thick MoGe film, deposited on a Si substrate.*

normal state, typical for such films. T_c is 7.2 K while the width of the transition is approximately 0.1 K. Plotted is the resistivity measured using a four-point measurement.

In fig. 6.4 the transmission through a bare Si-substrate is depicted. From this we

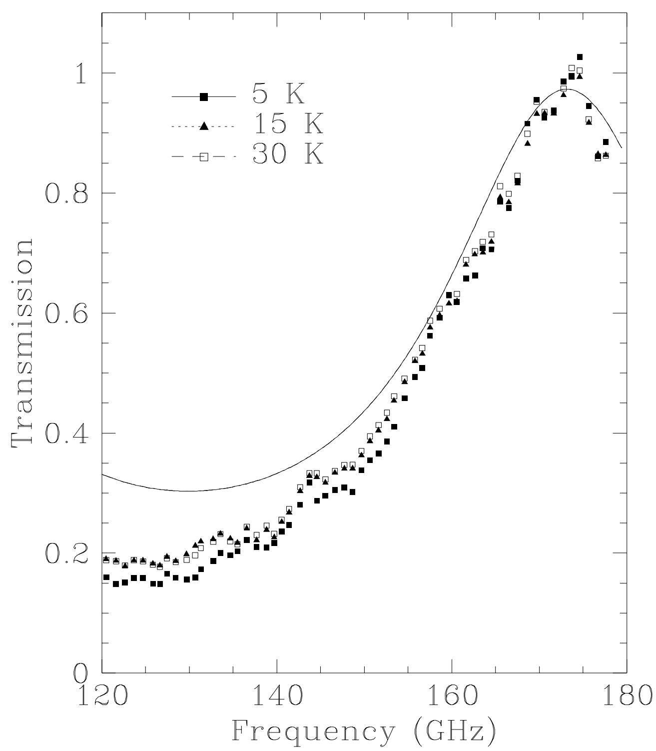

Figure 6.4: *Transmission through a bare Si substrate. The obtained optical constants are:* $\eta = 3.32$ *and* $\kappa = 0.004$.

obtained the optical constants for the substrate, $\eta = 3.32$ and $\kappa = 0.004$. We see that there is no temperature dependence in the range of interest, below 30 K. At higher temperatures the transmission started to be reduced due to thermally activated carriers, introduced by the inhomogeneties within the silicon. Using the experimentally determined optical constants of the substrate, we can model the transmission through the entire system, i.e. the MoGe thin film on a Si substrate.

The transmission coefficient has been depicted in fig. 6.5 as a function of frequency, for three different temperatures (4.5, 7.0 and 30 K, from bottom to top). In the normal state the absolute magnitude of the transmission is determined by the real part of the conductivity σ_1, which is nearly temperature independent. The best fit is obtained using $\sigma_1 = 17,300\,(\Omega\mathrm{cm})^{-1}$. This cannot be directly compared to the value obtained from the dc-resistivity, however, as we will also see in the next section, the magnitude is reasonable for such a film. Due to the high conductivity of the metallic film the interference pattern has been shifted compared to the observed spectrum for the bare substrate. Notice furthermore that the interference pattern shows no major changes besides the reduced amplitude upon entering the superconducting state. These phenomena will be treated in more detail in

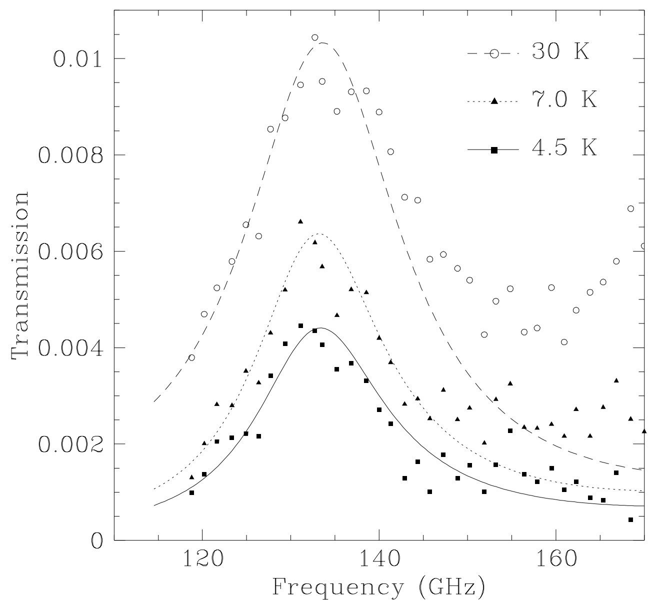

Figure 6.5: *Frequency dependence of the mm-wave transmission through a MoGe film on Si, plotted for several temperatures.*

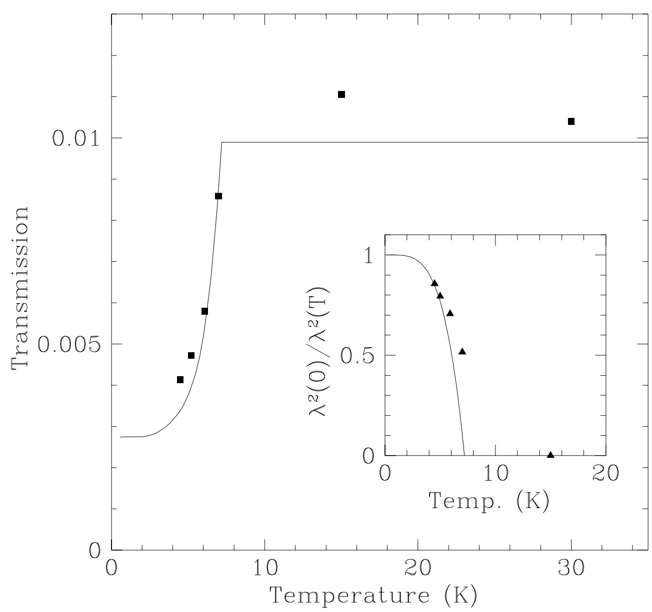

Figure 6.6: *Temperature dependence of the transmission through a MoGe film on a Si substrate along with the calculated transmission for a BCS-superconductor having* $\sigma(10) = 17,300(\Omega\text{cm})^{-1}$ *and* $\lambda(0) = 5000\AA$. *Inset: temperature dependence of the superfluid density compared to the BCS-prediction.*

section 6.4.

The discrepancy at higher freqencies can presumably be attributed to the presence of radiation traversing a different path. Its temperature dependence, resembling the temperature dependence of the superconducting thin film, is strong evidence against assigning this contribution to leakage radiation. If the beam would pass the sample under a nonzero angle of incidence, the effective thickness of the substrate would be larger, giving rise to additional peaks, most likely broadened, in the Fabry-Perot resonance pattern.

In the superconducting state we assume that the dielectric function of the thin film is dominated by the superfluid contribution, yielding an absolute value for the penetration depth, since $\lambda \sim 1/\omega_{ps}$. The lowest value obtained for the fit at 4.5 K is approximately 5410 $\mathring{A}$.

In fig. 6.6 the transmission is shown as a function of temperature, at a fixed frequency of 133 GHz. The reduction of transmission at T_c due to the strongly enhanced screening caused by the presence of the superfluid is evident. At the lowest temperature the transmission starts to level off, but still is not temperature independent, which indicates that the gap has not fully opened yet. The measured transmission agrees fairly well with the predicted BCS-behavior represented by the solid line. In the normal state a temperature independent σ_1 was used, having a value of 17,300 $(\Omega\text{cm})^{-1}$. In the superconducting state σ_1 vanishes according to the Mattis-Bardeen relations [14] and λ obeys [15]

$$\lambda(T) \;=\; \lambda(0)\left[1 \;-\; \left(\frac{T}{T_c}\right)^4\right]^{-1/2} \tag{6.1}$$

Using this temperature dependence we can also calculate the superfluid density n_s, according to $\lambda^2(0)/\lambda^2(T)$, taking $\lambda(0) = 5000\mathring{A}$. The agreement with the measured superfluid density has been shown in the inset of fig. 6.6. In addition we can see that the T_c of this material is too low to observe the temperature independence of λ, typical for a BCS-superconductor exhibiting activated behavior.

6.3.2 NbN

NbN is a conventional superconductor having a much higher critical temperature than MoGe. T_c can range from 16 upto 18 K by the inclusion of carbon. We measured the transmission of mm-waves through a 55 nm thick NbN film deposited on a 490 μm thick MgO substrate. The sample preparation has been described in chapter 5, where the same film was used to measure the transmission and reflection coefficient in the FIR-range.

In fig. 6.7 the dc-resistivity, R_{dc} has been plotted. The resistivity has a negative temperature coefficient observed more often for thin metallic films and shows a transition at starting at 17 K, having a width of approximately 0.8 K. The transmission through a bare MgO substrate, having a thickness of 640 μm, is shown in fig. 6.8. The obtained optical constants are $\eta = 3.43$ and $k = 0.006$. Please note that the thickness of the substrate used for the reference measurement is not the same as the one on which the NbN film was deposited. The possibility of using substrates of unequal thicknesses is given by the system of modeling the transmission through the complete stratified sample.

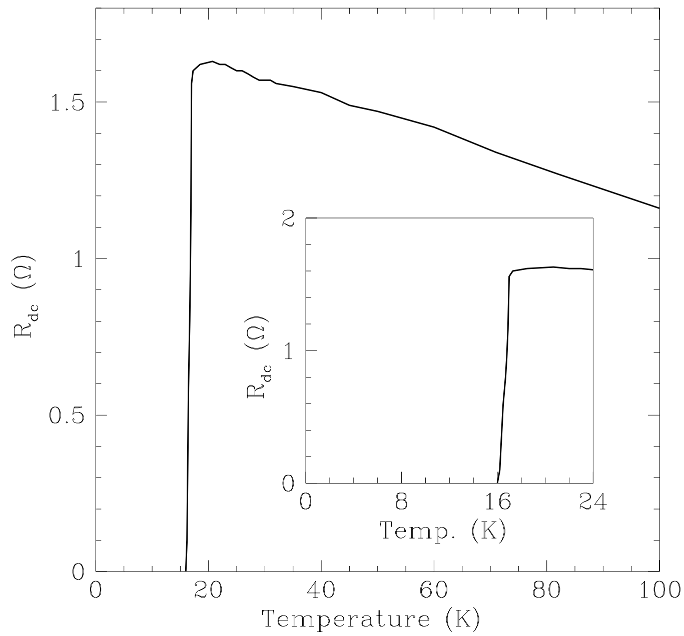

Figure 6.7: *dc-Resistivity measurements for a 55 nm thick NbN film, deposited on a MgO substrate.*

In fig. 6.9 the transmission through the NbN film on MgO is shown as a function of frequency, for several temperatures, both above and below T_c. The peak in the interference spectrum is determined by the MgO substrate. We are able to fit the spectra using the two fluid description of equation (3.25). As expected for a metallic film, $\epsilon'' \gg \epsilon'$, while in the superconducting state the opposite is valid, $\epsilon' \gg \epsilon''$. For the fit we have focused our attention on the main peak around 135 GHz. The poor fit at higher frequencies has the same origin as the discrepancies seen in the MoGe analysis. Also in this case the magnitude of the contribution follows the temperature dependence of the main peak. In later experiments the control over undesired reflections and standing waves was improved even further, thereby removing this phenomenon.

Plotting the temperature dependence at one particular frequency (140 GHz) as shown in fig. 6.10, the dramatic change in transmission at T_c is more easily observed. The temperature dependence of the transmission coefficient can be fitted very well using the assumptions that $\lambda(\mathrm{T})$ can be described by the Gorter Casimir relation given in eq. (6.1), $\sigma_1(\mathrm{T})$ follows the Mattis-Bardeen relations and $2\Delta\,/\,\mathrm{kT} = 4.0$. The only adjustable parameters used in the calculation were the normal state conductivity ($\sigma_1\,(17K) = 15,000\ \Omega^{-1}\mathrm{cm}^{-1}$) determining the transmission at 17 K and the London penetration depth ($\lambda_L = 400$ nm) giving the transmission at low temperatures. Although this penetration depth is somewhat higher than the lowest reported values of about 100 nm [16], there is considerable variation in the literature due to a wide range of film structures.

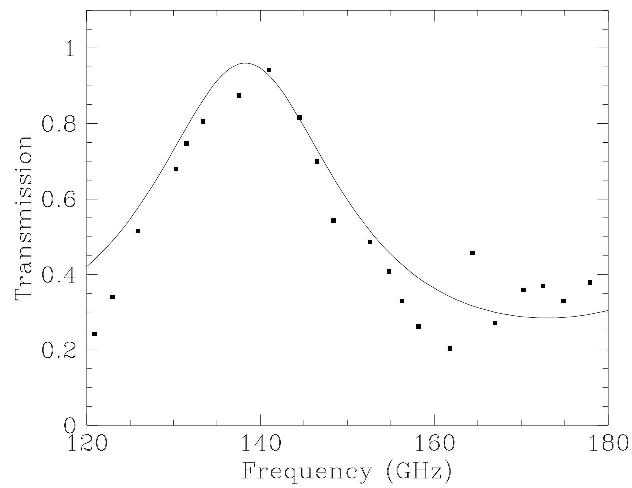

Figure 6.8: *Transmission through a bare MgO substrate. The obtained optical constants are: η = 3.43 and κ = 0.*

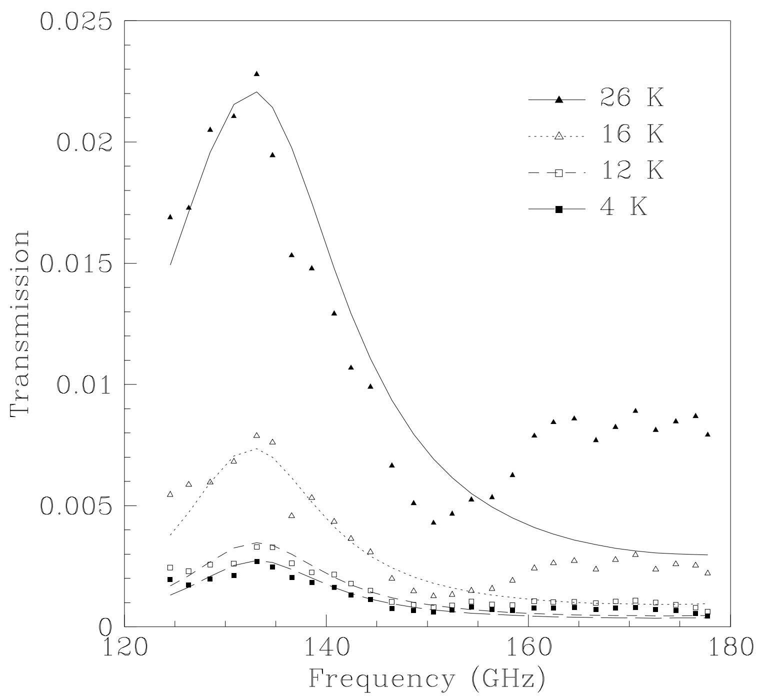

Figure 6.9: *Transmission of NbN on MgO (thickness = 55 nm, T_c = 17 K) for 4 different temperatures (4 K: solid squares, 12 K: open squares, 16 K: open triangles and 26 K: solid triangles) together with their fit. Inset: temperature dependence at 140 GHz together with a BCS-fit.*

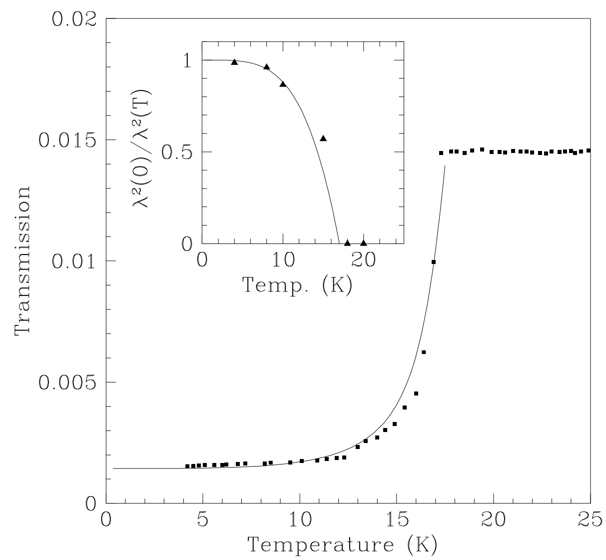

Figure 6.10: *Temperature dependence at 140 GHz together with a BCS-fit using* $\sigma_1(17K) = 15{,}000\ \Omega^{-1}cm^{-1}$ *and* $\lambda_L = 400\,nm$. *Inset: Temperature dependence of the superfluid density, along with the expected BCS-behavior.*

The conductivity agrees well with the value of 14,000 $\Omega^{-1}\mathrm{cm}^{-1}$ given in chapter 5, which was obtained using FIR-spectroscopy. In contrast to the case of MoGe the temperature independence of the transmission coefficient, due to the exponential behavior of λ is clearly visible. In the inset of fig. 6.10 the superfluid density has been plotted along with its predicted behavior, showing a satisfactory agreement.

6.4 $DyBa_2Cu_3O_{7-\delta}$

Sample Preparation

The $DyBa_2Cu_3O_{7-\delta}$ films of thicknesses ranging from 20 to 80 nm, were deposited by RF sputtering on $LaAlO_3$ substrates using the (100) surface. The substrate temperature was 745 °C while a mixture of argon and oxygen gas was used, at pressures of 105 and 45 mTorr respectively. After the deposition the samples were annealed in 200 mTorr oxygen for 30 minutes at 450 °C. The quality of the surface was checked with X-ray diffraction, which showed a very good crystallization. Due to the high crystallinity of the films, the oxygen diffusion process was rather slow resulting in a somewhat reduced T_c (88 K) for one of the films (20 nm).

Transmission Results

In this section the influence of the thickness of the superconducting film on the mm-wave transmission, in particular its temperature dependence, will be presented. The results on a series of films, having a thickness ranging from 20 to 80 nm will be analyzed. We demonstrate that taking the film thickness into account is essential for obtaining the intrinsic temperature dependence of the material properties. Moreover, by selecting the right film thickness we are able to choose the sensitivity such that either the conductivity or the superfluid density ($\sim 1/\lambda^2$) dominates the temperature dependence of the transmission coefficient. We will show that for certain values of the London penetration depth λ_L and the normal state conductivity σ_n, one can choose the film thickness such that even in the superconducting state downto rather low temperatures ($\sim$ 60 K) the superfluid density appears to be absent.

In fig. 6.11 the transmission through a 20 nm thick $DyBa_2Cu_3O_{7-\delta}$ film on a $LaSrO_3$ substrate is shown. Similar results as presented below have been reproduced on a different batch of films. The interference pattern of the substrate at room temperature was shown already in fig. 6.2 in section 6.2, from which we obtained $\eta = 4.70$ and $\kappa = 0$. As expected the optical constants are temperature independent for the perovskite substrate. The additional oscillations present in the transmission are caused by internal reflections within the sampleholder. Due to the slightly modified standing wave pattern, these do not cancel completely after division by the transmitted signal through a reference hole.

In contrast to the results for the MoGe and the NbN film presented in the previous section, the interference pattern of the $DyBa_2Cu_3O_{7-\delta}$ thin film changes dramatically when the temperature is lowered. This is due to the stronger change in conductivity of the film, thereby altering the matching of the impedances of both film and substrate. This effect can be demonstrated by modeling the transmission through a similar stratified system, changing either the optical conductivity σ_1 of the film, keeping the thickness fixed at 20 nm (fig. 6.12a) or by altering its thickness at a fixed conductivity of 3000 Ω^{-1}cm^{-1} (fig. 6.12b). Both parameters will have a similar effect on the transmission since this is mainly affected by their product. For a certain set of parameters the interference effect disappears completely, showing that the light passes through the substrate only once. Additionally, the magnitude of the dielectric function matching this requirement determines the absolute value of transmission at the turning point.

This model calculation illustrates furthermore that one has to be careful with the interpretation of transmission curves measured as a function of temperature at a fixed frequency. A curve taken at 130 GHz will show a much larger temperature dependence than a curve taken at 150 GHz, although they will yield the same intrinsic film properties, once interference effects are taken into account. This effect is demonstrated in fig. 6.13, where we plotted the temperature dependence of the transmission through the $DyBa_2Cu_3O_{7-\delta}$ film, for several frequencies.

At 150 GHz the transmission is nearly constant at temperatures higher than 60 K. At lower temperatures the amplitude of the interference peak drops and its width decreases rapidly. The transmission for the 34 nm film is depicted in fig. 6.14 for the same tempera-

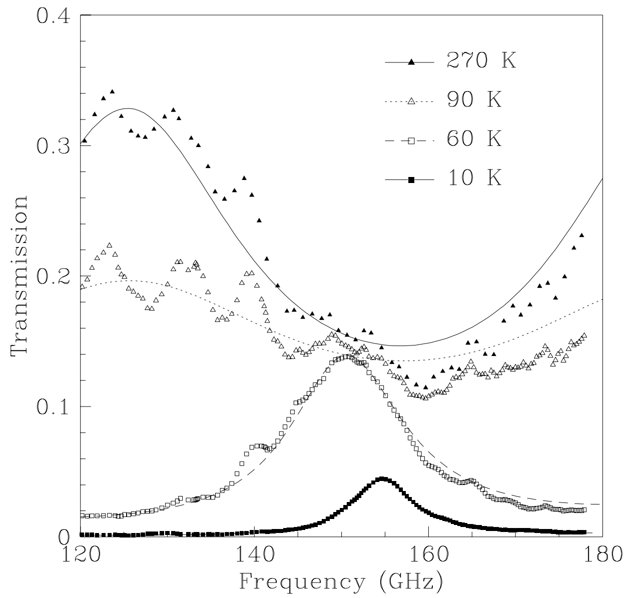

Figure 6.11: *Transmission of $DyBa_2Cu_3O_{7-\delta}$ on $LaAlO_3$ (thickness = 20 nm, T_c = 88 K) at 4 different temperatures together with their fit (10 K: solid squares, 60 K: open squares, 90 K: open triangles and 270 K: solid triangles).*

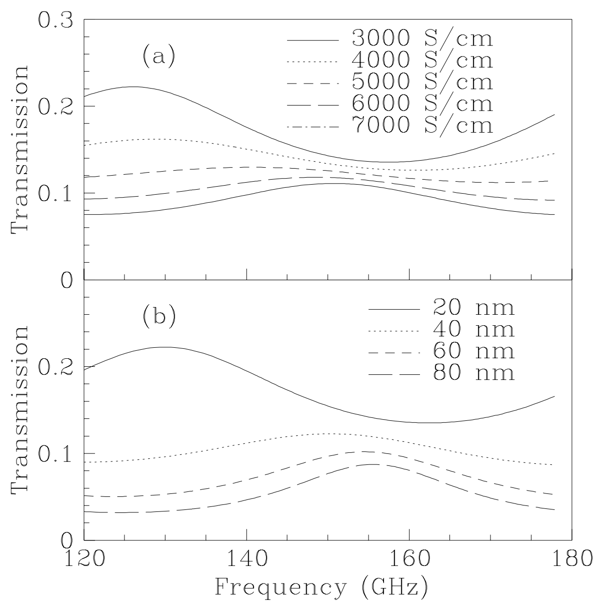

Figure 6.12: *Calculated transmission through a layered system (thin film on a substrate) as a function of conductivity (a) or thickness (b). For the substrate the optical constants of the $LaAlO_3$ were used (η = 4.70 and κ = 0), while the film thickness for (a) was 20 nm and the conductivity for (b) was 3000 $\Omega^{-1}cm^{-1}$.*

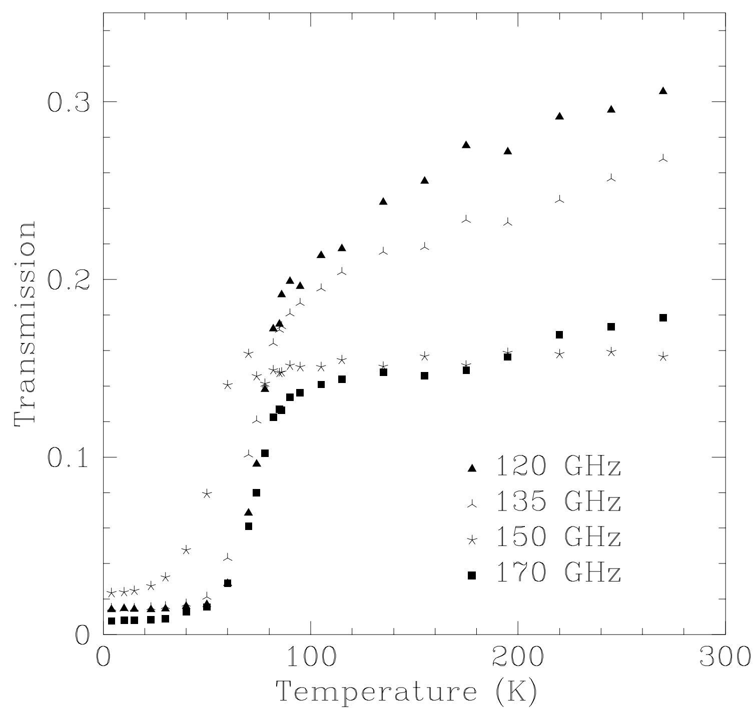

Figure 6.13: *Transmission as a function of temperature, at several fixed frequencies, clearly demonstrating the different behavior due to interference effects.*

tures as the 20 nm film (270, 90, 60 and 10 K). We see that the reduction in transmission at intermediate temperatures is much larger in the thicker film. As we will argue below, this is due to the stronger contribution of the superfluid in the 34 nm film. The transmission data for the 80 nm film, depicted in the inset of fig. 6.14, show qualitatively similar behavior as the 34 nm thick film.

Data Analysis, yielding σ_1 and ϵ'

To fit the transmission data presented in fig. 6.11 we use two different approaches. First we start in the normal state, knowing that there is no superfluid fraction present (approach A). This yields both ϵ' and ϵ'', where the sensitivity in the metallic case is most extensive for ϵ'' ($\sim \nu_{pn}^2/\gamma$). We continue this approach even when the sample is cooled below T$_c$ where the addition of a superfluid contribution does not influence the fit for the 20 nm film significantly. We proceed until the peak becomes too narrow and fitting is no longer possible. The second approach (B) is to start at the lowest possible temperature (5 K) and assume that the superfluid fraction is the dominant contribution. We proceed to higher temperatures until the peak starts to broaden and the maximum remains nearly constant, thus inhibiting fitting with the superfluid as the only contribution. Obviously there will

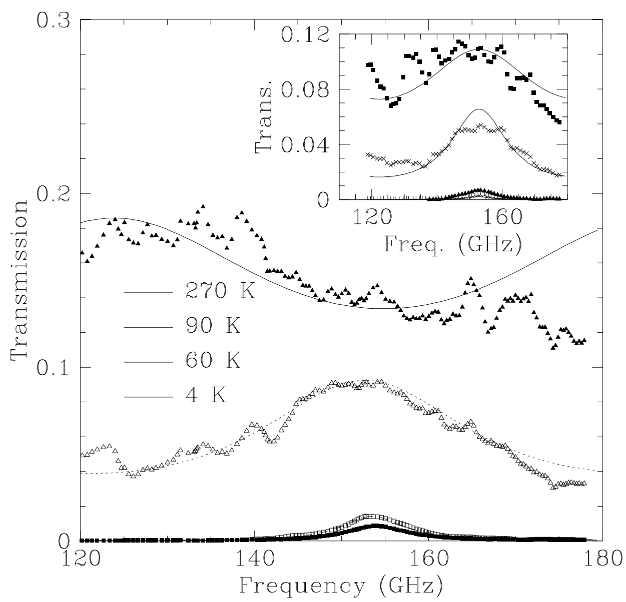

Figure 6.14: *Transmission of $DyBa_2Cu_3O_{7-\delta}$ on $LaAlO_3$ (thickness = 34 nm, T_c = 91 K) at 4 different temperatures (10, 60, 90 and 270 K) along with their fit. Inset: Transmission of $DyBa_2Cu_3O_{7-\delta}$ (d = 80 nm) at the same temperatures.*

be a temperature range for which both terms are comparable, in which case a quantitative description is more complicated.

In fig. 6.15 σ_1 is shown, while in fig. 6.16 the total ϵ', including the superfluid contribution, has been depicted. Both σ_1 and ϵ' have been determined at the center frequency, $\nu = 5$ cm^{-1}, using $\sigma_1 = \nu_{pn}^2\gamma(\nu(\nu^2 + \gamma^2))^{-1}$ and $\epsilon' = -\nu_{pn}^2(\nu^2 + \gamma^2)^{-1} - c^2(2\pi\nu\lambda)^{-2}$. To determine σ_1 we used the values for ν_{pn} and γ obtained from the fit following approach A. In the analysis for the normal state the transmission is determined by σ_1, i.e. ν_{pn}^2/γ in the case of a large scattering rate. In order to obtain an absolute value for γ we therefore needed to assume a value for ν_{pn}, which is expected to be temperature independent in the normal state. Using ν_{pn} = 8000cm^{-1}, we obtained the values for γ presented in the inset of fig. 6.15. Below T_c σ_1 exhibits a rapid increase for all films. For comparison, the conductivity for a BCS-superconductor with a T_c of 88 K is included as the solid line. The conductivity was normalized to the value of σ_1 for 20 nm $DyBa_2Cu_3O_{7-\delta}$ film at 88 K. This emphasizes the strikingly different behavior of the high T_c superconductor. Similar behavior has been observed before in $YBa_2Cu_3O_{7-\delta}$ [17, 18], and is taken to be evidence of a rapidly suppressed scattering rate γ below T_c. Since, within the model used, $\sigma_1 \sim \nu_{pn}^2/\gamma$, two competing effects determine its temperature dependence. Below T_c the density of normal carriers will be reduced thereby reducing the plasma frequency, ν_{pn}, while the scattering of quasiparticles will also be reduced when the temperature is lowered. Having two different temperature dependencies produces a maximum in the conductivity.

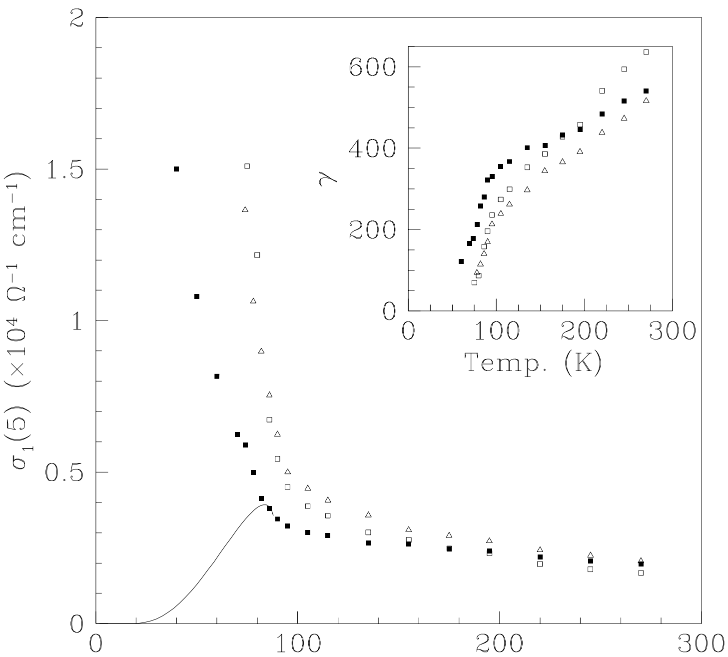

Figure 6.15: *Temperature dependence of σ_1 for three $DyBa_2Cu_3O_{7-\delta}$ films with different thicknesses (20 nm: solid squares, 34 nm: open triangles and 80 nm: open squares). The normalized conductivity for a BCS-superconductor having a T_c of 88 K is included as the solid line. The inset shows γ for all three films.*

This maximum also resembles, superficially, a BCS coherence peak but shows a different temperature and frequency behavior.

The total dielectric response, ϵ', is mainly determined by the superfluid contribution. For the 20 nm film ϵ' can not be determined accurately from 50 to 90 K, caused by the insensitivity of the transmission to ν_{ps} in this range. The solid curve in fig. 6.16 corresponds to an estimate of ϵ' based on the expression $\epsilon' = -2\sigma_1/\gamma$ which is valid for the Drude model.

Knowing the approximate values for the dielectric properties we return to our analysis in chapter 3, section 3.1.2 in order to show that the earlier claim that the sensitivity shifts from $\sigma_1(T)$ to $\lambda(T)$ in this temperature range was valid. Using equation (3.27) and the measured values for σ_1 and ϵ' we can calculate the critical thickness. The result can be seen in the inset in the fig. 6.16. Since the values used to calculate d_c are *intrinsic* material properties the curve looks similar when we use the dielectric properties obtained for the 34 and the 80 nm film. We can hence estimate at which temperature the critical thickness is approximately equal to the film thickness. These temperatures have been indicated in fig. 6.16 by three arrows, where the thinnest film is represented by the lowest temperature. Around these temperatures both approaches A and B are inefficient, resulting in a larger

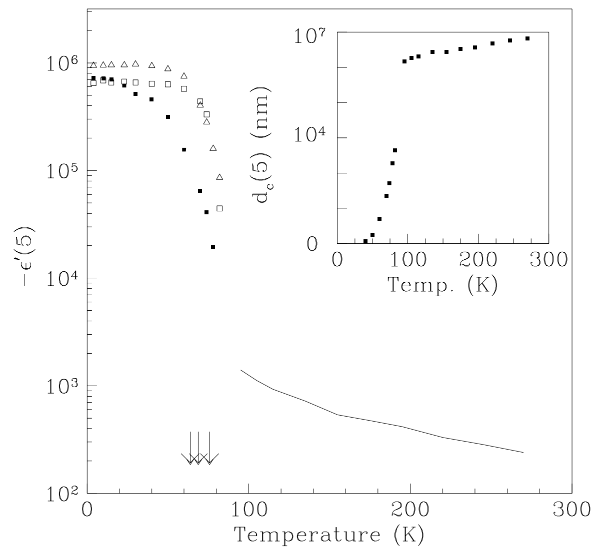

Figure 6.16: *Temperature dependence of ϵ' for three $DyBa_2Cu_3O_{7-\delta}$ films with different thicknesses (20 nm: solid squares, 34 nm: open triangles and 80 nm: open squares). The arrows indicate the temperatures where the critical thickness, d_c (inset), is approximately equal to the film thickness (20, 34 and 80 nm from left to right). The tentative line at higher temperatures shows the qualitative behavior calculated using the values for ω_{pn} and , obtained from σ_1. All quantities have been calculated at the center frequency, $\nu = 5\ cm^{-1}$.*

uncertainty in the obtained absolute values of both σ_1 and ϵ'.

Results for ρ_{dc} and λ(T)

More results of the fitting procedure are displayed in fig. 6.17 for all three films. The resistivity ρ is shown on the right hand side, while on the left hand side of fig. 6.17 the superfluid density $(\lambda(0)^2/\lambda(T)^2)$ is plotted. The results at low temperatures have been obtained using approach B. At higher temperatures ρ has been calculated by direct inversion of σ_1 obtained using approach A, assuming that σ_2 can be neglected. These results can be compared to the dc-resistivity depicted in fig. 6.18, which were obtained on samples prepared under identical conditions. The results show $\rho(300) = 650\,\mu\Omega$cm and $\rho(T_c) = 230\,\mu\Omega$cm, which is in good agreement with the mm-wave data in fig. 6.17. In the normal state the mm-wave data show a linear temperature dependence of the resistivity, similar to the dc-behavior. However, the slope tells us that there is a fairly large residual scattering. For instance for the 20 nm film the intercept at T = 0 K is about 225 $\mu\Omega$cm. Moreover, the slope is about twice as large as values measured for single crystals (1.05 $\mu\Omega$cm/K vs. 0.45 $\mu\Omega$cm/K), indicating that the difference cannot be explained by merely adding a temperature *in*dependent residual resistivity term.

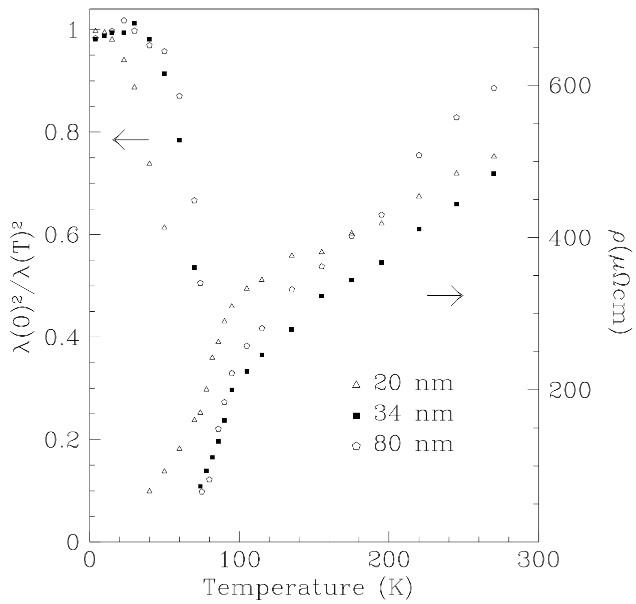

Figure 6.17: *Temperature dependence of the resistivity (right hand side) and the superfluid density $\lambda(0)^2/\lambda(T)^2$ (left hand side) for three $DyBa_2Cu_3O_{7-\delta}$ films with different thicknesses. (20 nm: solid squares, 34 nm: open triangles and 80 nm: open squares).*

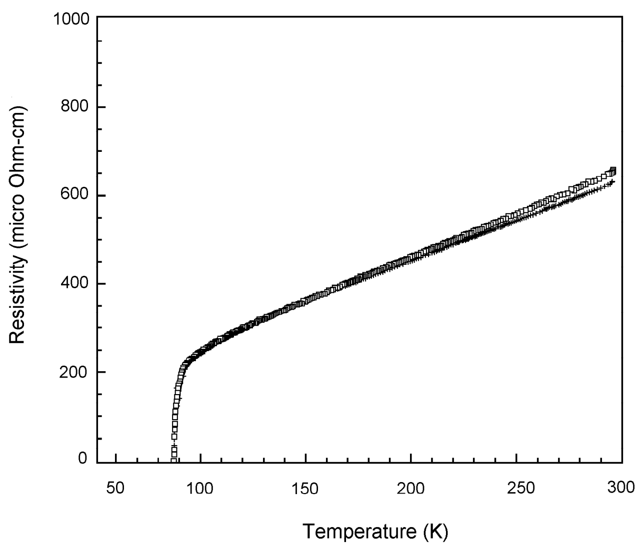

Figure 6.18: *dc-Resisitivity data taken on $YBa_2Cu_3O_{7-\delta}$ films prepared under identical conditions as the films used for the mm-wave transmission measurments.*

The absolute penetration depth of the 20 nm film is shown in fig. 6.19. as a function of T^2. The penetration depth shows a T^2-dependence at lower temperatures and a rather large

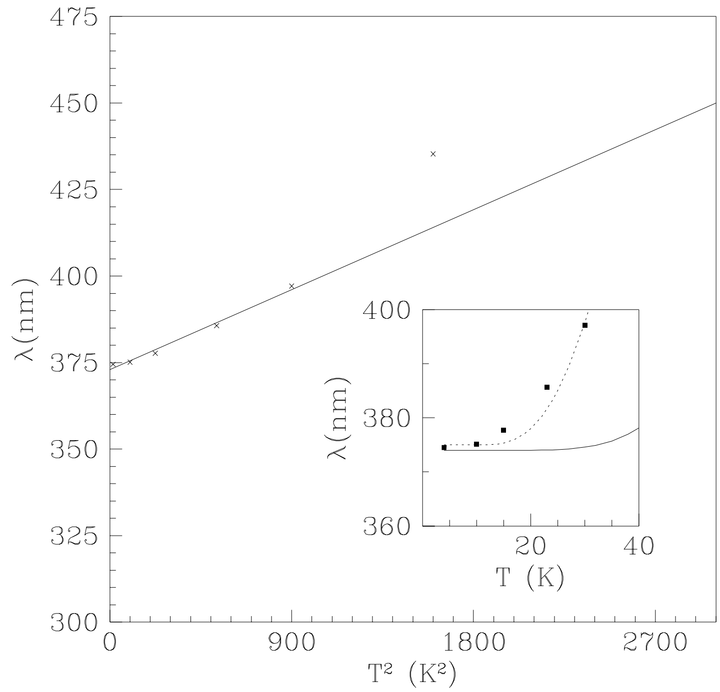

Figure 6.19: *The penetration depth for the 20 nm film vs. T^2. In the inset the penetration depth calculated using the BCS relations is shown along with the experimental data.*

λ_L of 370 nm. A strong objection to the interpretation of having a activated behavior can be seen in the inset, where the same results have been plotted together with a fit obtained a BCS-dependence [19].

$$1 - \left(\frac{\lambda(0)}{\lambda}\right)^2 = 2\pi \frac{e^{-\pi/\gamma t}}{\sqrt{2\gamma t}} \tag{6.2}$$

where $\pi/\gamma = \Delta/k_BT_c$ and $t = T/T_c$. We used several different values for the gap and obtained the "best" fit for $2\Delta/k_BT = 1.46$ (dashed line). The value for the BCS-ratio is rather small and disagrees with for instance tunneling and ARPES-data yielding values ranging from 4 to 7 [20, 21]. Also shown as the solid line is a fit using $2\Delta/k_BT_c = 2.76$, clearly demonstrating the inability to describe $\lambda(T)$ in this fashion. The factor 2.76 has been chosen in order to show the fashion in which the curvature changes when a larger gap ratio is chosen. An even more realistic choice, such as $2\Delta/k_BT_c = 3.74$ shows no temperature dependence in the plotted temperature range.

An interesting possibility might be that we are sensitive to the smallest of two gaps [22], however, at low temperatures the solution for the superconductor having an finite energy gap tends to become temperature independent, whereas the measured values for λ still show an appreciable temperature dependence. The other films show similar behavior with a slightly different zero temperature penetration depth (325 and 360 nm for the 34 and 80 nm films respectively).

Similar behavior, having a correlation between a large absolute penetration depth and the quadratic temperature dependence was observed before by de Vaulchier *et al.* [5] and was taken to be evidence for the extrinsic nature of the temperature dependence, due to the existence of weak links within the film. This provides a more likely explanation for the observed T^2-dependence, namely the d-wave scenario, where the power-law temperature dependence of λ is lifted to a higher order by the presence of additional scattering [23]. The slope of the quadratic curve (~ 0.025 $\mathring{A}/K^2$) is about the same as that reported for one of the films in ref. [5], although due to the extrinsic nature of the phenomenon there is no need for these values to be the same.

6.5 Conclusions

We used mm-wave transmission as a complimentary technique to characterize and study superconducting thin films on a fundamental level. From the MoGe and the NbN-data we see that we are able to resolve the intrinsic behavior and obtain absolute values for both the real and imaginary part of the dielectric function. In both cases we can deduce values for σ_1 ($17,300$ and $15,000$ $\Omega^{-1}\text{cm}^{-1}$) and λ_L (500 and 400 nm). The temperature dependencies follow the expected BCS-behavior for transmission as well as the superfluid density $\lambda^2(0)/\lambda^2(T)$.

We have studied the transmission through $DyBa_2Cu_3O_{7-\delta}$ films of different thickness (20, 34 and 80 nm). We observed an enhanced conductivity in going into the superconducting state, indicative of a large reduction in the scattering rate γ just below T_c. For the resistivity in the normal state, we find the linear behavior typical for the cuprates. From the intercept at T = 0 K we learn that there is an additional residual scattering in the film, probably due to the same oxygen deficiency that reduces T_c slightly. The London penetration depth is fairly large for all films (325 - 370 nm), and has a T^2 dependence, consistent with a d-wave symmetry picture plus an additional extrinsic scattering source. For the thinnest film (20 nm), the superfluid density has no influence on the transmission coefficient down to temperatures well below T_c. Therefore the temperature dependence of the transmission is completely determined by σ_1, even at temperatures down to 60 K. The thicker films show a more conventional behavior, where ϵ' indeed dominates the transmission in most of the superconducting range.

References

[1] W. N. Hardy, D. A. Bonn, D. C. Morgan, Ruixing Liang and Kuan Zhang, Phys. Rev. Lett. **70**, 3999 (1993).

[2] Steven M. Anlage, Dong-Ho Wu, J. Mao, S. N. Mao, X. X. Xi, T. Venkatesan, J. L. Peng and R. L. Greene, Phys. Rev. B **50**, 523 (1994).

[3] T. Jacobs, S. Shridhar, C. T. Rieck, K. Scharnberg, T. Wolf and J. Halbritter, J. Phys. Chem. Solids **56** (12), 1945 (1995).

[4] for a complete reference on resonant cavity techniques see: O. Klein, S. Donovan, M. Dressel, K. Holczer and G. Grüner *Microwave Cavity Perturbation Technique: Part I, II and III*, International Journal of infrared and Millimeter Waves, **14**, 2423-2517 (1993).

[5] L. A. de Vaulchier, J. P. Vieren, Y. Guldner, N. Bontemps, R. Combescot, Y. Lemaître and J. C. Mage, Europhys. Lett. **33** (2), 153 (1996).

[6] J. Bardeen, L. N. Cooper and J. R. Schrieffer, Phys. Rev. **108** (5), 1175 (1957).

[7] R. E. Glover III and M. Tinkham, Phys. Rev. **104**, 844 (1956).

[8] D. M. Ginsberg and M. Tinkham, Phys. Rev. **118**, 990 (1960).

[9] J. M. Graybeal and M. R. Beasley, Phys. Rev. B **29**, 4167 (1984).

[10] Ali Yazdani, W. R. White, M. R. Hahn, M. Gabay, M. R. Beasley and A. Kapitulnik, Phys. Rev. Lett. **70**, 505 (1993).

[11] W. R. White, A. Kapitulnik and M. R. Beasley, Phys. Rev. Lett. **66**, 2826 (1991).

[12] D. G. Steel, W. R. White and J. M. Graybeal, Phys. Rev. Lett. **71**, 161 (1993).

[13] J. M. Graybeal, J. Luo and W. R. White, Phys. Rev. B **49**, 12923 (1994).

[14] D. C. Mattis and J. Bardeen, Phys. Rev. **111**, 412 (1958).

[15] M. Tinkham, *Introduction to Superconductivity*, (McGraw-Hill, New York, 1975 and Krieger, New York, 1980).

[16] A. Shoji, S. Kiryu and S. Kohjiro, Appl. Phys. Lett. **60** (13), 1624 (1992)

[17] D. A. Bonn, P. Dosanjh, R. Liang and W. N. Hardy, Phys. Rev. Lett. **68**, 2390 (1992).

[18] Martin C. Nuss, P. M. Mankiewich, M. L. O'Malley, E. H. Westerwick and Peter B. Littlewood, Phys. Rev. Lett. **66**, 3305 (1991).

[19] B. Mühlslegel, Z. Phys. **155**, 313 (1959).

[20] Matthias C. Schabel, C.-H. Park, A. Matuura, Z. X. Shen, D. A. Bonn, Ruizing Liang and W. N. Hardy, Phys. Rev. B. **55**, 2796 (1997).

[21] for a review of tunneling experiments see for instance: Tetsuya Hasegawa, Hiroshi Ikuta and Koichi Kitazawa, Chapter 7 of *Physical Properties of High Temperature Superconductors, vol. III*, D. M. Ginsburg ed. (World Scientific, London, 1992), 525.

[22] N. Klein, N. Tellmann, H. Schulz, K. Urban, S. A. Wolf and V. Z. Kresin, Phys. Rev. Lett. **71**, 3355 (1993).

[23] P. J. Hirschfeld and N. Goldenfeld, Phys. Rev. B **48**, 4219 (1993).

Chapter 7

Nonequilibrium Superconductivity studied by Photo Induced Activation of Mm-Wave Absorption (PIAMA)

7.1 Introduction

For both the fundamental aspects and for applications, a proper understanding of the dynamical behavior of quasiparticles in the high T_c cuprates is essential. Fundamentally, the behavior of the quasiparticle scattering rate, τ, as a function of frequency and temperature yields important information on the interior of the HTSC's. In the normal state, the linear dependencies of $1/\tau$ on T and ω are indicative of a breakdown of the Landau Fermi liquid formulation applicable to normal metals [1]. The linear dc-resistivity, which extrapolates to $\rho = 0$ for $T = 0$, leads to the very surprising conclusion that phonon scattering is insignificant over a large range of several hundreds of Kelvins. Moreover, since the Fermi liquid theory is one of the basic ingredients of the BCS-theory, these experimental observations have posed an important question as to which approach one should use in attempting to explain the superconductivity in the cuprates [2].

In the superconducting state, the quasiparticle scattering rate also yields important information. Most importantly, a strong enhancement of τ has been observed just below T_c [3,4]. This observation provides additional evidence that the scattering has an electronic rather than a phononic origin. Much of the contemporary data on τ have been acquired indirectly, for instance by assuming that the two-fluid description is valid for these materials [5, 6]. A direct measurement of the decay processes is therefore desirable.

For applications, the presence of quasiparticles and their dynamics are of crucial importance, since a large number of low-energy excitations will inevitably lead to undesired losses. Furthermore, high T_c films are considered to have considerable potential as FIR-detectors [7]. In order to make optimal use of such detectors one needs to disentangle the bolometric and non-bolometric contributions, since the latter is thought to give rise to very fast response times [8].

In the seventies, similar motivations to distinguish the bolometric and non-bolometric contributions lead to a widespread interest in experiments exploring non-equilibrium superconductivity. Both experimentally and theoretically, people have been trying to answer questions such as the influence of the excess energy given to quasiparticles in the pair-breaking process [9,10] and the processes determining the quasiparticle lifetime [11–13]. A more detailed overview of the research concerning these topics has been given in section 2.3.

In all the above considerations the symmetry of the order parameter will be an essential ingredient. Not only will it have a large influence on the quasiparticle density, but it will also greatly affect their dynamics. Obviously, when the superconductor has an isotropic gap a certain minimum energy is needed to create quasiparticles. Therefore, at sufficiently low temperatures, the thermally excited quasiparticle density will be negligible. However, the presence of nodes opens up a channel in which quasiparticles can be created at infinitesimally small energies. As a result the quasiparticle density has a power law dependence on temperature, as opposed to the exponential dependence for the case of an s-wave gap. Moreover, one can imagine that having an anisotropic energy gap will modify the decay channels for excited quasiparticles, thereby altering their relaxation rate.

In this chapter we present a new method to study the quasiparticle dynamics: Photo Induced Activation of Mm-wave Absorption (PIAMA). With this technique we use two independent sources in a pump-probe configuration. The first creates a temporary excited state within the superconducting thin film, while the second monitors the time evolution of the state. A more detailed description of the experimental setup can be found in chapter 4. As the pump, we used the free electron laser, FELIX, located at the user facility of the FOM-institute "Rijnhuizen" in Nieuwegein, The Netherlands [14]. FELIX is tunable over a wide frequency range (100 - 2000 cm^{-1}), reaching energies comparable to the relevant energy scales in HTSC's, such as phonon energies and the superconducting energy gap. PIAMA resembles earlier photoconductivity [15,16] and pump-probe experiments [17,18], although there are some essential differences. First of all, the frequencies of the pump and probe differ by approximately two orders of magnitude, in contrast to most pump-probe experiments where they have the same frequency. Secondly, we measure the system response at ac-frequencies (5 cm^{-1}) instead of using the dc-response, as is done in photoconductivity experiments. This facilitates measurements in the superconducting state since the *ac*-resistivity of a superconductor is nonzero. Furthermore, the pump frequency is tunable and has a relatively low energy, within the FIR and MIR region, whereas in most other experiments a single frequency visible laser was used. This allows us to study PIAMA both as a function of frequency and temperature.

First we will present the scope of the experiment, explaining in detail what happens to a superconductor when it is illuminated by an FIR-pulse. In particular, the relevant time scales and decay processes will be treated, with attention to the question of the symmetry of the order parameter. In the next section, results on a conventional superconductor, NbN, will be presented, while in section 7.4 the results of the PIAMA experiments on one of the cuprates, $DyBa_2Cu_3O_{7-\delta}$, will be discussed. In both cases attention will be paid to disentangling equilibrium and non-equilibrium contributions. Furthermore, in section

7.4 the correlation between the quasiparticle dynamics and the pairing symmetry will be discussed, demonstrating the drastic consequences of a d-wave symmetry on the recombination process.

7.2 Scope of the Experiment

What Happens during an FIR-pulse?

First we need to visualize what will happen to a superconductor when it is subjected to a pulse of far-infrared radiation. The FIR-radiation will change the initial state of the superconductor by changing the balance between the number of Cooper pairs, n_{CP}, and the number of quasiparticles, n_{qp}. In fig. 7.1 we have sketched the effective electron temperature, T*, and the quasiparticle density, n_{qp}. Indicated are several processes which are occurring, each having their own specific time scales:

A - build up

B - cascade

C - thermalization

D - recombination

E - bolometric response

During the FIR-pulse, the build up (A) of a temporary excited state occurs, having a response time of about 1 ps. During this process, both the electron temperature and the number of quasiparticles are enhanced. After the termination of the pulse, indicated by the first vertical dashed line in fig. 7.1, a cascading process (B) reduces the average energy of the electrons, thereby lowering T*. During the cascade, quasiparticles having sufficient kinetic energy, break up additional Cooper pairs. Therefore, even though T* decreases, n_{qp} increases even further. The time constant associated with the cascading process has been estimated to be approximately 1 ps or even faster [17]. On a longer time scale of about 1 ns [15] thermalization (C) via scattering processes lowers T* even further, while now the quasiparticle density remains constant. In order to reduce also n_{qp} to its initial value, quasiparticles will have to recombine to form Cooper pairs (D). The time scale involved in the recombination process is rather difficult to disentangle from other processes and will be discussed in detail for the case of $DyBa_2Cu_3O_{7-\delta}$ at the end of this chapter.

In addition to the electronic processes mentioned above, a simple heating of the sample can also be present (E). This bolometric effect will have a slow relaxation time within the μs to ms-range, which is closely connected to the experimental configuration, since the additional thermal energy of the sample has to be carried away via its environment.

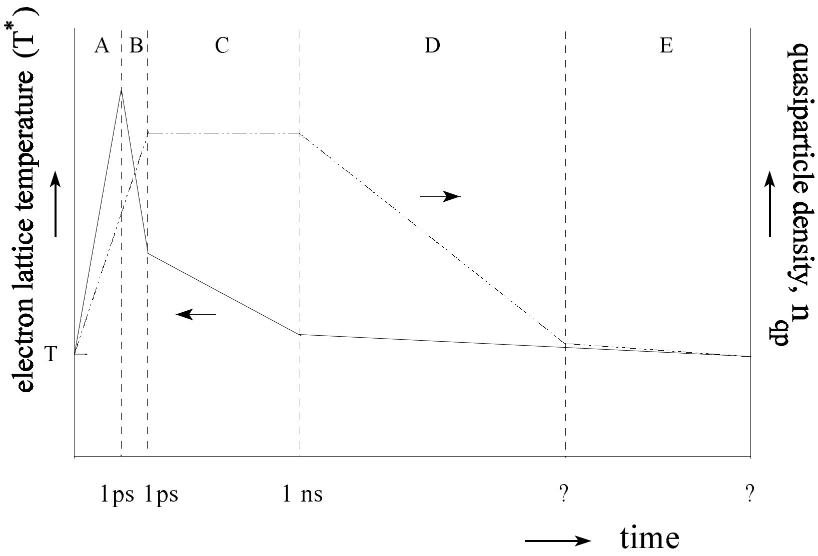

Figure 7.1: *Schematic representation of the effective electron temperature T^* (solid line), and the number of quasiparticles in a superconductor, n_{qp} (dash-dotted line), during and after being illuminated with an FIR-pulse.*

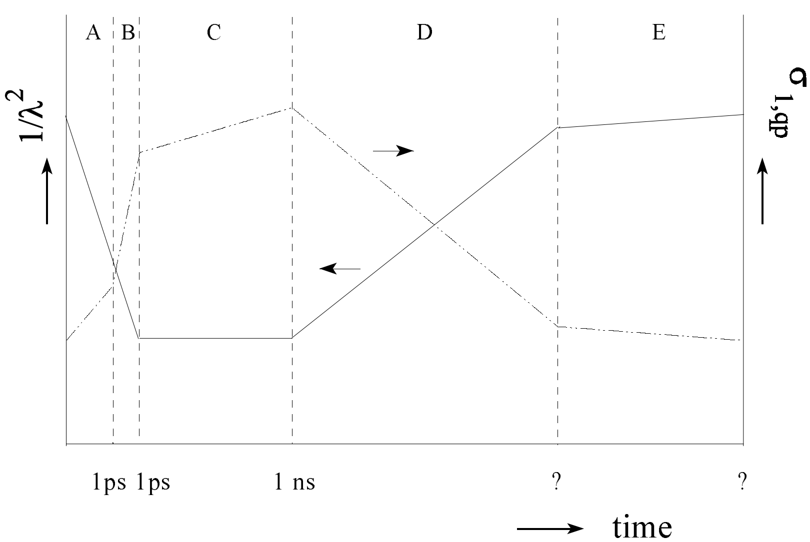

Figure 7.2: *Schematic representation of the optical response functions $1/\lambda^2$ (solid line) and $\sigma_{1,qp}$ (dash-dotted line) of a superconductor, during and after being illuminated with an FIR pulse.*

Optical Response Functions

The changes in quasiparticle and Cooper pair densities are reflected in the *complex* optical conductivity, which is, in the low temperature limit, given by:

$$\begin{aligned}\sigma_1 &= \frac{e^2 \tau_{qp}}{m_{qp}} * n_{qp} \\ \sigma_2 &= \frac{e^2}{\pi \nu m_e} * n_{CP} = \frac{c^2}{8\pi^2 \nu \lambda^2}\end{aligned} \tag{7.1}$$

which is the physical quantity that determines the mm-wave transmission coefficient, Tr.

$$Tr = \frac{4p^2}{(1+p^2)^2 + (1+p^2)[\frac{4\pi d\sigma_1}{c}]^2 + (1+p^2)\frac{8\pi d\sigma_1}{c} + \frac{d^2c^2}{\lambda^4\omega^2}} \tag{7.2}$$

where p is the complex refractive index of the substrate. We use the approximate transmission coefficient for the case of a minimum in the interference pattern of the bare substrate. From fig. 6.11 on page 105, it can be seen that for the 20 nm thick $DyBa_2Cu_3O_{7-\delta}$ film used during the PIAMA experiments, this is approximately valid at the probe frequency, 150 GHz. The time dependence of both σ_1 and $1/\lambda^2$ has been depicted in fig. 7.2. Since $1/\lambda^2 \sim n_{CP}$ and $2n_{CP} = n_{el,tot} - n_{qp}$, the changes in $1/\lambda^2$ during the subsequent processes A-E are simply opposite to the changes in n_{qp}, indicated in fig. 7.1.

However, as can be seen in equation (7.1), the change in the real part of the conductivity due to the quasiparticles, $\Delta\sigma_{1,qp}$, not only depends on the density, but also on the scattering rate, $\gamma_{qp} = 1/\tau_{qp}$. As mentioned above, the thermalization process connected to the modifications in the quasiparticle scattering rate, apart from the bolometric contribution, occur on a time scale of approximately 1 ns. This indicates that while $\Delta\sigma_{1,qp}$ is due to a combined effect of n_{qp} and τ_{qp} on this time scale, in our case, having a temporal resolution of about 1 μs, we will merely be sensitive to changes in σ_1 due to an altered n_{qp}.

Equilibrium vs. Non-equilibrium

We can divide the response of the optical conductivity to the presence of a short FIR-pulse into two specific cases:

- Equilibrium or bolometric
- Non-equilibrium or non-bolometric

The real part of the optical conductivity, σ_1 is plotted schematically in fig. 7.3 for both cases, where the left panel represents the initial state and the right panel represents the temporary state caused by the pulse. The pertinent parameters are given in table 7.1. In all panels n_{qp} is represented by a Drude contribution having a width equal to γ_{qp}, while n_{CP} is represented by a δ-function, indicated here as the arrow at zero frequency. The strength of the δ-function is equivalent to the Cooper pair density, and therefore also

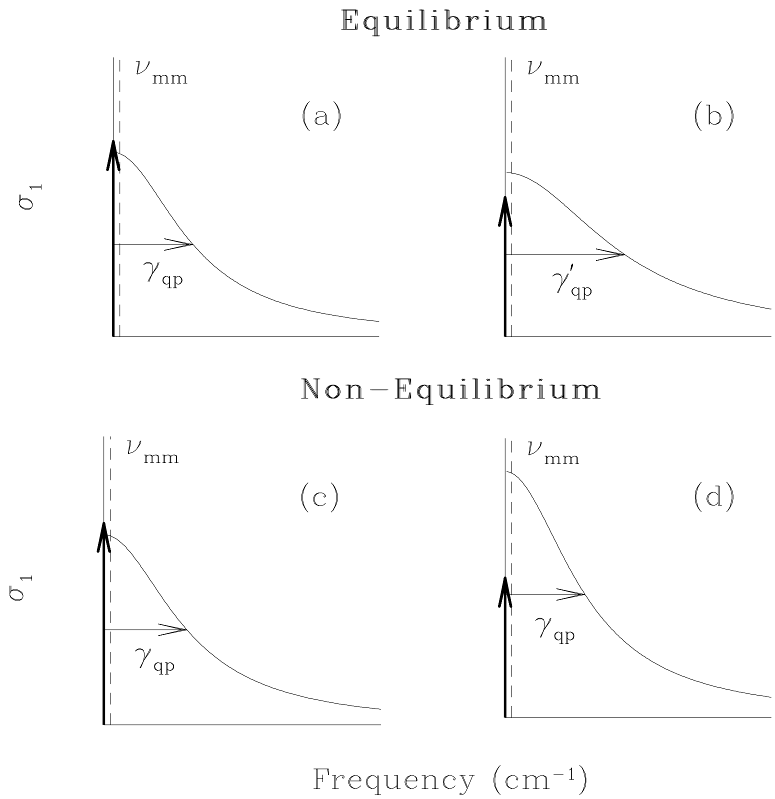

Figure 7.3: *Upper panels: change in optical conductivity, assuming an equilibrium response. a: initial state, b: superconductor at an elevated temperature. Lower panels: change in σ_1 in the non-equilibrium case. c: initial state, d: superconductor having a shifted chemical potential at the same temperature as the initial state.*

directly related to the magnitude of the dispersive part of the conductivity, σ_2, as was shown in eq. (7.1).

In the upper panel of fig. 7.3 we indicate what we choose to call the equilibrium process. In this scenario the absorbed radiation will temporarily raise the temperature of the entire sample, while the quasiparticle chemical potential, μ_{qp} remains in equilibrium with its environment. At the elevated temperature the number of Cooper pairs will be reduced and hence the penetration depth λ will be enhanced. Looking at the transmission given by eq. (7.2) we see that as a result, the last term in the denominator will be smaller and hence the transmission will increase. At the same time, the spectral weight removed from the superfluid δ-function will be transferred into the quasiparticle peak, thereby enhancing σ_1 and thus *reducing* the transmission coefficient. In addition to the transfer of spectral weight, the scattering rate γ_{qp} will also be enhanced, since the sample is now at an elevated temperature. This in turn tends to reduce σ_1 and thus enhance the transmissivity. The result will be a competition of all three phenomena mentioned above. In order to get

panel	ω_{pn} (cm^{-1})	γ_{qp} (cm^{-1})	ω_{ps} (cm^{-1})
a	7700	300	6400
b	8900	450	4600
c	7700	300	6400
d	8900	300	4600

Table 7.1: *Parameters used for the calculation of the real part of the conductivity, σ_1, presented in fig. 7.3.*

an idea of what might happen in this equilibrium case, it is very instructive to monitor the temperature dependence of the *unperturbed* transmission coefficient, since the process described above is not different from having a superconductor at a temporary elevated temperature. The results presented in chapter 6 show that at all frequencies the temperature dependence is monotonic. Therefore the equilibrium response will always show an enhanced transmissivity due to the presence of an FIR-pulse.

In the lower two panels we consider what we call the non-equilibrium response. In contrast to the equilibrium response, it is envisaged that the quasiparticle density is increased, while the actual sample temperature remains the same. Therefore, in this case the sample temperature is in equilibrium with its environment, while the quasiparticle chemical potential, μ_{qp}, is shifted. Just as in the equilibrium situation there are two competing contributions determining the value of the mm-wave transmissivity: on the one hand λ will be larger, or equivalently the screening of the superfluid will be reduced, enhancing the transmissivity. On the other hand the increased quasiparticle density will give rise to a larger σ_1, or equivalently a larger absorption, thereby *reducing* the transmission. Moreover, in contrast to the equilibrium response, the scattering rate γ_{qp} will be identical to the scattering rate in the initial state up to first order, justifying the conclusion that the enhanced absorption due to σ_1 will tend to reduce the mm-wave transmission. The resulting response will depend on the relative significance of both superfluid and quasiparticle contribution. A more quantitative analysis will be given in section 7.4.

Relaxation Processes and Relaxation Times

In order to obtain a better understanding of the time scales involved, it is essential to imagine the nature of the processes involved in quasiparticle relaxation. The main scattering processes in conjunction with the recombination process have been represented in fig. 7.4 by their corresponding Feynman diagrams. As was shown in fig. 7.1, the thermalization process (B+C) occurs within approximately 1 ns. This involves all of the scattering processes given in fig. 7.1, including both *elastic* and *inelastic* scattering.

Relaxation times obtained in earlier experiments, both equilibrium and non-equilibrium-like, span a rather large time domain. From microwave cavity perturbation experiments, Bonn and co-workers [5] estimated the scattering time to be around 10^{-12} to 10^{-13} s,

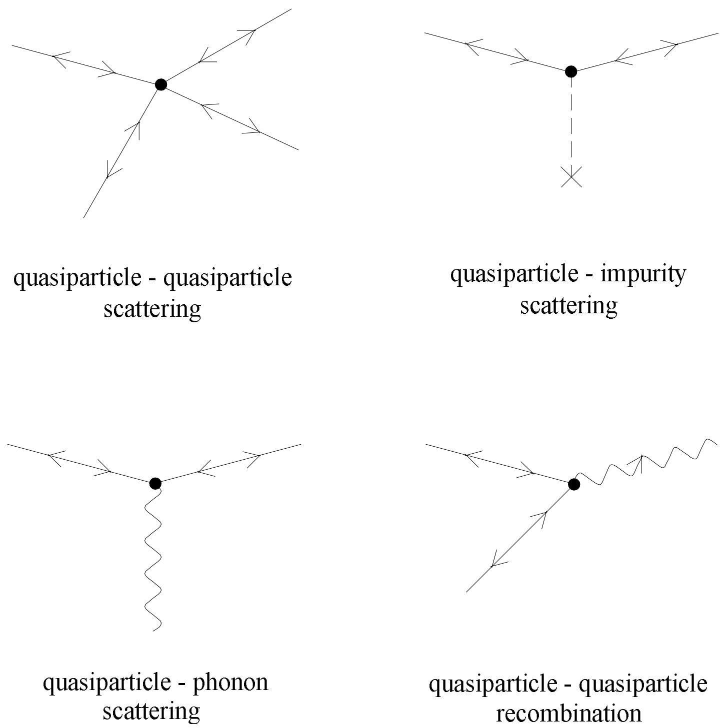

Figure 7.4: *Main scattering processes taking care of the thermalization of the excess quasiparticles depicted by their corresponding Feynman diagram. Also indicated is the recombination process.*

where they used the two-fluid model to obtain the absolute magnitude. In addition, data obtained by FIR-spectroscopy and dc-resistivity [19, 20], and results presented in chapter 6 of this thesis yield comparable scattering times. In all of these experiments however, one measures a combination of all relaxation processes, including elastic and inelastic scattering and the recombination process. In contrast, Doettinger *et al.* reported the scattering time to be strongly temperature dependent and rather long, up to a value of 10^{-8} s at 40 K [21]. In this experiment, they measured the critical vortex velocity which is predicted to be inversely proportional to the inelastic scattering time by Larkin and Ovchinnikov [22]. The physical reason for the close correlation is that inelastic scattering tends to move the quasiparticles within the vortex back to their equilibrium distribution, and therefore a vortex can reach a higher velocity before going through a transition. Since *elastic* scattering makes no contribution to the relaxation, one expects to measure a longer scattering time. This argument may explain the apparent discrepancy between their results and the microwave data. This also implies that it is natural to expect the pure recombination term to be on an even longer time scale than the one measured in the experiment of Doettinger *et al.*, since in this case neither elastic nor inelastic processes contribute.

In the PIAMA experiments the time resolution is around or slightly better than 1 μs. However, cascading and thermalization processes occur on a much faster time scale. Combining the information given above with the picture described in fig. 7.3, we can conclude that PIAMA is mainly sensitive to the *number* of quasiparticles. Therefore, since scattering merely changes the energy and not the density of quasiparticles, we measure only the recombination contribution.

Quasiparticle Relaxation in a d-wave Superconductor

A large variety of pump-probe and photoconductivity experiments have been performed in an attempt to determine the quasiparticle relaxation time [15–18, 23–27]. In all cases known to us, a high energy laser (> 1eV) has been utilized to create the excited state. Most workers found two contributions to the response, one having a fast and one having a relatively slow relaxation time. The fast contribution ranges from a few ps [17, 27] to several hundreds of ps [15, 24] and is usually attributed to non-equilibrium or non-bolometric effects.

This term covers many different phenomena such as a hot electron effect [27,28] and a rapid change of the kinetic inductance [15,23]. In our case the temporal resolution ($\sim 1\mu$s) is insufficient to measure such responses. The second, slower response ranges from several ns [16] up to values in the μs-regime [24, 26, 29] and is usually attributed to bolometric effects. However, alternative explanations have also been given for the long-lived component such as photoinduced localized states [26] or the photofluxonic effect [30]. In the latter case a vortex-antivortex pair is created using a photon.

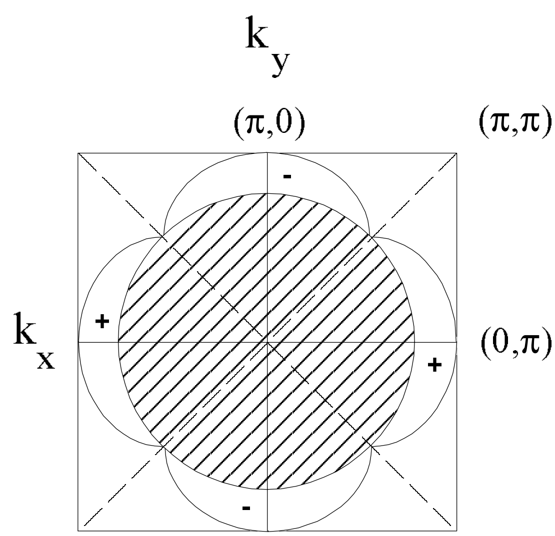

Figure 7.5: *Representation of an energy gap having a $d_{x^2-y^2}$ symmetry, showing the nodes at ($\pm\pi/2$, $\pm\pi/2$).*

It is essential to realize that in contrast to all the above presented photoconductivity and pump-probe experiments, in our case the "pump" energy is relatively low, within the FIR-range. The reason why this is important can be understood pictorially using fig. 7.5, where the d-wave gap has been drawn in k-space. The functional form of a d-wave gap symmetry can be described by

$$\Delta(\mathbf{k}) \;=\; \Delta_{max}[\cos(k_x\,a) \;-\; \cos(k_y\,a)] \tag{7.3}$$

where Δ_{max} is the maximum gap, which is estimated experimentally to be around 200-250 cm^{-1} [31]. This means that the phonon energy provided by FELIX is comparable to or even smaller than $2\Delta_{max}$, thereby putting the quasiparticles into preferred excited states. The time constant of thermalization has been estimated to be around 1 ns [15], and hence it is natural to assume that the quasiparticles will thermalize before they recombine, i.e. decay towards the nodes, according to the Fermi-Dirac distribution:

$$f_k(E, T, n) \;=\; \frac{1}{1 + e^{[E-\mu_{qp}]/k_B T}} \tag{7.4}$$

where E is the quasiparticle energy, μ_{qp} is the quasiparticle chemical potential and T is their equilibrium temperature. However, in the case of a d-wave symmetry, this implies that the quasiparticles end up in a well defined state having a momentum k close to $(\pm\pi/2, \pm\pi/2)$. This has been demonstrated more clearly in fig. 7.6, where the quasiparticle dispersion has been depicted for cuts along two different directions in k-space. The left panels show the

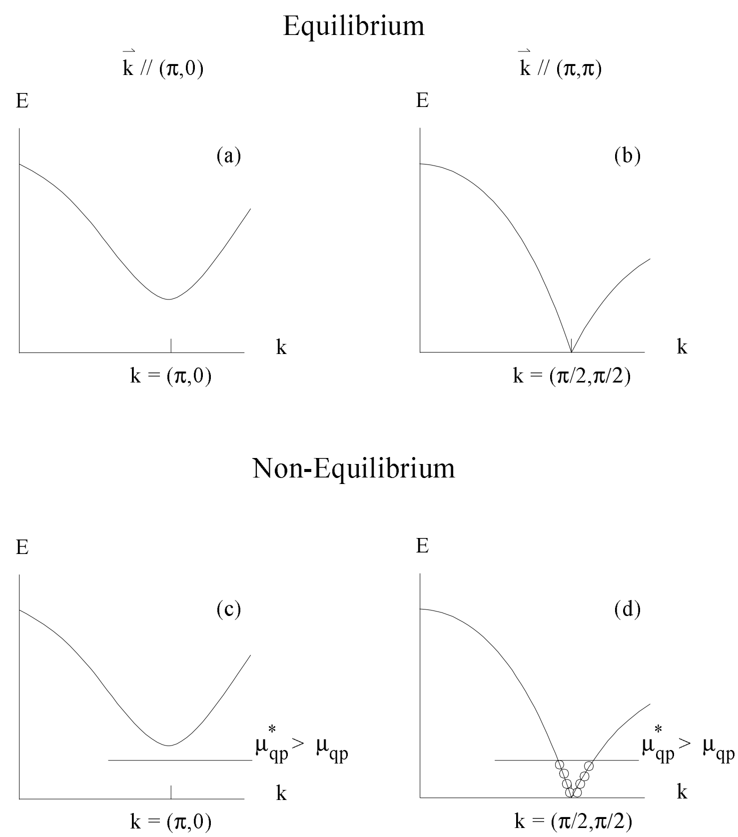

Figure 7.6: *Quasiparticle dispersion, showing the influence of the modified quasiparticle chemical potential μ^*_{qp}. The upper panels show the equilibrium response, whereas the lower panels depict the non-equilibrium case. In both cases the left panel is a cut taken along the $(\pi, 0)$ direction, while the right panel is a cut taken along the (π, π) direction.*

cut taken along the $(\pi$,0) direction, reaching the largest value for the gap, Δ_{max}. The right panels show the cut taken along the (π, π) direction, i.e. in the direction of the nodes. As before we can make a distinction between the two possible cases, the equilibrium response (upper two panels) and the non-equilibrium response (lower two panels). In the upper case the quasiparticle chemical potential is in equilibrium with its environment, and hence the Cooper pair and quasiparticle distribution functions attain their usual values, as if the sample resides at an elevated temperature. In contrast, in the lower panel the system temperature is in equilibrium, while μ_{qp} has been shifted. This clearly demonstrates that in the non-equilibrium case the probability for quasiparticles to be situated in the proximity of the nodes is much higher than the probability for other positions in k-space.

Realizing furthermore that in order to recombine, two quasiparticles have to fulfill kinematic quantum restrictions in order to conserve both energy and momentum, it is reasonable to expect that for carriers residing near the nodes, recombination is exceedingly difficult. This implies that in case of a d-wave symmetry the recombination time can be enhanced by orders of magnitude. A more quantitative analysis together with the precise formulation of the kinetic equations will be given in section 7.4.

7.3 NbN

In order to test the new technique of Photo Induced Activation of Mm-wave Absorption (PIAMA), we began by measuring a conventional superconductor. We used a NbN film with a thickness of 55 nm deposited on a 490 μm thick MgO substrate. The same film was studied in chapter 6 using mm-wave transmission measurements.

During all measurements a spurious oscillation, something in addition to the FIR induced changes, was observed. This oscillation was caused by cross talk between the laser electronics and our system, as could be checked by blocking the FELIX-beam with the free electron laser on. The oscillation was very reproducible and therefore we were able to eliminate its contribution by measuring with and without the FIR-radiation present on the sample. An example of two typical data sets, and the corrected transient is shown in fig. 7.7. The curves have been given an arbitrary vertical offset for the sake of clarity. We clearly see the oscillation in the data both with and without FELIX incident on the sample. After subtracting the reference signal, the photo induced change in transmission (PIT-signal) shows a smooth decay. The same correction procedure has been performed on all data presented below. In addition to the oscillation, all the data presented here have been corrected for the transfer function of the differentiating circuit connected to the diode detector, having a time constant of 45 μs. This was done by convoluting the measured responses with the exponential response function of the measurement circuit.

In fig. 7.8 we show the photo induced transmission (PIT-signal) for the NbN film measured at five different temperatures (4, 10, 12, 16 and 18 K from top to bottom). The pump frequency is 666 cm^{-1}, while the probe frequency is 150 GHz (5 cm^{-1}). The macropulse power was 16.0 mJ/pulse. The curves have been given an arbitrary vertical offset. Using the absolute unperturbed transmission in combination with the absolute value of the diode output, we can estimate the *change* in transmission coefficient from the measured voltages. We observe a positive change in the transmission coefficient due to the

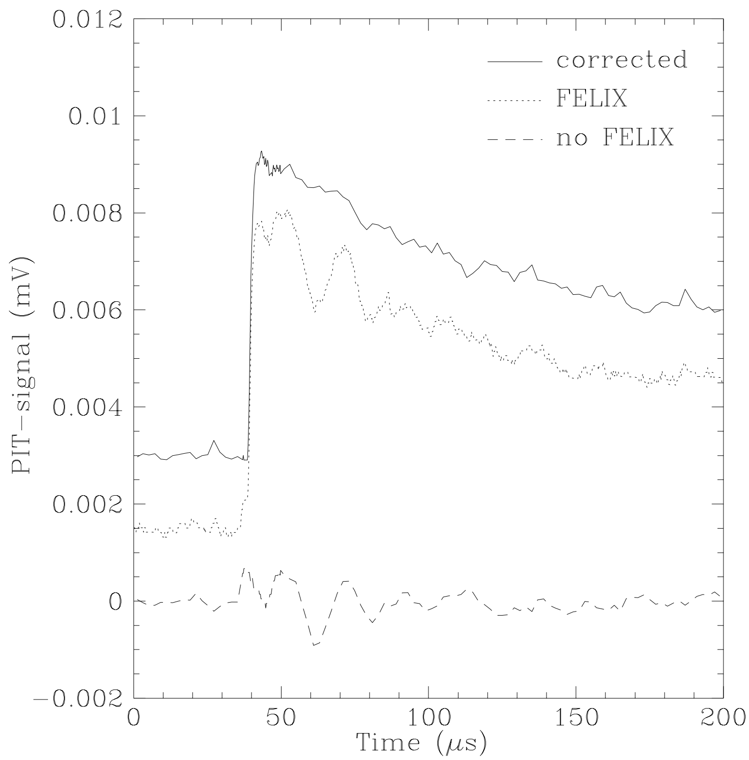

Figure 7.7: *Photo induced transmission shown both before (dotted line) and after (solid line) correcting for the spurious oscillation present in the transient. Also shown is the reference curve measured without the FELIX-beam incident on the sample (dashed line). The curves have been given an arbitrary vertical offset.*

presence of the FIR-radiation at all temperatures, up to T_c (17 K). This by itself is not sufficient information to conclude whether the response is bolometric or non-bolometric. However, we will argue below that, combining all the available information, we can conclude that in this case the superconductor remains in an equilibrium state, and the photo induced changes are due to a bolometric effect.

Evidence for the Bolometric Nature of the Response

When the signals are plotted on a logarithmic scale, as is done in the inset for the 4 and 16 K data, we see that the transmission decays exponentially, having a very slow relaxation time of the order of 100-200 μs. The exponential behavior and the long time constants are characteristic of a bolometric response, and are indicative of the photo induced transmission being due to an effective heating of the sample by the FIR-pulse. Upon lowering the temperature, two competing effects determine the thermal time constant of the system, since both the heat capacity and the thermal conductivity will be reduced. In fig. 7.9

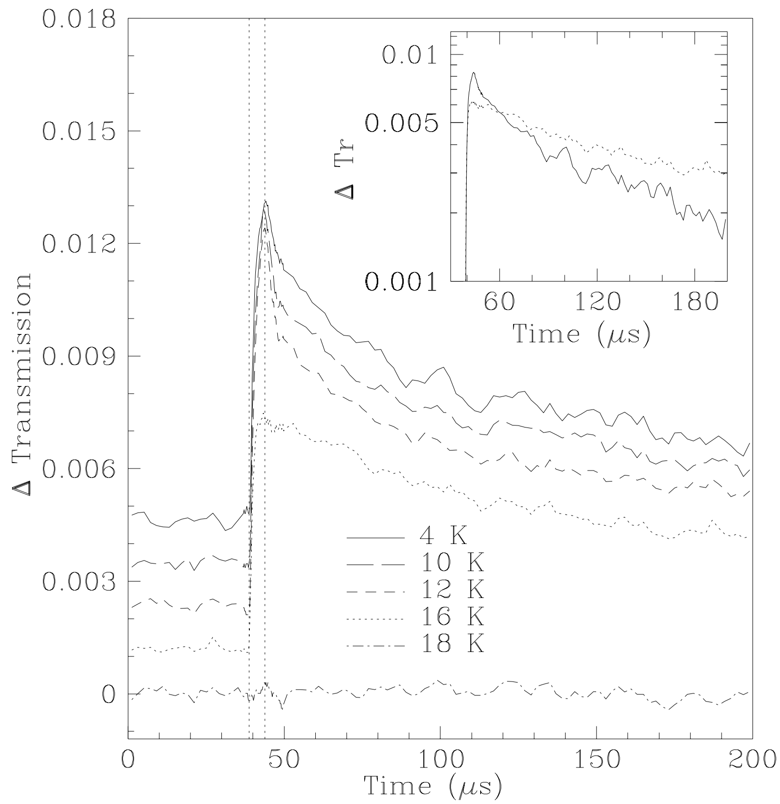

Figure 7.8: *Photo induced transmission for NbN on MgO at 4 K (solid), 10 K (dashed), 12 K (short dash), 16 K (dotted) and 18 K (dash-dotted). The curves have been given an arbitrary vertical offset. Inset: Δ Transmission plotted on a logarithmic scale at 4 and 16 K.*

the relaxation time is plotted as a function of temperature, again at a pump frequency of 666 cm^{-1} and a mm-wave frequency of 150 GHz. From the fact that the decay time is considerably faster at lower temperatures we conclude that in this particular case the heat capacity is reduced more severely.

In the upper panel of fig. 7.10 the maximum change in transmission, ΔTr, has been plotted as a function of temperature for the same frequencies as used above. In the lower panel, on the same temperature scale, the *unperturbed* transmission at 140 GHz through the same NbN film has been depicted. As was explained in chapter 6, the transmission at 150 GHz will be quantitatively slightly different due to interference effects, but the qualitative behavior, essential for the argument below, will be same.

Using the temperature dependence of the specific heat and the absorbed power, we can estimate the induced temperature rise, ΔT. We assume that the temperature rise will be homogeneous within the entire sample, hence ΔT can be calculated by $P/((C_p + C_e)V_f + C_sV_s)$. The specific heat of the MgO substrate, C_s, has been obtained by extrapolating

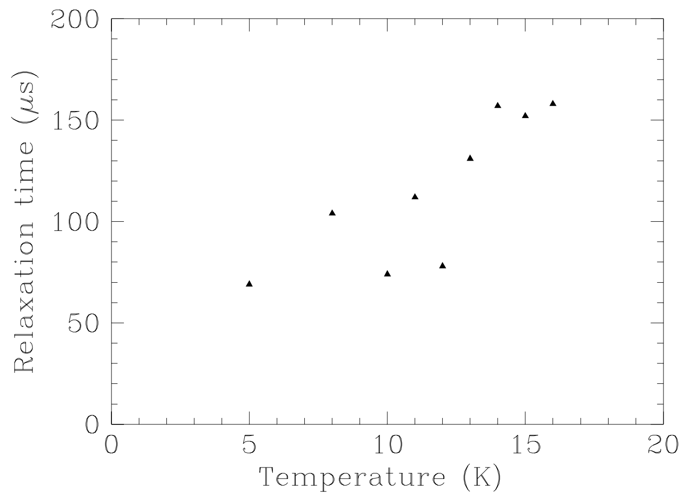

Figure 7.9: *Relaxation time of the photo induced transmission as a function of temperature, at $\nu_{fir} = 666\,cm^{-1}$ and $\nu_{mm} = 150\,GHz$.*

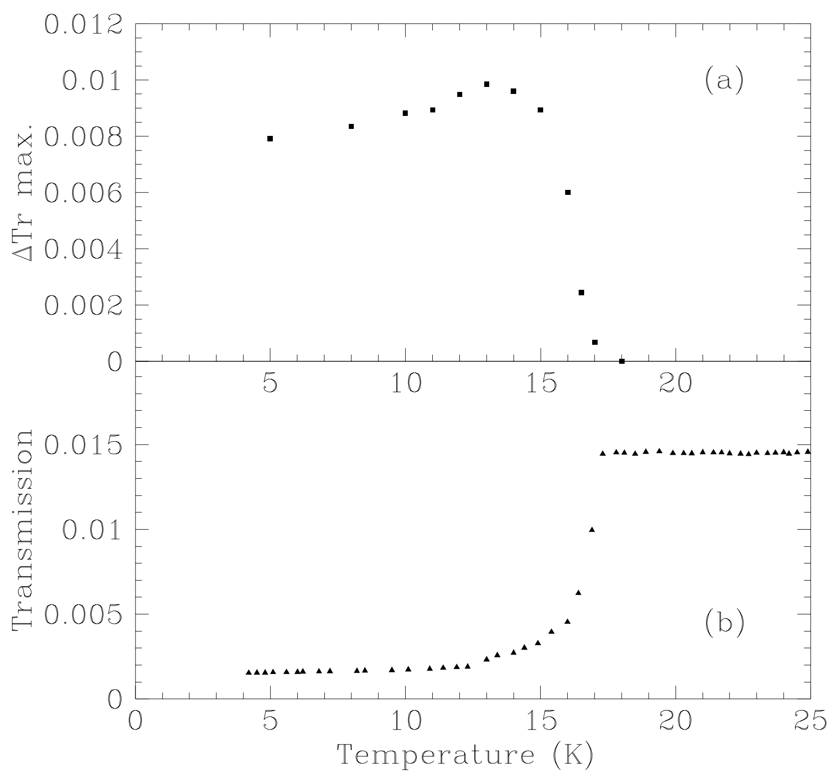

Figure 7.10: *a: Temperature dependence of the peak amplitude of the photo induced transmission at $\nu_{\mathrm{fir}} = 666\,\mathrm{cm}^{-1}$ and $\nu_{\mathrm{mm}} = 150\,\mathrm{GHz}$. b: Temperature dependence of the unperturbed transmission at $\nu_{\mathrm{mm}} = 140\,\mathrm{GHz}$.*

experimental data from ref. [32] to low temperatures. Since there are no experimental data of the phonon specific heat for NbN known to us, this quantity has been calculated using the Debye temperature ($\Theta_D \sim 250K$) [33]. This yields $C_p = (12\pi^4/5)nk_B(T/\Theta_D)^3 = 5.0 \times 10^{-3}\,\mathrm{Jcm^{-3}K^{-1}}$ where we used $n = 4.8 \times 10^{22}$ cm^{-3}, the atom density of NbN. The electronic specific heat is 1.5×10^{-3} Jcm^{-3}K^{-1}, where both values were calculated at 8 K. In order to calculate the temperature dependence we used a T^3 dependence for C$_p$ and e$^{-\Delta/kT}$ for C$_e$. We estimate the actual power absorbed within the sample to be $0.7\times0.7\times0.35\times0.5\times16\times10^{-3} = 1.37\times10^{-3}J$. In this case 0.7 is the transmissivity of one KRS-5 window, 0.35 is the absorptivity of the sample, 0.5 is the loss due to the nonzero angle of incidence, elongating the spot at the sample position, and 16 mJ is the power of a single macropulse, measured just before the cryostat. This yields ΔT of approximately 9.4 K starting at 4 K, while ΔT is gradually reduced to approximately 3 K at 15 K. In table 7.2 we compare the calculated temperature changes with the measured ones, while also the specific heat values are given for both substrate and film. Furthermore, the volume of the film was 55×10^{-7} cm^3 and the substrate contained 7.5×10^{-3} moles of $LaAlO_3$. The comparison demonstrates the fair agreement supporting the bolometric nature of the changes. The measured changes have been determined by combining the maximum change in the PIT-signal and the unperturbed transmission. The agreement is quite good, even

T (K)	ΔT_{th} (K)	ΔT_{exp} (K)	C$_{film}$ (mJ/cm^3 K)	C$_s$ (mJ/mole K)
4	9.4	12.5	1.2	4.9
8	6.8	8.8	6.5	13.1
10	5.4	6.9	17.1	21.8
11	4.8	5.9	26.3	26.6
12	4.3	4.9	38.5	31.8
13	3.8	> 4	54.0	38.6
14	3.4	> 3	73.0	45.6
15	2.9	> 2	97.7	53.2
16	2.6	> 1	121.9	62.1

Table 7.2: *Comparison of the theoretical and experimental temperature changes for NbN.*

though the model to estimate ΔT is rather crude. The remaining discrepancy is most probably caused by these simple assumptions. The strongly temperature dependent specific heat therefore provides a natural explanation for the fact that the peak amplitude is reduced less severely at low temperatures than one would expect if ΔT were assumed to be equal at 5 and 15 K.

This scenario explains furthermore the apparent correlation between the induced signal and the superconducting state. Since the temperature dependence of the transmissivity is rather small in the normal state due to the nearly constant conductivity, the PIT-signal vanishes above T$_c$. The PIT-signal is therefore not directly related to the presence of the superconducting condensate, but to the *rate* at which the transmission changes.

Similar results as presented above were obtained at other pump frequencies. This is to be expected since the superconducting energy gap (2Δ) for NbN is approximately 50 cm^{-1}. Hence the frequency of FELIX is much larger than 2Δ. This inhibits a spectroscopic study of the energy gap in this material using FELIX.

7.4 $DyBa_2Cu_3O_{7-\delta}$

7.4.1 Results

In contrast to conventional superconductors, for high temperature superconductors the energy gap (or the maximum energy gap, Δ_{max}, in case of a d-wave superconductor) is of the order of several hundreds of wavenumbers, as are other relevant energy scales, such as phonon frequencies. This energy coincides nicely with the energy scale that can be covered using FELIX, allowing us to study the quasiparticle dynamics both as a function of frequency and temperature.

Temperature Dependence

In fig. 7.11 the unperturbed mm-wave transmission through a $DyBa_2Cu_3O_{7-\delta}$ film of 20 nm thickness, deposited on a 520 μm thick $LaAlO_3$ substrate is depicted for two frequencies, 120 and 150 GHz. The transmission at these frequencies is rather different, mainly due to interference effects within the film-substrate system. This has been explained in more detail in chapter 6. For the analysis below, the most significant property of the transmission coefficient is its *monotonic* temperature dependence over the entire range, at *all* frequencies. Focusing the attention on the 150 GHz curve, since we used this frequency in all PIAMA experiments, we see a nearly temperature independent transmission at higher temperatures, showing no evident drop at T_c ($\sim$ 88 K). Only at lower temperatures the transmission is reduced more strongly, due to the enhanced significance of the superfluid fraction (see chapter 6).

In fig. 7.12 the photo induced transmission (PIT-signal, i.e. ΔTr) of the same film is shown for temperatures ranging from 5 to 70 K. The pump frequency is 800 cm^{-1}, while the probe frequency is 150 GHz. The curves have been corrected for long term instabilities in the incident power. The exact correction procedure will be explained in detail later in this section. We see that for temperatures lower than 40 K, the FIR-radiation *enhances* the transmissivity of the thin film. However, around 40 K the situation changes and the FIR pulse starts to *reduce* transmission instead. Moreover, exactly at 40 K the enhancement and the reduction of the PIT-signal are present simultaneously. Having the additional knowledge of the ordinary, *monotonic* behavior seen in the temperature dependence of the unperturbed mm-wave transmission we reason that a simple heating of the sample can never account for such a crossover. Furthermore, we see that the photo induced signal persists at 65 K, although it has a reduced amplitude. At this temperature however, the unperturbed transmission is already nearly temperature independent. This provides

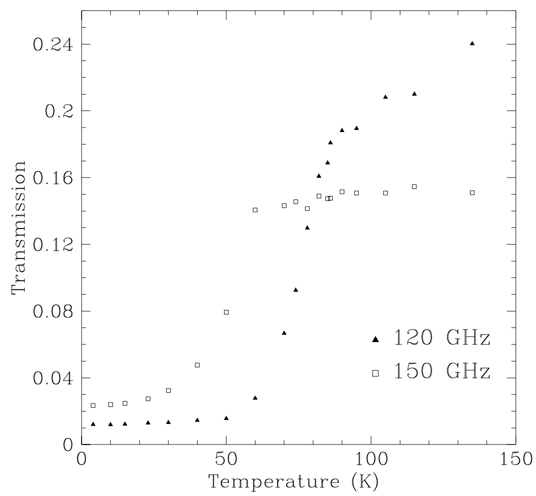

Figure 7.11: *Unperturbed transmission through a $DyBa_2Cu_3O_{7-\delta}$ film on $LaAlO_3$, film thickness 20 nm, at ν=120 GHz (solid triangles) and 150 GHz (open squares).*

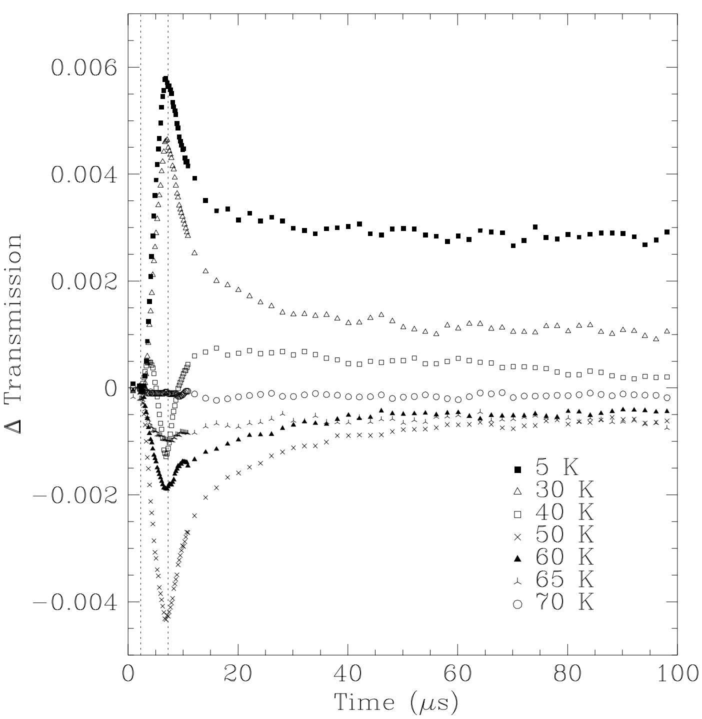

Figure 7.12: *Photo Induced Transmission for $DyBa_2Cu_3O_{7-\delta}$ on $LaAlO_3$, film thickness 20 nm, shown for several temperatures. The FIR-pulse enhances transmission at low temperatures, while it reduces it at temperatures higher than 40 K.*

additional evidence that the response cannot be due to an ordinary heating effect, since a purely bolometric signal would vanish. Around 70 K the PIT-signal drops below our detection limit, which inhibits us to draw definite conclusions about its evolution toward T_c. Also above T_c no change in transmission was observed.

In order to explain the observed behavior we return to the argument given in section 7.2. We now concentrate on the lower two panels of fig. 7.3 on page 120, in which the non-equilibrium response is sketched. Assuming that we can describe the superconducting state using a two-fluid model, we are sensitive to the contribution of both the superfluid and the normal fluid fraction. The former is represented by the δ-function at zero-frequency, responsible for the superconductivity. The spectral weight within the δ-function is determined by the number of Cooper pairs present, and will be reduced during the presence of a FIR-pulse. This will result in a less effective screening of the incident field and therefore the transmission will be enhanced temporarily, as can be seen in eq. (7.2). The quasiparticle contribution is represented by the Drude-peak in σ_1, centered around zero-frequency and having a finite width ($\gamma_{qp} = 1/\tau_{qp}$). During the pair-breaking process, the spectral weight within this peak is strongly enhanced. Under the assumption that the electron temperature relaxes within a few nanoseconds, which is considerably faster than our time resolution, on our time scale the shifted chemical potential will be the dominant effect. We can therefore regard the scattering rate γ_{qp} to retain its equilibrium value. Hence, at lower frequencies, the conductivity due to the quasiparticle peak will be considerably higher than in the initial state, thereby temporarily enhancing the *absorption* within the superconductor. When this contribution is more dominant than the reduced Cooper pair density the transmission will be reduced.

The explicit behavior, such as the temperature at which the crossover from a positive to a negative PIT-signal occurs, will strongly depend on several parameters. First, the precise values and temperature dependencies of the intrinsic sample properties such as σ_1 and the penetration depth λ will be vital. In principle, since σ_1 has a non-monotonic behavior as a function of temperature, for cuprates a situation can occur in which even the unperturbed response will be non-monotonic. In this particular situation however, we know that this is not the case and an alternative explanation for the sign change in the PIT-signal is needed. A second parameter becomes clear from fig. 7.3: if we would tune the probe frequency to a considerably higher value, the increase in absorption due to the enhanced conductivity will be less pronounced and the negative PIT-signal will subdue.

Frequency Dependence

The dependence of the PIT-signal on the frequency of the pump at T = 40 K is shown in fig. 7.13. In order to correct the spectra for the altered output power of FELIX at different frequencies within one scan of the undulator magnetic field, we also studied the power dependence of the PIT-signal. The change in power is within 10 % for most of the band that can be reached in this way, except for the frequencies at both sides of the band where the output power diminishes rapidly. The results at 5 K using a pump frequency of 750 cm^{-1} are shown in fig. 7.14. The power indicated in the figure is measured for a single

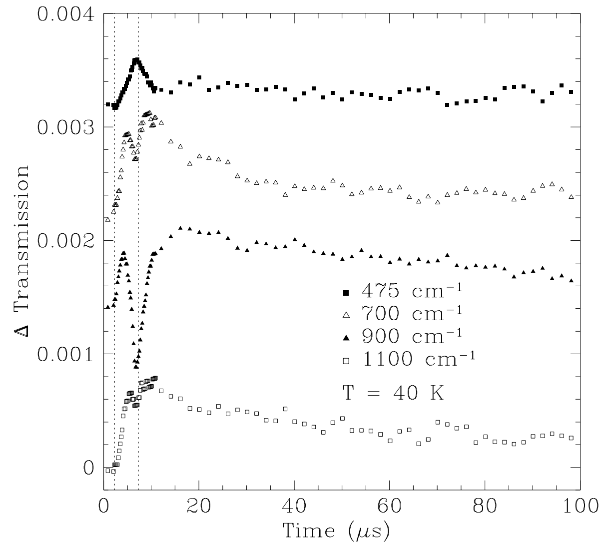

Figure 7.13: *Photo Induced Transmission shown for several different frequencies at $T = 40$ K. At this temperature for some of the frequencies both the positive and the negative influence of the FIR-pulse are clearly visible. The curves have been given an arbitrary vertical offset.*

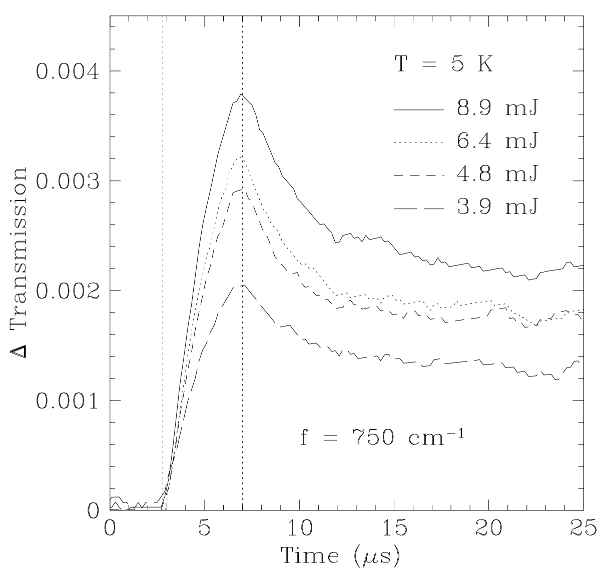

Figure 7.14: *Power dependence of the peak amplitude of the PIT-signal. The pump frequency is 750 cm^{-1}, while the temperature is 5 K.*

macropulse just before the cryostat. The normalized peak amplitudes, where we divided the maximum induced change in transmission by the input power, are 0.40, 0.48, 0.53 and 0.48 for the highest to the lowest incident power respectively. Therefore we assume that we are approximately within the linear regime and we can take the changing laser fluence into account by dividing the spectra by the measured pulse power. This was done after normalizing the pulse powers to the highest value within the band. Such a procedure conserves the observed absolute change in transmission, enabling us to obtain a direct correlation between ΔTr and ΔT. The power measured outside the cryostat is reduced by a factor of 0.5 in passing two KRS-5 windows, but since this factor is nearly frequency independent, as can be seen in fig. 4.6 on page 75, this does not enter the frequency or the temperature dependence. Moreover, from fig. 7.14 we conclude that within the power range used during the PIAMA experiments, the changes are not affected by saturation effects. In addition we conclude from the linear power dependence of the signal that one photon absorption processes govern the response.

In order to acquire the complete frequency dependence ranging from 320 - 1400 cm^{-1}, we needed two different settings for the accelerator voltage. The reproducibility of the observed changes has been carefully checked by examining the overlapping parts of the frequency ranges.

The experimental behavior presented above is indicative of reaching a critical quasiparticle density, both as a function of temperature and frequency. Returning to the equations (7.1) and (7.2) we can estimate the relative significance of both quasiparticle and Cooper pair density at all temperatures. Therefore we need to calculate the change in transmission coefficient due to changes in both σ_1 and λ. Equation (7.2) yields:

$$\Delta Tr \;=\; (Tr)^2\left[-2\pi(1+p^2+\frac{4\pi d\sigma_1}{c})\frac{d\sigma_1}{p^2c}\left(\frac{\Delta\sigma_1}{\sigma_1}\right) \;+\; \frac{d^2c^2}{2p^2\omega^2\lambda^4}\left(\frac{\Delta(\lambda^2)}{\lambda^2}\right)\right] \tag{7.5}$$

We can thus calculate the relative importance of both terms by determining α and β where we used:

$$\Delta Tr \;=\; -\alpha\left(\frac{\Delta\sigma_1}{\sigma_1}\right) \;+\; \beta\left(\frac{\Delta(\lambda^2)}{\lambda^2}\right) \tag{7.6}$$

Using the information we obtained from the unperturbed transmission experiments shown in fig. 6.15 and 6.16 we obtain the results given in table 7.3. For those values that are not available, we used extrapolations similar to the experimental results reported in references [34] and [35] for σ_1 and λ, respectively. Although β is larger than α up to about 60 K, it is clear that the σ_1-term attains considerable weight upon raising the temperature. Whereas it has no significant influence on ΔTr at 5 K, at higher temperatures it becomes much more dominant.

To establish the idea of reaching a critical quasiparticle density experimentally, we have studied the coexistence of the positive and negative PIT-signal at 40 K in more detail. The photo induced transmission has been plotted along with the FELIX pulse in fig. 7.15 for three different pulse lengths, using an arbitrary vertical offset for the sake of clarity. It is

T (K)	α ($\times10^{-3}$)	β ($\times10^{-3}$)
5	2.9	45.6
15	4.3	43.3
30	13.2	39.6
40	18.1	34.2
50	24.5	36.7
60	35.8	17.8
70	37.6	4.1

Table 7.3: *Prefactors α and β from eq. (7.6) demonstrating the significance of σ_1 and λ.*

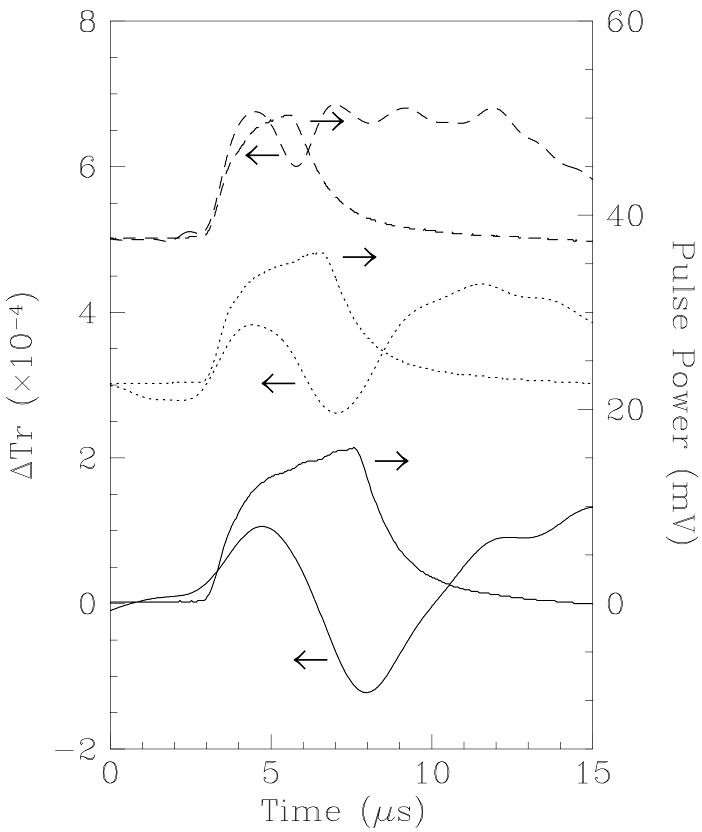

Figure 7.15: *left axis: Photo induced transmission at 40 K using $\nu_{fir} = 630\,cm^{-1}$. The curves are showing the response to FIR-pulses (right axis) of three different lengths, 4 μs (dashed), 5 μs (dotted) and 6 μs (solid). The curves have been given an arbitrary vertical offset for the sake of clarity.*

evident that the start of the dip in transmission is independent of the pulse length. At this point the number of excited quasiparticles is sufficiently large, thereby causing the absorption due to the enhanced conductivity to govern the PIT-signal. It is also clear that the onset of the second increase in transmission corresponds to the termination of the pulse. The PIT-signal returns to a positive value due to the remaining bolometric change in the sample state.

Comparison to Absorptivity

The changes in transmission as a function of pump frequency show a rather non-monotonic behavior and have been summarized in fig. 7.16 for several temperatures ranging from 5 to 60 K. Plotted are the absolute peak heights obtained after the correction for the changes in incident power. Here we divided the measured peak voltage by the pulse power directly. This procedure hence yields both positive and negative values. In order to include the 40 K data, the positive (A) and the negative contribution (B) have been determined separately, while the *total* induced change (A-B) is included in fig. 7.16. Remarkable is that the positive contribution, A, remains nearly constant, as soon as the negative contribution sets in.

In fig. 7.16, we have also plotted the frequency dependence of the absorptivity, A, within the *film*. This has been calculated using the Fresnel equations for a stratified system and the case of an anisotropic film.

$$A = 1 - |r_{lr}|^2 - |t_{lr}|^2 \tag{7.7}$$

The complex reflection and transmission coefficients r_{lr} and t_{lr} have been determined in section 3.2.2. In the calculation the angle of incidence was equal to 45° and a mixture of 50 % s- and 50 % p-polarized light was assumed, identical to the experimental situation. For the film properties we used the dielectric function at 10 K of $YBa_2Cu_3O_{7-\delta}$ obtained from reflectivity measurements [36,37]. Both the ab-plane and the c-axis dielectric function have been drawn in fig. 7.17 in the left and right panel respectively. The dielectric function of the substrate can be described by a sum of Lorentz phonon oscillators:

$$\epsilon = \epsilon_\infty + \sum_{j=1}^{N} \frac{S_j \omega_j^2}{\omega_j^2 - \omega\left(\omega + i\gamma_j\right)} \tag{7.8}$$

We utilized the experimental phonon parameters presented in ref. [38]. These parameters have been summarized in table 7.4. The substrate phonons modify the absorptivity

$\epsilon_\infty = 4.0$			
phonon	ω_j (cm^{-1})	γ_j (cm^{-1})	S_j
#1	185	3.1	15.0
#2	427	4.2	4.2
#3	498	6.5	0.014
#4	594	7	0.005
#5	651	15	0.27
#6	674	49	0.014

Table 7.4: *Substrate parameters used for the calculation of the absorptivity of the $DyBa_2Cu_3O_{7-\delta}$ film on a $LaAlO_3$ substrate.*

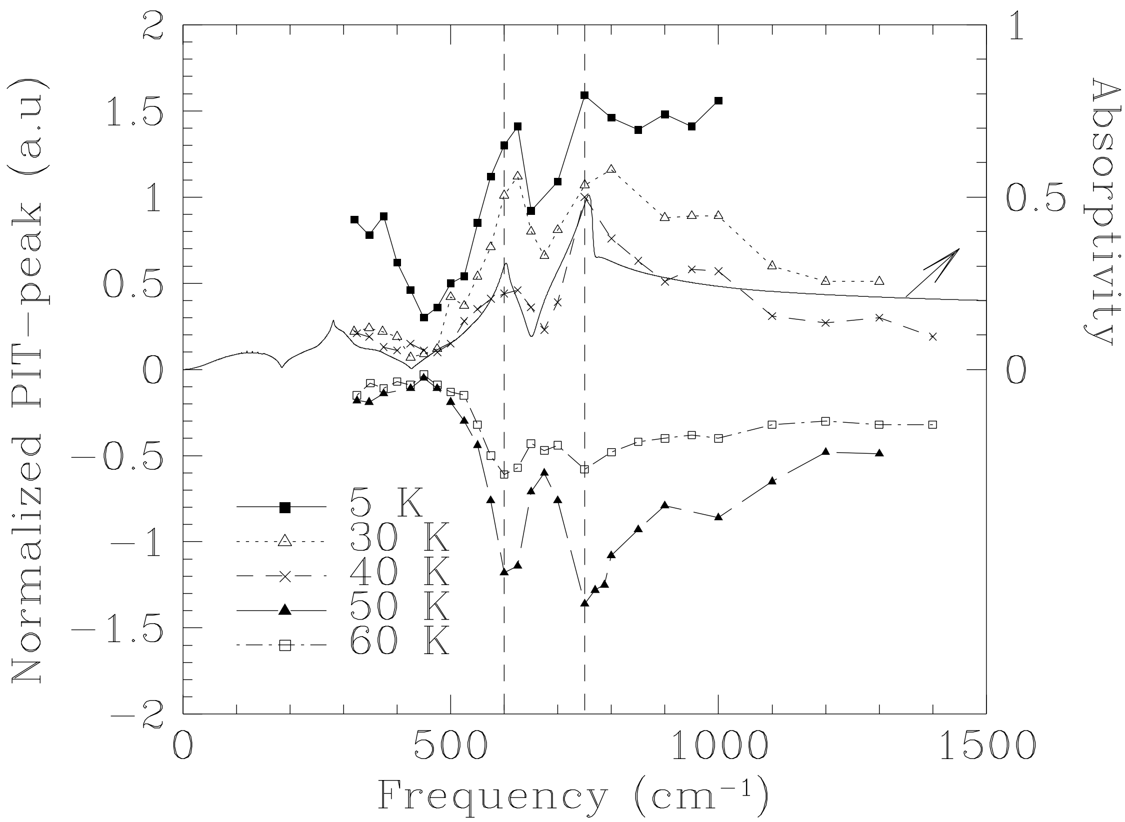

Figure 7.16: *Normalized peak intensity as a function of frequency, shown for several different temperatures, ranging from 5 to 60 K. At 40 K the sum of the positive and the negative peak has been plotted. The absorptivity within the film is shown as the solid line.*

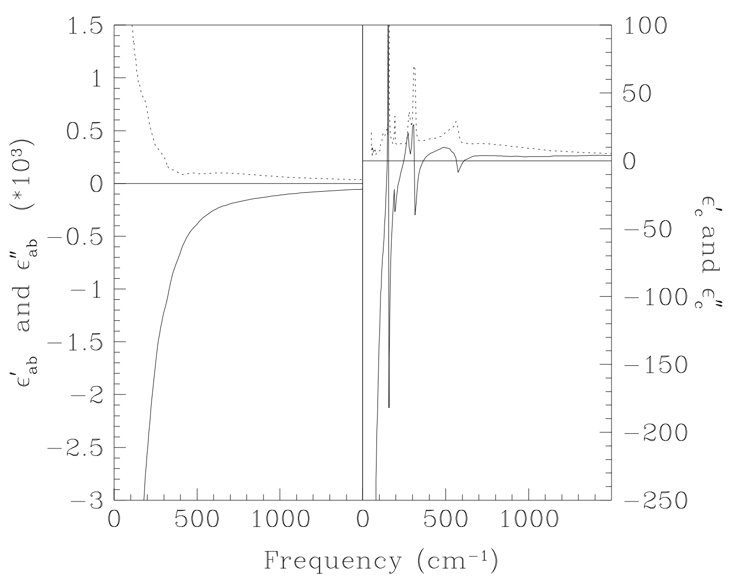

Figure 7.17: *Left: ab-plane dielectric function as a function of frequency for $YBa_2Cu_3O_{7-\delta}$. Right: c-axis dielectric function. In both cases ϵ' is indicated by the solid line and ϵ'' by the dotted line.*

within the film rather severely. Instead of having a smooth behavior expected in case of a single Drude contribution, peaks appear at frequencies corresponding to the *longitudinal* substrate phonon frequencies. Due to the high reflectivity of the substrate within its Reststrahlenbands the matching between the film and the substrate changes, giving rise to an enhanced absorption within the film, a phenomenon known as the Berreman effect [39]. Remarkable is that the c-axis phonons of the film, clearly visible in ϵ_c' and ϵ_c'', play no role in determining the absorptivity within the film. It has been shown under similar conditions in chapter 5 of this thesis and in ref. [40] that c-axis phonons appear in the reflectivity and they can therefore be expected in the absorptivity as well. The absence of these structures is most likely caused by the small film thickness.

We notice that the overall structure of the absorptivity within the film corresponds very well to the normalized peak amplitude of the PIAMA response. This demonstrates that it is possible to measure the absorption within the film very sensitively in this way.

It is important to note that the absorptivity of the substrate itself is in fact maximal *at* the transverse phonon frequencies, corresponding to the minima in the absorptivity within the film, presented in fig 7.16 as the solid line. This establishes that the observed features are not due to substrate heating, since the PIT-peak amplitude has minima at the transverse substrate phonon frequencies, in contrast to the substrate absorptivity.

7.4.2 Discussion of the Relaxation Times and the Kinetic Restrictions related to the d-wave Symmetry

Finally, in this section we will discuss the observed relaxation times in the context of bolometric and non-bolometric contributions. Furthermore a theoretical treatment will be presented, using the point of view of the dispersion relations as well as an approach using a set of coupled kinetic equations.

Time Constants

In fig. 7.18 a typical pulse shape, which has been renormalized for comparison, is shown in conjunction with the 30 K transient. We see clearly that the relaxation process does not follow the pulse at *any* time, implying that the measured relaxation time is indeed generic for the relaxation process within the sample, and *not* limited by the pulse shape. An exception to this observation might be the dip measured at 40 K. In the inset of fig. 7.18 a comparison between the same pulse and the 40 K transient is made. We see that the slope of the relaxation follows the pulse, indicating that the actual process might be even faster. Knowing from the negative response at higher temperatures that the induced changes in transmission are not due to a heating effect, and realizing that the relaxation time is not limited by experimental factors, we need to explain the unusually long life time of the non-equilibrium state.

In order to obtain a quantitative idea on the measured time constants, we fitted the

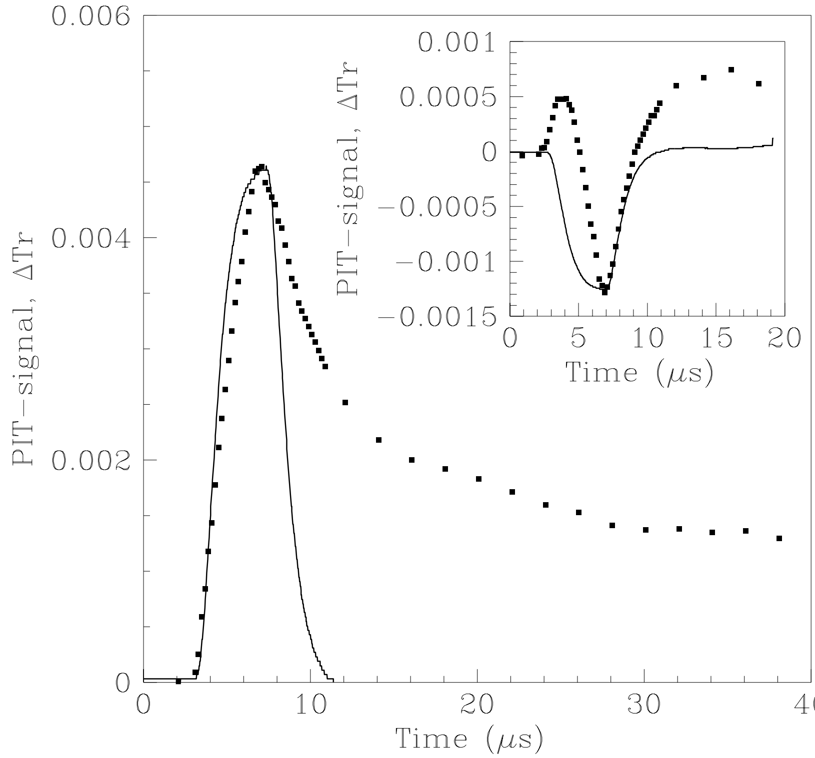

Figure 7.18: *Comparison of the incident pulse shape (solid line) and the observed changes in transmission at 30 K. The same comparison at 40 K is shown in the inset. In both cases the pulse has been renormalized for comparison.*

transients using a linear combination of two exponentially decaying signals.

$$\Delta Tr \;=\; I_1 e^{-t/\tau_1} + I_2 e^{-t/\tau_2} \tag{7.9}$$

The results of these fits can be seen in fig. 7.19. For the fit we have concentrated on the initial decay, up to 45 μs, because the slope of the decay on longer time scales is very sensitive to the magnitude of the differentiating time constant, used to correct the transients for the influence of the diode detector. The relaxation times obtained in this fashion, are given in table 7.5 and plotted in fig. 7.20 as a function of temperature. The second component was only needed at the lower temperatures (5, 30 and 40 K), to obtain a reasonable fit. The time constants of the second contribution have been indicated as τ_2 in table 7.5. We attribute the second, positive component to an appreciable bolometric response, only present at lower temperatures due to the much smaller specific heat.
Disregarding the fast response for this moment, we estimate that the PIT-signal would be due to a temperature rise of approximately 13 K by comparing the measured amplitude with the unperturbed transmission curve. Similar arguments lead to an experimental temperature rise of approximately 1.5 K for the 30 K response and 0.2 K for the 40

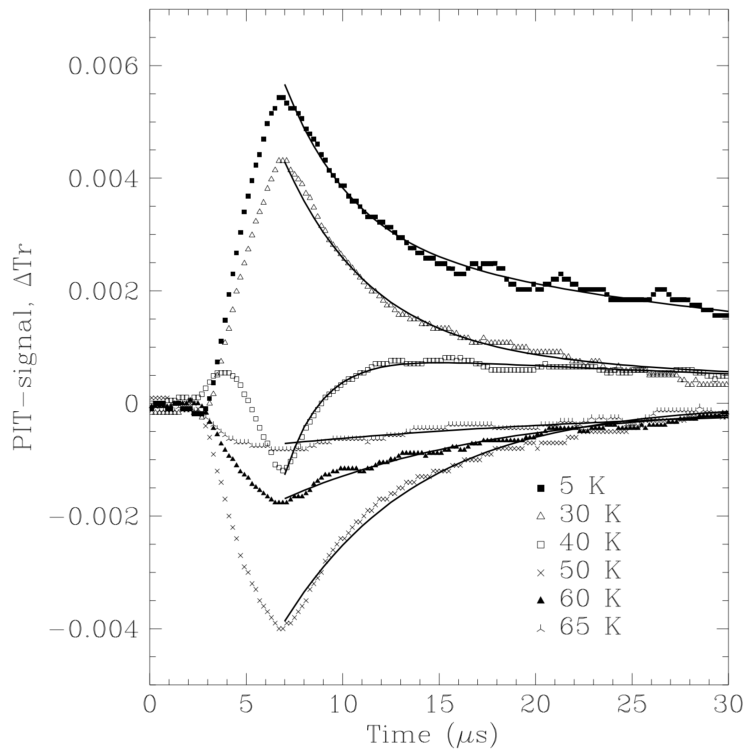

Figure 7.19: *Photo induced transmission plotted for several temperatures, together with an exponential fit. The pump frequency is 800 cm^{-1} and the probe frequency is 150 GHz.*

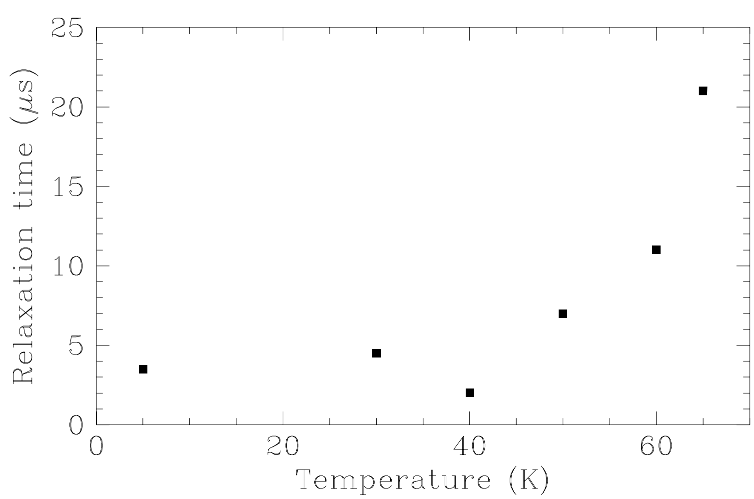

Figure 7.20: *Temperature dependence of the relaxation time obtained from the exponential fit of the PIAMA-transients at 800 cm^{-1}.*

T (K)	τ_1 (μs)	τ_2 (μs)
5	3.5	> 45
30	4.5	> 45
40	2.0 (-)	> 45 (+)
50	7	-
60	11	-
65	21	-

Table 7.5: *Relaxation times obtained from the exponential fit of the PIAMA-transients at 800 cm^{-1}.*

K transient. At 40 K we used the height of the positive peak directly after the fast non-bolometric dip. At temperatures higher than 40 K an experimental value for the temperature rise can not be obtained, since a resulting change in transmission will never be negative. Moreover, at temperatures higher than 60 K the unperturbed transmission is nearly temperature independent, implying that any observed change in transmission can not be bolometric.

In a similar fashion as for the NbN-film, we can *calculate* the expected temperature rise of the $DyBa_2Cu_3O_{7-\delta}$ film using the absorbed power and the specific heat of the entire system. The maximum pulse power during the temperature scan was 11.6 mJ/pulse, yielding $0.7 \times 0.7 \times 0.5 \times 0.25 \times 11.6 \times 10^{-3} = 0.71 \times 10^{-3}$ J as the power which is actually absorbed within the film. For the specific heat of the film we used the experimental values presented in ref. [41]. The specific heat of the substrate has been extrapolated using a T^3 dependence, starting from C_s = 30.2 J/mole K at 77 K and taking 720 K as the Debye temperature [42]. As the molar densities we used 2.5×10^{-7} and 1.45×10^{-3} for the film and the substrate respectively. These numbers immediately show that the influence of the film can be neglected in the calculation of ΔT. The results are summarized in table 7.6 in conjunction with the estimated experimental values. We find that the size of ΔT_{exp} for

T (K)	ΔT_{th} (K)	ΔT_{exp} (K)	C_{film} (J/mole K)	C_{sub} (J/mole K)
5	8.7	13	0.01	8.1×10^{-3}
30	0.34	1.5	1.9	1.8
40	0.18	0.2	3.7	4.2

Table 7.6: *Comparison of the experimental and theoretical temperature changes for $DyBa_2Cu_3O_{7-\delta}$.*

the slow contribution can be described fairly well in this way. Therefore we conclude that at higher temperatures, due to the much larger specific heat of both film and substrate, the incident power barely changes the sample temperature.

Dispersion Relations

In this section we want to make the inhibition of the recombination process somewhat more physically transparent by looking at the dispersion relations of the gap function, the quasiparticles and the phonons emitted during recombination.

Our main interest will be the transition probability from a state involving two quasiparticles and N Cooper pairs into a state with N+1 Cooper pairs and an emitted phonon, i.e. the recombination process:

$$\gamma_R \;=\; |<(N_{q\lambda}+1)|\gamma_{k\uparrow}\gamma_{k'\downarrow}a^{\dagger}_{q\lambda}|N_{q\lambda}, k\uparrow k'\downarrow>|^2 \tag{7.10}$$

where $\gamma_k, \gamma_{k'}$ are the quasiparticle operators, written in terms of the electron operators C and C† [43]:

$$\begin{aligned} \gamma^{\dagger}_{ek0} &= u_k C^{\dagger}_{k\uparrow} \;-\; v_k S^{\dagger}_k C_{-k\downarrow} \\ \gamma^{\dagger}_{ek1} &= u_k C^{\dagger}_{-k\downarrow} \;+\; v_k S^{\dagger}_k C_{k\uparrow} \\ \gamma^{\dagger}_{hk} &= S_k \gamma^{\dagger}_{ek} \end{aligned} \tag{7.11}$$

Here S (†) is the *pair* annihilation (creation) operator and u$_k$ and v$_k$ are the well-known BCS coherence factors

$$\begin{aligned} v_k^2 &= \frac{1}{2}\left[1 - \frac{\xi_k}{E_k}\right] \\ u_k^2 &= 1 - v_k^2 \end{aligned} \tag{7.12}$$

where ξ_k is the quasiparticle energy at momentum k and $E_k \;=\; (\Delta_k^2 \,+\, \xi_k^2)^{1/2}$.

In the quasiparticle recombination process the coherence factor for pair creation is

$$(v_k u_{k'} \;+\; u_k v_{k'})^2 \;\approx\; \frac{1}{2}\left(1 + \frac{\Delta_k^2}{E_k E_k}\right) \tag{7.13}$$

assuming that $|\vec{k}| \;\approx\; |\vec{k}'|$. Substituting eq. (7.13) into (7.10) finally yields

$$\tau_R \;=\; \frac{1}{\gamma_R} \;\sim\; \frac{1}{\Delta_k} \tag{7.14}$$

This result can be understood intuitively, knowing that the transition probability is in fact a measure of the overlap of the quasiparticle wavefunction and the superconducting energy gap function. Therefore, in case of a smaller gap the transition probability will be smaller and hence the quasiparticle lifetime will be longer. In fact, precisely at the nodes the energy gap vanishes, and consequently the recombination time would be infinite. In reality there are always physical processes breaking the symmetry yielding a finite τ_R, such as scattering processes involving two phonons. However, since these are second order processes having a lower probability, τ_R is likely to be long.

Obviously, both momentum and energy conservation laws will have to be satisfied in the recombination process, yielding:

$$\begin{aligned} \vec{k} + \vec{k'} &= \vec{q} \\ E_k + E_{k'} &= v_s|q| \end{aligned} \tag{7.15}$$

where v_s is the sound velocity within the material. By plotting the dispersion relation for quasiparticles close to the nodes, it becomes clear that, for a gap dispersion which is steep compared to the linear phonon dispersion, satisfying both conservation laws simultaneously is problematic. A qualitative sketch can be seen in fig. 7.21. In order to improve the lucidity of the figure, we have used a few transformations that do not affect the validity of the argument. First we only consider two quasiparticles close to opposite nodes, such as for instance close to $(\pi/2, \pi/2)$ and $(-\pi/2, -\pi/2)$. (see fig. 7.5 for the d-wave gap symmetry). Since, in the other cases, the difference in momentum taken up by the phonon will be very large, and consequently the emitted phonon energy will be rather large, the transition becomes less probable. In order to move the cones on top of each other, we have plotted δk and δq according to

$$\vec{k} = \left(\frac{\pi}{2}, \frac{\pi}{2}\right) + \delta k, \quad \vec{q} = \left(\frac{\pi}{2}, \frac{\pi}{2}\right) + \delta q \tag{7.16}$$

where $\vec{k}$ is the momentum vector parallel and $\vec{q}$ the momentum vector perpendicular to the Fermi surface. Furthermore, for the case of the node at $(-\pi/2, -\pi/2)$, we define the difference in momentum as $-\delta k$ and the energy as $-E_{\delta k}$. This transformation rotates this cone by 180° around the $\vec{k}_z$-axis and by 180° around the $\vec{q}$-axis. The conservation laws given in eq. (7.15), under these transformations become:

$$\begin{aligned} \delta\vec{k} - \delta\vec{k'} &= \vec{q} \\ E_{\delta k} - E_{\delta k'} &= v_s|q| \end{aligned} \tag{7.17}$$

The functional form of the dispersion of the quasiparticles, plotted in fig. 7.21, is given by

$$E_{\delta k} = \hbar\sqrt{(\delta k)^2\left(\frac{\partial\Delta_k}{\partial k}\right)^2 + (\delta q)^2 v_F^2} \tag{7.18}$$

where the functional form of the energy gap, Δ_k, has been given in eq. (7.3) and v_F is the Fermi velocity. For a quasiparticle in a state $(\delta k, 0)$, indicated by the large dot, there is a range of possible quasiparticle states in the lower cone available for recombination, indicated by the ellipse. However, if the phonon dispersion, represented by the dashed lines, is considerably shallower than the slope of the gap around the nodes, there will be no phonon states available to consume the remaining momentum and energy.

Assuming that the only effect of an increased sample temperature is a reduction of the size of the maximum gap at $(\pi, 0)$, the slope of the quasiparticle dispersion will decrease at higher temperatures. Hence, around a certain temperature the dispersion of the gap and the phonons will be comparable, yielding a minimum in the relaxation time. In contrast, upon approaching T_c from below, $\Delta_{max} \to 0$, implying, using eq. (7.14), that τ_R will be consequently enhanced.

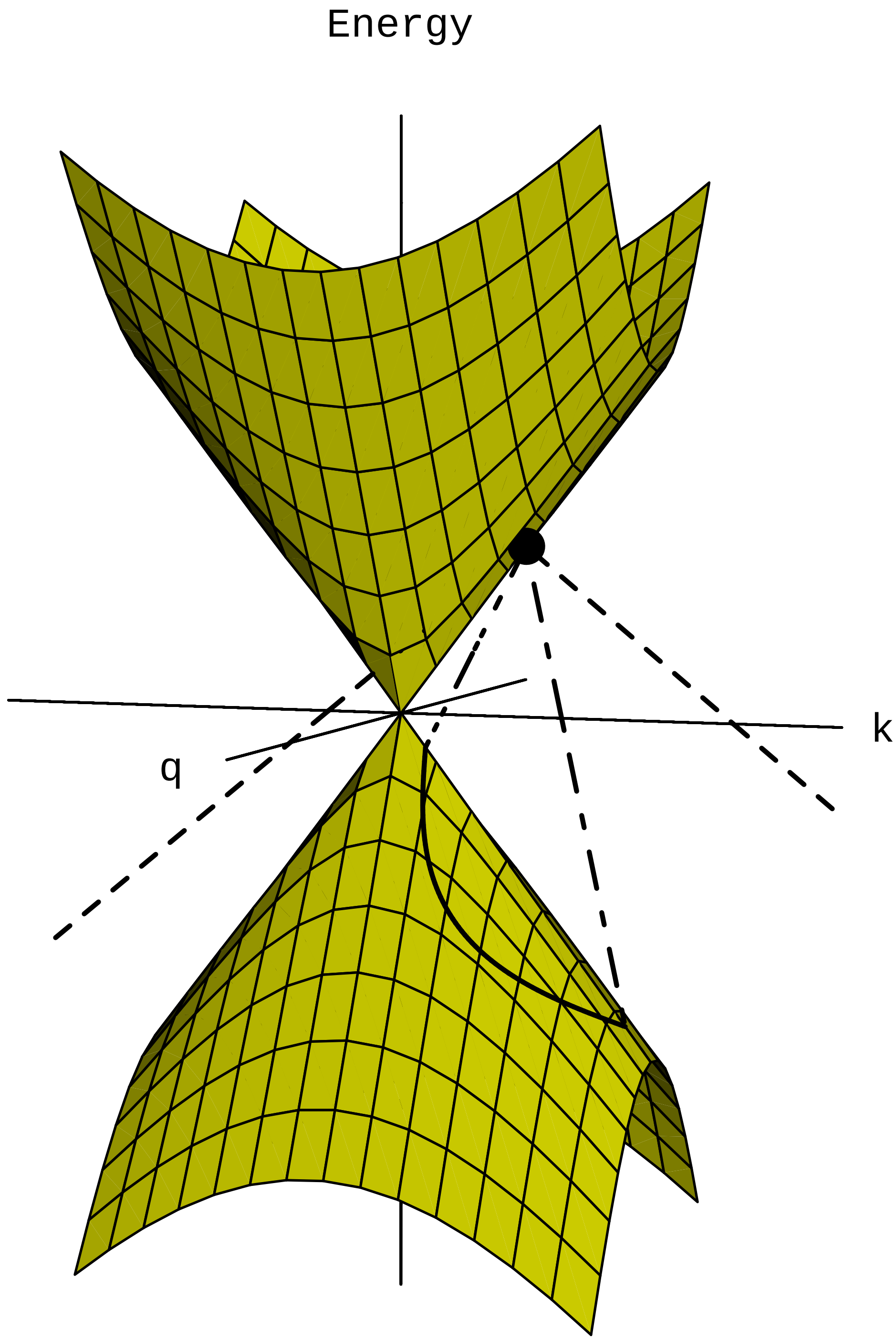

Figure 7.21: *Qualitative sketch of the quasiparticle dispersion in opposite nodes in conjunction with a linear phonon dispersion (dashed line). This clearly demonstrates the occurrence of a bottleneck if the former is too steep.*

Kinetic Equation Approach

We used a kinetic equation approach to describe a superconductor in a non-equilibrium state, in order to obtain a *quantitative* idea about the relaxation and recombination processes. The kinetic approach was first introduced by Bardeen *et al.* [44] to study the thermal conductivity of a superconductor and was later adapted to the strong coupling case by Ambegeokar and Tewordt [45] and Prange and Kadanoff [46,47]. Considering the superconductor as a combined system involving three different components (quasiparticles, phonons and Cooper pairs) leads to the construction of set of coupled equations describing their respective distribution functions. This approach is equivalent to the more rigorous Green's function approach [48], while the resulting equations are rather transparent while still incorporating the essential physics within the problem.

We begin by constructing the coupled equations describing the non-equilibrium distribution functions of the quasiparticles, $f(E_k)$, and the phonons, $n(\Omega_q)$.

$$\begin{aligned} \frac{df(E_k)}{dt} &= I_{qp}(E_k) + \frac{\partial f(E_k)}{\partial t} \\ \frac{dn(\Omega_q)}{dt} &= I_{ph}(\Omega_q) + \frac{\partial n(\Omega_q)}{\partial t} \end{aligned} \tag{7.19}$$

Here $I_{qp}(E_k)$ and $I_{ph}(\Omega_q)$ are energy spectra of the quasiparticle and phonon injection rate, respectively. We will restrict our discussion here to the case where a pulsed optical source is used to create the non-equilibrium state. Therefore $I_{ph}(\Omega_q)$ is always equal to zero, whereas $I_{qp}(E_k)$ is nonzero only during the pulse. Immediately after the pulse we study a *free* quasiparticle relaxation. The second terms in both expressions describes the changes in time of the respective distribution functions.

Concentrating first on this part of the coupled equations for the case of the quasiparticles, the resulting contribution will be a combination of many scattering processes. The main processes have been treated in the beginning of this chapter, and it is important to realize once again that elastic and inelastic scattering and recombination all contribute in the relaxation process. In our case, we have established that, due to the temporal resolution, the transients are not affected by the fastest processes, such as quasiparticle-quasiparticle scattering and the cascading process in which quasiparticles decay via additional pair-breaking. Moreover, the quasiparticle-impurity scattering only contributes to the collision rate if the process is inelastic. The contribution of the elastic processes vanishes due to the cancellation of coherence factors. Such processes however, still play a role in the relaxation process for an anisotropic superconductor because, although leaving the energy unaffected, they can still modify the momenta of the quasiparticles.

Our main aim will be to calculate the quasiparticle-phonon scattering. Not only we can estimate the phonon scattering time and its temperature dependence, but most importantly we can make a direct comparison between the *scattering* and the *recombination* process due to their similarity. The Hamiltonian for the electron-phonon interaction can be written as [49]:

$$H_{e-ph} \;=\; \sum_{p\sigma,q\lambda} g_{q\lambda} C^{\dagger}_{p+q,\sigma} C_{p\sigma}\,(a_{q\lambda} \,+\, a^{\dagger}_{-q\lambda}) \tag{7.20}$$

where C(†) is the electron annihilation (creation) operator and p, σ and q, λ are the momenta and spin quantum numbers for electrons and phonons respectively, while $g_{q\lambda}$ is the electron-phonon coupling parameter. In order to rewrite this in a useful form for quasiparticles, we use the Bogoliubov transformation to the quasiparticle operators. Substituting eq. (7.11) into (7.20) yields:

$$\begin{aligned} H_{e-ph} = \sum_{p,q,\lambda} g_{q\lambda} \Big\{ & L(p+q,p) \left[\gamma^{\dagger}_{e(p+q)0}\gamma_{ep0} \,+\, \gamma^{\dagger}_{ep1}\gamma_{e(p+q)1}\right] \\ & + M(p+q,p) \left[\gamma_{e(p+q)0}\gamma_{hp1} \,-\, \gamma_{ep0}\gamma_{h(p+q)1}\right]\Big\}\,(a_{q\lambda} \,+\, a^{\dagger}_{-q\lambda}) \end{aligned} \tag{7.21}$$

where the coherence factors are now given by:

$$\begin{aligned} L(p',p) \equiv u_{p'}u_p \,-\, v_{p'}v_p \;&=\; \frac{1}{2}\left(1 \,-\, \frac{\Delta_p^2 - \xi_p\xi_{p'}}{E_pE_{p'}}\right) \\ M(p',p) \equiv u_{p'}v_p \,+\, v_{p'}u_p \;&=\; \frac{1}{2}\left(1 \,+\, \frac{\Delta_p^2 - \xi_p\xi_{p'}}{E_pE_{p'}}\right) \end{aligned} \tag{7.22}$$

for scattering and pair creation or annihilation respectively. Furthermore, Δ_p is the superconducting energy gap, ξ_p is the quasiparticle excitation energy and $E_p \;=\; (\xi_p^2 \,+\, \Delta_p^2)^{1/2}$. Finally, using Fermi's golden rule for the transition rate, we can formulate the quasiparticle-phonon contribution to the kinetic equations.

$$\begin{aligned} \frac{\partial f(\xi_p)}{\partial t} = & \frac{2\pi}{\hbar}\sum_{q\lambda}\Big\{|g_{q\lambda}|^2\, L^2(p+q,p)\,\left[f(\xi_{p+q})\,(1-f(\xi_p))\,(n(\Omega_{q\lambda})+1)\right. \\ & \left. -\,(1-f(\xi_{p+q}))f(\xi_p)n(\Omega_{q\lambda})\right]\delta(\Omega_{q\lambda}+E_p-E_{p+q}) \,-\, \{p \leftrightarrow (p+q)\}\Big\} \\ & -\,\frac{2\pi}{\hbar}\sum_{q\lambda}\Big\{|g_{q\lambda}|^2 M^2(p+q,q)\left[f(\xi_p)f(\xi_{p+q})(n(\Omega_{q\lambda})+1)\right. \\ & \left. -\,(1-f(\xi_p)(1-f(\xi_{p+q}))n(\Omega_{q\lambda})\right]\delta(E_p+E_{p+q}-\Omega_{q\lambda})\Big\} \end{aligned} \tag{7.23}$$

Here f(ξ_i), for i = p,p+q, and n($\Omega_{q\lambda}$) are the occupation numbers for the quasiparticles and the phonons respectively. Using an identical argumentation as above one can write down a similar term for the phonon kinetic equation. We will restrict the discussion to the most essential part, the quasiparticle non-equilibrium distribution.

We can distinguish four different terms in eq. (7.23), which are easily recognizable from their occupation numbers. The first two terms are the quasiparticle-phonon scattering contributions, where the first involves phonon emission, and the second phonon absorption. The last two terms describe the quasiparticle recombination contribution, involving the emission of a phonon, and the phonon induced pair breaking, respectively.

Since all terms, in fact, describe the rate at which the densities grow or diminish, (7.23) still needs to be divided by the density f(ξ_p), in order to obtain the actual scattering rates for a quasiparticle having momentum p. This yields, for instance, for the recombination term:

$$,_{R} \;=\; \frac{1}{\tau_R} \;=\; \frac{2\pi}{\hbar}\sum_{q,\lambda} |g_{q\lambda}|^2\, M^2(p+q,p)\, f(\xi_{p+q})\,(n(\Omega_{q\lambda})+1)\delta(E_p+E_{p+q}-\Omega_{q\lambda}) \tag{7.24}$$

where the other terms are calculated in a similar fashion.

For f(ξ_i) we used the Fermi-Dirac distribution

$$f_k(\xi_i,T,n) \;=\; \frac{1}{1+e^{[\xi_i-\mu]/k_BT}} \tag{7.25}$$

while for the phonon density of states the Boltzmann distribution was used

$$n(\Omega_{q\lambda}) \;=\; \frac{1}{e^{\hbar\omega_q/k_BT}-1} \tag{7.26}$$

Using the information given above and the temperature dependence of the energy gap, and therefore the temperature dependence of the occupation numbers L(p',p) and M(p',p), we are able to calculate all four contributions individually at all temperatures, besides the unknown electron-phonon coupling parameter $g_{q\lambda}$. However, $g_{q\lambda}$ appears in all contributions, allowing a direct comparison, even though the absolute magnitudes of the scattering rates are unknown. In fig. 7.22 the scattering time, τ_{in}, resulting from a sum of both scattering processes (phonon absorption and emission) is depicted in conjunction with the recombination time, τ_R. The time constants were calculated using a Monte-Carlo approach, averaging over the entire k-space, where the fact that quasiparticles are mainly situated in the nodes is included via the Fermi-Dirac distribution. The most striking observation is the enhancement of more than two orders of magnitude of τ_R compared to τ_{in}. In the calculation we assumed a perfect two-dimensional system, allowing no dispersion in the c-axis direction. A finite hopping in the c-axis direction might tend to bring both curves closer to one another.

Moving our focus to the temperature dependence of both quantities, we see that the scattering time is reduced upon increasing the temperature, as expected. The temperature dependence of τ_{in} is not as strong as the one observed experimentally by Doettinger *et al.* [21], which can be attributed to the presence of additional inelastic scattering contributions such as quasiparticle-quasiparticle scattering in the latter case. These contributions cannot be compared directly to the recombination process due to the different prefactors. However, we know from the rapid reduction of the scattering rate just below T_c [4,50] that quasiparticle-quasiparticle scattering is in fact very important in these materials. Inclusion of this process in the calculation of τ_{in} will tend to move both curves in fig. 7.22 further apart, while the temperature dependence of τ_{in} will be enhanced.

The recombination time, τ_R, is fairly temperature independent at low temperatures and has a minimum around $0.8 \times T_c$ due to an optimal matching of the phonon and the

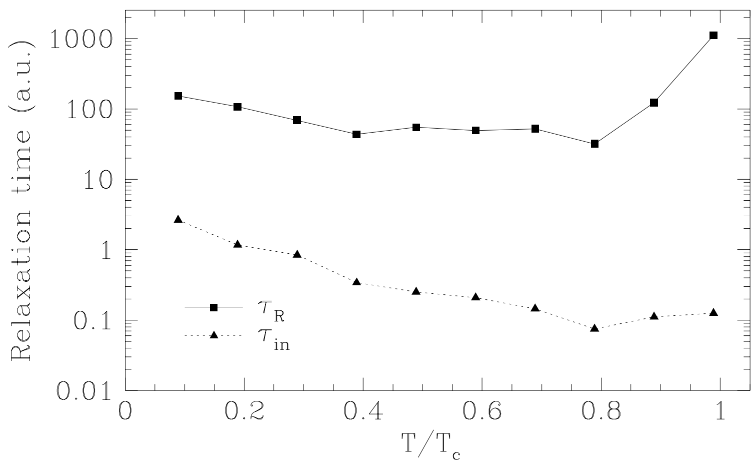

Figure 7.22: *Temperature dependence of the quasiparticle-phonon scattering time (τ_{in}, triangles) and the quasiparticle recombination time (τ_R, squares).*

quasiparticle dispersion. At the higher temperatures τ_R shows a tendency to increase due to the reduced size of the gap. The experimental recombination times plotted in fig. 7.20 show a temperature dependence in accordance with the one observed in fig. 7.22, including the weak temperature dependence at low temperatures, while showing an increase upon approaching T_c. The minimum, predicted by the calculations, seems to be present as well, explaining the fact that the 40 K transient is the only one presumably limited by the pulse shape.

Noteworthy is furthermore, that Frenkel and co-workers [16] observed a similar temperature dependence, but explained the enhancement of τ by a factor of 4 by a growing contribution of the bolometric component within the total response.

7.5 Conclusions

We have observed non-equilibrium superconductivity within $DyBa_2Cu_3O_{7-\delta}$ using Photo Induced Activation of Mm-wave Absorption (PIAMA), whereas we observed a purely bolometric response for NbN. For NbN the calculated temperature changes agree fairly well with the experimentally observed changes in transmission. The bolometric explanation is supported furthermore by the long time scales (100-200 μs) and the reduced amplitude at low temperatures.

The unique tunability of the free electron laser (FELIX) allowed us to study PIAMA as a function of frequency for energies both below and above the relevant energy scales in $DyBa_2Cu_3O_{7-\delta}$. The frequency dependence resembles the calculated absorptivity spectrum for a thin film deposited on a $LaAlO_3$ substrate. Since the PIAMA response is minimum at frequencies corresponding to the Reststrahlen absorptions in the substrate, we conclude that substrate heating is unimportant.

As a function of temperature the induced changes cross over from being positive at $T < 40$ K, indicating an enhanced transmission, to being negative at $T > 40$ K, due to a reduced transmission. The temperature dependence is indicative of reaching a critical quasiparticle density at which the photo induced signal starts to be dominated by the dissipative part of ϵ, rather than the inductive part. This behavior can be explained qualitatively by assuming a two-fluid description in the superconducting state. The reduced Cooper pair density is causing an enhancement of transmissivity, while an enhanced absorption due to the influence of the non-equilibrium quasiparticles reduces the transmission at higher temperatures. It is impossible to explain the sign change by a purely bolometric effect, since the unperturbed mm-wave transmission shows a monotonic behavior as a function of temperature. Moreover, heating of the sample has been calculated to become rather insignificant at higher temperatures, which is supported by the presence of a second, slow ($> 45\mu$s) contribution. This contribution is only present at $T \leq 40$ K and shows an enhanced transmission for all cases.

The observed relaxation time of the non-equilibrium state is unusually long, 2 to 20 μs. We propose that, due to the unique use of a FIR laser in this experiment in combination with a high T_c superconductor, the quasiparticles, after thermalization, end up in the nodes of the d-wave energy gap. Having a well defined momentum state, recombination of quasiparticles is inhibited due to kinetic considerations. This picture is supported by calculations comparing the quasiparticle-phonon scattering time and the recombination time directly, showing an enhancement of about two orders of magnitude of the latter. The predicted temperature dependence of τ_R, being nearly constant at low temperatures while showing an enhancement at temperatures close to T_c, corresponds fairly well to the experimentally observed behavior.

References

[1] for a review of the normal state properties in relation to the Fermi liquid approach see: K. Levin *et al.*, Physica C **175**, 449-522 (1991).

[2] Basically the theoretical approaches can be subdivided into two streams. First the modified Fermi liquid theories such as the Marginal Fermi liquid theory (Varma *et al.*, PRL **63**, 1996 (1989)) and the Nearly Antiferromagnetic theory of Pines and co-workers (Monthoux *et al.*, PRL **69**, 961 (1992)) and Scalapino and co-workers (N. Bulut *et al.*, PRB **47**, 2742 (1993)). The second stream are the non-Fermi liquid approaches, such as the interlayer coupling model of Anderson and co-workers (S. Chakravarty *et al.*, Science **261**, 337 (1993)). See also chapter 2 of this thesis.

[3] Martin C. Nuss, P. M. Mankiewich, M. L. O'Malley, E. H. Westerwick and Peter B. Littlewood, Phys. Rev. Lett. **66**, 3305 (1991).

[4] D. A. Bonn, P. Dosanjh, R. Liang and W. N. Hardy, Phys. Rev. Lett. **68**, 2390 (1992).

[5] D. A. Bonn, S. Kamal, Kuan Zhang, Ruixing Liang, D. J. Baar, E. Klein and W. N. Hardy, Phys. Rev. B **50**, 4051 (1994).

[6] O. Klein and G. Grüner, Comment on "Microwave Determination of the Electronic Scattering Time in $YBa_2Cu_3O_7$", Phys. Rev. Lett. **72**, 1390 (1994).

[7] P. L. Richards, J. Clarke, R. Leoni, Ph. Lerch, S. Verghese, M. R. Beasly, T. H. Geballe, R. H. Hammond, P. Rosenthal and S. R. Spielman, Appl. Phys. Lett. **54**, 283 (1989).

[8] R. S. Nebosis, R. Steinke, P. T. Lang, W. Schatz, M. A. Heusinger, K. F. Renk, G. N. Gol'tsman, B. S. Karasik, A. D. Semenov and E. M. Gershenzon, J. Appl. Phys. **72**, 5496 (1992).

[9] C. S. Owen and D. J. Scalapino, Phys. Rev. Lett. **28**, 1559 (1972).

[10] Jhy-Jiun Chang and D. J. Scalapino, Phys. Rev. B **9**, 4769 (1974).

[11] W. H. Parker, Phys. Rev. B **12**, 3667 (1975).

[12] L. R. Testardi, Phys. Rev. B **4**, 2189 (1971).

[13] A. Rothwarf, G. A. Sai-Halasz and D. N. Langenberg, Phys. Rev. Lett. **33**, 212 (1974).

[14] see for instance: G. M. Knippels, R. F. X. A. M. Mols, A. F. G. van der Meer, D. Oepts and P. W. van Amersfoort, Phys. Rev. Lett. **75**, 1755 (1995).

[15] N. Bluzer, Phys. Rev. B **44**, 10222 (1991).

[16] A. Frenkel, M. A. Saifa, T. Venkatesan, P. England, X. D. Wu and A. Inam, J. Appl. Phys. **67**, 3054 (1990).

[17] S. G. Han, Z. V. Vardenay, K. S. Wong, O. G. Symko and G. Koren, Phys. Rev. Lett. **67**, 3054 (1990).

[18] G. L. Eesley, J. Heremans, M. S. Meyer, G. L. Doll and S. H. Liou, Phys. Rev. Lett. **65**, 3445 (1990).

[19] F. Gao, J. W. Kruse, C. E. Platt, M. Feng and M. V. Klein, Appl. Phys. Lett. **63**, 2274 (1993).

[20] M. I. Flik, Z. M. Zhang, K. E. Goodson, M. P. Siegal and Julia M. Phillips, Phys. Rev. B **46**, 5606 (1992).

[21] S. G. Doettinger, R. P. Huebener, R. Gerdemann, A. Kühle, S. Anders, T. G. Träuble and J. C. Villégier, Phys. Rev. Lett. **73**, 1691 (1994).

[22] A. I. Larkin and Yu. N. Ovchinnikov, Zh. Exsp. Teor. Fiz. **68**, 1915 (1975)[Sov. Phys. JETP **41**, 960 (1976)].

[23] F. A. Hegmann, D. Jacobs-Perkins, C.-C. Wang, S. H. Moffat, R. A. Hughes, J. S. Preston, M. Currie, P. M. Fauchet and T. Y. Hsiang, Appl. Phys. Lett. **67**, 285 (1995).

[24] W. R. Donaldson, A. M. Kadin, P. H. Ballentine and R. Sobolewski, Appl. Phys. Lett. **54**, 2470 (1989).

[25] C. J. Stevens, D. Smith, C. Chen, J. F. Ryan, B. Podobnik, D. Mihailovic, G. A. Wagner, J. E. Evetts, Phys. Rev. Lett. **78**, 2212 (1997).

[26] C. J. Stevens, T. N. Thomas, S. Choudhury, J. F. Ryan, D. Mihailovic, L. Forro, G. A. Wagner and J. E. Evetts, SPIE **2696**, 313 (1996).

[27] M. Danerud, D. Winkler, M. Lindgren, M. Zorin, V. Trifonov, B. S. Karasik, G. N. Gol'tsman and E. M. Gershenzon, J. Appl. Phys. **76**, 1902 (1994).

[28] M. Zorin, M. Lindgren, M. Danerud, B. S. Karasik, D. Winkler, G. Gol'tsman and E. Gershenzon, J. Supercond. **8**, 11 (1993).

[29] H. S. Kwok, J. P. Zheng, Q. Y. Ying and R. Rao, Appl. Phys. Lett. **54**, 2473 (1989).

[30] A. M. Kadin, M. Leung and A. D. Smith, Phys. Rev. Lett. **65**, 3193 (1990).

[31] Matthias C. Schabel, C.-H. Park, A. Matsuura, Z.-X. Shen, D. A. Bonn, Ruixing Liang and W. N. Hardy, Phys. Rev. B. **55**, 2796 (1997).

[32] E. S. R. Gopal, *Specific Heats at Low Temperatures*, (Plenum, London, 1966).

[33] A. D. Semenov, R. S. Nebosis, Yu. P. Gousev, M. A. Heusinger and K. F. Renk, Phys. Rev. B **52**, 581 (1995).

[34] U. Dähne, Y. Goncharov, N. Klein, N. Tellmann, G. Kozlov and K. Urban, J. Supercond. **8**, 129 (1995).

[35] L. A. de Vaulchier, J. P. Vieren, Y. Guldner, N. Bontemps, R. Combescot, Y. Lemaitre and J. C. Mage, Europhys. Lett. **33** (2), 153 (1996).

[36] D. van der Marel, M. Bauer, E. H. Brandt, H.-U. Habermeier, D. Heitmann, W. König and A. Wittlin, Phys. Rev. B **43**, 8606 (1991).

[37] M. Bauer, Graduate Dissertation, University of Tübingen, 1990.

[38] Z. M. Zhang, B. I. Choi, M. I. Flik and A. C. Anderson, J. Opt. Soc. Am. B **11**, 2252 (1994).

[39] D. W. Berreman, Phys. Rev. **130**, 2193 (1963).

[40] J. H. Kim, B. J. Feenstra, H. S. Somal, D. van der Marel, Wen Y. Lee, A. M. Gerrits and A. Wittlin, Phys. Rev. B **49**, 13065 (1994).

[41] M. B. Maple, Y. Dalichaouch, J. M. Ferreira, R. R. Hake, B. W. Lee, J. J. Neumeier, M. S. Torikachvili, K. N. Yang, H. Zhou, R. P. Guertin and M. V. Kuric, Physica B **148**, 155 (1987).

[42] Peter C. Michael, John U. Trefny and Baki Yarar, J. Appl. Phys **72**, 107 (1992).

[43] M. Tinkham, *Introduction to Superconductivity*, (McGraw-Hill, New York, 1975 and Krieger, New York, 1980).

[44] J. Bardeen, G. Rickazen and L. Tewordt, Phys. Rev. **113**, 982 (1959).

[45] V. Ambegeokar and L. Tewordt, Phys. Rev. **34**, 805 (1964).

[46] R. E. Prange and L. P. Kadanoff, Phys. Rev. **34**, 566 (1964).

[47] for a review on the kinetic equation approach see: Jhy-Jiun Chang, Chapter 9 in *Nonequilibrium Superconductivity, Phonons and Kapitza Boundaries*, Kenneth E. Gray ed. (Plenum Press, New York, 1981).

[48] G. M. Eliashberg, Zh. Exsp. Teor. Fiz. **38**, 966 (1960) [Sov. Phys. JETP Lett. **11**, 696 (1960)].

[49] J. R. Schrieffer, *Theory of Superconductivity*, (Benjamin, New York, 1964).

[50] B. J. Feenstra, F. C. Klaassen, D. van der Marel, Z. H. Barber, R. Pérez Pinaya and M. Decroux, Physica C **278**, 213 (1997).

Samenvatting

Laat ik eens beginnen met een grap. Dat heeft twee voordelen, ten eerste staat de altijd lastige eerste zin meteen op papier en het tweede is dat met een beetje mazzel een aantal lezers denkt dat er misschien nog meer grappen komen, en dus doorleest.

"Ik rijd een tijdje geleden door het mooie Friese landschap, zie ik plotseling een kip met enorme snelheid van de andere kant komen, en mij passeren. Ik snap er niks van, maar rij gewoon door. Een tijdje later, zie ik een boer aan de kant van de weg staan, hij is een hek aan het repareren. Ik stop, en vraag hem of hij die kip ook heeft gezien. "Tsja", zegt hij, "weet u, mijn vrouw en ik zijn gek op kippevlees, en vooral de pootjes zijn erg lekker. Dus ik aan het kweken, en ja hoor, een kip met vier poten gemaakt! Maar goed, nu ik weet hoe ik ze moet maken, moet ik ook nog leren hoe ik ze weer moet vangen!"

Hetzelfde gevoel heb ik een beetje bij de status van de *hoge temperatuur* supergeleiding. Aan de hooggespannen verwachtingen, geschapen na de aankondiging van supergeleiding beneden -181 °C in $YBa_2Cu_3O_{7-\delta}$, is tot nu toe nog niet echt voldaan. Om aan te geven wat ik hiermee bedoel zal ik in het eerste stuk van deze samenvatting proberen een aantal "vaktermen" begrijpelijk te maken. Laat ik als eerste eens uitleggen wat *supergeleiding* is.

Een aantal materialen om ons heen (bijv. kwik, tin en aluminium) vertoont een verrassend gedrag als ze worden afgekoeld naar zeer lage temperaturen. Beneden een bepaalde temperatuur, de zogenaamde kritische temperatuur, ook wel T_c genoemd, verdwijnt in deze materialen de electrische weerstand. Ieder materiaal heeft zijn eigen karakteristieke kritische temperatuur. Bijvoorbeeld bij kwik, het eerste materiaal waarvoor dit fenomeen werd waargenomen door de Nederlander Kamerlingh Onnes in 1911, treedt supergeleiding op beneden -269 °C. Dit betekent dat als ik aan één kant van een draad, gemaakt van een supergeleider, er een bepaalde hoeveelheid energie in stop, er aan de andere kant precies evenveel uitkomt. De energie wordt vervoerd in de vorm van een elektrische stroom, die altijd precies even groot is. Dit in tegenstelling tot de situatie in de koperdraden die iedereen in huis heeft. Voor koperdraden geldt dat er altijd energie verloren gaat als er een stroom van de ene naar de andere kant loopt. Een eigenschap zoals supergeleiding is natuurlijk van groot belang en kan gebruikt worden in vele toepassingen. Supergeleiders worden nu bijvoorbeeld al gebruikt bij het maken van een hersenscan in het ziekenhuis en bij grote computers in sommige rekencentra. Ook voor het opwekken van hoge magneetvelden bespaart het gebruik van supergeleiders vele kilowatts aan energie.

Er ligt echter een kleine boa constrictor onder het gras, namelijk dat het verschijnsel slechts optreedt bij vreselijk lage temperaturen, zo'n 270 tot 260 graden onder nul. Dit betekent dat alle energie die gewonnen wordt dankzij de verliesloze toestand van de supergeleider, eerst geïnvesteerd moet worden in het afkoelen van het materiaal.

Deze overweging brengt mij bij de toevoeging *"hoge temperatuur"*. In 1986 werd door een tweetal Zwitsers, J. George Bednorz en Karl Alex Müller, een nieuwe klasse van materialen ontdekt waarbij supergeleiding al optreedt bij veel hogere temperaturen. Met dien verstande dat "hoge temperatuur" nog altijd een relatief begrip is, zoals blijkt uit de gemeten kritische temperaturen, die variëren van -235 °C voor $La_{2-x}Ba_xCuO_4$ (het materiaal dat werd ontdekt door Bednorz en Müller), tot -139 °C voor $Hg_2Ba_2Ca_2Cu_3O_{10}$, het huidige record. De ultieme droom van een supergeleider bij kamertemperatuur lijkt nog altijd ver weg, maar is dankzij het fundamentele onderzoek niet langer volstrekt ondenkbaar.

De ontdekking is des te verassender wanneer men in aanmerking neemt dat het hier gaat om zogenaamde keramische materialen, vergelijkbaar bijvoorbeeld met uw en mijn theekopjes. En ik kan u verzekeren, een stroom sturen door een theekopje gaat verdraaid slecht.

De voornaamste reden voor het enorme enthousiasme bij de ontdekking van de keramische materialen, was het doorbreken van een magische temperatuursgrens, -196 °C. Om deze grens uit te leggen moet ik eerst wat dieper ingaan op de techniek van het afkoelen van materialen naar dergelijke lage temperaturen. Om een supergeleider af te koelen wordt het gemonteerd in een zogenaamde *cryostaat*. Dat is een duur woord, voor iets wat in feite niets anders is dan een thermosfles. Het binnenste van de cryostaat is thermisch zo goed mogelijk geïsoleerd van de buitenkant, waardoor het binnenste een tijdlang koud gehouden kan worden, net zoals het bier in een thermosfles aan het strand een tijdlang koud blijft. Dit koud houden wordt gedaan m.b.v. *cryogene vloeistoffen*, die speciaal voor dit doeleinde worden geprepareerd. Deze vloeistoffen hebben een goed gedefinieerd kookpunt, net als water dat heeft bij 100 °C. Zolang het een vloeistof blijft, is de bijbehorende temperatuur lager of gelijk aan dat kookpunt. Door de supergeleider in het binnenste van de cryostaat dichtbij zo'n vloeistof te brengen, wordt ook dat materiaal afgekoeld tot dezelfde temperatuur.

De meest gebruikte cryogene vloeistoffen zijn helium en stikstof, met een kookpunt van respectievelijk -269 en -196 °C. Het grote verschil tussen deze beide vloeistoffen, behalve het kookpunt, is het gemak en de kosten gemoeid met het gebruik. Stikstof, met name vanwege een veel grotere beschikbaarheid, is veel goedkoper en tevens eenvoudiger in het gebruik. Dit betekent dat de ontdekking van supergeleiding boven het kookpunt van stikstof in potentie het gebruik van supergeleiders in nuttige toepassingen sterk vereenvoudigd.

Dat dit tot nu toe echter nog niet is gebeurd, heeft meerdere oorzaken. Allereerst is het nogal lastig om deze hoge temperatuur supergeleiders (HTSC's) te fabriceren, zoals al is af te zien aan de chemische formules die ik eerder heb gegeven. De HTSC's bestaan uit een fors aantal elementen, zoals bijvoorbeeld yttrium (Y), barium (Ba), koper (Cu) en zuurstof (O). Dit maakt het uitermate lastig om het juiste materiaal in de juiste samenstelling te maken. Om een voorbeeld te geven: $YBa_2Cu_3O_{7-\delta}$ is een supergeleider met een kritische temperatuur van -181 °C, maar als je van dit materiaal van elke 7 aanwezige zuurstof atomen er 1 verwijdert, resteert een voor elektrische toepassingen nutteloze isolator in plaats van de gewenste supergeleider. Ook het bewerken van de HTSC's is moeilijk, omdat keramische materialen van nature nogal bros zijn. Op een kleine schaal (micro tot millimeters) gaat het nog wel, maar stel je voor dat je een lange draad moet trekken van het eerder genoemde theekopje, dat is voorwaar geen eenvoudige taak.

Alsof de problemen met de fabricage nog niet erg genoeg zijn, hebben deze materialen ook nog eens zgn. *intrinsieke* eigenschappen die het gebruik in toepassingen bemoeilijken. Met intrinsiek worden die eigenschappen bedoeld die bij een specifiek materiaal horen, ofwel eigenschappen die je altijd in dat materiaal zult aantreffen, hoe goed of hoe slecht het ook is geprepareerd. Een aantal van die intrinsieke eigenschappen zijn het onderwerp van het proefschrift wat nu voor u ligt.

In dit proefschrift worden een aantal experimentele resultaten beschreven waarbij de optische eigenschappen van de hoge temperatuur supergeleiders worden onderzocht, ofwel:

De Electrodynamica van Hoge T_c Supergeleiders bij Lage Energieën.

Alvorens te concentreren op de preciese experimenten, resultaten en conclusies van dit proefschrift zal ik als laatste proberen de begrippen *lage energieën* en *optisch* wat beter uit te leggen.

Meestal, als men over licht praat, wordt daar *zichtbaar* licht mee bedoeld. De kleurige lichten van de neon reklames, het witte licht van een gloeilamp, enz. Het zichtbare licht is echter slechts een miniem deel van alle straling om ons heen. Andere soorten straling (allemaal met het oog niet waarneembaar) zijn bijvoorbeeld ultraviolette straling (u kent het wel, daar worden we in de zomer bruin van) en Röntgen-straling, wat gebruikt wordt voor het maken van foto's van botbreuken e.d. Een manier om al die verschillende soorten straling uit elkaar te houden is door te kijken naar de *energie*. Straling, ook zichtbaar licht, bestaat eigenlijk uit hele kleine afzonderlijke pakketjes energie, fotonen genaamd. Voor alle verschillende soorten straling hebben die fotonen een andere energie. Zeer laag energetische straling gebruikt men bijv. voor radiocommunicatie (dus ook Radio 3 en Kink FM). Straling met een iets grotere energie (microgolf straling) is tegenwoordig in vele keukens te vinden, in de magnetron. Vervolgens, voor een nog iets hogere energie komen we in het gebied terecht waar dit proefschrift zich bevindt, de millimeter-golf en ver-infrarood straling. Deze straling is nog steeds relatief laag energetisch, vandaar de titel van dit proefschrift. Een grotere energie hebben het "gewone" infrarood (waar zouden we zijn zonder de afstandbediening?), het zichtbare licht en de al eerder genoemde ultraviolette en Röntgen-straling.

In dit proefschrift hebben we millimeter-golf en ver-infrarood straling benut om iets te weten te komen over het binnenste van de HTSC's. De wijze waarop dit wordt gedaan ligt verborgen in de term *optisch*. M.b.v. verschillende optische meettechnieken hebben we supergeleiders onderzocht ten einde meer te weten te komen over de eerder genoemde intrinsieke eigenschappen. We richten in dit soort experimenten een goed gedefinieerde stralenbundel op de supergeleider (het "sample"), wat zich in de cryostaat bevindt. In het algemeen, als straling een stuk materiaal raakt, kunnen er drie dingen gebeuren. Ten eerste, het kan gereflecteerd worden. Is niks nieuws, we staan tenslotte met zijn allen elke dag voor de spiegel! De tweede mogelijkheid is transmissie. Ook dat kent iedereen, het is namelijk de reden dat iedereen glazen ruiten heeft. De laatste optie is absorptie, in dit geval wordt de energie van de straling "opgeslokt" door het materiaal. Omdat uiteindelijk er geen energie verloren gaat, weten we dat de som van de reflectie, transmissie en absorptie coefficienten 100% moet zijn, gelijk aan hetgeen waarmee we begonnen zijn.

Door nu één, of nog beter, twee van de bovengenoemde eigenschappen te meten, voor licht met verschillende energieën, kunnen we bepaalde informatie winnen over het binnenste van het materiaal, ofwel de intrinsieke eigenschappen. Deze intrinsieke eigenschappen geven ons vervolgens informatie over het ontstaan van de supergeleiding. We weten dat supergeleiding ontstaat en bij welke temperaturen, maar wat precies de oorzaak van het ontstaan is in de HTSC's is nog altijd niet volledig duidelijk, iets waar ik later nog weer op terug zal komen.

In de laatste drie hoofdstukken zijn resultaten voor alle drie mogelijke metingen beschreven. Voordat we echter de experimentele resultaten beschrijven, wordt in de eerste vier hoofdstukken de benodigde achtergrondinformatie gegeven. Na de introduktie in hoofdstuk 1, wordt in hoofdstuk 2 de theorie behandeld die nodig is om de experimentele resultaten te kunnen begrijpen. Tevens is een overzicht gegeven van gerelateerde resultaten, door andere onderzoeksgroepen gerapporteerd. Hoofdstuk 3 behandelt de wiskundige formules die worden gebruikt om de metingen te beschrijven. Door deze modellen zo goed mogelijk aan de experimentele resultaten te "fitten", d.w.z. de berekende waarden zo dicht mogelijk bij de gemeten waarden te brengen, kunnen we de microscopische optische eigenschappen van het materiaal bepalen. In hoofdstuk 4 is de experimentele opstelling beschreven die tijdens het eerste deel van mijn promotieonderzoek is opgebouwd. Deze opstelling is gebruikt om bijna alle in het proefschrift beschreven resultaten te verkrijgen.

In het eerste experimentele hoofdstuk (5), worden reflectiemetingen beschreven aan verschillende supergeleiders. Zowel "lage" als "hoge" temperatuur supergeleiders komen aan bod, waarbij de eerste soort gebruikt wordt als testsample, omdat van deze klasse materialen wel de oorsprong van de supergeleiding bekend is.

Een belangrijke factor in het ontstaan van supergeleiding is het feit dat elektronen, de deeltjes die voor een elektrische stroom zorgen, paartjes gaan vormen. Het ontstaan van elektronparen is iets wat zowel in lage als in hoge temperatuur supergeleiders gebeurt. Echter, onder normale omstandigheden stoten twee elektronen elkaar af, wat betekent dat er kennelijk beneden T_c een extra aantrekkingskracht is die de afstotende kracht overwint. Voor die aantrekkingskracht, ofwel de lijm die beide elektronen bindt, zijn verschillende mogelijkheden. Voor de lage temperatuur supergeleiders, die ook wel *klassieke supergeleiders* worden genoemd, wordt deze lijm geleverd door het trillen van het rooster waarin de atomen zich bevinden. U kunt het zich voorstellen alsof het eerste elektron ergens een kuiltje maakt, en het tweede elektron er gezellig bij in rolt. Wat de lijm in de HTSC's is, is echter nog steeds niet volledig bekend.

Een mogelijkheid om wat meer informatie over de lijm te krijgen, is door te kijken naar de energie die het kost om de beide elektronen weer uit elkaar te krijgen. In klassieke supergeleiders is er een minimum hoeveelheid energie nodig om paren "op te breken". Energieën beneden deze waarde, waarvoor het niet mogelijk is een paar te breken, liggen in de zogenaamde energie kloof, ofwel de *energy gap*, de Engelse term die ook door vele Nederlanders wordt gehanteerd. Zowel de energy gap en zijn preciese gedaante, en ook de lijm die twee elektronen verbindt, zijn eigenschappen van een supergeleider die ik eerder met de term ”intrinsiek” heb aangegeven.

Als we dus straling met een energie die in de energy gap ligt op een supergeleider schijnen, kan deze straling geen paren opbreken, en dus niet geabsorbeerd worden. Als het materiaal dik genoeg is, kan er ook niets worden doorgelaten, en dus wordt al het licht gereflecteerd. De reflectie coefficient is 100%.

Voor hoge temperatuur supergeleiders is de situatie heel anders. Er wordt veelvuldig gespeculeerd dat in dit geval al bij oneindig kleine energieën een klein aantal paren gebroken wordt. Dat betekent dat de reflectie coefficient bij die hele lage energieën al niet meer 100% is, omdat een deel van de opvallende straling geabsorbeerd wordt. En naarmate de energie van de straling groter en groter wordt, kunnen er steeds meer paren gebroken worden, en gaat de reflectie coefficient meer en meer afwijken van 100%.

Het is echter heel moeilijk om de afwijking experimenteel vast te stellen, vooral bij lagere energieën, waar maar weinig paren gebroken worden en dus de absorptie klein is. Een alternatief is dan om de transmissie door een dunne supergeleidende laag te meten, omdat het tenslotte makkelijker is om iets van niets te onderscheiden dan iets van iets anders. Dit is gedaan in hoofdstuk 6. Ook hier worden eerst resultaten aan een tweetal klassieke supergeleiders gepresenteerd, voornamelijk om te laten zien dat de opstelling zoals die in hoofdstuk 4 is beschreven, werkt. In hoofdstuk 6 laten we zien d.m.v. het meten van de transmissie van mm-golf straling, dat inderdaad bij heel lage energieën er al een aantal paren worden gebroken, en dat dus de situatie voor HTSC's heel anders is dan voor klassieke supergeleiders. Met als logisch gevolg dat hoogstwaarschijnlijk ook de lijm anders is dan de roostertrillingen in het klassieke geval.

In hoofdstuk 7 gaan we de dingen nog een beetje gecompliceerder maken. (Waarom makkelijk doen als het moeilijk kan, nietwaar?) Niet alleen willen we nu de absorptie bij verschillende energieën heel precies meten, maar ook willen we weten hoe *snel* het absorptieproces is. Of, om het iets anders te formuleren, we willen niet alleen weten of en hoeveel paren er worden gebroken, maar tevens willen we weten hoe snel die elektronen weer paartjes vormen. Tenslotte is dat de toestand waar ze zich het prettigst bij voelen, dus zullen ze snel weer op zoek gaan naar een nieuwe partner.

De manier waarop dit experiment gedaan wordt is nieuw, en we hebben het experiment *PIAMA* gedoopt. Dit is de afkorting van het Engelse: ”Photo Induced Activation of Mm-wave Absorption”. In dit geval laten we *twee* lichtbundels tegelijkertijd op de supergeleider vallen. De ene (mm-golf straling) is altijd aanwezig, en hiervan wordt gemeten hoeveel straling er door de dunne supergeleidende laag komt.

Echter, die supergeleider wordt zo nu en dan in een andere toestand ”geschopt”, door een zeer sterke laser die korte ver-infrarood lichtpulsen uitzendt. In deze nieuwe toestand hebben we, m.b.v. het laserlicht, een groot aantal elektronparen gebroken. Op het moment dat de supergeleider in een andere toestand zit, is ook de transmissie en absorptie van de mm-golf straling veranderd. Een nogal verassend en niet eerder gemeten verschijnsel is dat we, afhankelijk van de temperatuur waarbij de supergeleider zich bevindt, m.b.v. de laser de transmissie van mm-golf straling zowel kunnen verhogen als verlagen. Door nu als functie van tijd te volgen hoe de transmissie terug gaat naar zijn oude waarde, nadat de laserpuls is afgelopen, weten we hoe snel de elektronen weer paren vormen.

In onze PIAMA-metingen komen we tot de conclusie dat paren worden gevormd binnen ongeveer 1 miljoenste seconde. Dat klinkt nogal snel, maar gezien het feit dat de meeste processen binnen een supergeleider (zowel in de klassieke als in de hoge temperatuur supergeleiders) plaats vinden binnen een duizendste van een miljoenste seconde, is deze observatie toch behoorlijk verassend. Deze constatering, samen met het eerder genoemde feit dat de transmissie zowel verhoogd als verlaagd kan worden, doet ons concluderen dat de tijdelijke toestand, geïnduceerd door de laserpuls, een bijzondere is. Ook concluderen we dat het "anders" zijn van de energy gap en de lijm in de hoge temperatuur supergeleiders een essentieel ingredient is in het ontstaan van deze bijzondere toestand.

Acknowledgements

Een van de meest gevaarlijke stukken dat voor een proefschrift geschreven wordt, is altijd de *acknowledgements*. Niet alleen omdat dit een van de weinige stukken van het proefschrift is wat door iedereen gelezen wordt, maar vooral omdat het trekken van de grens wie wel en wie niet te bedanken altijd erg moeilijk is. Hierbij wil ik dan ook iedereen bedanken die ook maar enigszins een bijdrage heeft geleverd aan het plezier en succes wat ik de laatste +/- vijf jaar tijdens het verrichten van mijn promotieonderzoek heb gehad. (Kan niemand zeggen dat hij/zij niet genoemd is!).

Van al die mensen zijn er een aantal die ik graag met naam en toenaam zou willen bedanken. Als eerste zou ik graag Dick willen bedanken voor alle input die hij mij gegeven heeft tijdens deze jaren. Ik weet zeker dat het proefschrift er heel anders uit had gezien zonder alle goede raad, berekeningen en kennis van jouw kant! Veel van de ontwikkeling die ik heb doorgemaakt tot de wetenschapper die ik nu ben, heb ik aan jouw te danken.

Minstens net zo belangrijk zijn mijn ouders en mijn familie geweest met hun begrip en steun, hoewel ze soms wel eens wat moeite hadden om te begrijpen waarom iemand in hemelsnaam vrijwillig tot diep in de nacht zou willen doorwerken.

Dat doorwerken zou nooit mogelijk zijn geweest, als dit geen collectief gebeuren was. Soms zou je denken dat sommige mensen bij het interieur horen (nietwaar, Anna-Maria?). Anna-Maria, bedankt voor de vele malen dat je bereid was mijn eindeloze gezever aan te horen, en dan ook nog met zinnig commentaar terug te komen. Amico mio! Come va? Well, I guess it's better to omit the other Italian words you taught me. Thanks, Andrea, for all the risotto you fed me! Markus, hartelijk bedankt voor je bereidheid om te discussieren. Of het nu om fysica ging of om iets anders, het was nimmer onmogelijk om je aandacht te krijgen. Dan is er nog de ”eeuwige” kamergenoot, Jeroen, zonder wie onze auto al jaren geleden op de schroothoop zou zijn beland. Mijn hartelijke dank voor deze reddingsakties.

Veel plezier heb ik ook gehad aan het samenwerken met de afstudeerders, wat altijd een leerproces van beide kanten oplevert. Alex, Frodo en Peter, bedankt voor alle plezierige momenten, jullie inbreng in het ontstaan van dit proefschrift is niet gering geweest!

The knowledge I have accumulated via the exchanges with ”our” post-docs Jae Kim and Jürgen Schützmann is immeasurable. Both are familiar with the Bruker spectrometer as if they had one at home. I would like to thank Jürgen for his help during the very pleasant time I had in Nieuwegein, I hope you enjoyed it just as much as I did. Furthermore, I would like to thank J. D. and J. W. for their unconditional presence when I needed them. Voor alle hulp die ik heb gehad tijdens beide periodes dat ik bij FELIX heb gemeten, wil ik graag het hele FELIX-team bedanken.

Dan is er nog diegene die niet genoemd wil worden, dat zal ik dan ook niet doen. Hartelijk dank Cor (oeps), voor het mogen putten uit die schier onuitputtelijke hoeveelheid kennis, waarvan ik met name in de eerste jaren, de opbouwfase, veelvuldig gebruik heb gemaakt. Verder mijn hartelijke dank aan Hermen, Hans, Jeroen van der Brink, Diana, Herpertap, Artem, Michel, Dennis, Karina, Gerhard, Klaas-Jelle, Hajo, Ronald, Salvatore, Stefania en Oana, voor hun commentaren en andere bijdragen aan het plezier wat ik heb gehad tijdens mijn promotietijd.

Right before the end of my graduate research, it was made clear to me that there it still much more that I should learn, thanks to the visit of and the collaboration with Walter Hardy. Thanks, Walter, for sharing some of your vast knowledge with me, and doing it in such a way that I didn't need to feel like a complete fool.

One of the highlights of my PhD-period, in many respects, has been a workterm of three months at the University of California in Los Angeles. This was made possible by the generous invitation of Professor George Grüner, for which I now have the opportunity to thank him. Also I would like to thank Andy, Martin, Francois, Sylvie, B. A., Boris and last but not least Viki, for the great time I had!

Als allerlaatste wil ik Steven en Annemarie bedanken voor de ontelbare keren dat zij er in zijn geslaagd mijn aandacht van het lab los te peuteren, hetzij om eens iets anders te eten dan diepvriespizza of om een potje te boerenbridgen. Wat het excuus ook was, jullie steun, gezelschap en gewillige oren zijn van onschatbare waarde geweest.